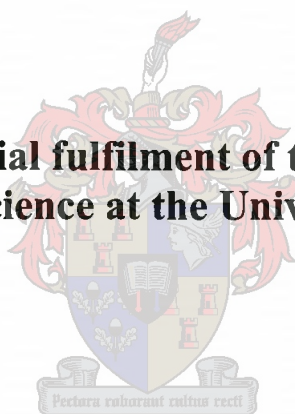


Development and Optimisation of a Solid-State Pulsed Power Supply for a CO₂ TEA Laser

by

Timo Stehmann

**Thesis presented in partial fulfilment of the requirements for the
degree of Master of Science at the University of Stellenbosch**



**Supervisors: Prof. H.M. von Bergmann
Prof. T. Mouton**

December 2003

Declaration / Verklaring

I, the undersigned, hereby declare that the work contained in this thesis is my own original work and that I have not previously in its entirety or in part submitted it at any other university for a degree.

Ek, die ondergetekende, verklaar hiermee dat die werk in hierdie tesis vervat, my eie oorspronklike werk is en dat ek dit nie vantevore in die geheel of gedeeltelik by enige ander universiteit ter verkryging van 'n graad voorgelê het nie.

Timo Stehmann

Date / Datum

Abstract

With technological advances in solid-state switches the modernization of conventional pulsed power supplies utilizing thyratrons has become possible. A novel pulsed power supply is designed where two series-stacked IGBTs (rated at 1700 V and 300 A each) are used to replace a thyatron-driven pulsed power supply for a mini CO₂ TEA laser.

The mini CO₂ TEA laser is firstly characterized in order to optimize the design of the pulsed power supply. It is found that stable laser discharges can be obtained with electrode voltage rise-times of 150 ns or less. Furthermore, the optical output energy and the efficiency of the laser have been significantly increased by reducing the peaking capacitor size of the pulsed power supply.

The two stacked IGBTs switch a C-C transfer loop and the generated pulse is stepped up by a pulse transformer and is compressed by a two-stage magnetic pulse compression unit. Theoretically and through measurements it is shown that automatic voltage sharing between the two IGBTs can be obtained if the turn-on time of the IGBTs is much faster than the transfer time of the switched C-C transfer loop. Lifetime tests reveal that high-power IGBTs are able to reliably switch pulses with peak currents between 4 and 5 times the rated average current of the device. Under laser fault conditions, i.e. laser arcing or missing laser discharges, the reliability of the pulser can be increased by using over-voltage snubbers. In addition, it was found that the internal diode of IGBT modules can eventually fail under the prevalence of laser fault conditions.

A modular construction approach is used where components of the pulsed power supply are pre-assembled. A new rectangular layout of the magnetic pulse compression unit is utilized in order to minimize size and simplify the final construction and assembly.

Opsomming

Nuwe ontwikkeling in vastetoestand-skakelaars het die modernisering van laser-pulskragbronne moontlik gemaak. 'n Nuwe kragbron wat gebruik maak van twee seriegeskakelde IGBT's is ontwerp om 'n Tiratron-gedrewe laserkrugbron te vervang, wat vir 'n mini-CO₂-TEA-laser gebruik word.

Die laser is vooraf eers gekarakteriseer om sodoende die laserkrugbron te optimeer. Daar is bevind dat stabiele laserontladings verkry kan word met spanningstygtye van 150 ns of minder. Verder kan die uittree-energie van die laser beduidend verhoog word deur die uittreekapasitore (eng.: *peaking capacitors*) van die laserkrugbron te verminder.

Die twee serie-geskakelde IGBT's skakel 'n C-C oordraglus. Die spanning van die gegenereerde puls word deur 'n pulstransformator verhoog en die stygtyd van die puls word met 'n twee-stadium magnetiese pulskompressor verlaag. Teoreties en deur metings kan getoon word dat eweredige spanningsverdeling tussen die twee IGBT's outomaties verkry kan word indien die skakeltye van die IGBT's baie vinniger as die oordragtyd van die C-C oordraglus is. Toetse het getoon dat IGBT's pulse met piekstrome van tussen vier tot vyf keer die gespesifiseerde gemiddelde stroom betroubaar kan skakel. Tydens laserfouttoestande kan die betroubaarheid van die IGBT verhoog word deur oorspanningsgapsers te gebruik, maar onder fouttoestande wat voortduur, kan die IGBT se interne diode vernietig word.

Die komponente van die laserkrugbron is as modules vervaardig, wat op 'n maklike wyse gemonteer kan word. 'n Nuwe reghoekige uitleg is gebruik vir die konstruksie van die magnetiese pulskompressor, waarmee die grootte van die pulskompressor geminimeer en die konstruksie vergemaklik is.

Acknowledgment / Erkennings

I want to thank the following people and institutions for their help during this project:

- SDI (Scientific Development and Integration) for supplying the mini CO₂ TEA laser for this project.
- The National Research Foundation for providing funding for this project.
- Department of Labour for providing Scarce Skills Bursaries.

Ek wil graag my dank en opregte waardering teenoor die volgende persone uitspreek:

- Ilse Jordaan, vir haar liefde, bystand en ondersteuning.
- My ouers, vir hulle ondersteuning en motivering.
- Ulrich Deutschländer, wat die bestellings en aankoop van komponente vir hierdie projek behartig het.
- Hencharl Strauss - 'n medestudent en goeie vriend.

Contents

Symbols and Abbreviations	xi
List of Figures	xiii
List of Tables	xviii
1. Introduction	1
1.1. Problem statement.....	1
1.2. Aim.....	3
1.3. Outline.....	3
2. Laser pulsed power supply circuit topologies and components	5
2.1. Topology overview.....	5
2.1.1. C-C transfer topology.....	6
Directly switched C-C transfer loop.....	7
LC-inversion circuit.....	8
2.1.2. Conclusion.....	9
2.2. Primary switching unit.....	10
2.2.1. Circuit analysis.....	10
2.2.2. Optimisation.....	14
Optimisation of C-C transfer loops without losses ($\alpha = 0$).....	14
Optimisation of C-C transfer loops with losses ($\alpha > 0$).....	14
2.2.3. Switching currents.....	18
2.3. Magnetic pulse compression unit.....	19
2.3.1. Saturable inductors as passive current-controlled switches.....	20
2.3.2. Series magnetic pulse compression topology.....	24
2.3.3. Voltage hold-off and MPC timing.....	27
2.3.4. Estimate and minimization of total magnetic core volume.....	29
2.4. Pulse transformers.....	31
2.4.1. Characteristics of a pulse transformer in a C-C transfer loop.....	32
2.4.2. Leakage inductance.....	33
2.4.3. Core magnetization.....	34

2.4.4. Transformer losses	35
Eddy current losses	35
Hysteresis losses	37
Conduction (copper losses)	38
2.5. Conclusion	39
3. Characteristics of an IGBT in a pulsed power supply	41
3.1. IGBT circuit model	41
3.2. IGBT dynamic response in a C-C transfer loop	44
3.2.1. Turn-on delay time	46
3.2.2. Voltage fall-time	46
3.2.3. On-state	50
3.2.4. Decoupling criteria and magnetic assist	51
3.2.5. Simulations of IGBT turn-on transient	53
3.3. Conduction losses and thermal design considerations	56
3.3.1. Average conduction losses	56
3.3.2. Thermal considerations	57
3.4. Series stacking and paralleling of IGBTs	59
3.4.1. Series stacking	59
3.4.2. Paralleling	61
3.5. Over-current capability of IGBTs	62
3.6. Conclusion	63
4. Characteristics of a pulsed mini CO₂ TEA laser	64
4.1. Test set-up	64
4.2. Discharge stability	66
4.2.1. Pre-ionisation and stability	66
Parallel pre-ionisation	67
Series pre-ionisation	69
4.2.2. Stable operating region and peaking capacitor size	70
4.2.3. Voltage rise-time and stability	71
4.2.4. Matching and stability	73
4.3. Output energy and efficiency	76
4.3.1. Peaking capacitor size and excitation approaches	76
4.3.2. Output energy and efficiency for $C_s = C_p$	77

4.3.3. Output energy and efficiency for $C_s > C_p$	81
4.3.4. Output energy and efficiency for commercial thyatron based pulsed power supply.....	84
4.4. Voltage and current waveforms.....	88
4.4.1. Comparison of discharge voltages.....	90
4.4.2. Comparison of current waveforms.....	91
4.4.3. Comparison of discharge energies.....	92
4.4.4. Comparison of optical pulse shapes.....	93
4.5. Summary.....	94
5. Laser pulsed power supply design and construction	95
5.1. Pulsed power supply design.....	96
5.1.1. Design outline.....	96
5.1.2. Design results.....	98
5.1.3. Pulsed power components.....	104
5.1.4. Pulsed power circuit simulation.....	105
5.2. Primary switching unit construction.....	109
5.2.1. Charging of the storage capacitor.....	109
5.2.2. IGB drivers.....	110
5.2.3. Transfer inductance.....	111
5.3. Pulse transformer design and construction.....	111
5.3.1. Design outline.....	112
5.3.2. Design and construction.....	114
5.3.3. Transformer measurements.....	120
5.4. MPC unit construction.....	121
5.4.1. Saturable inductor module assembly.....	121
5.4.2. MPC unit assembly.....	123
6. Reliability	127
6.1. Lifetime testing.....	127
6.1.1. Test set-up.....	128
6.1.2. Measurement of IGBT characteristics.....	130
Thermal resistance.....	131
Electrical characteristics.....	134
6.1.3. Results.....	135
6.1.4. Conclusion.....	138

6.2. Fault handling capability.....	139
6.2.1. Fault conditions and behaviour.....	139
6.2.2. IGBT protection.....	141
IGBT timing.....	142
Over-voltage snubber.....	142
6.2.3. IGBT lifetime under fault conditions.....	144
6.2.4. Conclusion.....	147
6.3. Electromagnetic interference (EMI).....	148
7. Pulsed power supply measurements	150
7.1. Voltage and current waveforms.....	150
7.1.1. Normal operating conditions.....	151
7.1.2. Fault conditions.....	154
No laser discharge.....	155
Laser arcing.....	156
7.1.3. IGBT voltage sharing.....	157
7.1.4. Conclusion.....	157
7.2. Stability.....	158
7.3. Output energy and efficiency.....	158
7.3.1. Conclusion.....	162
8. Conclusion	163
8.1. IGBTs in laser pulsed power supplies.....	163
8.2. IGBT peak current rating, lifetime and reliability.....	164
8.3. MPC unit construction.....	165
8.4. Optimisation of a mini CO ₂ TEA laser.....	166
8.5. Future work.....	167
A. Appendix: PSpice simulation models	168
A.1. Saturable inductor model.....	168
A.2. Discharge model of high-pressure CO ₂ laser.....	169
B. Appendix: Circuit diagrams	173
B.1. IGBT timing unit.....	173
B.2. IGBT driver unit.....	174

B.3. Current limiter.....	175
B.4. Over-voltage snubber.....	176
C. Appendix: IGBT data sheets	177
Bibliography	184

Symbols and Abbreviations

Symbols

a	transformer turns ratio
B	magnetic flux density, T
C	capacitance, F
D	duty cycle
E	energy, J
f	frequency, Hz
F	timing factor
g	magnetic compression ratio per stage
G	total magnetic compression ratio
H	applied magnetic field, A/m
I	constant (fixed) current, A
i	time-dependent current, A
k	capacitor ratio, switching ratio
L	inductance, H
N	number of windings
p	packing factor (ratio)
R	resistance, Ω
r	small-signal resistance, Ω
R	thermal resistance, K/W
t	time, s
T	period, s, temperature, K
V	constant (fixed) voltage, V
v	time-dependant voltage, V
Z	thermal impedance, K/W
$\Delta\Phi$	magnetic flux change, Wb
Φ	transfer efficiency
ϕ	phase angle, rad
α	damping factor, s^{-1}
ρ	conductivity,
τ	transfer time, s
μ	magnetic permeability, $H.m^{-1}$
ω	radian frequency ($2\pi f$), $rad.s^{-1}$

Subscripts:

0	starting, initial, beginning
avg	average
C	collector, capacitor
CE	collector-emitter
charge	charging path
core	core
cs	case to heatsink
Cu	copper
d	delay
ec	eddy current

equ	equivalent
<i>f</i>	fall, forward
<i>G</i>	gate
<i>GE</i>	gate-emitter
hold	hold-off
hys	hysteresis
<i>i</i>	initial
in	input
inv	inversion
<i>J</i>	current density
<i>j</i>	junction
<i>jc</i>	junction to case
<i>L</i>	inductor
leak	leakage
loss	losses
mag	magnetization
max	maximum
<i>n</i>	index, number of MPC stage
opt	optimum
out	output
<i>p</i>	primary
par	parasitic
peak	peak, maximum
pulse	for pulse duration
rep	repetition rate
rise	voltage rise
RMS	root-mean-square
<i>s</i>	switch, saturated, secondary
<i>sa</i>	heatsink to ambient
sat	saturated
sp	specific
<i>ss</i>	steady-state
<i>sw</i>	switching
<i>t</i>	transfer, total
<i>th</i>	thermal
<i>Th</i>	threshold
<i>u</i>	unsaturated
unsat	unsaturated
<i>w</i>	winding

Abbreviations

GTO	Gate Turn-Off Thyristor
IGBT	Insulated Gate Bipolar Transistor
IR	Infrared
MOSFET	Metal-Oxide-Semiconductor Field-Effect Transistor
MPC	Magnetic Pulse Compression
TEA	Transverse Excited Atmospheric
UV	Ultra-violet

List of Figures

Figure 2-1:	Basic C-C transfer pulsed power supply layout.....	6
Figure 2-2:	Circuit diagram of a directly switched C-C transfer loop.....	7
Figure 2-3:	Circuit diagram of a directly switched C-C transfer loop with pulse transformer.....	7
Figure 2-4:	Circuit diagram of LC-inversion topology.....	8
Figure 2-5:	Circuit diagram of a super inversion pulser topology.....	9
Figure 2-6:	Circuit diagram of a directly switched C-C transfer loop.....	10
Figure 2-7:	Normalized waveform of the input voltage $v_{C1}(t)$ of a C-C transfer loop.....	12
Figure 2-8:	Normalized waveform of the output voltage $v_{C2}(t)$ of a C-C transfer loop.....	12
Figure 2-9:	Normalized current waveform of the C-C transfer current $i_t(t)$	13
Figure 2-10:	Two-dimensional colour contour graph of the C-C transfer efficiency as a function of the capacitor ratio k for two different optimisation approaches.....	15
Figure 2-11:	Capacitor ratio for two different optimisation methods vs. transfer losses in a C-C transfer loop.....	16
Figure 2-12:	Transfer efficiency for two different optimisation methods vs. transfer losses in a C-C transfer loop.....	16
Figure 2-13:	True transfer losses for two different optimisation methods vs. transfer losses in a C-C transfer loop.....	17
Figure 2-14:	Remaining energy on input capacitor C_1 for two different optimisation methods vs. transfer losses in a C-C transfer loop.....	17
Figure 2-15:	Transfer time for two different optimisation methods vs. transfer losses in a C-C transfer loop.....	17
Figure 2-16:	BH-curve of a saturable inductor.....	21
Figure 2-17:	Simple example illustrating the switching behaviour of a saturable inductor.....	23
Figure 2-18:	Typical pulsed power supply topology with series MPC stages.....	24
Figure 2-19:	Typical voltage and current waveforms obtained in a series MPC topology.....	25
Figure 2-20:	Series magnetic pulse compression stage based on the C-C transfer loop.....	25
Figure 2-21:	Voltage and current waveforms in a Magnetic pulse compression stage.....	26
Figure 2-22:	Saturated flux content of the core of a saturable inductor vs. the switching ratio k_{sw}	29
Figure 2-23:	Circuit diagram of C-C transfer loop with pulse transformer.....	31

Figure 2-24:	Equivalent T-network pulse transformer model in a C-C transfer loop.....	32
Figure 3-1:	IGBT as a combination of a MOSFET and BJT.....	42
Figure 3-2:	Transfer characteristics of an IGBT.....	43
Figure 3-3:	Saturated collector current of an IGBT as a function of the gate-emitter voltage.....	43
Figure 3-4:	Equivalent circuit model of an IGBT.....	44
Figure 3-5:	Equivalent circuit model of an IGBT in a C-C transfer loop.....	44
Figure 3-6:	General turn-on switching waveforms of an IGBT.....	45
Figure 3-7:	Equivalent circuit model during the turn-on delay.....	46
Figure 3-8:	Equivalent circuit during the voltage fall period.....	47
Figure 3-9:	Equivalent circuit during the IGBT on-state.....	50
Figure 3-10:	Equivalent circuit during initial voltage fall-time with injection of an external C-C transfer current.....	51
Figure 3-11:	IGBT turn-on transient decoupling by magnetic assist.....	53
Figure 3-12:	IGBT gate-emitter and collector-emitter voltages during the turn-on transient.....	54
Figure 3-13:	IGBT gate-emitter and gate-collector capacitor currents during the turn-on transient.....	54
Figure 3-14:	Simulated IGBT turn-on transient demonstrating the effect of decoupling.....	55
Figure 3-15:	Power dissipation in an IGBT in a pulsed power supply.....	56
Figure 3-16:	Junction-case temperature difference of an IGBT in a pulsed power supply.....	58
Figure 3-17:	Typical graph specifying the transient thermal impedance of an IGBT.....	58
Figure 3-18:	Circuit diagram of series stacked IGBTs in a C-C transfer loop.....	60
Figure 3-19:	Circuit diagram of paralleled IGBTs in a C-C transfer loop.....	61
Figure 4-1:	Excitation test circuit to determine the electrical characteristics of the laser.....	65
Figure 4-2:	Excitation circuit with parallel pre-ionisation.....	67
Figure 4-3:	Timing of parallel pre-ionisation discharge.....	68
Figure 4-4:	Discharge voltage for insufficient and sufficient pre-ionisation.....	68
Figure 4-5:	Excitation circuit with series pre-ionisation.....	69
Figure 4-6:	Timing of series pre-ionisation discharge.....	70
Figure 4-7:	Stable operating region for parallel and series pre-ionisation.....	71
Figure 4-8:	Stable operating region for different voltage rise-times (1:1:8 mixture).....	72
Figure 4-9:	Stable operating region for different voltage rise-times (1:1:3 gas mixture).....	73
Figure 4-10:	Arcing during reverse voltage overshoot.....	74

Figure 4-11: Stable operating region as a function of the peaking capacitor size for two transfer inductances. (1:1:3 gas mixture).....	75
Figure 4-12: Optical output energy vs. inductance L_t for three charging voltages V_0 . (1:1:8 mixture).....	78
Figure 4-13: Optical output energy vs. charging voltage V_0 and inductance L_t . (1:1:8 mixture).....	78
Figure 4-14: Efficiency vs. inductance L_t for three charging voltages V_0 . (1:1:8 mixture).....	79
Figure 4-15: Efficiency vs. charging voltage V_0 and inductance L_t . (1:1:8 mixture).....	79
Figure 4-16: Optical output energy vs. charging voltage V_0 and inductance L_t . (1:1:3 mixture).....	80
Figure 4-17: Efficiency vs. charging voltage V_0 and inductance L_t . (1:1:3 gas).....	81
Figure 4-18: Optical output energy vs. charging voltage and peaking capacitor size. (1:1:8 mixture).....	82
Figure 4-19: Efficiency vs. charging voltage and peaking capacitor size. (1:1:8 mixture).....	82
Figure 4-20: Optical output energy vs. charging voltage and peaking capacitor size. (1:1:3 mixture).....	83
Figure 4-21: Efficiency vs. charging voltage and peaking capacitor size. (1:1:3 mixture).....	84
Figure 4-22: Optical output energy vs. charging voltage and gas pressure for commercial thyatron based pulsed power supply. (1:1:8 mixture).....	85
Figure 4-23: Efficiency vs. charging voltage and gas pressure for commercial thyatron based pulsed power supply. (1:1:8 mixture).....	85
Figure 4-24: Optical output energy vs. charging voltage and gas pressure for commercial thyatron based pulsed power supply. (1:1:3 mixture).....	86
Figure 4-25: Efficiency vs. charging voltage and gas pressure for commercial thyatron based pulsed power supply. (1:1:3 mixture).....	86
Figure 4-26: Comparison of optical output energy of commercial and optimised experimental pulsers.....	87
Figure 4-27: Comparison of efficiency of commercial and optimised experimental pulsers.....	88
Figure 4-28: Diagram to indicate measured voltages and currents.....	88
Figure 4-29: Comparison of discharge voltages for $C_s = C_p$ and $C_s > C_p$	90
Figure 4-30: Comparison of inductor currents for $C_s = C_p$ and $C_s > C_p$	91
Figure 4-31: Comparison of discharge currents for $C_s = C_p$ and $C_s > C_p$	91
Figure 4-32: Comparison of energy transfers into discharge for $C_s = C_p$ and $C_s > C_p$	92

Figure 4-33:	Optical pulse shape for $C_s = C_p$ and $C_s > C_p$.	93
Figure 5-1:	Flow chart of a laser pulsed power supply design procedure.	96
Figure 5-2:	Proposed topology for the pulsed power supply.	99
Figure 5-3:	Simulated pulsed power supply circuit.	106
Figure 5-4:	Simulated current waveforms.	106
Figure 5-5:	Simulated voltage waveforms.	107
Figure 5-6:	Close-up of simulated output voltage, discharge current and transfer current of Loop2.	108
Figure 5-7:	Energy deposited into discharge.	108
Figure 5-8:	Charging supply protection.	109
Figure 5-9:	IGBT driver unit layout.	110
Figure 5-10:	Flow chart of a pulse transformer design procedure.	112
Figure 5-11:	U-type core assembly.	115
Figure 5-12:	Cross-sectional diagram of the pulse transformer.	118
Figure 5-13:	Assembly of a MPC inductor module.	122
Figure 5-14:	PCB artwork used for the winding configuration of MPC inductors.	123
Figure 5-15:	Basic electrical and mechanical layout of the MPC unit assembly.	124
Figure 5-16:	Three-dimensional model of complete MPC unit assembly (front view).	125
Figure 5-17:	Three-dimensional model of complete MPC unit assembly (elevated view).	125
Figure 5-18:	Approximation of MPC stage parasitic inductance for rectangular MPC unit layout.	126
Figure 6-1:	Experimental set-up for IGBT lifetime testing.	128
Figure 6-2:	Current waveform obtained for IGBT lifetime testing.	130
Figure 6-3:	Measurement set-up to determine the thermal resistance of an IGBT.	132
Figure 6-4:	Forward voltage drop vs. junction temperature ($I_f = 1$ mA) of the internal reverse diode of the SKM300GB174D IGBT module from Semikron.	133
Figure 6-5:	Measurement set-ups to determine the electrical characteristics of an IGBT.	134
Figure 6-6:	Measured thermal junction-to-case resistance of IGBT during lifetime test.	136
Figure 6-7:	Measured IGBT C-to-E electrical characteristics during lifetime test.	137
Figure 6-8:	Measured IGBT G-to-E electrical characteristics during lifetime test.	137
Figure 6-9:	Measured IGBT CG-to-E electrical characteristics during lifetime test.	138
Figure 6-10:	Simulated IGBT switching current under laser fault condition (laser fails to discharge).	141

Figure 6-11:	Circuit diagram of an over-voltage snubber.....	142
Figure 6-12:	Over-voltage snubber behaviour.....	143
Figure 6-13:	Experimental set-up for IGBT lifetime testing under fault conditions.....	144
Figure 6-14:	Waveforms obtained under mimicked fault conditions with IGBT timing, but without snubber.....	146
Figure 6-15:	Waveforms obtained under mimicked fault conditions with IGBT timing and over-voltage snubber.....	146
Figure 6-16:	Shielding of laser head and MPC unit.....	149
Figure 7-1:	Voltage and current waveforms of the primary switching unit under normal operating conditions.....	151
Figure 7-2:	Voltage waveforms of the MPC unit under normal operating conditions.....	152
Figure 7-3:	Output (laser excitation) voltage waveform.....	153
Figure 7-4:	Comparison of the simulated and measured output voltage waveforms.....	154
Figure 7-5:	IGBT current and voltage waveforms in the absence of a laser discharge.....	155
Figure 7-6:	IGBT current and voltage waveforms in the absence of a laser discharge with IGBT timing and over-voltage snubber.....	156
Figure 7-7:	IGBT current and voltage waveforms in case of laser arcing with IGBT timing and over-voltage snubber.....	156
Figure 7-8:	IGBT voltage sharing during turn-on and turn-off under fault conditions.....	157
Figure 7-9:	Optical output energy vs. input energy and laser gas pressure with new solid-state pulsed power supply. (1:1:3 mixture).....	159
Figure 7-10:	Optical output energy vs. input energy and laser gas pressure with new solid-state pulsed power supply. (1:1:3 mixture).....	159
Figure 7-11:	Optical output energy vs. input energy for the optimised experimental and new solid-state pulser. (1:1:3 mixture).....	161
Figure 7-12:	Efficiency vs. input energy for the optimised experimental and new solid-state pulser. (1:1:3 mixture).....	161
Figure A-1:	Ionisation and attachment coefficients as a function of E/N in CO ₂ TEA lasers with a 1:1:8 gas mixture.....	170
Figure A-2:	Drift velocity as a function of E/N in CO ₂ TEA lasers with a 1:1:8 gas mixture.....	170
Figure A-3:	Polynomial fits of the attachment and ionisation coefficients vs. E/N	171
Figure A-4:	Polynomial fit of the drift velocity vs. E/N	171
Figure A-5:	Implementation of the physical discharge model in PSpice.....	172

Figure B-1:	Circuit diagram of IGBT timing unit.....	173
Figure B-2:	Circuit diagram of IGBT driver unit.....	174
Figure B-3:	Circuit diagram of solid-state current limiter.....	175
Figure B-4:	Circuit diagram of over-voltage snubber.....	176

List of Tables

Table 4-1:	Summary of electrical measurement results.....	94
Table 5-1:	Design specifications of the pulsed power supply.....	95
Table 5-2:	Ratings of IGBT module used in primary switching unit.....	100
Table 5-3:	Core parameters and dimensions of MPC unit.....	101
Table 5-4:	Spreadsheet-aided design results for the MPC and primary switching units.....	103
Table 5-5:	Practical capacitor values.....	105
Table 5-6:	Design specifications of the IGBT driver unit.....	111
Table 5-7:	Design specifications of the pulse transformer.....	114
Table 5-8:	Transformer core dimensions and parameters.....	115
Table 5-9:	Number of primary and secondary transformer windings.....	116
Table 5-10:	Primary winding configuration.....	117
Table 5-11:	Secondary winding configuration.....	117
Table 5-12:	Summary of transformer losses.....	120
Table 5-13:	Summary of transformer measurements.....	121
Table 6-1:	Circuit values for lifetime test set-up.....	130
Table 6-2:	Test conditions for lifetime testing.....	136
Table 6-3:	Measured IGBT parameters.....	138
Table 6-4:	Circuit values for test set-up to simulate fault conditions.....	145
Table 6-5:	Results of lifetime tests under fault conditions.....	147
Table 7-1:	Transfer efficiencies of primary switching unit and 1st MPC stage.....	153
Table A-1:	Parameters of the Jiles-Atherton core model.....	168

Chapter 1

Introduction

Since the construction of the first laser in 1960 by Maiman great advances have been made in laser development. Although the laser built by Maiman was a solid-state ruby laser, gas lasers were the first type of lasers manufactured on a large scale and applied in industry. Among the most widely used gas lasers in industry today are the CO₂ and Excimer lasers. The CO₂ laser emits in the infrared spectrum and can be operated in continuous or pulsed mode. The most common applications for CO₂ lasers include photo-chemistry (isotope separation) and materials processing, i.e. cutting, drilling and welding. The Excimer laser on the other hand emits in the ultraviolet and is widely used for lithography as well as photo-chemistry, by virtue of the short laser wavelength emitted.

1.1 Problem statement

Continuous mode CO₂ lasers are operated at low gas pressures and the laser gas medium is excited by low-pressure electric discharges. The current densities of the discharges are normally relatively small and the electric excitation of low-pressure CO₂ lasers does not pose a large technological problem.

However, it can be advantageous to operate gas lasers at higher pressures (between 1 and 10 bar). Higher gas pressures result in larger optical gain and efficiency, but the electric excitation of the

laser medium becomes a greater challenge. For the excitation of the laser medium uniform discharges are needed, which at higher gas pressures (> 0.5 bar) can only be obtained by applying fast rising high-voltage pulses to the gas medium. Needless to say high-pressure CO₂ TEA (Transverse Excited Atmospheric) lasers and Excimer lasers are operated in pulsed mode. For the excitation of high-pressure CO₂ TEA lasers voltage rise-times between 50 and 100 ns are needed, whereas in Excimer lasers even faster pulses with rise-times less than 50 ns are required. Depending on the laser electrode spacing and gas pressure excitation voltages between 20 and 100 kV are required. In Excimer lasers the excitation voltages are normally higher than in CO₂ lasers.

Pulsed power supplies are used to generate the fast high-voltage pulses for the excitation of high-pressure gas lasers. The key component in a pulsed power supply is an electric switch, which is used in the generation of the fast excitation pulses. Historically the first pulsed power supplies utilized spark gaps. Although spark gaps are very robust they have a limited lifetime due to erosion of the spark gap electrodes. In order to improve the lifetime, thyratrons which are based on vacuum tube technology were employed and are still used in industry today. However, the thyatron also has a limited lifetime, which depends on the working conditions of the switch and is therefore difficult to predict.

With advances in solid-state technology new high-performance solid-state switches have become available. Thyristors and GTOs (Gate Turn-off Thyristor) have already been widely used for pulsed power applications and currently even a stacked thyristor switch is available to directly replace thyratrons [26]. The drawback of the thyristors and GTOs are that they are relatively slow compared to thyratrons. Consequently, more magnetic pulse compression is needed to compress the generated voltage pulses to obtain sufficiently fast voltage rise-times to excite a laser. Recently new types of high-performance solid-state switches have become available, including the Insulated Gate Bipolar Transistor (IGBT). The advantage of IGBTs above thyristors and GTOs is that IGBTs have increased switching speeds and are more easily turned off. Therefore, for this thesis an IGBT was used as pulsed power switching device. Although solid-state switches lack the robustness of thyratrons, they are much cheaper and allow for a more compact design. Furthermore, the modern solid-state switches, like MOSFETs and IGBTs, are more controllable, i.e. can easily be turned on and off, and need smaller driving circuits compared to thyratrons, thyristors and GTOs. The replacement of thyratrons by modern solid-state switches has almost become mandatory, from both an economical and technological viewpoint. However, the solid-state switches should be

implemented with the same robustness and reliability as thyratrons. If used correctly solid-state switches can outlast thyratrons.

1.2 Aim

In this thesis a systematic approach in designing a laser pulsed power supply utilizing a solid-state switch, in this case an IGBT, is presented. The final goal is therefore to replace a thyatron driven laser pulsed power supply with an optimised IGBT driven power supply. In order to achieve this goal it is important to acquire a sound understanding of the dynamic behaviour of an IGBT. Secondly, to optimise the system the laser is characterized, thereby determining the effect of the excitation circuit on the laser output energy, efficiency and stability. Another important aim is to determine the reliability of IGBTs in laser pulsed power supplies in order to design a robust system. Finally, a detailed outline of the design process is presented, which can be used as a reference for future work.

1.3 Outline

In Chapter 2 a brief overview of existing pulsed power supply topologies is given followed by a more detailed discussion of the C-C transfer topology in Section 2.2, which was the topology of choice for this project. The different components of a pulsed power supply, which includes magnetic pulse compression (MPC) circuits and pulse transformers, are also discussed. In Section 2.4 special attention is given to the behaviour and characteristics of pulse transformers.

The next step is to analyse the behaviour of an IGBT in a pulsed power supply and in Chapter 3 a detailed analysis of the behaviour of IGBTs is presented. In Section 3.2 the behaviour of an IGBT in a C-C transfer topology is analysed from which some basic design considerations can be deduced. Furthermore, in Section 3.4 the series stacking and paralleling of IGBTs is considered followed by a short discussion of the possible over-current capabilities of IGBTs.

In Chapter 4 the results of the CO₂ TEA laser characterization are presented and the basic excitation circuit that was used for characterization is described in Section 4.1. The effect of the excitation

circuit on the laser's stability and output efficiency is investigated and discussed in Sections 4.2 and 4.3, respectively.

In Chapter 5 an outline of the design process is given followed by a more detailed description of the construction of the different components of the pulsed power supply. This includes the IGBT unit, pulse transformer and magnetic pulse compression unit, discussed in Sections 5.3, 5.4 and 5.5, respectively.

Before finally testing the newly constructed pulsed power supply, the reliability of IGBTs is discussed in Chapter 6. The lifetime of IGBTs when used in pulsed supplies, where the pulse current exceeds the current rating of the IGBT, is experimentally tested. The lifetime test set-up and results are presented in Section 6.1. Additional attention is given in Section 6.2 to the protection and the lifetime of the IGBT under fault conditions.

Finally, in Chapter 7 the test results of the solid-state pulsed power supply are given. Measured voltage and current waveforms are shown in Section 7.1 followed by a discussion in Section 7.2 of the laser output energy and efficiency for the new laser pulsed power supply.

In Chapter 8 conclusions about the performance and reliability of laser pulsed power supply utilizing IGBTs, are made. Important suggestions are also given that could further improve the reliability of the laser pulsed power supplies.

Chapter 2

Laser pulsed power circuit topologies and components

In order to make a choice in the circuit topology it is important to perform a preliminary analysis of different pulsed power circuit topologies and to determine the peak circuit currents, circuit voltages and energy transfer times. Better knowledge of the circuit currents and voltages will also aid in the choice of solid-state switch ratings, where for this project an Insulated Gate Bipolar Transistor (IGBT) is used. Special emphasis is placed on the optimisation of pulsed power supplies in order to yield better supply efficiencies.

In the second part of this chapter magnetic pulse compression circuits (MPCs) are discussed in more detail. Additional focus is placed on the minimization of the magnetic volume that will be needed in a pulse compression circuit, in order to cut costs. This is followed by an analysis and revision of pulse transformers used in pulsed power applications.

2.1 Topology overview

As mentioned in the introduction the main purpose of a laser pulsed power supply is to supply short high-voltage pulses to generate stable laser discharges. In this section a short overview of different laser pulsed power supplies is given outlining the basic principle of the different topologies.

The most common topology used for pulsed power supplies is the C-C transfer circuit [12][18][45] of which the LC-inversion circuit is a special variation. In a C-C transfer topology the laser is excited by a single short pulse. Alternatively another type of excitation method is the pre-pulse-main-pulse topology, where a short pre-pulse initiates the laser discharge followed by a longer main pulse depositing the larger part of the excitation energy into the laser discharge [9]. Other types of topologies, which will only be mentioned, are the Marx generator and voltage multiplier topologies [24].

2.1.1 C-C transfer topology

The general layout of a C-C transfer pulsed power supply is shown in Figure 2-1. It consists of two main components, the primary switching unit and the magnetic pulse compression unit. The primary switching unit contains an active switching device (e.g. IGBT) to generate the initial voltage pulse. Normally the rise-time of the initially generated voltage pulse is too slow to excite the laser discharge and would result in unstable discharges. Therefore, a magnetic pulse compression (MPC) unit is used to temporally compress the initial voltage pulse in order to decrease the rise-time of the pulse. This will result in stable and efficient laser excitation. Some switching units are able to generate voltage pulses which have sufficiently fast rise-times, and in these cases no magnetic pulse compression unit is needed. The electrical power for the primary switching unit is supplied by a high-voltage charging unit.

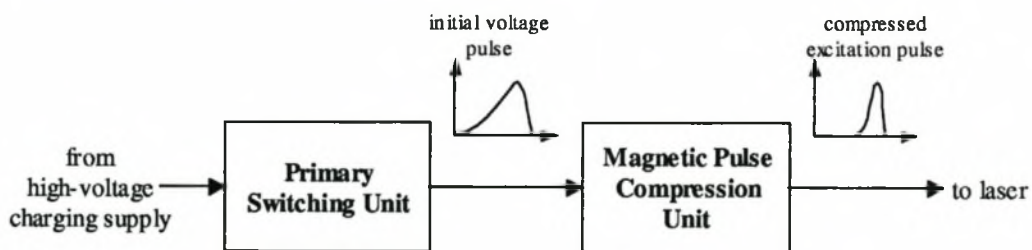


Figure 2-1: Basic C-C transfer pulsed power supply layout.

Furthermore, there are two basic topologies for the primary switching unit, the directly switched C-C transfer loop and the LC-inversion circuit.

Directly switched C-C transfer loop

The circuit diagram of the directly switched C-C transfer loop shown in Figure 2-2 is fairly simple. The input capacitor C_{in} is initially charged by a high-voltage charging supply through the charging inductor L_{charge} . As soon as the switching device is turned on energy is transferred by a resonant C-C transfer from the input capacitor C_{in} to the output capacitor C_{out} . The energy transfer causes the output voltage to rise and a voltage pulse is obtained at the output of the C-C transfer loop. The output of the C-C transfer loop can then either be connected to an MPC unit or directly to a laser if the obtained voltage rise-time is sufficiently fast. The transfer inductance L_t can also be replaced by a saturable inductor, which then acts as a magnetic assist [12][15][49]. The magnetic assist delays the C-C transfer and allows the switch to first fully turn on. Under ideal lossless and matched conditions the pulse energy generated by the circuit is equal to the initially stored energy in the input capacitor.

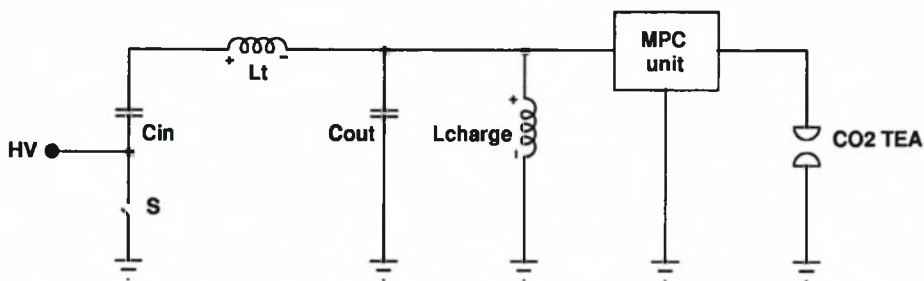


Figure 2-2: Circuit diagram of a directly switched C-C transfer loop.

In modern pulsed power supplies solid-state switches are used which have a limited voltage rating and are not able to directly switch the high voltages needed for gas laser excitation. To overcome this problem a step-up pulse transformer can be inserted into the C-C transfer loop [12][24][49] as indicated in Figure 2-3. The switch can therefore be operated at a lower voltage not exceeding the voltage rating of the switch. The generated pulses are stepped up to a voltage needed for the laser excitation.

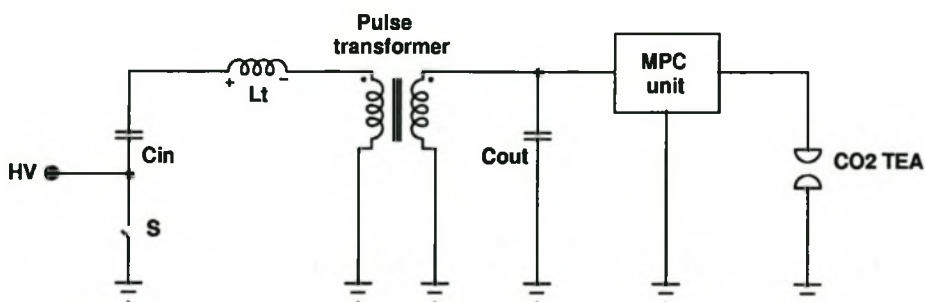


Figure 2-3: Circuit diagram of a directly switched C-C transfer loop with pulse transformer.

LC-inversion circuit

The basic topology of the LC-inversion circuit [24][42] is shown in Figure 2-4. It resembles the directly switched C-C transfer loop, except that two input capacitors are used. Furthermore, the circuit makes use of a magnetic switch L_{sat} , which is discussed in more detail in Section 2.3. The two input capacitors C_{in1} and C_{in2} are charged in parallel through L_{sat} and L_{charge} . Initially the voltage v_{12} across the two capacitors is zero. When the switch is turned on the voltage across the switched capacitor C_{in1} is resonantly inverted through the inversion inductor L_{inv} . After the inversion the two capacitors are connected in series. Ideally double the charging voltage is obtained across the two input capacitors. The magnetic switch is designed to be in an unsaturated high-impedance state during the voltage inversion and switches to a saturated low-impedance state as soon as the voltage inversion is completed. When the magnetic switch saturates a C-C transfer from the two input capacitors to the output capacitor is obtained. The inversion time of the input capacitor has to be much longer (at least 4 to 5 times longer) than the C-C transfer time, i.e. $L_{inv} \gg L_{sat}$. Consequently, in this topology initial pulse compression is already obtained by the use of a magnetic switch resulting in a LC-inversion time that is longer than the C-C transfer time.

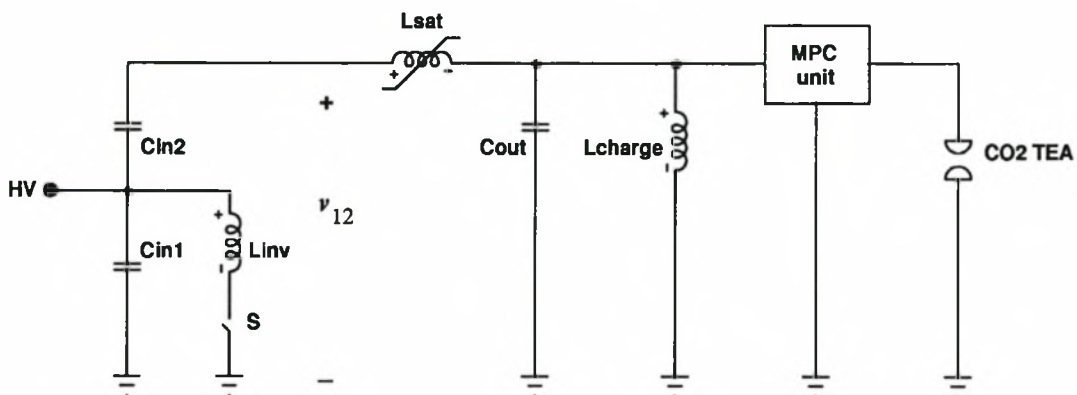


Figure 2-4: Circuit diagram of LC-inversion topology.

It is also possible to design an LC-inversion circuit without the use of a magnetic switch L_{sat} , replacing it by a normal air-core inductor. The air-core inductor has to be tuned in order to obtain good transfer efficiency. This eliminates the need for a magnetic switch and reduces costs.

Another variation on the LC-inversion topology is the super inversion pulser topology [42]. An additional switched C-C transfer is added to the input of the LC-inversion circuit and the active switch in the LC-inversion loop is replaced with a magnetic switch as shown in Figure 2-5. With

the super inversion pulser topology the ratings of the active switch can further be reduced and in conjunction with modern solid-state switches this topology can probably be used for high pulse energy ($> 100 \text{ J/pulse}$) applications.

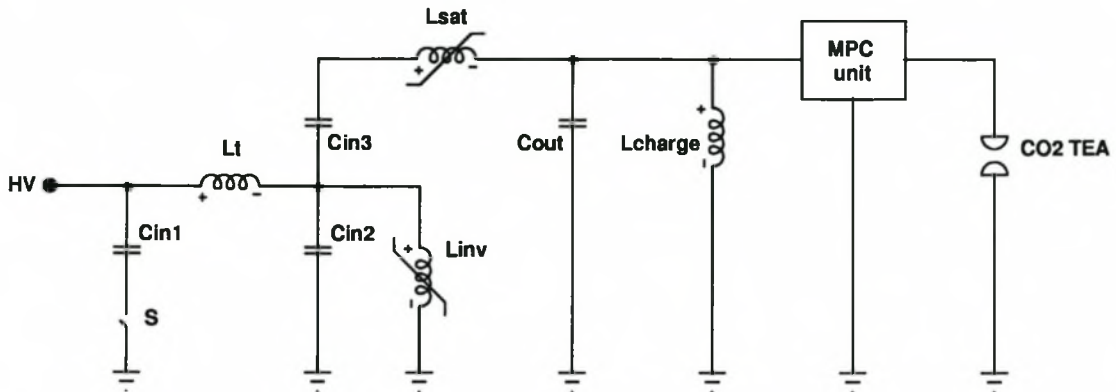


Figure 2-5: Circuit diagram of a super inversion pulser topology.

2.1.2 Conclusion

In order to concentrate on the behaviour and reliability of an IGBT the C-C transfer topology is the preferred choice due to its simplicity and wide use. The topology will have to include a pulse transformer, due to the limited voltage ratings of IGBTs. A LC-inversion topology also seems to be viable, but the use of a saturable inductor in conjunction with a fast solid-state switch (e.g. IGBT or MOSFET) causes the generated voltage pulse to be too fast for step-up pulse transformers constructed with thin laminated iron cores. Consequently, a more expensive special high-speed transformer core (e.g. amorphous core or Finemet core) has to be used.

At this stage a pre-pulse-main-pulse topology is not considered due to the more complex set-up. The construction of a PFL (pulse forming line) also necessitates the use of a large number of components thereby increasing construction costs. It is advisable to consider the pre-pulse-main-pulse topology as a next stage to increase the output efficiency of the laser and to lengthen laser pulses for materials processing.

Summarizing, the C-C transfer topology consisting of a primary switching unit and a MPC unit is chosen as the basic pulsed power supply topology for this project. Furthermore, a directly switched C-C transfer loop with pulse transformer is considered as the primary switching unit topology. In

the following sections the primary switching unit, MPC unit and pulse transformer of the C-C topology are discussed in more detail.

2.2 Primary switching unit

As mentioned earlier, in a C-C transfer topology the primary switching unit generates the initial voltage pulse by using an active switching device. In this section the directly switched C-C transfer circuit, which is the topology used for the primary switching unit, is discussed and special emphasis is placed on the optimisation of the C-C transfer loop. The switched C-C transfer loop also forms the basic building block of the series MPC unit.

2.2.1 Circuit analysis

The behaviour of a C-C transfer loop is well documented and in this sub-section a summary of the voltage and current response of a C-C transfer loop is given. The detailed circuit diagram of a switched C-C transfer loop is shown in Figure 2-6. The components C_1 , L_t , R_t and C_2 form a damped C-C transfer loop, where R_t corresponds to the equivalent losses in the circuit, mainly consisting of conduction losses. Initially the switch S is open and the storage capacitor C_1 is charged to a voltage V_0 , thus $v_{C1}(t=0) = V_0$. Furthermore, the transfer inductor L_t and the output capacitor C_2 have initial conditions of zero, i.e. $i_t(t=0) = 0$ A and $v_{C2}(t=0) = 0$ V. As soon as the switch is closed at $t = 0$, energy can be transferred from C_1 to C_2 and a voltage rise is obtained over the output capacitor C_2 .

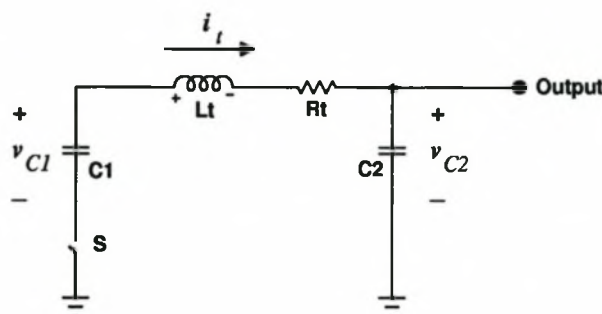


Figure 2-6: Circuit diagram of a directly switched C-C transfer loop.

The waveforms for v_{C1} , v_{C2} and i_t , for $t > 0$ can be calculated by performing a Laplace transform analysis [31] of the damped C-C transfer circuit and the following results for $t > 0$ are obtained [41]:

$$i_t(t) = \frac{V_0}{\omega L_t} e^{-\alpha t} \sin(\omega t), \quad (2.1)$$

$$v_{C1}(t) = V_0 \left\{ 1 - \frac{C_2}{C_1 + C_2} \left[1 - \frac{\omega_0}{\omega} e^{-\alpha t} \cos(\omega t + \phi) \right] \right\}, \quad (2.2)$$

$$v_{C2}(t) = V_0 \frac{C_1}{C_1 + C_2} \left[1 - \frac{\omega_0}{\omega} e^{-\alpha t} \cos(\omega t + \phi) \right], \quad (2.3)$$

$$\text{with } \alpha = \frac{R_t}{2L_t}, \quad \phi = \arctan(-\alpha / \omega), \quad \omega_0 = \frac{1}{\sqrt{L_t \frac{C_1 C_2}{C_1 + C_2}}}, \quad \omega = \sqrt{\omega_0^2 - \alpha^2}.$$

For a weakly damped C-C transfer loop the damping factor α is comparatively small, i.e. $\alpha \ll \omega$. Therefore, the following approximations can be used:

$$\left. \begin{array}{l} \phi \cong 0 \\ \omega \cong \omega_0 \end{array} \right\} \text{for weakly damped CLC - transfer loop}$$

With the above approximations Equations 2.1, 2.2 and 2.3 can be simplified:

$$i_t(t) = \frac{V_0}{\omega_0 L_t} e^{-\alpha t} \sin(\omega_0 t), \quad (2.4)$$

$$v_{C1}(t) = V_0 \left\{ 1 - \frac{C_2}{C_1 + C_2} \left[1 - e^{-\alpha t} \cos(\omega_0 t) \right] \right\}, \quad (2.5)$$

$$v_{C2}(t) = V_0 \frac{C_1}{C_1 + C_2} \left[1 - e^{-\alpha t} \cos(\omega_0 t) \right]. \quad (2.6)$$

At the end of the transfer period τ the transfer current drops to zero, $i_t(\tau) = 0$, and the output voltage v_{C2} reaches a maximum. By using either Equation 2.4 or 2.6 it can be shown that the transfer period (transfer time) is given by the following equation:

$$\tau = \frac{\pi}{\omega_0} = \pi \sqrt{L_i \frac{C_1 C_2}{C_1 + C_2}} \quad (2.7)$$

The resonant transfer time and the voltage rise-time of the output voltage are closely related. For the discussions in this and the following chapters the voltage rise-time is defined as the time needed for the voltage to rise from 10% to 90% of the peak voltage. From Equation 2.6 and using the mentioned criteria for the rise-time the relationship between the rise-time and the transfer time can be deduced:

$$t_{\text{rise}} = t|_{v_{C2}=0.9v_{C2,\text{max}}} - t|_{v_{C2}=0.1v_{C2,\text{max}}} \cong 0.6\tau \quad (2.8)$$

Voltage and current waveforms for the ideal transfer without losses ($\alpha = 0$) are shown in Figures 2-7, 2-8 and 2-9 for different capacitor ratios $k = C_1/C_2$. The output voltage rise over the capacitor C_2 and the sinusoidal transfer current pulse can be clearly seen in Figure 2-8 and 2-9, respectively. Note how the final voltages $v_{C1}(\tau)$ and $v_{C2}(\tau)$ at the end of the transfer period change with the capacitor ratio k .

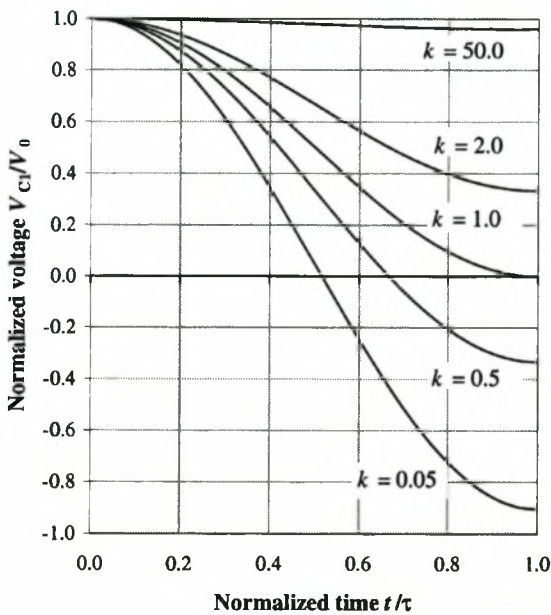


Figure 2-7: Normalized waveform of the input voltage $v_{C1}(t)$ of a C-C transfer loop.

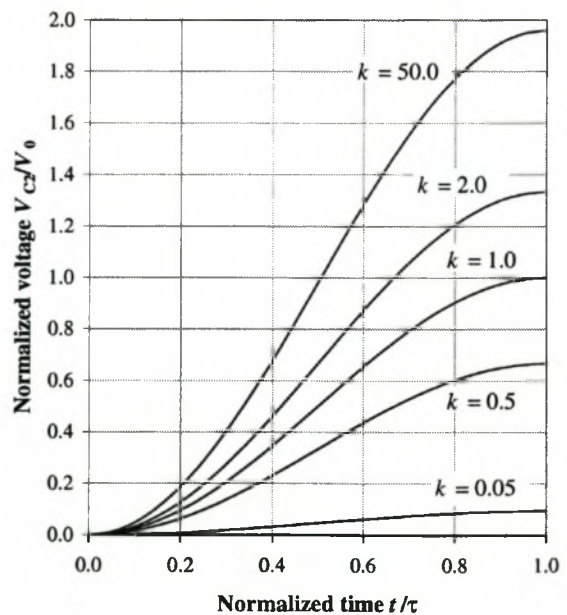


Figure 2-8: Normalized waveform of the output voltage $v_{C2}(t)$ of a C-C transfer loop

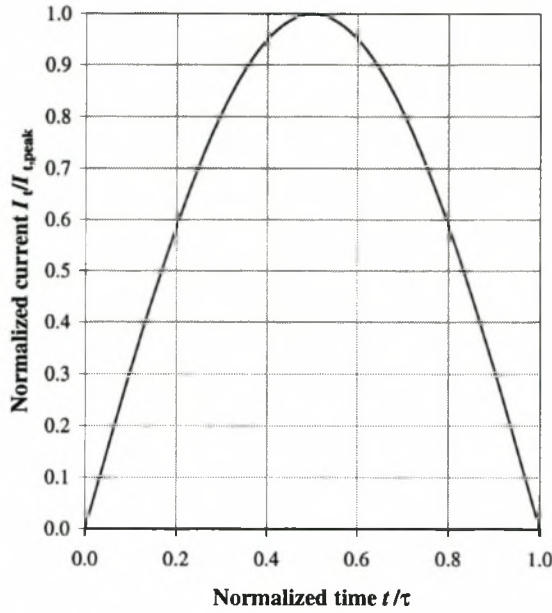


Figure 2-9: Normalized current waveform of the C-C transfer current $i_t(t)$.

Equations 2.5 and 2.6 can be used to calculate the final capacitor voltages [41][44] at the end of the transfer period τ :

$$v_{C1}(\tau) = V_0 \left[1 - \frac{1}{1+k} (1 + e^{-a}) \right], \quad (2.9)$$

$$v_{C2}(\tau) = V_0 \frac{k}{1+k} (1 + e^{-a}). \quad (2.10)$$

The aim of the C-C transfer loop is not only to obtain an output voltage pulse over capacitor C_2 , but also to maximize the energy transfer from the initially charged capacitor C_1 to the output capacitor C_2 . The transfer efficiency Φ of the C-C transfer loop is defined as follows [41]:

$$\Phi = \frac{E_{C2}(\tau)}{E_{C1}(0)} = \frac{E_{C1}(0) - E_{C1}(\tau) - E_{\text{loss}}}{E_{C1}(0)}, \quad (2.11)$$

where E_{loss} is the transfer energy loss dissipated in the transfer resistance R_t and E_{C1} and E_{C2} are the stored energies in capacitors C_1 and C_2 , respectively. Note that the transfer efficiency can be maximized by minimizing the remaining energy on capacitor C_1 and/or minimizing the transfer losses. Equation 2.11 can now be rewritten as a function of the capacitor ratio k and the damping

factor α by using the final capacitor voltages defined in Equations 2.9 and 2.10 [47]:

$$\Phi(k, \alpha) = \frac{\frac{1}{2} C_2 v_{C_2}^2(\tau)}{\frac{1}{2} C_1 v_{C_1}^2(0)} = \frac{k(1 + e^{-\alpha\tau})^2}{(k+1)^2}. \quad (2.12)$$

2.2.2 Optimisation

Optimisation of C-C transfer loops without losses ($\alpha = 0$)

For ideal transfer conditions without losses the optimisation of the transfer efficiency is straightforward. From Equation 2.11 it becomes clear that in the absence of losses the remaining energy on capacitor C_1 must be zero to get a 100 % transfer efficiency. Therefore, the final voltage over capacitor C_1 must be zero. From Equation 2.9 or 2.12 this results in an optimum capacitor ratio $k = 1$. [41]

Optimisation of C-C transfer loops with losses ($\alpha > 0$)

The optimisation of the transfer efficiency using Equation 2.12 is not straightforward, because the exponent $\alpha\tau$ in Equation 2.12 is a function of the circuit values C_1 , C_2 , L_t and R_t , where

$$\alpha\tau = \frac{\pi}{2} R_t \sqrt{\frac{1}{L_t} \frac{C_1 C_2}{C_1 + C_2}} \quad (2.13)$$

Normally, the transfer inductance L_t and resistance R_t are fixed in the design, which leaves two degrees of freedom: C_1 and C_2 . The degrees of freedom can further be reduced by adopting one of two design approaches [47]:

Method A. The input parameters are fixed, i.e. capacitor C_1 and the initial charging voltage V_0 are fixed. The output capacitor C_2 is varied to obtain the maximum transfer efficiency [8]. Thus, the only degree of freedom is capacitor C_2 , which can also be expressed as C_1/k_2 , where k_2 is the capacitor ratio with C_1 kept constant. For this design approach Equation 2.13 can be rewritten as

$$\alpha\tau = \frac{\pi}{2} R_t \sqrt{\frac{C_1}{L_t} \frac{1}{k_2 + 1}}, \quad \text{with } k_2 = k|_{C_1=\text{constant}}. \quad (2.14)$$

Method B. In laser pulsed power supply designs the output parameters (output voltage and energy) are normally specified. Therefore, the output parameters are fixed, i.e. the output energy $E_{C2}(\tau)$ and voltage $v_{C2}(\tau)$ are fixed. This in turn fixes the value of capacitor C_2 . In this case the input capacitor C_1 is varied to obtain the maximum transfer efficiency [41][47]. The value of capacitor C_1 is the only degree of freedom, with $C_1 = k_1 \cdot C_2$, where k_1 is the capacitor ratio with C_2 kept constant. Equation 2.13 can also be rewritten for this design approach

$$\alpha\tau = \frac{\pi}{2} R_l \sqrt{\frac{C_2}{L_l} \frac{k}{k+1}}, \quad \text{with } k_1 = k|_{C_2=\text{constant}}. \quad (2.15)$$

The above-mentioned approaches can be visualized on a two-dimensional contour graph as depicted in Figure 2-10 where the efficiency is plotted versus the capacitor ratios k_1 and k_2 for a transfer loss of approximately 10%. For the special case where $k_1 = k_2 = 1$, the capacitor ratio and capacitor values C_1 and C_2 corresponds to values that would have been used for the ideal transfer without losses. For the ideal case the two mentioned design methods are equivalent with $\alpha = 0$.

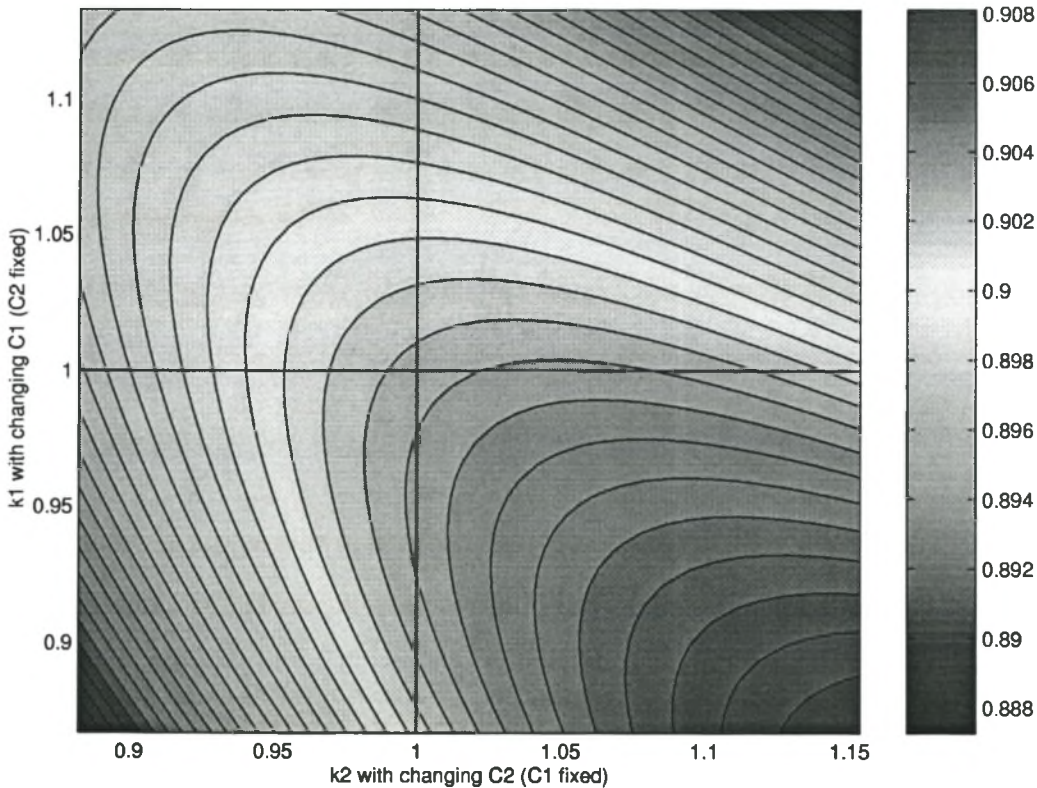


Figure 2-10: Two-dimensional colour contour graph of the C-C transfer efficiency as a function of the capacitor ratio k for two different optimisation approaches. (approx. 10% transfer losses). Bar on the right hand indicating transfer efficiency.

Design approach A (fixed input parameters) can be visualized by the horizontal line in Figure 2-10 with $k_1 = 1$. The output capacitor C_2 is varied, effectively varying k_2 , to optimise the transfer efficiency. For this case the optimum transfer efficiency is obtained at $k_2 \cong 1.05$ (approx. 10% transfer losses), which implies $C_1 > C_2$. It is interesting to note that for this design approach the capacitor ratio will always be larger than one. This can be deduced from the geometry of the contour plot in Figure 2-10. Analogue to the first design approach, design approach B (fixed output parameters) can be visualized by the vertical line in Figure 2-10 with $k_2 = 1$ and varying k_1 to obtain the optimum transfer efficiency. The optimum transfer efficiency is obtained at $k_1 \cong 0.95$ (approx. 10% transfer losses), which implies $C_1 < C_2$ and for this design method the capacitor ratio will always be smaller than one.

As mentioned earlier, the design method B is normally used for the design of laser pulsed power supplies, because the output energy and voltage are determined by the laser parameters and are therefore fixed. In order to directly compare the two design approaches as applied to laser pulsed power supplies, optimisation method A has to be adjusted to attain the same output energy and voltage as for method B, since for method A the input energy and voltage are normally specified. Optimisations using the two methods have been performed for a range of different transfer losses and the results, i.e. transfer efficiencies, capacitor ratios, transfer losses, remaining input energy and transfer time, are shown in Figures 2-11 to 2-15, respectively.

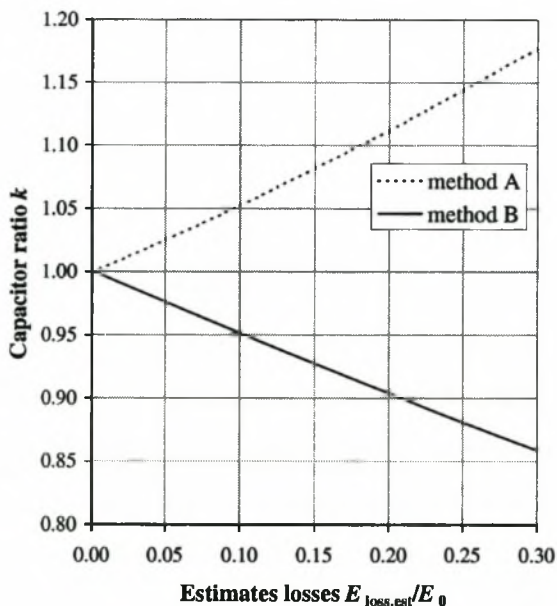


Figure 2-11: Capacitor ratio for two different optimisation methods vs. transfer losses in a C-C transfer loop.

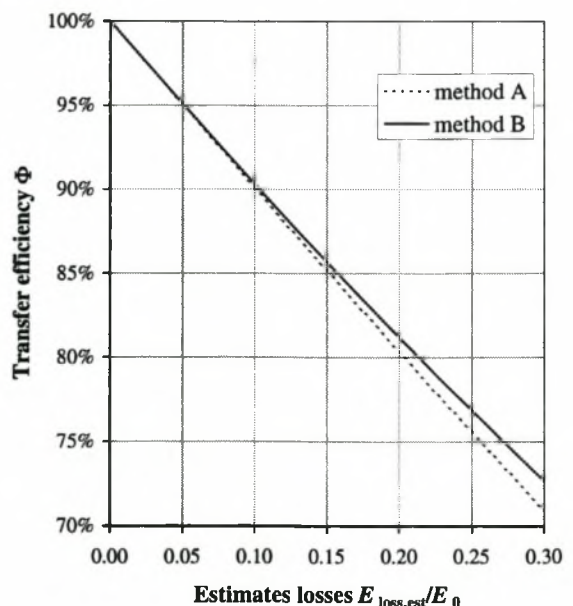


Figure 2-12: Transfer efficiency for two different optimisation methods vs. transfer losses in a C-C transfer loop.

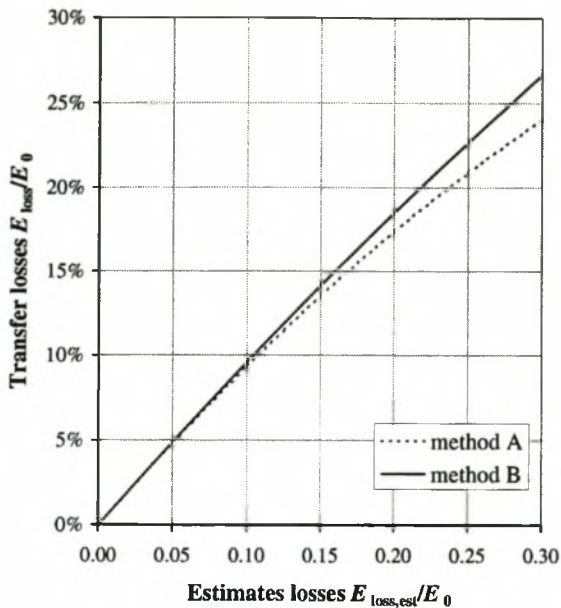


Figure 2-13: True transfer losses for two different optimisation methods vs. transfer losses in a C-C transfer loop.

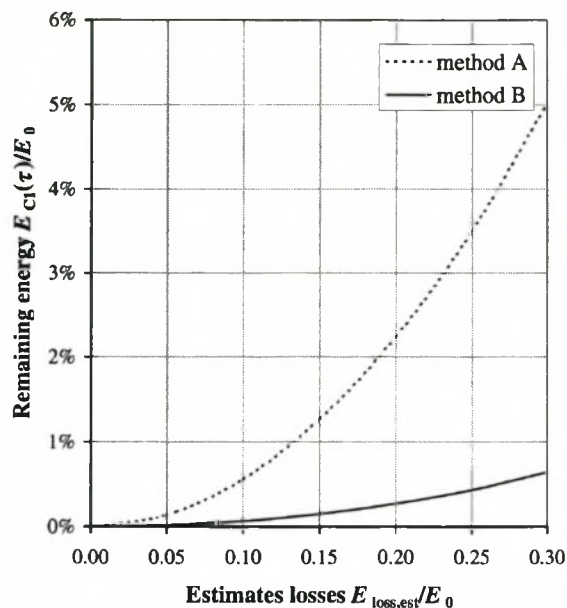


Figure 2-14: Remaining energy on input capacitor C_1 for two different optimisation methods vs. transfer losses in a C-C transfer loop.

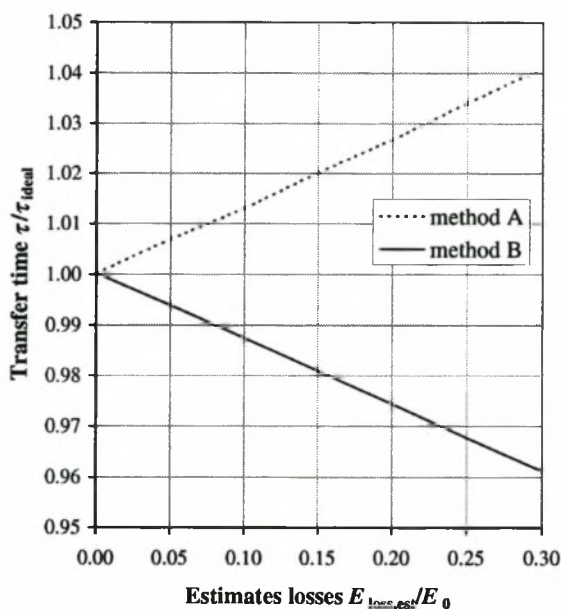


Figure 2-15: Transfer time for two different optimisation methods vs. transfer losses in a C-C transfer loop.

The graphs in Figure 2-11 to 2-15 are all plotted versus an estimated transfer loss, $E_{loss,est}$. The estimated loss is the transfer loss that would be obtained with capacitor values as used for the ideal, lossless case where $k_1 = k_2 = 1$. From Figure 2-11 it can be seen that for method A (fixed input parameters) the capacitor ratio is always greater than unity, $k_1 > 1$, whereas for method B (fixed output parameters) the capacitor ratio is always less than unity, $k_2 < 1$. As mentioned earlier for an

ideal circuit with no losses the two design methods coincide, resulting in the same capacitor ratio ($k_1 = k_2 = 1$), transfer efficiency ($\Phi = 1$) and transfer time. The main differences between the two design methods become apparent in Figures 2-13 and 2-14. Design method A results in lower transfer losses, due to lower transfer currents caused by longer transfer times (see Figure 2-15 and Equations 2.4 and 2.16). On the other hand design method B results in lower remaining energies $E_{C1}(\tau)$ in the input capacitor C_1 . Finally, as applied to laser pulsed power supply design method B yields a slightly better transfer efficiency than method A, as can be seen in Figure 2-12.

2.2.3 Switching currents

From Figure 2-6 it is apparent that the transfer current is equal to the switching current. Therefore, the peak transfer current is also equal to the peak switching current and can be calculated from Equation 2.4. For an ideal circuit without losses ($\alpha = 0$)

$$I_{s,\text{peak}} = \frac{V_0}{\omega_0 L_t}, \quad (2.16)$$

where $I_{s,\text{peak}}$ is the peak switching current. In many pulsed power supply designs the charging voltage V_0 and pulse energy are fixed design parameters and it is useful to rewrite Equation 2.16 in terms of the pulse energy and charging voltage. The pulse energy is equal to the initially stored energy in the input capacitor C_1 of the C-C transfer loop. It was also shown that for optimum energy transfer the input and output capacitors are equal, $C_1 = C_2$. Thus, for an ideal circuit the following can be stated:

$$E_{\text{pulse}} = \frac{1}{2} C_1 V_0^2 \quad \text{and} \quad \tau = \frac{\pi}{\omega_0} = \pi \sqrt{\frac{1}{2} L_t C_1}.$$

These two equations are applied to Equation 2.16 and the following result is obtained:

$$I_{s,\text{peak}} = \frac{\pi E_{\text{pulse}}}{\tau V_0}. \quad (2.17)$$

For fixed pulse energies the peak switching current can therefore be reduced by either increasing the initial charging voltage and/or increasing the transfer time. Although the above analyses were performed for an ideal circuit, Equations 2.16 and 2.17 can still be used to obtain good approximations of the peak switching current in practical circuits, because the losses in practical C-C transfer loops normally do not exceed 10%.

It is useful to calculate the average and RMS (root-mean-square) switching currents, which can be used to determine the losses of the switching device in the C-C transfer loop. Both the average and RMS switching currents of a single pulse can be calculated for a C-C transfer with low losses using Equation 2.4, where

$$I_{s,avg} \Big|_{\text{pulse}} = \frac{1}{\pi} \frac{V_0}{\omega_0 L_t} (e^{-\alpha\tau} + 1) \cong \frac{2}{\pi} I_{s,peak} , \quad (2.18)$$

and

$$I_{s,RMS} \Big|_{\text{pulse}} = \frac{1}{\sqrt{2}} \frac{V_0}{\omega_0 L_t} = \frac{1}{\sqrt{2}} I_{s,peak} . \quad (2.19)$$

Generating the pulses at a repetition rate f_{rep} results in a total average and total RMS current given by

$$I_{s,avg} = f_{rep} \tau \left(I_{s,avg} \Big|_{\text{pulse}} \right) = f_{rep} \tau \frac{2}{\pi} I_{s,peak} , \quad (2.20)$$

and

$$I_{s,RMS} = \sqrt{f_{rep} \tau} \left(I_{s,RMS} \Big|_{\text{pulse}} \right) = \sqrt{f_{rep} \tau} \frac{1}{\sqrt{2}} I_{s,peak} , \quad (2.21)$$

where τ is the pulse duration, i.e. transfer time of the switched C-C transfer loop.

2.3 Magnetic pulse compression unit

Some switching devices are fast enough to generate voltage pulses with sufficiently fast rise-times to excite CO₂ TEA lasers without the need of magnetic pulse compression (MPC). It is for example possible to excite a CO₂ laser with a directly switched C-C transfer loop using a thyatron or spark gap as active switch, where the laser is connected parallel to the output capacitor C_2 (see Figure 2-6). However, most often the switching devices are not capable of directly generating

excitation pulses with adequately fast rise-times. This can be blamed on one of two limitations of the switching device:

1. *Slow switching times*: This limitation is inherent in the switch and is difficult to overcome. It is possible to decrease the switching time by increasing the driver signal, which turns the switching device on, but care must be taken not to damage the device. This type of limitation is normally experienced with older types of solid-state switches, e.g. thyristors.
2. *Limited current ratings*: It was shown that the peak switching current in C-C transfer loops is inversely proportional to the transfer time and charging voltage of the C-C transfer loop (see Equation 2.17). Therefore, the minimum rise-time of the generated voltage pulse can also be limited by the peak current rating of the switching device. This problem can be overcome by increasing the charging voltage of the C-C transfer loop, but the maximum voltage rating of the switch may not be exceeded. This limitation is often encountered with modern solid-state switches, e.g. MOSFET's and IGBTs. These devices have sufficiently fast switching times, but are less robust than thyratrons and have limited voltage and current ratings.

For situations where the initially generated voltage pulse is too slow for laser excitation, magnetic pulse compression stages can be used to compress the pulse and to decrease the rise-time. In the following sections the basic principle and optimisation of MPC circuits are discussed.

2.3.1 Saturable inductors as passive current-controlled switches

Saturable inductors are the key component in MPC units and in this sub-section the basic properties of saturable inductors are discussed. Special magnetic materials (e.g. Finemet, Metglass, etc.) are used for the cores of saturable inductors [36][37] and a typical BH-curve of such a core is shown in Figure 2-16.

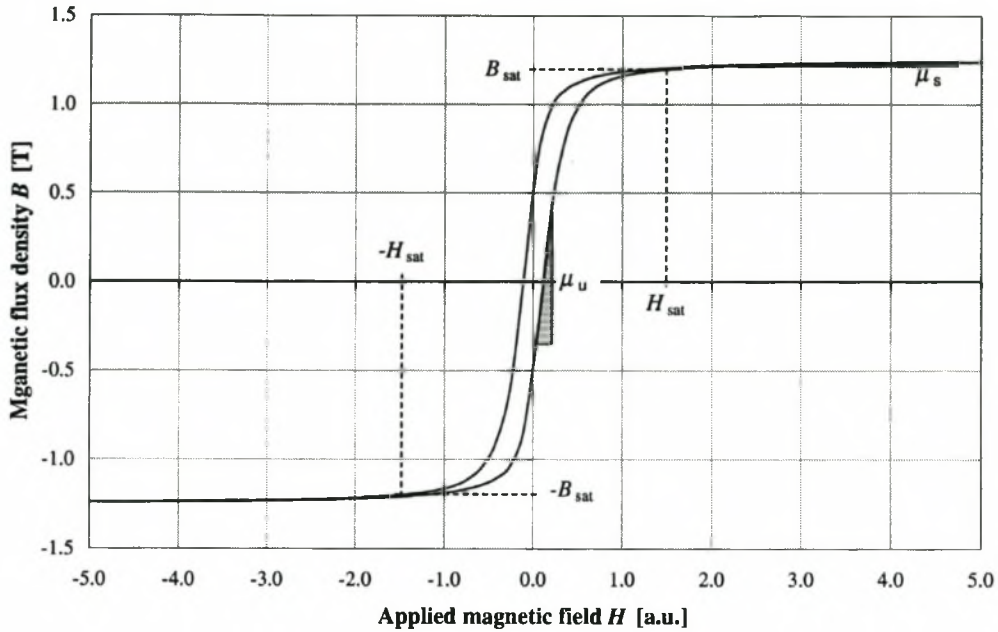


Figure 2-16: BH-curve of a saturable inductor.

Ignoring hysteresis, the saturable inductor has two operating regions, the unsaturated and the saturated regions [32]:

1. *Unsaturated region*, $|H| < H_{\text{sat}}$: The magnetic flux density B is below the saturated flux density, B_{sat} , and the BH-curve can be approximated by the following linear equation:

$$B \cong \mu_u H, \quad (2.22)$$

where μ_u is the unsaturated permeability as indicated in Figure 2-16. The unsaturated permeability is relatively large resulting in a large inductance L_{unsat} with

$$L_{\text{unsat}} \cong \mu_u \frac{N^2 A_{\text{core}}}{l_{\text{core}}}, \quad (2.23)$$

where N is the number of inductor turns, A_{core} the equivalent core cross-section and l_{core} the equivalent magnetic path length of the inductor core.

2. *Saturated region*, $|H| > H_{\text{sat}}$: When the applied magnetic field is increased beyond the saturation magnetic field H_{sat} , the gradient of the BH-curve decreases dramatically and the

magnetic flux density is more or less clamped at the saturated flux density B_{sat} . For the saturated region the BH-curve can again be approximated by a linear equation:

$$B \cong \mu_s H + B_{\text{sat}}, \quad (2.24)$$

where μ_s is the saturated permeability as indicated in Figure 2-16. Due to the decrease in permeability the inductance of the saturable inductor also decreases strongly. For complete saturation the permeability μ_s will approach the permeability of air, μ_0 , resulting in approximately equal magnetic field strengths inside and outside the core. The magnetic flux has to be calculated over the whole cross-section A_t of the saturable inductor and the saturated inductance is given by

$$L_{\text{sat}} \cong \mu_s \frac{N_{\text{sat}} A_t}{l_{\text{core}}} = \mu_s \frac{N_{\text{sat}} A_{\text{core}}}{p l_{\text{core}}} = \frac{\mu_s}{p \mu_u} L_{\text{unsat}} \quad (\mu_s \rightarrow \mu_0), \quad (2.25)$$

where p is the fill factor (packing factor) of the inductor, with $p = A_{\text{core}}/A_t$.

If a voltage pulse is applied to a saturable inductor the inductor is initially in an unsaturated state with a relatively high inductance. The inductor current will increase relatively slowly and the saturable inductor is effectively in an “off” state. As the current through the inductor increases, the applied magnetic field also increases proportionally until the saturation field strength H_{sat} is reached. At this point the inductance decreases rapidly allowing a much faster increase in the inductor current and the saturable inductor effectively switches to an “on” state [32].

The switching behaviour of the saturable inductor is illustrated by a simple example [32] consisting of a saturable inductor connected to a resistive load. The circuit diagram and simulated waveforms are shown in Figure 2-17. Initially no current is flowing through the saturable inductor and a voltage step is applied to the circuit. After the voltage step is applied the inductor current starts to increase causing a small voltage drop over the load resistor, but the main portion of voltage is dropped over the inductor. Eventually the inductor saturates, the inductor current starts increasing rapidly and the inductor voltage drops to zero, i.e. the saturable inductor switches. Analogous to other types of switches, the inductor current flowing before the inductor switches is called the leakage current of the saturable inductor.

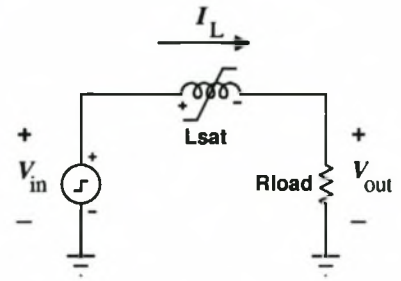
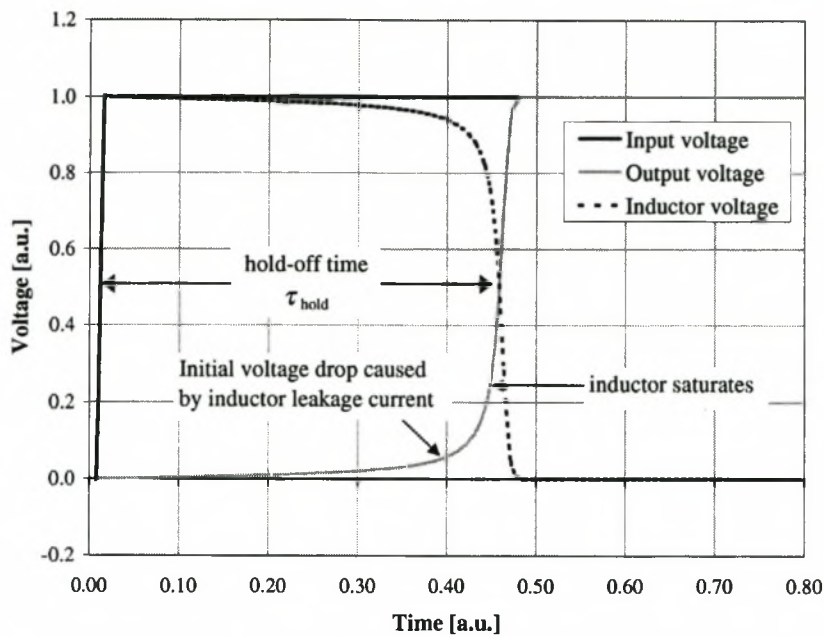


Figure 2-17: Simple example illustrating the switching behaviour of a saturable inductor.

In Figure 2-17 the voltage hold-off time, i.e. the time needed for the inductor to saturate, can clearly be seen. The hold-off time τ_{hold} is defined by the following equation [32]:

$$\int_0^{\tau_{\text{hold}}} v_L(t) dt = NA_t p \Delta B = \Delta \Phi, \quad (2.26)$$

with v_L the inductor voltage, N the number of inductor turns, A_t the total area enclosed by the winding of the saturable inductor, p the core packing factor ($p = A_{\text{core}}/A_t$) and ΔB the change in magnetic flux density before the saturated flux density B_{sat} is reached. Note that the above equation is equal to the change in magnetic flux content $\Delta \Phi$.

The hold-off time of a saturable inductor core can be increased by reverse biasing the core. This is achieved by using an additional reset winding through which a constant current is passed to initially drive the core into reverse saturation. Ideally, the maximum available change in the magnetic flux density that can be achieved with a constant DC reset current is twice the saturated flux density, $\Delta B_{\text{max}} = 2B_{\text{sat}}$. For a pulsed reset current the maximum change in magnetic flux density is typically $\Delta B_{\text{max}} = B_{\text{sat}} + B_r$, with B_r the remnant flux density. [32][48]

Series magnetic pulse compression topology

The most widely used MPC topology is based on the C-C transfer loop, which is also known as a Melville line or series pulse compression. Other types of MPC topologies are the parallel MPC and the transmission line MPC circuits [32]. In the following sections only the series MPC topology will be considered. A typical pulsed power supply topology making use of series MPC stages is shown in

Figure 2-18.

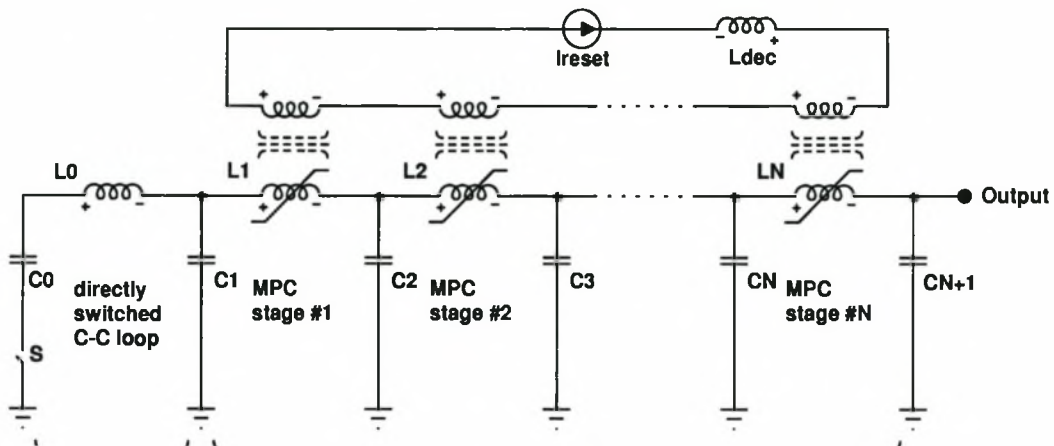


Figure 2-18: Typical pulsed power supply topology with series MPC stages.

The series MPC unit consists of multiple connected C-C transfer loops, where the output capacitor of each loop is also the input capacitor of the next C-C transfer loop. The saturable inductors of the MPC unit are each reverse biased by a reset winding with a constant reset current I_{reset} in order to increase the total flux swing before saturation occurs as mentioned earlier. Each saturable inductor is designed to saturate as soon as the voltage over the input capacitor of the corresponding MPC stage reaches a maximum. The hold-off time of every stage is thus equal to the transfer time of the previous stage, thereby allowing the C-C transfer in a previous stage to be completed before the next C-C transfer in the following stage occurs. Pulse compression is now obtained by decreasing the transfer time of each successive stage. Due to the faster transfer times, the peak transfer current of each successive stage increases and the MPC unit has therefore also a current gain. Typical voltage and current waveforms obtained in an MPC unit are shown in Figure 2-19, where the pulse compression and the current gain of a series MPC unit can be clearly seen. Summarizing, the initial pulse is generated by the primary switching unit and propagates through the MPC unit by consecutive and increasingly faster C-C transfers [32].

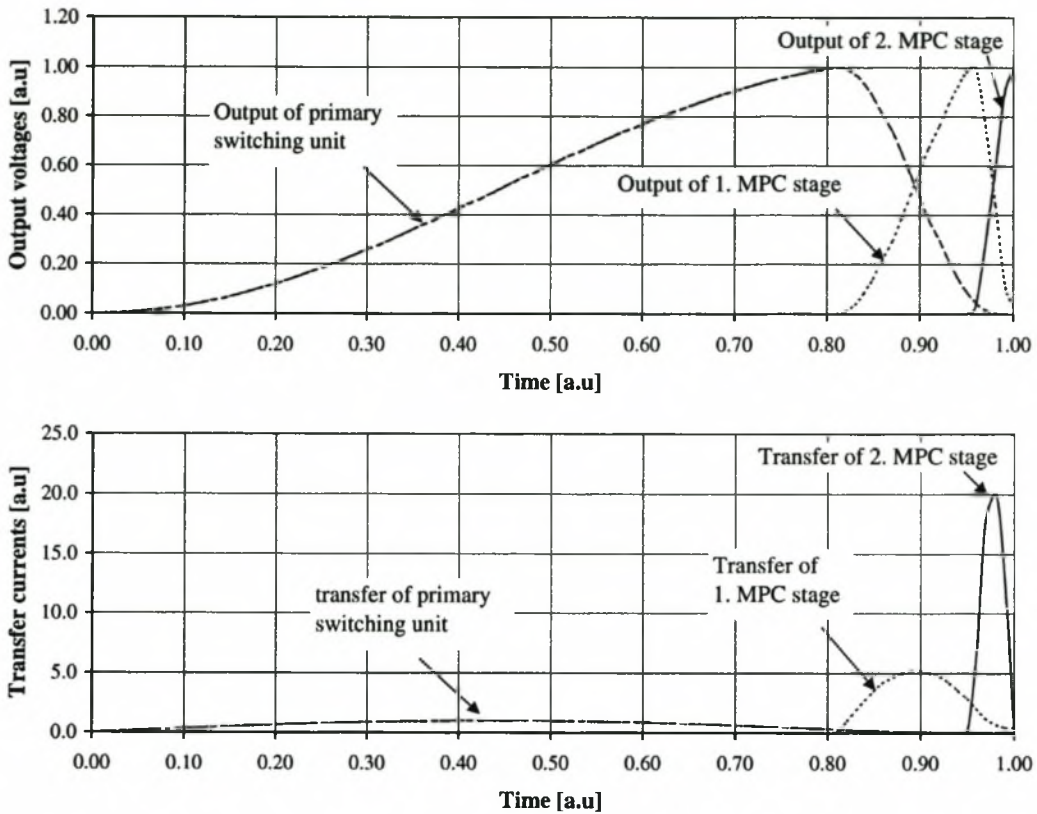


Figure 2-19: Typical voltage and current waveforms obtained in a series MPC topology.

A single MPC stage is now considered and the basic circuit diagram of a single MPC stage is shown in Figure 2-20.

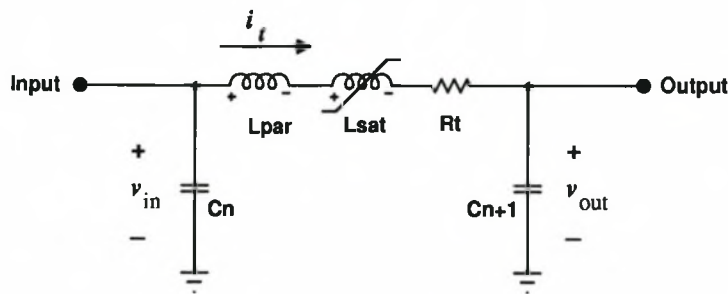


Figure 2-20: Series magnetic pulse compression stage based on the C-C transfer loop.

The C-C transfer loop in Figure 2-20 is in principle identical to the C-C transfer loops discussed in Section 2.2.1 (see Figure 2-6). Instead of utilizing an active switch the MPC stage makes use of a saturable inductor acting as a passive current-controlled switch. The input voltage waveform v_{in} is equal to the output voltage waveform of the previous C-C transfer stage, which is described by Equation 2.6 (output waveform of a C-C transfer loop). After the inductor saturates a normal C-C transfer, as described in Section 2.2.1 occurs. The total transfer inductance consists of the saturated

inductance L_{sat} and the parasitic inductance L_{par} . The parasitic inductance is introduced by the electrical connections between the saturable inductor and the input and output capacitors. The MPC circuit can be optimised using the same methods as described in Section 2.2.2. Typical voltage and current waveforms of a single MPC stage are shown in Figure 2-21.

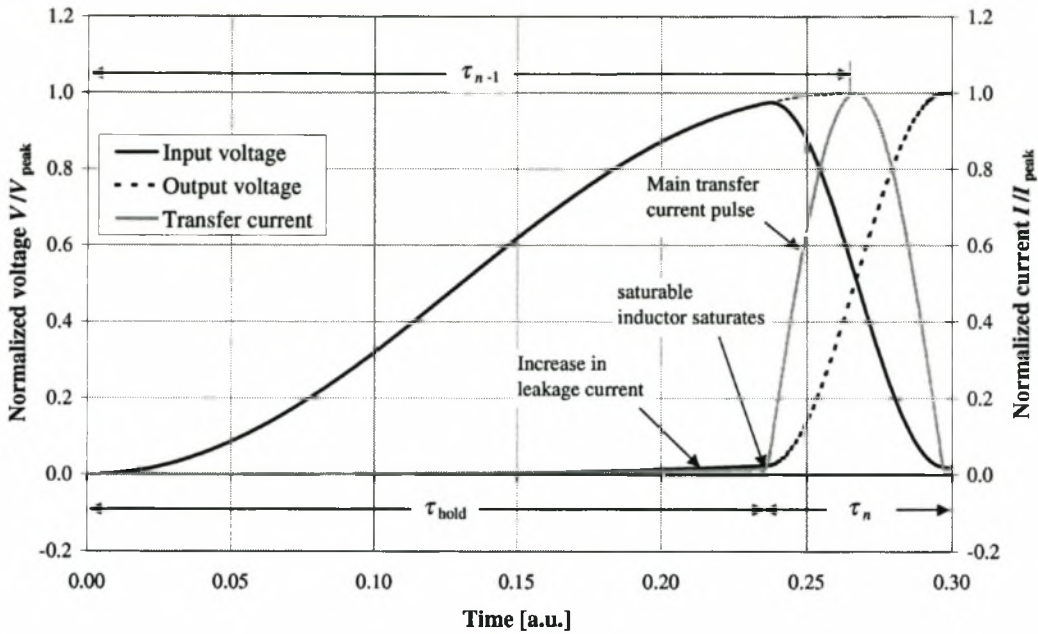


Figure 2-21: Voltage and current waveforms in a magnetic pulse compression stage.

The hold-off of the saturable inductor can be clearly seen and the inductor saturates shortly before the input waveform reaches a maximum. The timing of the core saturation is discussed in more detail in the next section. Furthermore, pulse compression is also visible, where the rise-time of the input waveform is much slower than the rise-time of the output waveform. The ratio of the input to output voltage rise-time of the n^{th} MPC stage is called the compression ratio g_n , with

$$g_n = \frac{\tau_{n-1}}{\tau_n}, \quad (2.27)$$

where τ_{n-1} is the transfer time of the previous (input) C-C transfer stage and τ_n the transfer time of the current C-C transfer stage.

Voltage hold-off and MPC timing

The hold-off time τ_{hold} of an MPC stage can be chosen equal to the transfer time τ_{n-1} of the previous transfer stage, but normally the hold-off time is chosen slightly smaller than τ_{n-1} [1]. There are mainly two reasons for this choice:

- Choosing a smaller hold-off time reduces the integral in Equation 2.26, resulting in smaller inductor core volumes, as will be seen in the next section.
- The transfer time in an MPC transfer loop has a finite duration. For better transfer timing the main C-C transfer should start before the input voltage reaches a maximum so that the peak transfer current of the MPC stage coincides with the time at which the input voltage would have reached a maximum. This can be seen in Figure 2-21 where the saturable inductor switches when the input voltage has reached approximately 95% of the peak input voltage.

The MPC timing is very sensitive for changes in the pulse voltage, especially for pulse voltages larger than the designed for value. For lower pulse voltages the MPC timing is less sensitive. It is therefore advisable to optimise the MPC timing for the maximum pulse voltage.

To determine the needed change in magnetic flux of a saturable inductor for a given hold-off time, the inductor voltage v_L has to be determined first. During the voltage hold-off the saturable inductor can be approximated by an open circuit. Considering Figures 2-20 and 2-21 it becomes clear that the inductor voltage is equal to the input voltage of the MPC stage during voltage hold-off. As mentioned earlier, the input voltage of the MPC stage is described by Equation 2.6, i.e. the output voltage of the previous C-C transfer loop. Assuming an optimised ideal circuit without losses ($\alpha = 0$, $k = 1$) the following inductor voltage waveform is obtained for $0 < t < \tau_{\text{hold}}$

$$v_L(t) \cong v_{\text{in}}(t) = \frac{V_0}{2} \left[1 - \cos\left(\frac{\pi}{\tau_{n-1}} t\right) \right],$$

where V_0 is the peak output voltage (i.e. peak pulse voltage) of the previous stage. At this point it is important to note, that the peak pulse voltage decreases as the pulse propagates through the MPC unit. The stage-to-stage voltage decrease is caused due to losses and matching of the input and output capacitors of the MPC stage for maximum energy transfer (see Section 2.2.2). This decrease in pulse voltage has to be taken into account during the MPC design.

As mentioned earlier the saturable inductor is designed to switch before the transfer in the previous C-C stage is completed and the input voltage reaches a maximum. The ratio of the switching voltage (input voltage level at which the inductor saturates) and the peak input voltage is called the switching ratio k_{sw} with

$$k_{sw} = \frac{v_{in}(\tau_{hold})}{v_{in}(\tau_{n-1})}. \quad (2.28)$$

A switching ratio of $k_{sw} = 1$ will therefore correspond to a hold-off time equal to the transfer time τ_{n-1} of the previous (input) C-C transfer stage. Normally the switching ratio is chosen between 0.9 and 0.95. Smaller switching ratios ($k_{sw} < 0.9$) will result in incomplete transfer in the consecutive C-C transfer stages thereby reducing the transfer efficiency [1][41]. Using the inductor voltage waveform $v_L(t)$ the relationship between the hold-off time and the transfer time of the previous (input) C-C transfer stage can be determined as a function of the switching ratio:

$$\tau_{hold} = \tau_{n-1} \frac{\arccos(1 - 2k_{sw})}{\pi}. \quad (2.29)$$

The total magnetic flux swing needed for a hold-off time τ_{hold} can now be determined by using the above equation and solving the integral in Equation 2.26. The following result is obtained:

$$\frac{V_0}{2} \tau_{n-1} F_t = NA_{core} \Delta B = \Delta \Phi, \quad (2.30)$$

$$\text{with} \quad F_t(k_{sw}) = \frac{\arccos(1 - 2k_{sw})}{\pi} \left[1 - \frac{2}{\pi} \sqrt{k_{sw}(1 - k_{sw})} \right], \quad (2.31)$$

where F_t is the timing factor, which is a function of the switching ratio k_{sw} . To illustrate the effect of the switching ratio k_{sw} on the required change of magnetic flux content, the timing factor F_t is plotted as a function of the switching ratio (see Figure 2-22). A switching ratio $k_{sw} = 1$ results in a timing factor $F_t = 1$ and by decreasing the switching ratio a fast initial decrease in the timing factor can be observed [1]. Thus, for a fixed input transfer time τ_{n-1} the needed change in the flux content $\Delta \Phi$ can be decreased significantly. Conversely for a fixed $\Delta \Phi$ the transfer time of the input C-C stage can be increased, thereby increasing the compression ratio of the MPC stage. Consequently, choosing a switching ratio smaller than unity will result in a reduction of the needed core volume (see Section 2.3.3) and/or an increase in the compression ratio of the MPC unit. This

reduces the size and costs of the MPC unit. Choosing switching ratios smaller than one has a marginal effect on the transfer efficiency Φ of the MPC stages. According to S.E. Ball [1] the transfer efficiency is reduced by not more than 5% for switching ratios between 1.0 and 0.8.

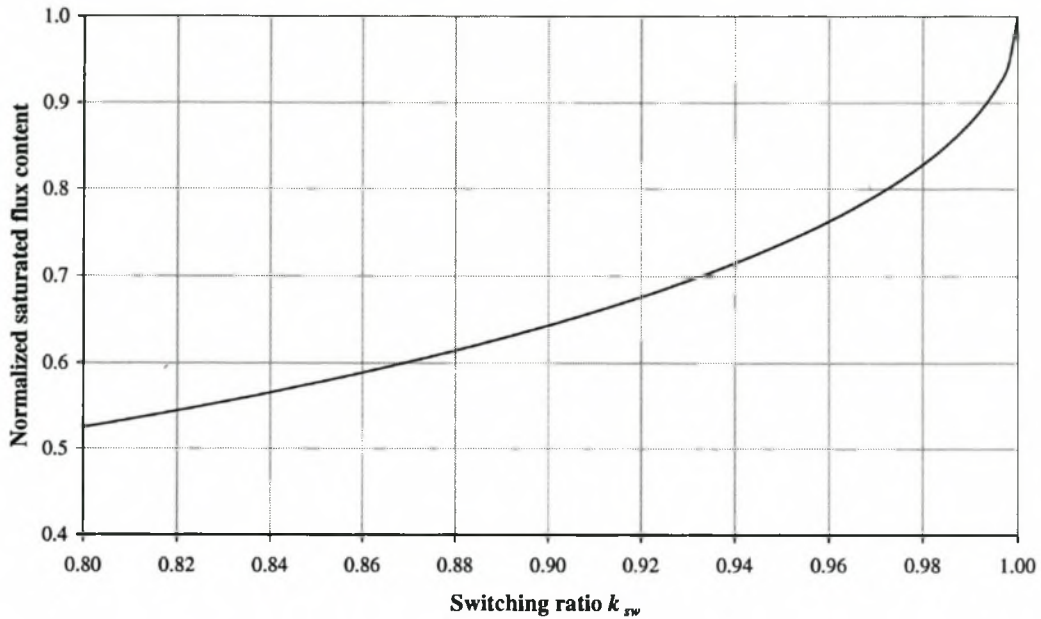


Figure 2-22: Saturated flux content of the core of a saturable inductor vs. the switching ratio k_{sw} .

2.3.2 Estimate and minimization of total magnetic core volume

An estimate of the total required magnetic core volume can aid in the design and optimisation process of MPC circuits. Methods can be determined to minimize the magnetic core volume, thereby reducing costs. In general the only two design parameters specified for a MPC unit are the overall compression ratio G and the energy E_0 of the transmitted pulse. The aim is to determine methods to minimize the magnetic core volume.

Firstly, the magnetic volume of a single MPC stage is determined. An ideal system with no losses is considered. Furthermore, it is assumed that the C-C transfer loops of the MPC stages are optimised ($k = 1$) and that the parasitic inductance L_{par} is negligibly small. Using Equations 2.7, 2.25, 2.27, 2.29, 2.30 and 2.31 the following general expression for the equivalent magnetic core volume of a single MPC-stage is obtained:

$$\text{Vol}_{s,\text{equiv}} = A_{\text{core}} l_{\text{core}} = g^2 \frac{\pi^2 \mu_{\text{sat}} E_0}{4p\Delta B^2} F_t^2. \quad (2.32)$$

It is important to note that the equivalent core volume is the product of the equivalent magnetic cross-section A_{core} and magnetic path length l_{core} of the core and is therefore not equal to the true magnetic volume. The relationship between the equivalent core volume and the true core volume is determined by the core geometry (e.g. toroidal, strip-line, etc). Toroidal cores are widely used for saturable inductors in MPC stages and therefore the true core volume $\text{Vol}_{s,\text{toroid}}$ for a toroidal core, as derived by I. Druckmann, et al. [7], is given by

$$\text{Vol}_{s,\text{toroid}} = g^2 \frac{\pi^2 \mu_{\text{sat}} E_0}{4p^2 \Delta B^2} \frac{r_o + r_i}{2(r_o - r_i)} \ln \left(\frac{r_o + \Delta r}{r_i - \Delta r} \right), \quad (2.33)$$

where r_o and r_i are the outer and inner core radii, respectively, and Δr is the winding clearance between the inductor windings and the toroidal core.

Nevertheless, Equation 2.32 shows the general relationship between the core volume and the MPC parameters. In order to reduce the core volume, the magnetic material must have a low saturated permeability and a large flux swing. The timing factor also has a large influence on the core volume, seeing that the core volume scales with the square of the timing factor. Normally a switching ratio k_{sw} of approximately 0.95 is chosen resulting in a timing factor of $F_t = 0.75$, thereby reducing the core volume by 45% compared to a switching ratio of unity. The compression ratio has the largest impact on the core volume and a strategy has to be used to reduce the compression ratio of individual MPC stages.

The compression ratio of the individual MPC stages can be reduced by using multiple MPC-stages and the total compression ratio of a MPC unit with a number of N stages is given by

$$G = \prod_{n=1}^N g_n = \frac{\tau_{\text{primary switching unit}}}{\tau_{\text{MPC output}}}. \quad (2.34)$$

Theoretically it can now be shown [7] that the total core volume of the MPC unit can be minimized by using equal compression ratios for each MPC stage, i.e. $G = g^N$. The optimum number N_{opt} of MPC stages is

$$N_{\text{opt}} = 2 \ln G, \quad (2.35)$$

with $g_{\text{opt}} = \sqrt{e} = 1.64,$ (2.36)

where g_{opt} is the resulting optimum compression ratio per MPC stage. Although the conditions specified by Equations 2.35 and 2.36 will theoretically result in the minimization of the total MPC core volume, it is just about always not practically viable. The optimum compression ratio g_{opt} is relatively small and can result in a large number of MPC stages. A greater number of MPC stages also implies a greater number of capacitor banks for the C-C transfer loops. This can be very costly and increases the size, complexity and losses of the MPC unit. On the other hand using large compression ratios per MPC stage results in excessive core volumes and can also increase the physical size of the MPC unit. There is thus a trade-off between minimizing the magnetic core volume and the number of MPC stages. The choice of the number of MPC stages is mainly a cost consideration [39][44].

2.4 Pulse transformers

The primary voltage pulse generated by the switching unit should have a sufficiently high peak voltage in order to excite a laser, in this case a mini CO₂ TEA laser, for which an excitation voltage of between 15 kV and 30 kV is needed. As mentioned earlier there are switching devices with which these high voltages can be switched directly, e.g. thyratrons and spark gaps. Unfortunately the maximum voltage rating of solid-state switches, e.g. insulated gate bipolar transistors (IGBTs) and thyristors, are only a few kilovolts. The generated voltage pulses have to be stepped up with a pulse transformer to obtain the high voltage pulses needed for laser excitation. In the case of a simple C-C transfer circuit the pulse transformer is simply inserted into the primary switched C-C transfer loop as shown in the circuit diagram in Figure 2-23.

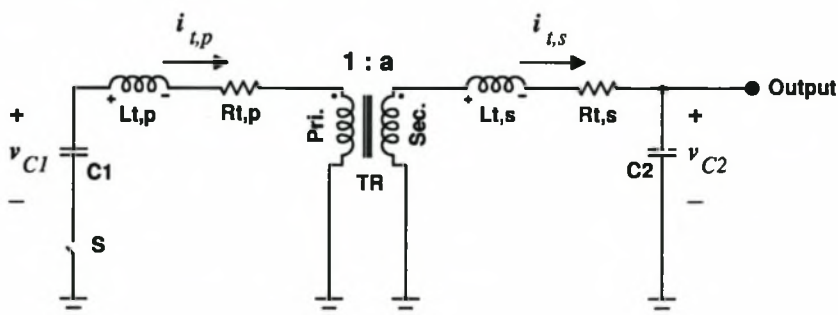


Figure 2-23: Circuit diagram of C-C transfer loop with pulse transformer.

Transformer characteristics and transformer losses are well documented for utility line and switch mode applications, but in laser pulsed power applications much shorter pulses are applied to the

transformer [43]. In addition, the voltage ratings of the transformer are also above average. In this section transformer behaviour and transformer losses are revised for pulsed power applications.

2.4.1 Characteristics of a pulse transformer in a C-C transfer loop

To analyse the behaviour of a pulse transformer in a C-C transfer loop the T-equivalent model of a transformer [31] is considered as shown in Figure 2-24. The secondary impedances, voltage and current are referenced to the primary side of the transformer, with

$$\begin{aligned}
 R'_{w,s} &= R_{w,s}/a^2, & L'_{l,s} &= L_{l,s}/a^2, & C'_2 &= a^2 C_2, & v'_{C2} &= v_{C2}/a, \\
 i'_{t,s} &= ai_{t,s}, & L'_{t,s} &= L_{t,s}/a^2, & R'_{t,s} &= R_{t,s}/a^2,
 \end{aligned}$$

where a is the turns ratio, N_s/N_p , of the pulse transformer with N_p the number of primary winding turns and N_s the number of secondary turns.

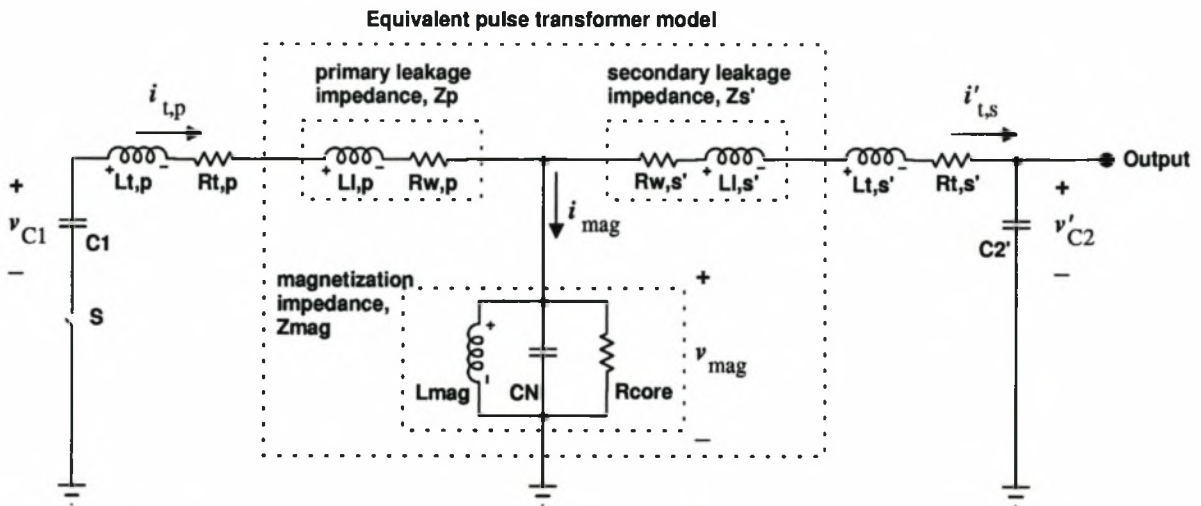


Figure 2-24: Equivalent T-network pulse transformer model in a C-C transfer loop.

The magnetization impedance Z_{mag} of the transformer consists of the magnetization inductance L_{mag} , the transformer core losses modelled as a resistance R_{core} , and the inter-turns capacitance C_N .

The transformer should not alter the C-C transfer characteristics. Ideally the primary and secondary winding resistances $R_{w,p}$ and $R'_{w,s}$ should be small in order to limit transfer losses. Furthermore, the magnetization impedance should be infinitely large, resulting in total current transfer through the

transformer with $|i_{t,p}| = |i'_{t,s}|$. In practical transformers the magnetization cannot be infinitely large. Nonetheless the transformer should be designed in such a way that the magnetization current is much smaller than the transfer current, $i_{\text{mag}} \ll i_{t,p}$, resulting in an almost total current transfer through the transformer, $i_{t,p} \cong i'_{t,s}$. If this condition holds true, the magnetization impedance can be ignored and approximated by an open circuit.

Ignoring the magnetization impedance results in a simplified model of the pulse transformer, consisting only of the primary and secondary leakage impedances, which are in series with the external transfer inductances, $L_{t,p}$ and $L'_{t,s}$, and resistances, $R_{t,p}$ and $R'_{t,s}$. The total transfer inductance L_t and transfer resistance R_t of the C-C transfer loop are therefore given by

$$L_t = L_{l,p} + L'_{l,s} + L_{t,p} + L'_{t,s}, \quad (2.37)$$

$$R_t = R_{w,p} + R'_{w,s} + R_{t,p} + R'_{t,s}. \quad (2.38)$$

A pulse transformer designed according to the abovementioned guidelines can be described by an equivalent circuit which is identical to the C-C transfer loops discussed in Section 2.2.1. The pulse transformer therefore does not change the characteristics of the C-C transfer loop and only adds additional inductance and resistance to the existing external transfer inductance and resistance. The equivalent C-C transfer loop can be calculated and optimised just as described in Section 2.2.2, with a total transfer inductance and resistance as defined in Equations 2.37 and 2.38.

2.4.2 Leakage inductance

The leakage inductance arises from magnetic leakage flux that does not link the primary and secondary windings of the transformer. All practical transformers will have a leakage inductance, because total flux linkage between the primary and secondary of the transformer would imply spatially overlapping the primary and secondary windings of the transformer. It is important to obtain an estimate of the transformer leakage inductance before commencing with the final transformer construction. The total primary equivalent leakage inductance can be calculated by the following expression [27]:

$$L_{\text{leak}} = \frac{\int \mu_o H^2 dV}{I_p^2}, \quad (2.39)$$

where V_w is the total transformer winding volume over which the volume integration is performed and I_p is the primary transformer current.

2.4.3 Core magnetization

Under normal operation the transformer core may not be saturated, i.e. the magnetic flux density generated by the magnetization inductance may not exceed the saturation flux density of the transformer core [27]. Saturation of the transformer core will lead to a strong drop in the magnetization impedance and an increase in the magnetization current. As discussed earlier the magnetization current should be kept small in comparison to the transfer current of the C-C transfer loop. An increased magnetization current due to core saturation may lead to distortion of the transformed voltage pulse. Unlike the MPC unit discussed in Section 2.3 the transformer core should not be saturated and using the integral Equation 2.26 the following must hold true to prevent saturation

$$\int_0^{\tau} v_{\text{mag}}(t) dt \leq N_p A_{\text{core}} \Delta B = \Delta \Phi, \quad (2.40)$$

where ΔB is the maximal allowable flux swing which will not saturate the transformer core, A_{core} the transformer cross-section and N_p the primary number of turns. The magnetization voltage v_{mag} is the voltage across the magnetization inductance as indicated in Figure 2-24, and during the transfer of the voltage pulse

$$v_{\text{mag}}(t) = v_{C1}(t) + (L_{l,p} + L_{l,p}) \frac{d}{dt} i_t(t).$$

The transformer voltage before and after the transferred pulse is zero. Therefore, ignoring both losses and magnetization current and assuming an optimised C-C transfer circuit ($C_1 = C_2$) Equations 2.4 and 2.5 can be used to determine the magnetization voltage

$$v_{\text{mag}}(t) = \begin{cases} \frac{V_0}{2} \left[1 + \left(1 - 2 \frac{L_{l,p} + L_{l,p}}{L_t} \right) \cos\left(\frac{\pi}{\tau} t\right) \right], & \text{for } 0 \leq t \leq \tau \\ 0 & \text{, elsewhere} \end{cases} \quad (2.41)$$

Using the above equation and solving the integral in Equation 2.40 results in the following design

condition that has to be met:

$$\frac{V_0 \tau}{2} \leq N_p A_{\text{core}} \Delta B. \quad (2.42)$$

Just as with the saturable inductors in the MPC unit, the transformer core can also be reset before a voltage pulse is applied. As discussed previously, this increases the total available swing in the magnetic flux density before the core is saturated, thereby reducing the required core cross-section and/or number of transformer turns.

Another important consideration is the core material, e.g. ferrite, laminated iron core, etc. Ferrite materials have smaller core losses [27], but in high-voltage applications the relatively small saturated magnetic flux density ($B_{\text{sat}} \approx 300$ mT) results in large core cross-sections and/or large number of turns. A small compact transformer design is thus not possible. The problem can be overcome by using laminated iron cores or special magnetic cores (Metglass, Finemet, etc.), which have larger saturation flux densities.

2.4.4 Transformer losses

Transformer losses consist of conduction (copper) losses, hysteresis losses and eddy current losses [27]. The conduction losses are dissipated in the transformer windings, whereas the eddy current and hysteresis losses are dissipated in the core and are thus called core or iron losses. In the following sections the different transformer losses are analysed. The same type of losses are encountered in saturable inductors [35], but in pulse transformers the losses are more critical, because these transformers are normally designed more compact and the power densities are higher.

Eddy current losses

Eddy current losses are mainly obtained in laminated iron cores, where eddy currents are induced in the core laminations due to flux changes in the transformer core. The specific eddy current losses $P_{\text{ec,sp}}$, i.e. the losses per unit volume, for a continuous applied sinusoidal transformer voltage of a laminated core, can be approximated by following expression [27]:

$$P_{\text{ec,sp}} = \frac{d^2 \omega^2 B^2}{24 \rho_{\text{core}}}, \quad (2.43)$$

where d is the lamination thickness, ω the angular frequency of the applied magnetic field, ρ_{core} the resistivity of the core iron and B the amplitude of the sinusoidal variation in the magnetic flux density due to an applied sinusoidal transformer voltage. However, in a pulsed power supply the magnetic flux in the transformer core is also pulsed. Through Fourier-transform analysis the applied pulse can be expressed as a spectrum $B(\omega)$ of superimposed sinusoidal waveforms [43], each of which are contributing to the eddy current losses. In general the eddy current energy loss $E_{\text{ec,sp}}$ due to a single applied voltage pulse can be obtained by using Equation 2.43 and integrating over the bandwidth of the applied voltage pulse:

$$E_{\text{ec,sp}} = \int_{-\infty}^{\infty} \frac{d^2}{24\rho_{\text{core}}} \omega^2 B^2(\omega) d\omega, \quad (2.44)$$

where $B(\omega)$ is the amplitude frequency spectrum of the magnetic flux density obtained by applying a voltage pulse to the transformer. The temporal waveform of the magnetic flux density can be obtained from the magnetization voltage v_{mag} with

$$B(t) = \frac{1}{N_p A_{\text{core}}} \int_{-\infty}^t v_{\text{mag}}(t') dt'. \quad (2.45)$$

The spectrum of the magnetic flux density of a pulse transformer used in a C-C transfer loop can now be obtained by considering the magnetization voltage given by Equation 2.41. In most transformer designs the total transfer inductance L_t of the C-C transfer loop is divided evenly between the primary and secondary side of the transformer, with $L_{t,p} + L_{t,p} \cong L'_{t,s} + L'_{t,s} = \frac{1}{2}L_t$. Equation 2.41 can hence be simplified:

$$v_{\text{mag}}(t) = \begin{cases} \frac{V_0}{2} & , \text{ for } 0 \leq t \leq \tau \\ 0 & , \text{ elsewhere} \end{cases} \quad (2.46)$$

The magnetization voltage is therefore approximated by a rectangular pulse with amplitude $V_0/2$ and width τ . Using Equations 2.45 and 2.46 the spectrum of the magnetic flux density can be determined [31]:

$$B(\omega) = \mathfrak{F}\{B(t)\} = \frac{2\Delta B}{\tau} \frac{\sin\left(\frac{\omega\tau}{2}\right)}{\omega^2}, \quad (2.47)$$

where ΔB is the flux change induced by the applied voltage pulse. Using the above equation and solving Equation 2.44 yields the eddy current loss $E_{ec,sp}|_{CLC}$ for a single pulse passed through the transformer used in a C-C transfer loop [13]:

$$E_{ec,sp}|_{CLC} = \frac{d^2 \Delta B^2}{24 \rho_{core}} \frac{4\pi}{\tau} \quad (2.48)$$

For a pulse repetition rate of f_{rep} the eddy current power loss $P_{ec,sp}|_{CLC}$ is simply

$$P_{ec,sp}|_{CLC} = \frac{d^2 \Delta B^2}{24 \rho_{core}} \frac{4\pi}{\tau} f_{rep} \quad (2.49)$$

It is interesting to note that for switch mode power supplies the eddy current loss can now be estimated by Equation 2.43, with $\omega = 2\pi f_s$, [27] where f_s is the switching frequency, which is comparable to the repetition rate in pulsed power supplies, i.e. $f_s \approx f_{rep}$. From this it can be shown that the ratio of the eddy current loss in pulsed power supplies to switch mode supplies is

$$\frac{P_{ec,sp}(\text{pulse power})}{P_{ec,sp}(\text{switch mode})} = \frac{1}{\pi D},$$

where D is the duty cycle of the applied pulses, with $D = \tau/T_{rep}$, where τ is the pulse width and T_{rep} the period between pulses ($T_{rep} = 1/f_{rep}$). However, in pulsed power supplies $D \ll 1$ ($\tau \ll T_{rep}$) and eddy current losses in pulsed power supplies are therefore much higher compared to switch mode supplies. Care must be taken to provide adequate cooling for the transformer core in pulsed power applications.

Hysteresis losses

Hysteresis losses are a function of the core material and the amplitude of the applied magnetic field. The energy per unit volume $E_{hys,sp}$ dissipated in the transformer core due to hysteresis losses after traversing the BH-curve of the core once is given by the well-known equation [13]

$$E_{hys,sp} = \oint HdB = \oint BdH.$$

Since in a pulsed power supply the BH-curve is traversed with each generated pulse, the power dissipated per unit volume due to hysteresis losses is similar to transformers used in switch mode power supplies and is given by

$$P_{\text{hys,sp}} = f_{\text{rep}} E_{\text{hys,sp}}, \quad (2.50)$$

where f_{rep} is the repetition rate of the applied pulses.

Conduction (copper) losses

The conduction losses can be calculated straightforward from the RMS primary and secondary transfer currents (see Figure 2-24), with

$$P_{\text{Cu}} = R_{w,p} I_{t,p,\text{RMS}}^2 + R_{w,s} I_{t,s,\text{RMS}}^2 \cong (R_{w,p} + R'_{w,s}) I_{t,p,\text{RMS}}^2, \quad (2.51)$$

with $R_{w,p}$ and $R_{w,s}$ the primary and secondary winding resistances, respectively. The transfer RMS currents can be calculated using Equation 2.21. Ignoring the skin effect the primary winding resistance is given by the following expression [27]

$$R_{w,p} = \frac{N_p^2 l_p \rho_{\text{Cu}}}{p_p A_{w,p}}, \quad (2.52)$$

where l_p is the average length of a single turn, ρ_{Cu} the resistivity of copper, $A_{w,p}$ the primary winding area and p_p the copper fill factor of the primary winding. The secondary winding resistance can be calculated in a similar fashion.

and

$$R_{w,s} = \frac{N_s^2 l_s \rho_{\text{Cu}}}{p_s A_{w,s}}. \quad (2.53)$$

The total winding window cross-section A_w is the area enclosed by the transformer core and into which the transformer windings are placed. The primary and secondary winding windows $A_{w,p}$ and $A_{w,s}$ are the portions of the total winding window occupied by the primary and secondary

windings, respectively. The copper fill factor p is the ratio of the total conductor area to the winding window area and is given by

$$p = \frac{NA_N}{A_w}, \quad (2.54)$$

where A_N is the conductor cross section and N the number of turns. The fill factor is mainly determined by the winding wire configuration (ribbon wire, Litz wire, etc.) and the amount of insulation, and may range between 0.2 and 0.6 [27].

The conduction losses can also be expressed in terms of the primary and secondary RMS current densities $J_{l,p,RMS}$ and $J_{l,s,RMS}$:

$$P_{Cu} = p_p A_{w,p} N_p l_p J_{l,p,RMS}^2 + p_s A_{w,s} N_s l_s J_{l,s,RMS}^2, \quad (2.55)$$

where the current density is simply $J_{RMS} = I_{RMS}/A_N$.

2.5 Conclusion

A C-C transfer topology is chosen for the IGBT driven pulsed power supply and a directly switched C-C transfer loop is utilized in the primary switching unit. The MPC unit is based on a series magnetic pulse compression topology.

It is found that the transfer efficiency of C-C transfer loops in laser pulsed power supply designs can be optimised with 'design method B' by fixing the output capacitor and varying the input capacitor of the C-C transfer loop as described in Section 2.2.2. Furthermore, it is shown that the switching current of a directly switched C-C transfer loop can be decreased by increasing the transfer time and/or the charging (switching) voltage of the C-C transfer.

The magnetic core volume of the MPC can be reduced by using switching ratios of less than unity (i.e. the MPC stages of the MPC unit are timed to switch before the transfer in the previous MPC stage is completed), resetting the MPC saturable cores and by optimising the number of MPC stages. The theoretical optimum number of MPC stages, which will minimize the core volume, is

not necessarily the most economical solution. Costs of the C-C transfer capacitors and construction costs have to be taken into account.

To increase the pulse voltage to the required level a pulse transformer can be simply inserted into a C-C transfer loop. The magnetization impedance of the transformer has to be large compared to the transfer impedance. The short voltage pulses obtained in pulsed power supplies can result in larger eddy current losses compared to other applications (e.g. switch mode power supplies) and special care must be taken to cool the transformer core.

Chapter 3

Characteristics of an IGBT in a laser pulsed power supply

In the previous chapter different pulsed power supply topologies and layouts were discussed and it was concluded that for this project the initial voltage pulse is generated by a switched C-C transfer loop. An IGBT will be used as the active switching device. A large amount of information is available on the switching behaviour of IGBTs in switch mode power supplies, but little is known on the switching behaviour of IGBTs in pulsed power supplies. The main difference between switch mode and pulsed power supplies is the switched current waveform. In switch mode power supplies existing circuit (inductor) currents are switched [27], whereas in a pulsed power supply the main switching current is only obtained after the IGBT has turned on. The turn-on transient of an IGBT in a pulsed power supply is therefore different than in switch mode power supplies. In the following sections the turn-on transient of an IGBT in a C-C transfer loop is analysed using an equivalent circuit model. Furthermore, aspects like over-current ratings, thermal characteristics, series stacking and paralleling of IGBTs are discussed.

3.1 IGBT circuit model

Before analysing the transient response of an IGBT in a C-C transfer loop the general characteristics of an IGBT have to be considered. The IGBT is a combination of a BJT (bipolar

junction transistor) and a MOSFET (metal-oxide-semiconductor field-effect transistor) as shown in Figure 3-1. The input of the IGBT therefore resembles the input gate of a MOSFET whereas the output resembles a BJT. Similar to a MOSFET the IGBT is a voltage-controlled device, where the collector-emitter current i_C is controlled by the gate-emitter voltage v_{GE} .

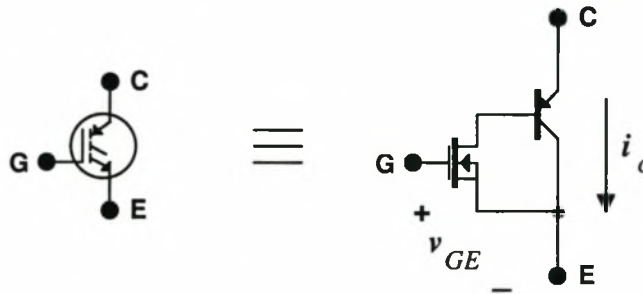


Figure 3-1: IGBT as a combination of a MOSFET and BJT.

Typical transfer functions of an IGBT are shown in Figure 3-2, where the collector current i_C is plotted as a function of the collector-emitter voltage v_{CE} for different gate-emitter voltages v_{GE} . The collector current is clearly a function of both the gate-emitter and collector-emitter voltages. Three operating regions can be identified:

1. $v_{CE} < v_{CE}(\text{sat})$: In this region the collector-emitter voltage is relatively constant with a slight dependence on the collector current. The collector-emitter voltage can be approximated by a constant on-state voltage drop V_{on} with a small equivalent collector-emitter resistance r_{CE} ,

$$v_{CE,\text{on}} \cong V_{\text{on}} + r_{CE} i_C \quad (3.1)$$

The on-state voltage drop of an IGBT is typical for a BJT, resulting in lower conduction losses in comparison to MOSFET's [27]. In this operating region the collector current is determined by the external circuit components and if the IGBT is used in switching applications this corresponds to the on-state of the IGBT.

2. $v_{CE} > v_{CE}(\text{sat})$: In this region the IGBT saturates and the collector-current is limited with the saturated current determined by the gate-emitter voltage as shown in Figure 3-3. The collector-current depends only slightly on the collector-emitter voltage, which can be modelled by the "early effect" [29], but will be ignored in this discussion. The IGBT

therefore resembles a voltage controlled current source where the saturated collector current is given by the following equation:

$$i_C(\text{sat}) = k(v_{GE} - V_{Th})^2, \quad (3.2)$$

where k is a constant, which depends on semiconductor doping and wafer geometry of the IGBT [29]. This region is not desirable in switching applications, due to the high power dissipation in the IGBT. Therefore, if the IGBT is used in switching applications, care must be taken that the collector current does not exceed the saturated current during the on-state. Excessive collector-currents will force the IGBT into saturation, thereby causing a sudden increase in the collector-emitter voltage coupled with large power dissipations.

3. $v_{GE} < V_{Th}$: If the gate-emitter voltage is below a given threshold voltage V_{Th} no collector current can flow and the IGBT turns off.

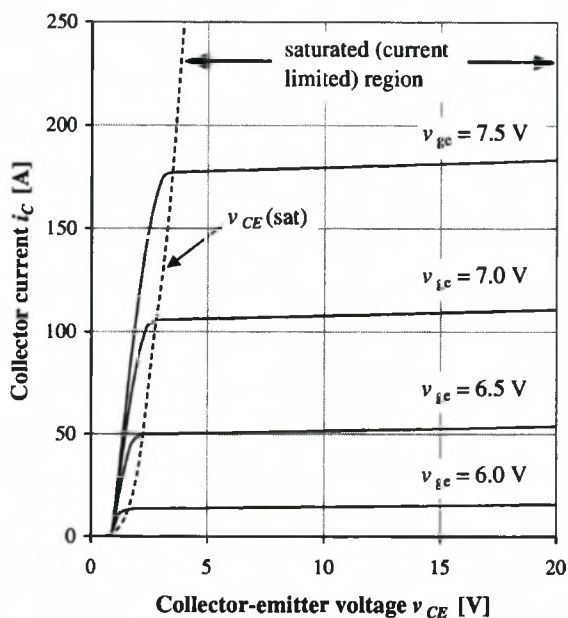


Figure 3-2: Transfer characteristics of an IGBT.

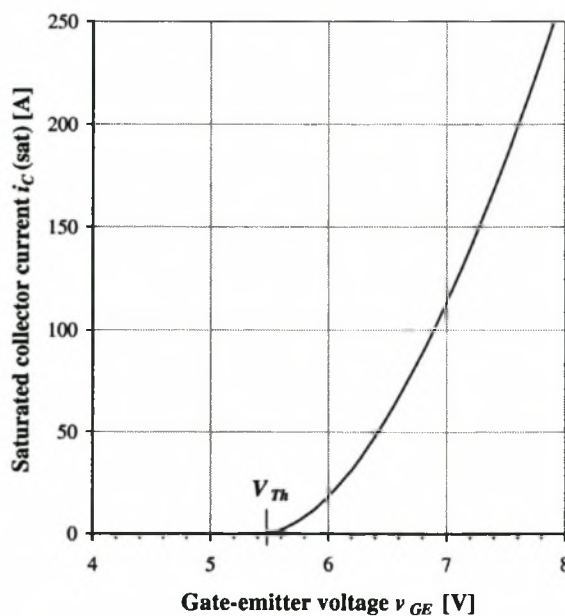


Figure 3-3: Saturated collector current of an IGBT as a function of the gate-emitter voltage.

The equivalent circuit model [27][29] of the IGBT is shown in Figure 3-4 and is similar to a MOSFET. The voltage-dependent current source G_C is the active component with a transfer function as described earlier and shown in Figures 3-2 and 3-3. The remaining circuit elements C_{gc} , C_{ge} , L_c and L_g are the parasitic capacitances and inductances of the IGBT, which dictate the dynamic response of the IGBT as discussed in the next section.

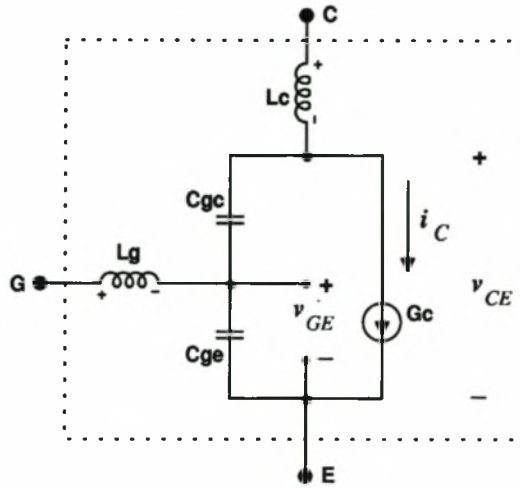


Figure 3-4: Equivalent circuit model of an IGBT.

3.2 IGBT dynamic response in a C-C transfer loop

As mentioned earlier in switch mode supplies the IGBT switches an existing circuit (inductor) current. However, in a pulsed power supply there is no initial current during turn-on and a sinusoidal current pulse, generated by a C-C transfer loop, is obtained after turn-on (see Chapter 2). In order to analyse the IGBT turn-on transient, the IGBT model shown in Figure 3-4 has to be considered within a C-C transfer loop as depicted in Figure 3-5.

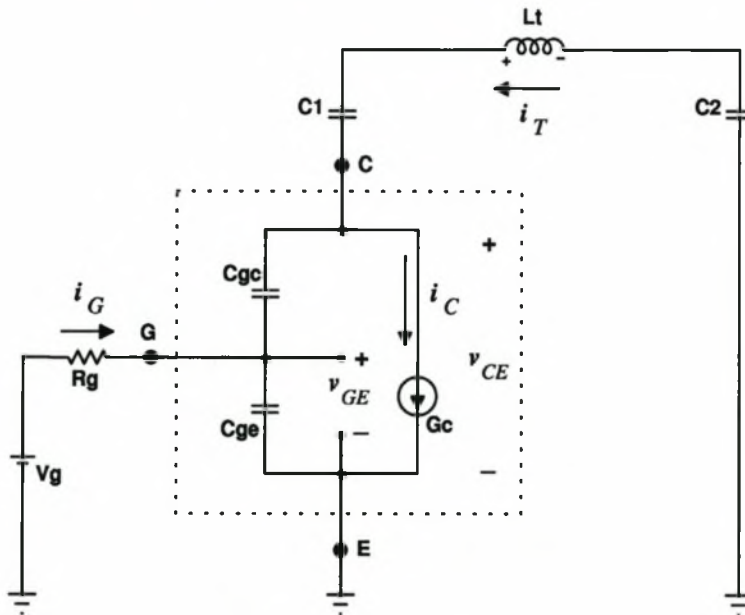


Figure 3-5: Equivalent circuit model of an IGBT in a C-C transfer loop.

The parasitic inductances have been ignored, because the collector inductor L_c is in series with the transfer inductance L_t of the C-C transfer loop, where $L_t \gg L_c$. The gate inductor L_g can also be ignored, because the external gate resistor is normally chosen big enough to sufficiently dampen possible oscillation that can be caused by the gate inductor and the parasitic capacitances C_{ge} and C_{gc} . As discussed in Chapter 2, the IGBT is initially in the off-state. The input capacitor C_1 is charged to an initial voltage V_0 , which is equal to the initial off-state voltage drop over the IGBT.

Evidently the IGBT is turned on by applying a positive voltage step to the gate, which is achieved by connecting a voltage source via a gate resistor to the gate of the IGBT as depicted in Figure 3-5. In general three phases can be identified (Figure 3-6) in the turn-on transient of the IGBT [17][27]:

1. *Turn-on delay time, t_d* : After a positive voltage step has been applied to the gate of the IGBT there is a turn-on delay. This is the time needed for the gate-emitter capacitor C_{ge} to charge up to a voltage larger than the threshold voltage V_{Th} in order to turn the IGBT on.
2. *Voltage fall-time, t_f* : The gate-collector (Miller) capacitor is initially charged to a voltage equal to the off-state voltage of the IGBT. The fall-time t_f is the time needed for the collector-gate capacitor C_{gc} to discharge and the voltage over the IGBT to drop. During this transient phase (between the on- and off-state) the IGBT is in a saturated state and the gate-emitter voltage is clamped.
3. *On-state*: After the voltage fall-time, the IGBT eventually reaches the unsaturated on-state with $v_{CE} < v_{CE(sat)}$, as described in the previous section. The gate-emitter voltage is not clamped anymore and increases to the maximum applied gate-emitter voltage, thereby further reducing the IGBT on-state voltage drop.

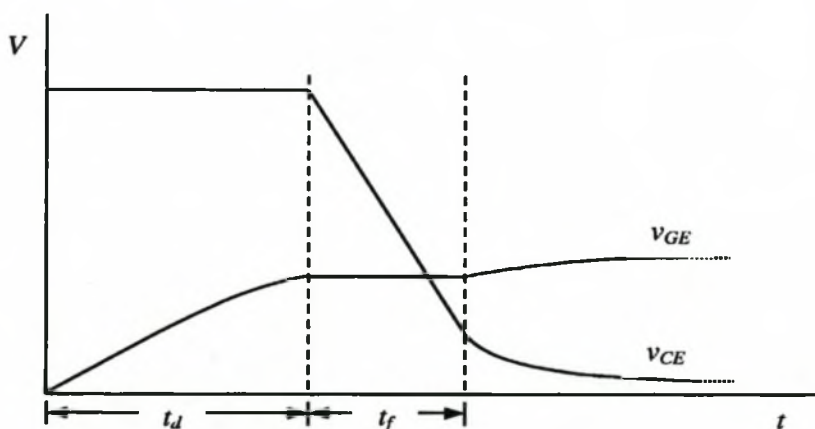


Figure 3-6: General turn-on switching waveforms of an IGBT.

In the following sub-sections each of the earlier mentioned phases of the turn-on transient of the IGBT within a C-C transfer loop is revised in more detail.

3.2.1 Turn-on delay

The turn-on delay in pulsed power supplies is identical to switch mode power supplies. During the turn-on delay period the gate-emitter capacitor is charged by the externally applied voltage V_G through the external gate resistor R_G . The gate-emitter voltage is still below the threshold voltage V_{Th} and the IGBT is in an off-state with zero collector current. During this phase very little current is flowing through the gate-collector capacitor and the gate-collector capacitor can be ignored. The equivalent circuit for this state is shown in Figure 3-7.

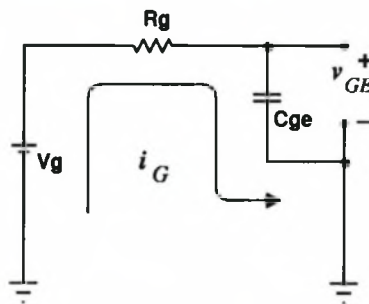


Figure 3-7: Equivalent circuit model during the turn-on delay.

From Figure 3-7 it becomes apparent that the circuit is a simple RC charging loop, with

$$v_{GE}(t) = V_g \left(1 - e^{-t/R_g C_{ge}} \right), \text{ for } v_{GE} < V_{Th}, t < t_d. \quad (3.3)$$

The turn-on delay time t_d is therefore

$$t_d = R_g C_{ge} \ln \left(1 - \frac{V_{Th}}{V_g} \right), \text{ with } v_{GE}(t_d) = V_{Th}. \quad (3.4)$$

3.2.2 Voltage fall-time

As soon as the gate-emitter voltage reaches the threshold voltage V_{Th} the IGBT starts conducting in a saturated state [27] and a current-rise through the transfer inductor L_t is initiated. If the voltage fall-time t_f is much faster than the initial current-rise of the transfer current i_T the transfer current

can be ignored. The transfer inductance effectively decouples the IGBT from the C-C transfer loop during the turn-on transient, but only if the IGBT switches fast enough in comparison to the transfer time τ of the C-C loop. Decoupling is desirable, because it decreases the voltage fall time and reduces switching and conduction losses in the IGBT. Criteria for effective decoupling are discussed in Section 3.2.4.

The equivalent circuit during the voltage fall-time period t_f is shown in Figure 3-8 where the C-C transfer loop is ignored due to the decoupling effect of the transfer inductance. The collector-gate capacitor C_{gc} is initially charged to V_0 , which is equal to the off-state voltage drop of the IGBT.

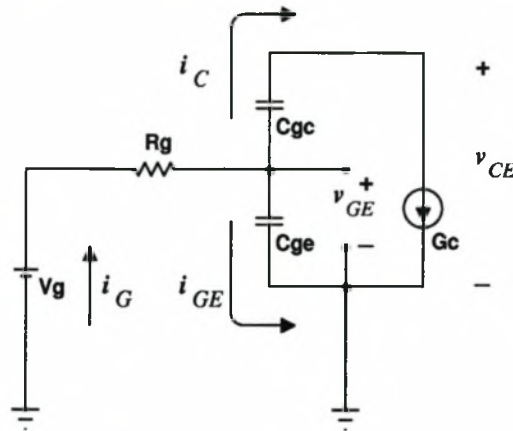


Figure 3-8: Equivalent circuit during the voltage fall period.

As seen in Figure 3-3 and Equation 3.2 the relationship between the collector current and the gate-emitter voltage is non-linear. In order to simplify the circuit analyses Equation 3.2 is linearized for a gate-emitter voltage close to the threshold voltage, $v_{GE} \cong V_{Th}$,

$$i_C = k(v_{GE} - V_{Th})^2 \cong a(v_{GE} - V_{Th}), \quad (3.5)$$

where a is the linearized trans-conductance of the IGBT. From Figure 3-8 it is apparent that the maximum possible collector current is equal to the maximum gate current, $i_{G,max} \cong (V_g - V_{Th})/R_g$. Therefore, for this analysis the trans-conductance a is approximated for the collector current range $0 < i_C < i_{G,max}$, with

$$a \cong \sqrt{k} \sqrt{\frac{V_g - V_{Th}}{R_g}}. \quad (3.6)$$

From Figure 3-8 it is clear that $i_G = i_{GE} + i_C$. Now using Equation 3.5 and the derivative of the gate-emitter capacitor voltage, the following differential equation is obtained

$$\frac{V_g - v_{GE}}{R_g} = C_{ge} \frac{dv_{GE}}{dt} + a(v_{GE} - V_{Th}). \quad (3.7)$$

The solution to the above linear differential equation with a starting condition of $v_{GE}(t_d) = V_{Th}$ is

$$v_{GE}(t) = V_{Th} + \frac{V_g - V_{Th}}{1 + aR_g} \left(1 - e^{-\frac{1+aR_g}{R_g C_{ge}}(t-t_d)} \right), \text{ for } v_{GE} > V_{Th}, t > t_d. \quad (3.8)$$

The IGBT collector current i_C , which is also the discharging current of the gate-collector (Miller) capacitor, can be determined by using Equation 3.5 with

$$i_C(t) = a \frac{V_g - V_{Th}}{1 + aR_g} \left(1 - e^{-\frac{1+aR_g}{R_g C_{ge}}(t-t_d)} \right), \text{ for } t > t_d. \quad (3.9)$$

Normally in high-voltage, high-power IGBTs the product aR_g is relatively large (see Appendix C), with $aR_g \gg 1$. From Equation 3.8 it is apparent that for $aR_g \gg 1$ the gate-emitter voltage is clamped just above the threshold voltage and it can be assumed that the gate-emitter voltage is more or less equal to the threshold voltage, $v_{GE} \cong V_{Th}$, during the voltage fall-time period. Furthermore, Equation 3.9 can be simplified for $aR_g \gg 1$:

$$i_C(t) \cong \frac{V_g - V_{Th}}{R_g} \left(1 - e^{-\frac{a}{C_{ge}}(t-t_d)} \right) = \bar{I}_C \left(1 - e^{-\frac{(t-t_d)}{\tau_{equ}}} \right), \text{ for } t > t_d, \quad (3.10)$$

$$\text{with } \bar{I}_C = \frac{V_g - V_{Th}}{R_g} \quad \text{and} \quad \tau_{equ} = \frac{C_{ge}}{a}.$$

The collector current behaves similar to the current build-up in an RL-circuit with an equivalent time-constant τ_{equ} and a steady state current \bar{I}_C . In the steady state the gate-emitter current i_{GE} drops to zero and the gate-emitter voltage stabilises and stays constant. As a consequence the entire gate

current i_G flows through the gate-collector capacitor of the IGBT. The steady-state gate current \bar{I}_G and gate-emitter current \bar{I}_{GE} are

$$\bar{I}_C = \bar{I}_G = \frac{V_g - V_{Th}}{R_g}, \quad (3.11)$$

$$\bar{I}_{GE} = 0. \quad (3.12)$$

Usually the equivalent time constant τ_{equ} is much faster than the voltage fall-time t_f . It can be assumed that the gate-collector capacitance C_{gc} is discharged by the constant steady state current \bar{I}_C [27]. The gate-collector capacitor is discharged until the IGBT collector-emitter voltage drops below the saturated voltage threshold $v_{CE}(\text{sat})$ and the IGBT has reached the on-state region as described in previous sections. The time for the gate-collector capacitor to discharge and the IGBT to reach the on-state is equal to the voltage fall-time t_f , which is given by the following equation:

$$t_f = \frac{(V_0 - v_{CE}(\text{sat}))C_{gc}}{\bar{I}_C} \cong \frac{V_0 C_{gc}}{\bar{I}_C} = \frac{V_0}{V_g - V_{Th}} R_g C_{gc}, \quad \text{for } t_f \gg \tau_{equ}. \quad (3.13)$$

Normally the initial collector-emitter voltage V_0 is much larger than the on-state voltage drop $v_{CE}(\text{on})$ and the on-state voltage drop can be ignored in the calculation of the voltage fall-time. The discharge rate and thus the voltage fall rate of the IGBT is given by the following expression:

$$\dot{v}_{CE} = \frac{\bar{I}_C}{C_{gc}} = \frac{V_g - V_{Th}}{R_g C_{gc}}, \quad \text{for } t_f \gg \tau_{equ}. \quad (3.14)$$

The voltage fall-time can be reduced by either increasing the externally applied gate voltage or reducing the value of the gate resistor R_g . However, there is a limit to both the applied gate voltage and the value of the gate resistor. The gate voltage may not exceed the rated gate voltage of the IGBT; otherwise the gate insulation can be destroyed. Furthermore, a too small gate resistor can result in oscillations of the gate-emitter voltage due to insufficient damping of the gate-emitter capacitance and the gate inductance. The minimum usable gate resistor is normally specified in the data sheets of the IGBT.

3.2.3 On-state

After the voltage fall-time period the IGBT reaches the on-state region and conducts in the unsaturated state with a relatively constant collector-emitter voltage. The gate-collector current drops to almost zero and there is no significant voltage change over the gate-collector capacitor. The collector current is now equal to the C-C transfer current i_t . The equivalent circuit model during the on-state is shown in Figure 3-9.

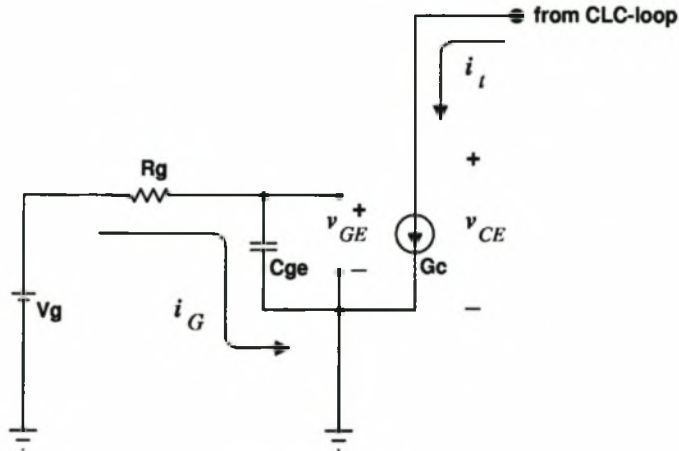


Figure 3-9: Equivalent circuit during the IGBT on-state.

The gate circuit is identical to the circuit model during the turn-on delay period. After the voltage fall-time period the gate-emitter voltage is no longer clamped and the applied gate voltage resumes charging the gate-emitter capacitor. As the gate-emitter voltage increases to the finally charged voltage V_g , the on-state voltage is decreased and the maximum possible saturated collector current $i_C(\text{sat})$ is increased as shown in Figure 3-3. It is important that the gate-emitter voltage has increased to a sufficiently high level before the C-C transfer current reaches a maximum. Otherwise the IGBT will saturate, clamping the transfer current and inducing a sudden voltage rise over the IGBT. Normally this is not a problem though and the gate-emitter capacitor is almost fully charged after only a few tens of nanoseconds.

3.2.4 Decoupling criteria and magnetic assist

The analysis in Section 3.2.2 was conducted for the special case where the IGBT switches much faster than the response time of the C-C transfer loop. This will reduce the switching losses and the voltage fall-time, due to the decoupling of the IGBT switching transient from the C-C response. In the following analysis it will be shown that sufficient decoupling is obtained, when the maximum possible current rise in the IGBT's collector-current is much higher than the initial current rise in the C-C transfer loop.

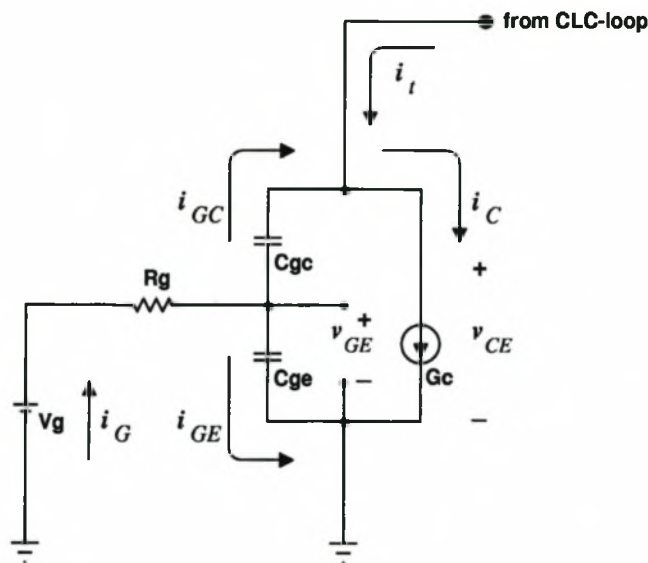


Figure 3-10: Equivalent circuit during initial voltage fall-time with injection of an external C-C transfer current.

The circuit diagram shown in Figure 3-10 is identical to the diagram shown in Figure 3-8 in the previous section, but takes the effect of the external C-C transfer current i_t into account. From Figure 3-10 a basic equation describing the gate-collector current i_{GC} can be derived:

$$i_{GC} = i_G - i_{GE} = i_G - C_{ge} \frac{dv_{GE}}{dt}.$$

Using Equation 3.5 and the fact that $i_C = i_{GC} + i_t$, the expression for the gate-collector current above can be rewritten as

$$i_{GC} = i_G - \frac{C_{ge}}{a} \frac{di_{GC}}{dt} - \frac{C_{ge}}{a} \frac{di_t}{dt}. \quad (3.15)$$

Ignoring the contribution of the transfer current in the above equation will result in a differential equation which is equivalent to Equation 3.7, with the solution given by Equation 3.9. The introduction of an additional current rise due to the C-C transfer current will clearly decrease the gate-collector current. This decreases the discharge rate of the gate-collector capacitor and increases the voltage fall-time. The rise in the C-C transfer current effectively decreases the portion of the gate current flowing into the gate-collector capacitor. To minimize the effect of the C-C transfer current the transfer current should be kept sufficiently small:

$$\frac{di_C}{dt} \ll \frac{a}{C_{ge}} i_G. \quad (3.16)$$

Equivalent to the analysis in Section 3.2.2 the collector current is relatively small and the gate-emitter voltage is clamped close to the threshold voltage V_{Th} . The gate current can therefore again be approximated by $i_G \cong (V_g - V_{Th})/R_g$. In Chapter 2 an expression for C-C transfer current was derived and is shown here again for convenience:

$$i_t(t) = I_0 \sin\left(\frac{\pi}{\tau} t\right), \quad 0 \leq t \leq \tau, \quad (\text{no losses}) \quad (3.17)$$

$$\text{with} \quad I_0 = \frac{\pi E_0}{\tau V_0},$$

where τ is the transfer time of the C-C loop, E_0 the stored energy in the input capacitor of the C-C loop and V_0 the initial charging voltage of the input capacitor. The initial current rise in the C-C loop, which is also the maximum IGBT current rise, is

$$\frac{di_t}{dt}(\text{max}) = \left. \frac{di_t}{dt} \right|_{t=0} = I_0 \frac{\pi}{\tau} = \frac{E_0}{V_0} \left(\frac{\pi}{\tau}\right)^2. \quad (3.18)$$

Using Equations 3.16 and 3.18 the decoupling criteria of the switching transient of an IGBT in a C-C transfer loop can be determined:

$$I_0 \frac{\pi}{\tau} = \frac{E_0}{V_0} \left(\frac{\pi}{\tau}\right)^2 \ll \frac{a}{C_{ge}} \frac{V_g - V_{Th}}{R_g}. \quad (3.19)$$

Often the charging voltage V_0 is determined by the IGBT voltage rating and is therefore more or less fixed. Furthermore, the transfer energy E_0 of the C-C loop is fixed by the design specifications of the pulsed power supply. The transfer time τ of the C-C loop has to be adjusted to assure decoupling of the IGBT during the turn-on transient. Consequently, it is useful to rewrite Equation 3.19 to obtain the decoupling criteria for the C-C transfer time:

$$\tau \gg \pi \sqrt{\frac{E_0}{V_0} \frac{C_{ge} R_g}{a(V_g - V_{Th})}}, \quad (3.20)$$

or

$$\tau \gg \pi I_p \frac{C_{ge} R_g}{a(V_g - V_{Th})}. \quad (3.21)$$

In cases where the decoupling criteria cannot be met a magnetic assist [12] can be used. This is simply a saturable inductor placed in series with the C-C transfer circuit (see Figure 3-11). The voltage hold-off of the saturable inductor, as discussed in Chapter 2, delays the transfer current, allowing the IGBT to first fully switch on before the magnetic assist saturates and a C-C transfer is obtained.

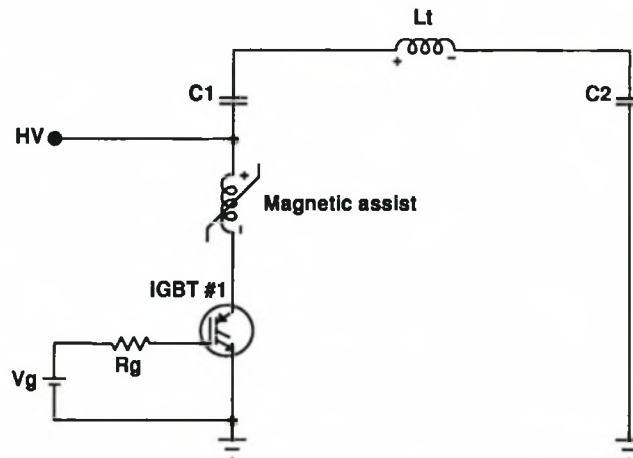


Figure 3-11: IGBT turn-on transient decoupling by magnetic assist.

3.2.5 Simulations of IGBT turn-on transient

The response of the IGBT in a C-C transfer loop was simulated with PSpice, a circuit simulation program. The PSpice model of an IGBT was obtained from Semikron, one of the IGBT manufacturers. The results of the simulated turn-on transient for a high-voltage, high-current IGBT (SKM300GB124, a 1200V / 300A IGBT from Semikron) are shown in Figures 3-12 and 3-13.

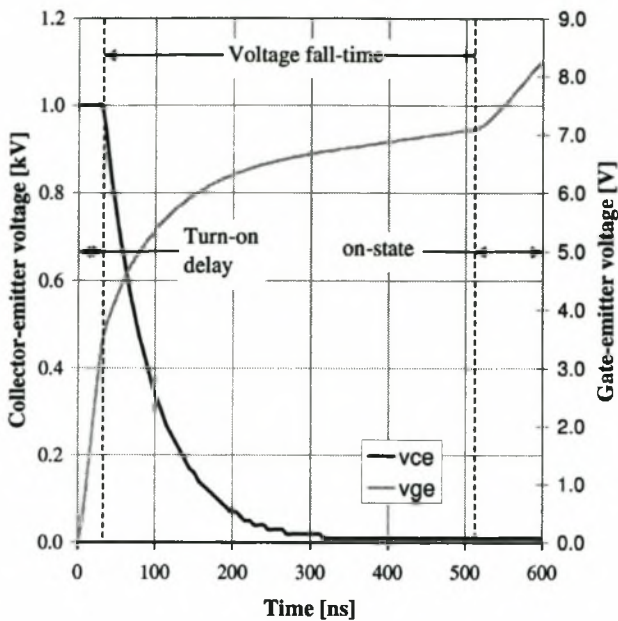


Figure 3-12: IGBT gate-emitter and collector-emitter voltages during the turn-on transient.

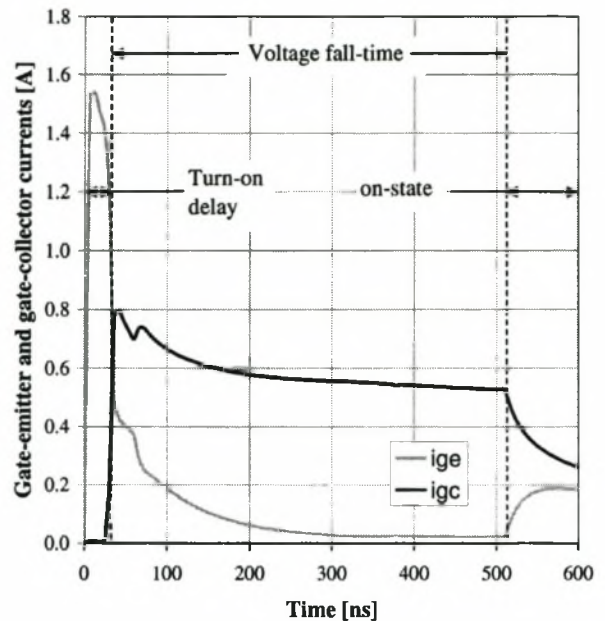


Figure 3-13: IGBT gate-emitter and gate-collector capacitor currents during the turn-on transient.

Figure 3-12 shows the gate-emitter and collector-emitter voltages and Figure 3-13 the gate-emitter and gate-collector capacitor currents. In both graphs the three phases in the turn-on transient can be clearly seen. During the turn-on delay the gate-emitter capacitor charging current is clearly visible. As predicted by Equation 3.8 the gate-emitter voltage is not immediately clamped at the beginning of the voltage fall-time period, but still increases for a relatively short period of time before it is eventually more or less clamped above the threshold voltage. As expected the gate-emitter current quickly drops to zero during the voltage fall-time period. At the same time the gate-collector current rapidly increases from zero to a more or less constant steady-state current, which discharges the gate-collector capacitor. The transition from the voltage fall-time period to the on-state can also be distinguished. Both the gate-emitter current and voltage abruptly start increasing as the gate-emitter capacitor continues to charge.

There are some differences between the simulated and theoretically predicted results, especially the voltage fall-time, which seems to be much faster than expected. Theoretically the collector-emitter voltage should decrease linearly during the voltage fall-time period. Instead the simulated waveforms show that the main decrease in the collector-emitter voltage is obtained over the first part of the voltage fall-time period. The model used for the transient analysis as shown in Figure 3-4 is very simple and it can be expected that a more realistic model, such as the one used for the

simulation, will yield different results. Nonetheless, the basic processes of the turn-on transient are explained by the simple model and is sufficient the analysis in this chapter.

The response of the IGBT for an adequately and inadequately decoupled C-C transfer loop during the switching transient is also simulated. The results are shown in Figure 3-14. The same IGBT model as for the previous simulation was used. The simulated IGBT, the SKM300GB124D from Semikron, has a gate-emitter capacitance of $C_{ge} = 11$ nF, a threshold voltage $V_{Th} = 5.5$ V and the linearized trans-conductance is approximately $a \cong 25$ A/V. Furthermore, a gate voltage of $V_g = 18$ V was used and the C-C transfer loop is initially charged to $V_0 = 1000$ V with a stored energy of $E_0 = 1$ J. Using Equation 3.20 it was calculated that for sufficient decoupling the transfer time of the switched C-C loop should be greater than $2 \mu\text{s}$. The IGBT turn-on transient was simulated for a C-C transfer time of $6 \mu\text{s}$ and $2 \mu\text{s}$. For the C-C transfer with a transfer time of $6 \mu\text{s}$ the IGBT switching behaviour is satisfactory, i.e. as soon as the IGBT switches the voltage over the IGBT drops quickly to zero and the C-C transfer current pulse is obtained. Whereas for the C-C transfer with a transfer time of $2 \mu\text{s}$ the current rise of the C-C transfer loop is too large. The IGBT is not capable of turning on completely. The need for sufficient decoupling during turn-on is therefore clearly demonstrated in this simulation.

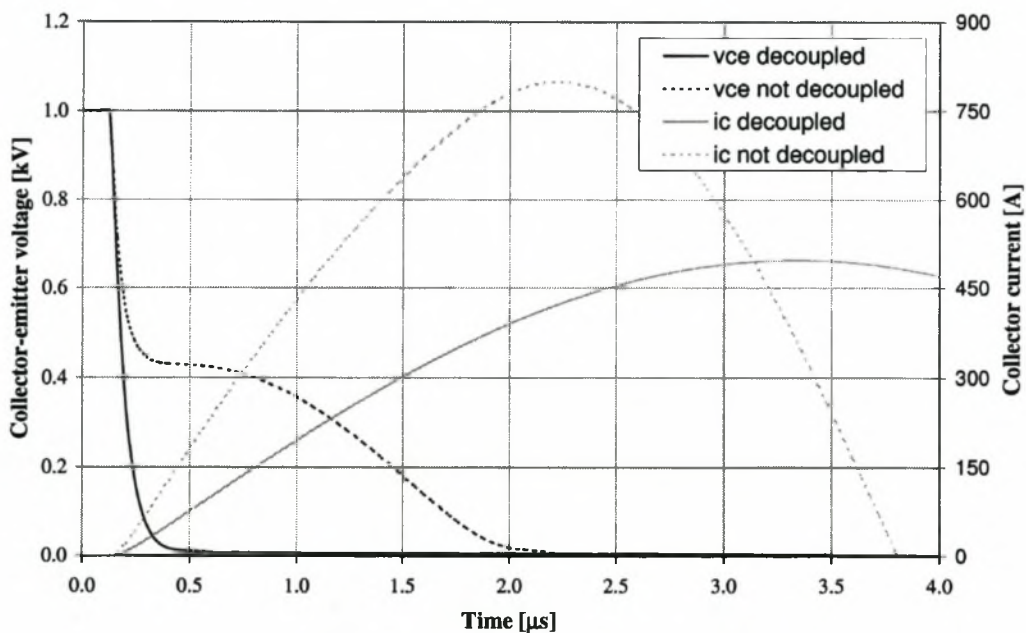


Figure 3-14: Simulated IGBT turn-on transient demonstrating the effect of decoupling.

3.3 Conduction losses and thermal design considerations

It is important to determine the conduction losses, which is necessary for thermal design considerations. The turn-on switching losses are ignored, because for sufficient decoupling as discussed earlier, the collector current is negligibly small and the switching losses are therefore minimal. Another aspect, which has to be taken into account, is the fact that in a pulsed power supply the IGBT switches short pulses with large instantaneous power dissipation, but with a very small duty cycle. A simple steady state thermal analysis is therefore not valid and a transient thermal analysis is needed to determine the instantaneous temperature inside the IGBT.

3.3.1 Average conduction losses

As indicated in Figure 3-15, the conduction losses are caused by the switched current pulses, which generate comparatively large power dissipation in the IGBT during the pulse period.

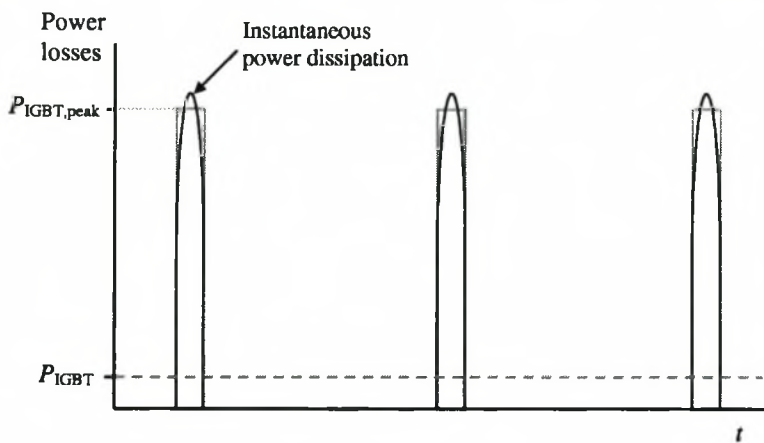


Figure 3-15: Power dissipation in an IGBT in a pulsed power supply.

The average pulse power dissipation $P_{IGBT,pulse}$ in the IGBT during the duration of the switched pulse can be calculated from the on-state voltage drop defined by Equation 3.1 and the average and RMS pulse switching currents given by Equations 2.18 and 2.19:

$$P_{IGBT,pulse} = V_{on} I_{s,avg}|_{pulse} + r_{CE} I_{s,RMS}|_{pulse}^2 = I_{s,peak} \left(\frac{2}{\pi} V_{on} + \frac{1}{2} r_{CE} I_{s,peak} \right). \quad (3.22)$$

The average conduction losses P_{IGBT} of a continuously switched pulse train can now be obtained by multiplying the pulse power dissipation $P_{\text{IGBT,pulse}}$ with the effective duty cycle D of the switched pulse train:

$$P_{\text{IGBT}} = DP_{\text{IGBT,pulse}} = DI_{s,\text{peak}} \left(\frac{2}{\pi} V_{\text{on}} + \frac{1}{2} r_{\text{CE}} I_{s,\text{peak}} \right), \quad (3.23)$$

where $D = \frac{\tau}{T_{\text{rep}}} = f_{\text{rep}} \tau$,

with τ the transfer time of the C-C transfer loop and f_{rep} the repetition rate of the switched pulses. The values for V_{on} and r_{CE} are normally specified in the manufacturer's data sheets of the IGBT.

3.3.2 Thermal considerations

In a pulsed power supply the IGBT is heated by the switched pulses, which cause relatively high instantaneous power dissipation in the IGBT. With each switched pulse the relatively large power dissipation causes the internal junction temperature of the IGBT to increase steeply. During the period between pulses there is no power dissipation and the junction of the IGBT is allowed to cool down again. Therefore, for a continuous pulse train the temperature difference ΔT_{jc} between the internal junction and outer case temperatures has a ripple [16], which varies around an average temperature difference $\Delta T_{jc,\text{avg}}$ as shown in Figure 3-16. The average temperature difference $\Delta T_{jc,\text{avg}}$ is simply given by

$$\Delta T_{jc,\text{avg}} = R_{thjc} P_{\text{IGBT}}, \quad (3.24)$$

with R_{thjc} the steady-state thermal resistance between the junction and case of the IGBT. The peak temperature difference $\Delta T_{thjc,\text{peak}}$ can be calculated in a similar fashion, but using the transient thermal impedance Z_{thjc} and the peak pulse power dissipation $P_{\text{IGBT,pulse}}$ of the switched pulse [16]

$$\Delta T_{jc,\text{peak}} = Z_{thjc} P_{\text{IGBT,pulse}}. \quad (3.25)$$

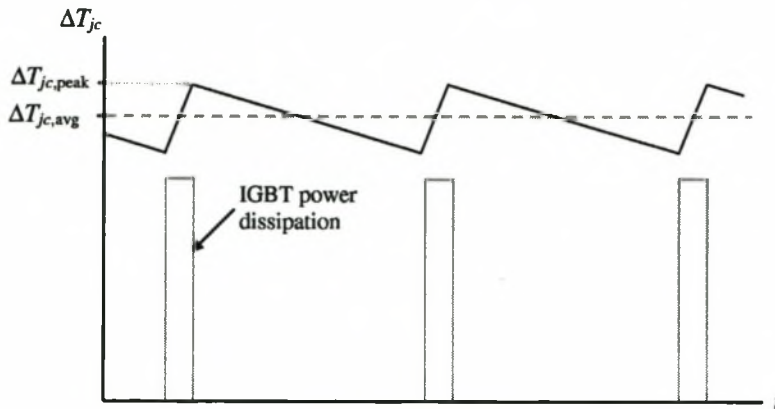


Figure 3-16: Junction-case temperature difference of an IGBT in a pulsed power supply.

The transient thermal impedance takes the heat capacities of the different internal structural layers (e.g. silicone substrate, metallic contacts, etc.) of the IGBT into account and is therefore a function of both the pulse duration and the duty cycle. Manufacturers normally give adequate specifications of the transient thermal impedance in the data sheets of the specific device. An example of a typical graph showing the transient thermal impedance of an IGBT (SKM300GB174D, 1700V/300A IGBT from Semikron) is shown in Figure 3-17. For long pulse durations and for duty cycles close to unity the transient thermal impedance corresponds to the steady state thermal resistance R_{thjc} . From Figure 3-17 can also be seen that for short pulses the transient thermal impedance can be much smaller than the steady state thermal resistance. Therefore, IGBTs are able to handle very large instantaneous power dissipations, which can be far beyond the average power handling capability of the device due to the heat capacity of the semiconductor wafer and special heat absorbing gels inside the IGBT.

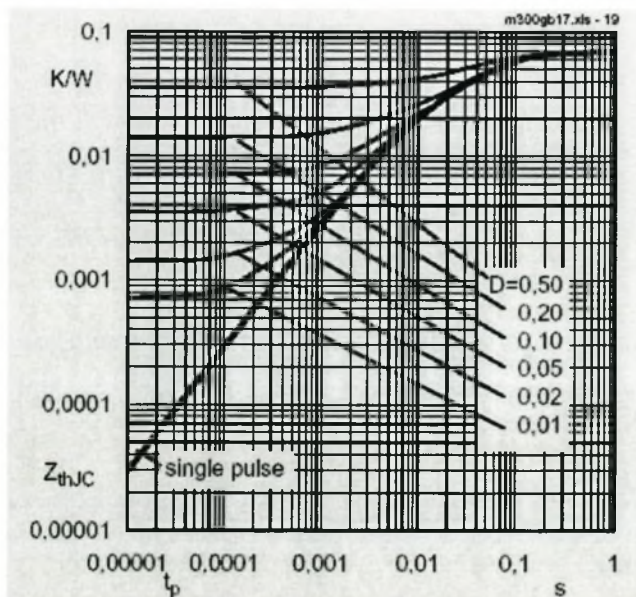


Figure 3-17: Typical graph specifying the transient thermal impedance of an IGBT.

Care must now be taken to keep the junction temperature T_j below the specified upper temperature limit. Although theoretically IGBTs can work with a junction temperature up to 150 °C, in practice the junction temperature should not exceed 100 °C. For higher temperatures the performance of the IGBT may degrade [21] and the lifetime of the device is shortened. For a given ambient temperature T_a the peak junction temperature is now given by

$$T_{j,\text{peak}} = Z_{thjc} P_{\text{IGBT,pulse}} + R_{thcs} P_{\text{IGBT}} + R_{thsa} P_{\text{IGBT}} + T_a, \quad (3.26)$$

where R_{thcs} is the thermal resistance between the case and the externally mounted heat sink and R_{thsa} is the thermal resistance from the heat sink to the surrounding environment.

Finally, it is very important to realize that even if the peak junction temperature of the IGBT is kept below the specified upper temperature limit, the short high dissipative pulses switched by the IGBT can induce very fast increases in the junction temperature. This leads to large temperature gradients inside the silicone wafer and between structural layers of the IGBT, causing large and potentially damaging thermal stresses. The thermal stresses can furthermore propagate the formation and growth of cracks inside the silicone wafer [6], thereby degrading the device and reducing the lifetime of the IGBT. The formation and growth of cracks inside the IGBT is difficult to predict and it is important to conduct lifetime tests to determine whether a specific IGBT is suitable for the target application. More information on lifetime testing and reliability of IGBTs in pulsed power supplies is given in Chapter 6.

3.4 Series stacking and paralleling of IGBTs

In the previous sections only a single IGBT was considered, but in order to increase either the switchable current or voltage IGBTs can be connected in parallel or in series, respectively.

3.4.1 Series stacking

It is advantageous to stack IGBTs in series in order to increase the switchable voltage. Increased switching voltages will result in smaller transfer peak currents as discussed in Chapter 2. Hence,

cheaper IGBTs with lower current ratings can be used.

The circuit diagram of a C-C transfer loop, which is switched by a stack of series-connected IGBTs is shown in Figure 3-18. Each IGBT is switched by a separate floating gate voltage V_g . All gate voltages are triggered simultaneously to turn on the IGBT stack. Parallel biasing resistors are connected to the IGBTs to ensure equal voltage sharing during the IGBTs off-state. Parallel capacitors for dynamic voltage sharing were not added, because this leads to increased switching times of the IGBT.

Sufficient decoupling from the C-C transfer loop as described in Section 3.2.4 will also result in decoupling of the IGBTs from each other. The voltage decrease over the IGBTs during the turn-on transient causes a corresponding voltage increase over the transfer inductance. Thus, with sufficient decoupling the voltage decrease over individual IGBTs will only cause an increase in the inductor voltage without an increase in voltage over other IGBTs. Consequently, faster switching devices will not cause an over-voltage over the slower switching devices and inherently voltages are equally shared between the IGBTs. Measurements on series-connected IGBTs are shown in Chapter 7.

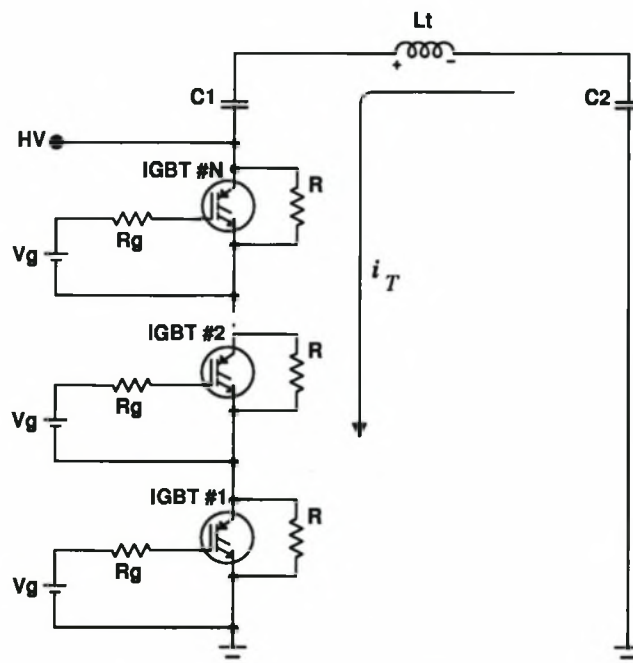


Figure 3-18: Circuit diagram of series-stacked IGBTs in a C-C transfer loop.

Drawbacks of series-stacked IGBTs are short-circuit failures and gate drive failures. A short-circuit failure of one or more IGBTs in the series stack will result in an increase of voltage across the

remaining IGBTs, which in turn can lead to over-voltage failure of the remaining devices. Furthermore, a gate drive failure of an IGBT will disable that IGBT resulting in the total switching voltage being dropped across the IGBT when the remaining IGBTs turn on. This will also lead to an over-voltage failure of the corresponding IGBT.

3.4.2 Paralleling

A different approach with which the maximum switchable current can be increased is the paralleling of IGBTs. In order to obtain equal current sharing between the paralleled IGBTs the circuit shown in Figure 3-19 can be used. The total transfer inductance L_t and storage capacitance C_t are split between the number (N) of paralleled IGBTs. To obtain a total equivalent transfer inductance L_t each split transfer inductance L_t' must be $L_t' = N \cdot L_t$, because the individual transfer inductances are effectively in parallel. Similarly each split storage capacitor C_s' must be $C_s' = C_t/N$.

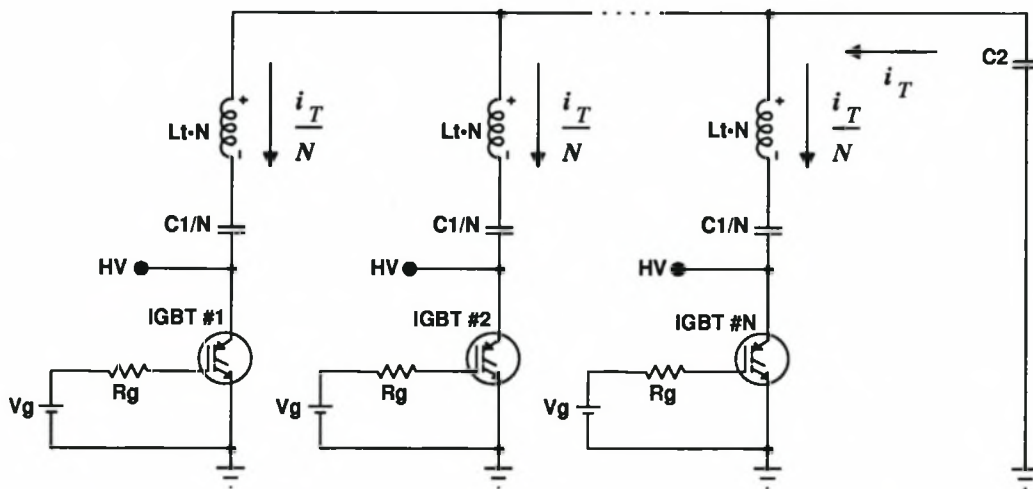


Figure 3-19: Circuit diagram of paralleled IGBTs in a C-C transfer loop.

It was found that IGBT modules are more sensitive to over-voltages than over-currents and this type of layout is more robust than series-stacked IGBTs. The drawbacks encountered with series stacking are not encountered with paralleling of IGBTs. In case of an IGBT short-circuit failure the high-voltage charging supply will simply be shorted out without causing over-voltages on the remaining IGBTs. Another advantage is that the IGBTs in a parallel layout are all grounded at the emitter, thereby allowing the IGBTs to be directly driven by the same gate driver unit. However, the lower switchable voltage of the paralleled IGBTs will necessitate the use of a step-up transformer

with a larger turns ratio and current rating. This can lead to increased transformer leakage inductance and primary conductor sizes. The parallel layout is also ideally suited for LC-inversion circuits.

3.5 Over-current capability of IGBTs

The current rating of IGBTs are specified for continuous DC currents, but in a pulsed power supply the IGBTs switch short current pulses with peak currents that are much higher than the rated average and RMS switching currents of the devices. In Chapter 2 the average and RMS currents in a C-C transfer loop are given by Equations 2.20 and 2.21. For most pulsed power supplies for CO₂ TEA lasers the transfer time in the switched C-C loop is of the order of a few microseconds and the repetition rate of the order of a few kilohertz. This results in a peak switching current $I_{s,peak}$ which is between 100 and 1000 times higher than the corresponding average current and between 10 and 100 times higher than the corresponding RMS current. It is therefore uneconomical to use an IGBT with a continuous current rating equal or higher than the peak switched C-C transfer current. Costs can be greatly reduced by using an IGBT with a continuous current rating much lower than the peak switching current. However, the peak current through the IGBT is limited by two factors, the peak saturated collector current $i_C(sat)$ and the thermal characteristics of the IGBT.

The largest limiting factor is the maximum saturated collector current. C-C transfer currents that would exceed the maximum saturated collector current are clamped. The IGBT is forced into the saturated region where the IGBT acts as a current limiter. The collector-emitter voltage will increase to counteract any further increase in the transfer current – the IGBT effectively turns off. The high collector current and increased collector-emitter voltage will cause a very large instantaneous power dissipation in the IGBT, which can induce damaging thermal stresses in the semiconductor wafer of the IGBT. The maximum saturated collector current can be increased by increasing the gate-emitter voltage as shown earlier in Figures 3-2 and 3-3, but the maximum rated gate-emitter voltage of the IGBT may not be exceeded. Gate-emitter voltages beyond the rated value may damage the gate insulation layer of the IGBT, thereby destroying the device. In general the limit on the collector current at maximum gate-emitter voltage is between 4 and 6 times the rated collector current.

The limitation on the peak switching current due to thermal considerations is normally less severe and has a larger effect on the lifetime of the IGBT as discussed in Chapter 6.

3.6 Conclusion

IGBTs can be used effectively in pulsed power applications and from a theoretical viewpoint it is possible to switch current pulses with peak currents several times the average rated current of the IGBT. However, it is important to conduct lifetime tests to verify whether a particular IGBT can switch these high current pulses for extended periods of time.

Both series stacking and paralleling of IGBTs are possible. Paralleling of IGBTs seems to be the most robust way of increasing the total switch rating. Series stacking has the advantage that higher voltages can be switched thereby reducing the total switching current and simplifying the pulse transformer design. Therefore, for this project two series-stacked IGBTs are considered. This will also enable the experimental verification of the reliability and voltage sharing of series connected IGBTs.

Chapter 4

Characterization of a pulsed mini CO₂ TEA laser

In order to design an optimised laser system, the laser must first be characterized before the final design of the pulsed power supply can be made. This includes the response of the laser to changes in electrical excitation pulse energy, voltage rise-time and circuit configuration [5]. The aim is to maximize the energy transfer into the discharge of the laser and minimize the remaining energy in the pulse circuit. It is important to minimize the remaining energy in the pulse circuit, because it can lead to undesired oscillations. These oscillations in turn can damage the solid state switches used in the pulsed power supply. The CO₂ TEA laser that was used has the following specifications:

- 10 mm electrode spacing, 360 mm electrode length
- 400 mm resonant cavity length
- 0.7 to 1.1 bar gas pressure
- gas mixtures (N₂:CO₂:He): fast 1:1:3 and standard 1:1:8 mixtures.

4.1 Test set-up

To characterize the laser, it must be possible to change the pulse energy, pulse voltage and voltage rise-time. In order to achieve this, a simple excitation circuit was constructed consisting of a single directly switched C-C transfer loop. The circuit diagram is shown in Figure 4-1.

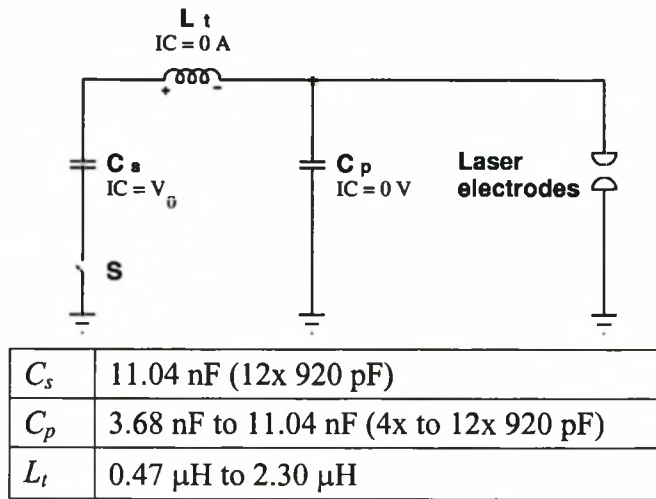


Figure 4-1: Excitation test circuit to determine the electrical characteristics of the laser.

The test circuit utilized a thyatron switch with which the high excitation voltage can be directly switched. To make the storage capacitor C_s , peaking capacitor C_p and transfer inductor L_t accessible, the circuit was constructed in air and was not enclosed. The storage and peaking capacitor banks were constructed from 920 pF high-voltage ceramic capacitors and the transfer inductor consisted of an exchangeable air core inductor. The charging voltage of the storage capacitor could be varied between 0 kV and 30 kV. The following circuit parameters can be set:

a. *Transfer time, τ :*

As discussed in Chapter 2, this is the time needed for the voltage over C_p to reach a maximum after the thyatron has switched. The transfer time of the C-C loop is given by

$$\tau = \pi \sqrt{L_t \frac{C_s C_p}{C_s + C_p}}. \quad (4.1)$$

For a given capacitance the transfer time can be adjusted by changing the inductance value of L_t .

b. *Energy, E_0 :*

The energy in the circuit is determined by the initial stored energy in the storage capacitor C_s and can be adjusted by the charging voltage V_0 and the capacitance of C_s

$$E = \frac{1}{2} C_s V_0^2. \quad (4.2)$$

c. *Relationship between C_s and C_p :*

The relative sizes of C_s and C_p can be varied. The conventional approach is to choose C_s and C_p equal for total energy transfer from C_s to C_p (losses are neglected).

4.2 Discharge stability

The stability of a laser discharge can be quantified by the laser's stable operating region. The stable operating region is bounded by the minimum and maximum charging voltages for which stable and arc-free discharges are obtained. The minimum and maximum voltages are normally a function of gas pressures p , circuit configuration and repetition rate f_{rep} . A minimum threshold voltage V_{min} is needed to obtain a gas breakdown, which initiates the laser discharge. Voltages above the maximum threshold V_{max} will cause arcing, because of too high energy densities within the discharge and/or bad matching (see Section 4.2.4).

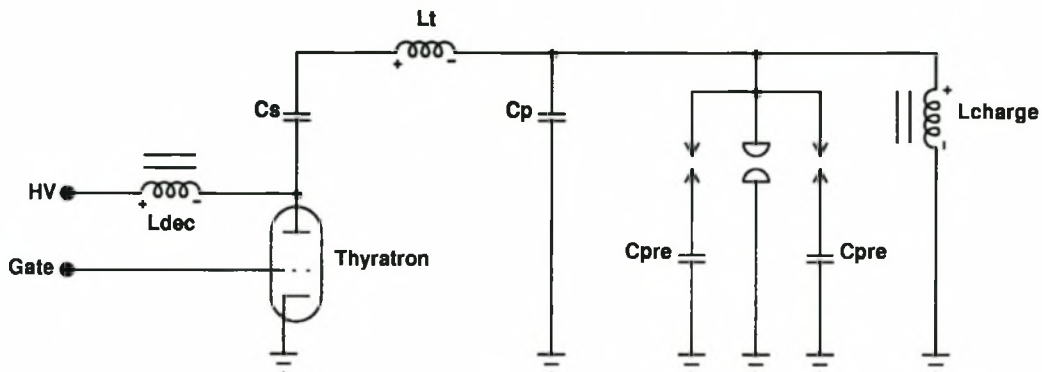
4.2.1 Pre-ionisation and stability

In high-pressure CO₂ lasers the gas medium between the electrodes has to be partially ionised before the laser discharge is initiated. Normally a free electron density of the order of $10^8/\text{cm}^3$ is needed. The ionisation of the gas prior to the laser discharge, also called pre-ionisation of the gas, is necessary to generate stable discharges. It is extremely difficult to obtain stable discharges without pre-ionisation. Pre-ionisation of the gas between the laser electrodes can be obtained by irradiating the gas with UV (ultra-violet) light or X-ray radiation. In the experimental CO₂ laser the pre-ionising UV light is generated by small discharges. These small discharges are generated between a series of pre-ionisation spark gaps located parallel alongside the laser electrodes. The pre-ionisation spark gaps can electrically either be connected parallel or in series with the laser electrodes.

The two pre-ionisation configurations, parallel and series, were tested. In both circuit configurations (see Figures 4-2 and 4-5) the storage capacitor C_s is charged through the inductances L_{dec} and L_{charge} . The inductance L_{dec} decouples the pulse circuit from the high voltage source during the switching period and the charging inductances L_{charge} ensure a DC path to ground during the charging phase of C_s .

Parallel pre-ionisation

The laser was first operated with parallel pre-ionisation. The detailed circuit diagram is shown in Figure 4-2.



C_s	11.04 nF (12x 920 pF)
C_p	3.68 nF to 11.04 nF (4x-12x 920 pF)
C_{pre}	360 pF (2x 180 pF)
L_t	0.47 μ H to 2.30 μ H

Figure 4-2: Excitation circuit with parallel pre-ionisation.

The storage capacitor C_s is charged through the inductors L_{dec} and L_{charge} . The decoupling inductor L_{dec} decouples the pulse circuit from the high voltage supply during the switching period and the charging inductor L_{charge} ensures a DC path to ground during the charging phase of capacitor C_s . The two inductances L_{dec} and L_{charge} act as open circuits during the switching period of the pulse circuit.

After the thyatron switches the pre-ionisation will fire as soon as the voltage over the peaking capacitor C_p has reached the pre-ionisation spark gap breakdown voltage (15 ± 5 kV). The pre-ionisation capacitors C_{pre} limit the energy that will pass through the pre-ionisation discharge. Shortly after (20 ± 10 ns) the pre-ionisation discharge, as the voltage over the peaking capacitor increases to approximately 25 kV, the main discharge is initiated. The timing diagram of the parallel pre-ionisation is shown in Figure 4-3.

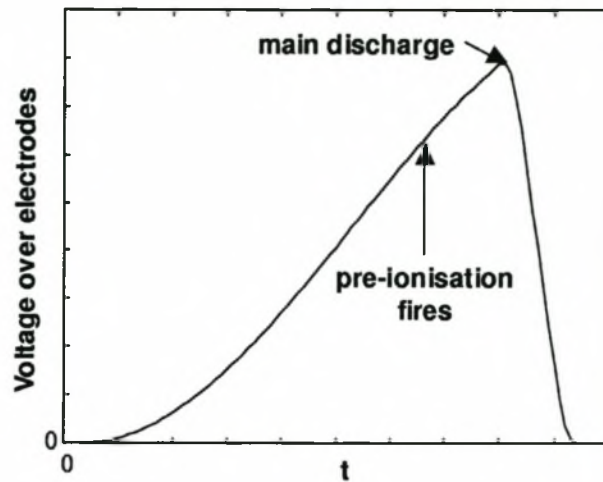


Figure 4-3: Timing of parallel pre-ionisation discharge.

Problems were experienced with the discharge stability (especially with 1:1:3 gas mixture), due to either absent or insufficient pre-ionisation discharges. Examples of measured discharge voltages for insufficient and sufficient pre-ionisation are shown in Figure 4-4.

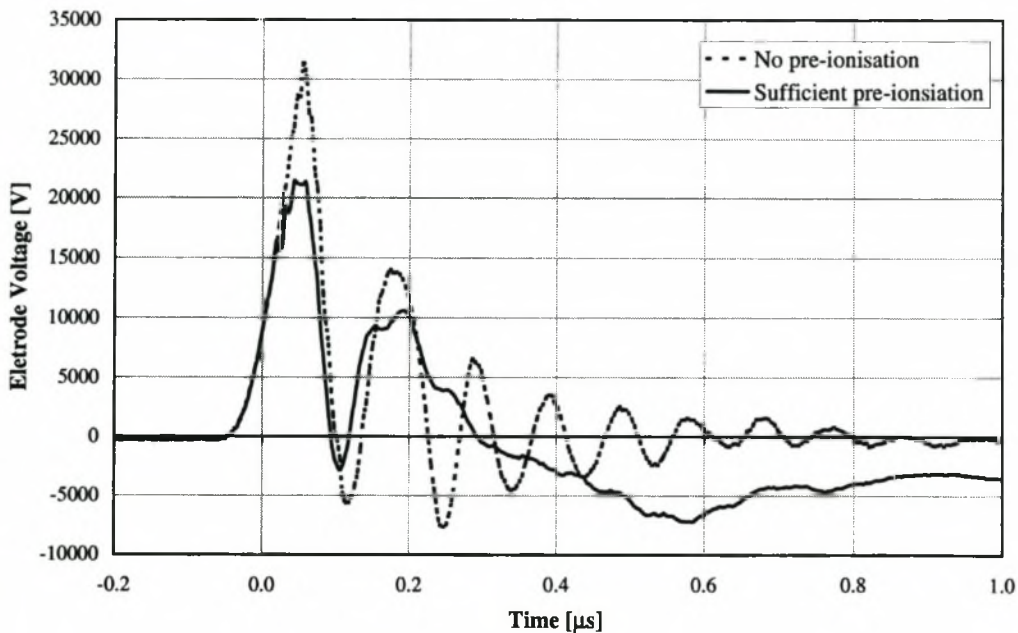


Figure 4-4: Discharge voltage for insufficient and sufficient pre-ionisation.

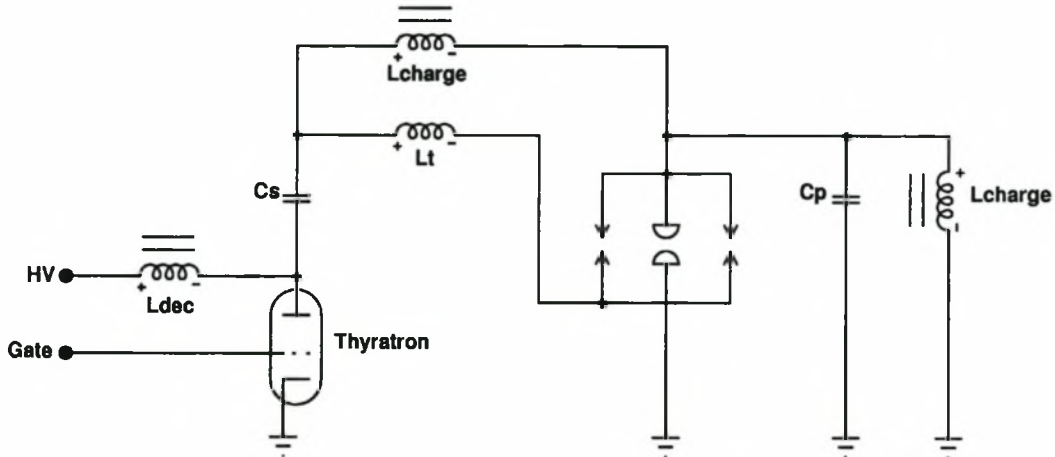
With sufficient pre-ionisation a uniform and arc-free main discharge is obtained and the oscillation in the electric pulse circuit can be minimized. In the case where no pre-ionisation is initiated, also no main discharge is obtained. The electric energy in the pulse circuit cannot be dumped into the

discharge. The voltage over the electrodes (discharge voltage) oscillates strongly, reaching peak voltages of 35 ± 5 kV well beyond the normal breakdown voltage of 20 ± 5 kV.

The problems with parallel pre-ionisation are presumably mainly caused by the intrinsic design of the pre-ionisation pins of the laser, which was used for the experiments. All the pre-ionisation pins were connected in parallel with only small decoupling inductors added between individual pins. This could lead to a bigger time jitter in the pre-ionisation discharge with respect to the voltage rise over the laser electrodes and can cause the pre-ionisation to fire too late or not at all. In the case where the pre-ionisation fires too late, the voltage over the electrodes reaches higher values than the normal breakdown voltage and arcing can be observed in the later stages of the discharge, which indicates bad matching conditions (see Section 4.2.4). This is also a clear indication of insufficient generation of free electrons by the pre-ionisation. Normally an average free electron density of $\sim 10^9/\text{cm}^3$ is needed for stable, uniform discharges. A time jitter of $t_{\text{jitter}} = 50 \pm 10$ ns was measured during the experiments.

Series pre-ionisation

The detailed circuit diagram of the series pre-ionisation configuration is shown in Figure 4-5.



C_s	11.04 nF (12x 920 pF)
C_p	3.68 nF to 11.04 nF (4x to 12x 920 pF)
C_{pre}	360 pF (2x 180 pF)
L_t	0.47 μH to 2.30 μH

Figure 4-5: Excitation circuit with series pre-ionisation.

The inductances L_{dec} and L_{charge} have the same function as with the parallel pre-ionisation configuration. Initially the pre-ionisation spark gap is not discharging and has a high impedance before the thyatron switches. There is a fast voltage rise over the pre-ionisation spark gap while the thyatron switches, which is equal to the voltage decrease over the thyatron. The voltage rise time of the spark gap is thus determined by the switching time of the thyatron, which is in the order of 10 ns. After the breakdown threshold of the pre-ionisation spark gap is reached, the spark gap fires and current can flow through the transfer inductance L_t from C_s to C_p and a voltage rise is attained over the peaking capacitor C_p . The timing diagram of the series pre-ionisation configuration is shown in Figure 4-6.

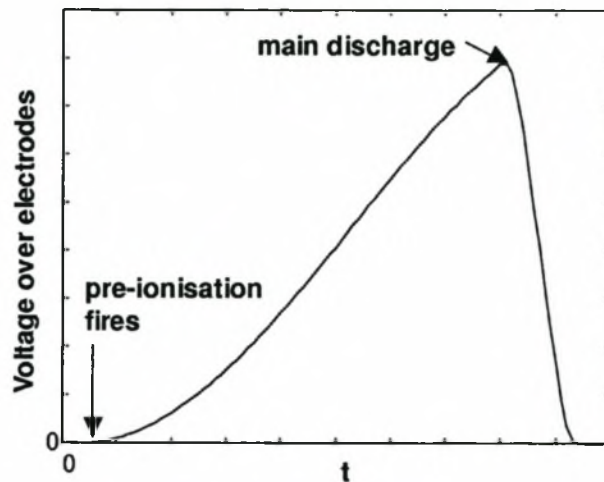


Figure 4-6: Timing of series pre-ionisation discharge.

The voltage rise over the laser electrodes is only obtained after the pre-ionisation discharge has fired. This is a big advantage, because there is very little pre-ionisation jitter with respect to the electrode voltage rise and much more stable discharges are obtained with this configuration. For this case a time jitter of $t_{jitter} = 10 \pm 2$ ns was measured.

The biggest disadvantage of series pre-ionisation is that all the excitation energy has to pass through the pre-ionisation gap first. This can probably lead to increased erosion of the pre-ionisation spark gaps compared to parallel pre-ionisation.

4.2.2 Stable operating region and peaking capacitor size

The stable operating regions of the parallel and series configuration were measured as a function of peaking capacitor size. The stable operating region is defined as the condition for which less than

1% of the discharges are unstable (i.e. arcing). The storage capacitor was kept constant at $C_s = 11.04$ nF with a transfer inductance of $L_t = 530$ nH. A 1:1:3 gas mixture at 1 bar gas pressure was used.

From Figure 4-7 it becomes clear that the series pre-ionisation configuration has a much larger stable operation region than the parallel pre-ionisation. Arcing occurs if the peaking capacitor size is too small. As will be shown later in this chapter (see Section 4.4), for reduced peaking capacitor sizes the laser discharge progresses in two steps. First an initial discharge is obtained where the main portion of the energy stored in the peaking capacitors is transferred into the laser discharge. This is followed by a secondary discharge where the remaining energy on the storage capacitor is transferred into the laser discharge. For too small peaking capacitor sizes the stored energy on the peaking capacitor is too small to initiate a strong and uniform initial discharge. During the secondary discharge this results in bad matching conditions between the laser power supply and the laser discharge. Bad matching conditions ultimately lead to unstable discharges (see Section 4.2.4). The minimum usable peaking capacitor size is approximately 1.84 nF (2x 920 pF) for both a 1:1:3 and 1:1:8 gas mixture.

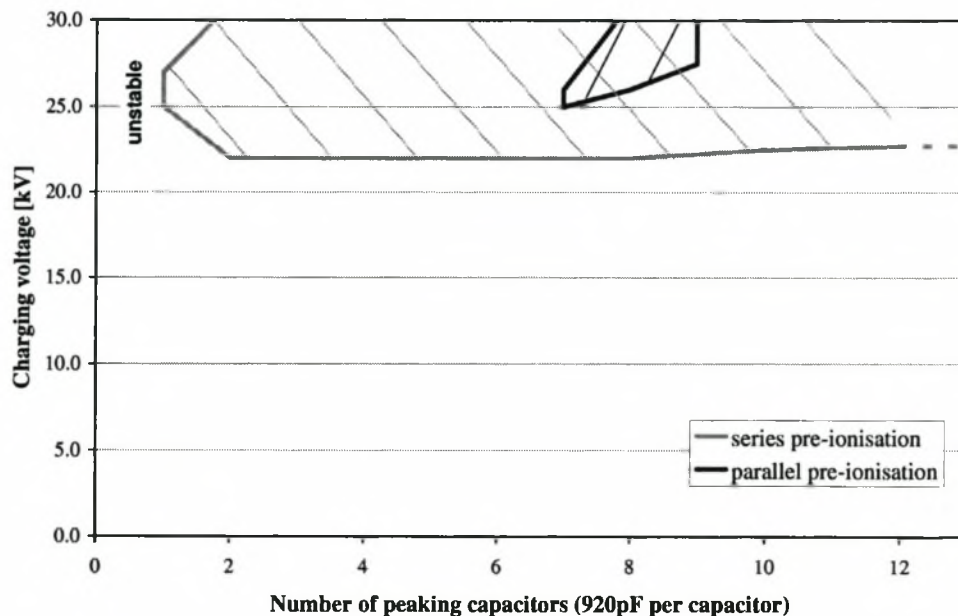


Figure 4-7: Stable operating region for parallel and series pre-ionisation.

4.2.3 Voltage rise-time and stability

The voltage rise-time is directly proportional to the transfer time τ of the C-C transfer circuit. As mentioned in Chapter 2 the definition for voltage rise-time in this discussion was chosen as 0.6τ

(voltage rise from 10% to 90% of peak voltage). In order to obtain a stable and uniform discharge the voltage rise-time over the laser electrodes has to be fast enough. If the rise-time is too slow the discharge will not be uniform and arcing will occur. In general rise-times of the order of 100 ns are needed.

Stability measurements were taken for $C_s = C_p$ and the voltage rise-time was changed by changing the size of the inductor L_t . Figure 4-8 shows the stable operating region for different transfer times and a 1:1:8 ($N_2:CO_2:He$) gas mixture ($C_s = C_p = 11.04$ nF, series pre-ionisation).

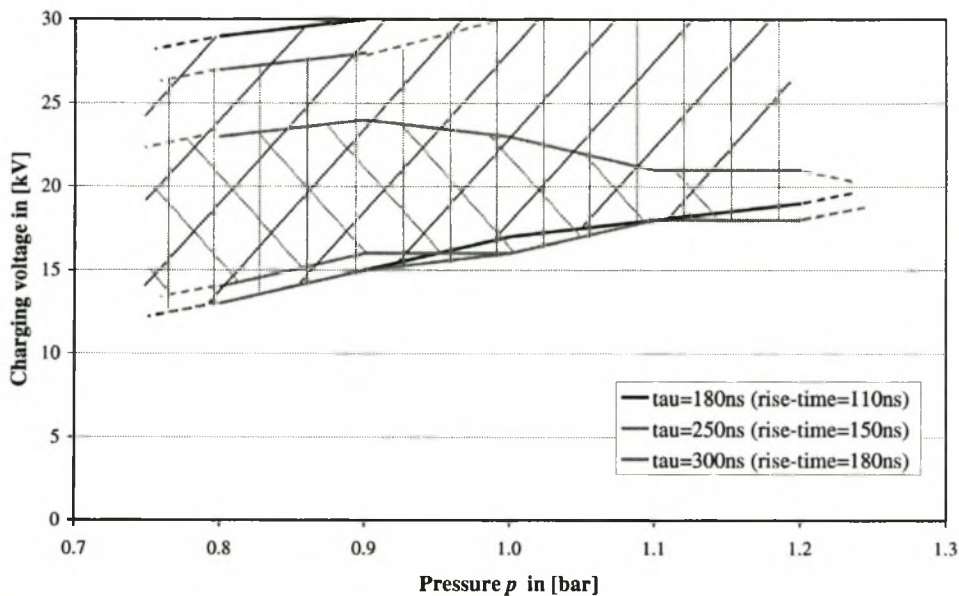


Figure 4-8: Stable operating region for different voltage rise-times (1:1:8 mixture).

There is a clear reduction in the stable operating region for a transfer time of 300 ns (rise-time approx. 180 ns). For the 1:1:3 ($N_2:CO_2:He$) gas mixture there is also a reduction in the stable operating region for a transfer time of 300 ns, as shown in Figure 4-9.

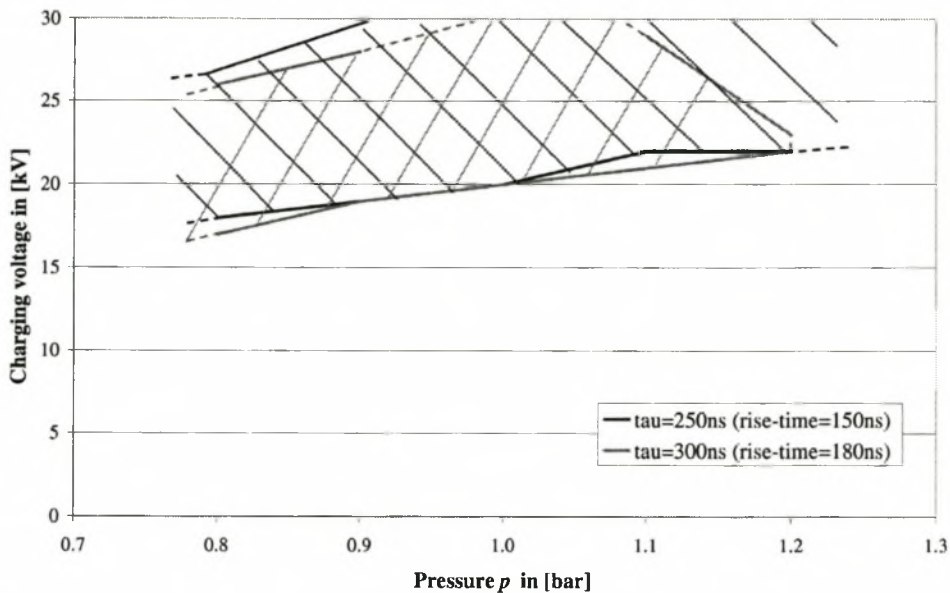


Figure 4-9: Stable operating region for different voltage rise-times (1:1:3 gas mixture).

The upper bound on the voltage rise-time is thus approximately 150 ns for both the 1:1:8 and 1:1:3 gas mixtures. It was also found that for rise-times slower than 110 ns the discharges turned from purple to white and the laser output power dropped by approximately 10% after a few minutes of operation at repetition rates of 20 Hz. This indicates less tolerance to O₂ build-up at slower rise-times due to dissociation of the CO₂ gas. This can be improved by including a catalyst within the laser chamber.

4.2.4 Matching and stability

Besides the voltage rise-time, matching plays a big role in the stability and efficiency of the laser. Matching is an indication of how much energy is transferred from the electric pulse circuit into the laser discharge. If the circuit is badly matched only a part of the electric energy in the pulse circuit is transferred into the discharge. A fair amount of energy remains in the electric circuit, which results in unwanted oscillations and reverse overshoot voltages over the laser electrodes.

If the reverse overshoot voltage is large enough it can cause arcing in the later stages of the discharge, as shown by the measured voltage traces in Figure 4-10. Note, the applied voltage pulse is negative and the reverse overshoot voltage is positive. The grey trace shows a discharge without

arcing and the black trace shows a discharge with arcing during the reverse overshoot. As soon as arcing occurs the voltage over the laser electrodes drops to zero, because of the low impedance of the arc discharge. Matching cannot be easily defined and quantified for pulsed laser discharges, because of the highly non-linear characteristics of the pulsed laser discharge.

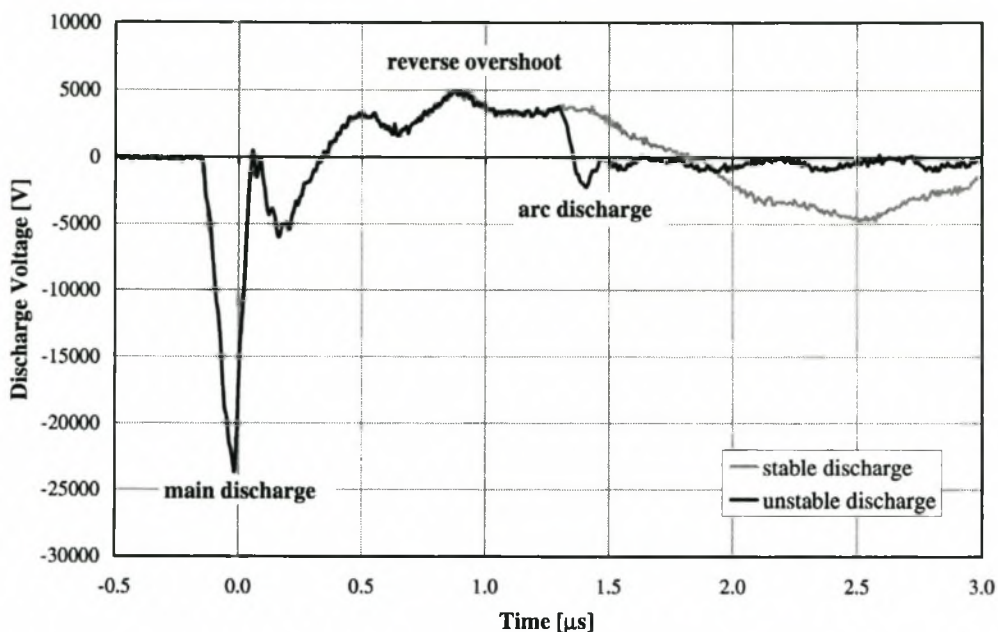


Figure 4-10: Arcing during reverse voltage overshoot.

For this project the best matching conditions were determined experimentally. As will be discussed later in this chapter (see Section 4.3), there are two approaches that can be used for the C-C transfer excitation circuit: $C_s = C_p$ and $C_s > C_p$.

For the case where $C_s = C_p$ matching is mainly determined by the size of the peaking capacitor and the charging voltage. Best stability, with the largest stable operating region for both the 1:1:3 and 1:1:8 gas mixtures, was obtained for a peaking capacitor size of $C_p = 12 \times 920 \text{ pF} = 11.04 \text{ nF}$. The initial voltage rise-time also has an effect on the matching condition. Better matching with smaller reverse overshoot voltages was obtained with faster voltage rise-times ($\tau < 100 \text{ ns}$). Faster excitation pulses result in more uniform discharges, which allow a more efficient energy transfer into the laser discharge.

For the approach where $C_s > C_p$ the size of the transfer inductance L_t also plays an important role in the matching stability. As mentioned earlier and also discussed in more detail in Section 4.4, the discharge for $C_s > C_p$ progresses in two steps. An initial discharge mainly fed from the peaking

capacitor followed by a secondary discharge mainly fed from the storage capacitor via the transfer inductance is obtained. The size of the transfer inductance thereby has a large influence on the energy transfer during the secondary discharge. The reduction of the peaking capacitor size will clearly result in shorter C-C transfer times and thus faster excitation voltage rise-times (see Equation 4.1). In the previous section it was found that voltage rise-times of up to 150 ns will result in stable discharges for the case where $C_s = C_p$. It can therefore be argued that for sufficiently fast voltage rise-times (< 150 ns) the transfer inductance can be increased for a reduction in the peaking capacitor size. However, it was found that an increase in transfer inductance for a corresponding decrease in peaking capacitor size greatly reduced the matching conditions during the secondary discharge. Insufficient energy transfer during the secondary discharge from the storage capacitor into the laser discharge was obtained. This resulted in reverse overshoot voltages and unstable discharges. Hence, faster initial excitation pulses are needed for the case where $C_s < C_p$ in order to obtain more uniform initial discharges. More uniform initial discharges reduce the risk of arc-formation during the secondary discharges and improve the matching conditions.

Measured stable operating regions for reduced peaking capacitor sizes ($C_s = 12 \times 920$ pF) and for two transfer inductances are shown in Figure 4-11.

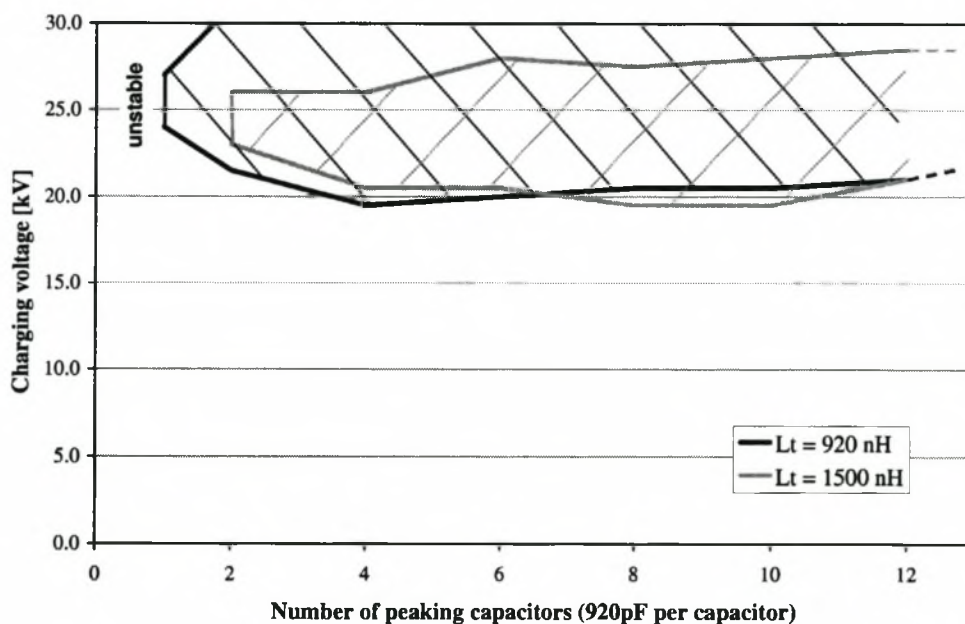


Figure 4-11: Stable operating region as a function of the peaking capacitor size for two transfer inductances. (1:1:3 gas mixture)

There is a clear reduction in the stable operating region for the increased transfer inductance, $L_t = 1500$ nH. The smaller transfer inductance, $L_t = 920$ nH, results in a transfer time of $\tau = 250$ ns for $C_s = C_p$. This transfer time was also found to yield a good stable operating region in Section 4.2.3 for $C_s = C_p$. The measurements thus illustrate that an increase in transfer inductance reduces the stable operating region. Best stability for all peaking capacitor sizes is obtained by using the same inductance that also yields good stability for the case where $C_s = C_p$. Consequently, with the reduction of the peaking capacitor size faster voltage rise-times are unavoidable.

4.3 Output energy and efficiency

The optical output energy was measured with a Gentec ED-500 pyro-electric energy meter. Measurements were performed for different circuit values by changing the peaking capacitor and inductor sizes. This was done in order to optimise the laser output energy and efficiency. Energy measurements were also taken for different gas mixtures to compare the effect of the circuit configuration on the output energy for different gas mixtures. The type of pre-ionisation - series or parallel - does not seem to have an influence on the output energy of the laser.

The efficiency η of the laser is calculated with respect to the initial stored electric energy in the storage capacitor C_s :

$$\eta = \frac{E_{\text{output}}}{E_{\text{stored}}} = \frac{2E_{\text{output}}}{C_s V_0^2}, \quad (2.3)$$

with E_{output} the optical output energy and V_0 the charging voltage. The calculated efficiency is close to the “wall plug”-efficiency of the laser, because the efficiency of the high-voltage source is very good (typically >90%) and losses during the charging period of C_s are also comparatively low.

4.3.1 Peaking capacitor size and excitation approaches

Two approaches were investigated in the excitation of the laser:

$C_s = C_p$: This is the conventional approach if losses are ignored [40]. Ideally all the energy is transferred from the storage capacitor C_s to the peaking capacitor C_p after the thyatron

switches. As the voltage over the peaking capacitor reaches a maximum the laser discharge is initiated and almost all the energy is transferred from the peaking capacitor into the discharge. The time during which energy is transferred into the discharge is in the region of 10 ns to 50 ns, depending on the internal inductance of the laser head between the laser electrodes and peaking capacitor.

$C_s > C_p$: The second approach is to reduce the peaking capacitor size. As the thyatron switches a partial energy transfer occurs from C_s to C_p and a fast voltage rise is obtained over the peaking capacitor. The maximum voltage obtainable over the laser electrodes is up to twice the charging voltage, V_0 (see Equation 2.10). In this case the peaking capacitor is used to initiate the laser discharge. After the discharge is initiated the remaining energy is transferred from C_s through L_t into the discharge. This causes the electrical excitation pulse to be stretched (see Section 4.4). The energy transfers into the discharge occurs over a period of between 100 ns and 200 ns [5][9]

The voltage and current traces for the two configurations are shown in Section 4.4, which gives more insight into the differences between the two configurations.

4.3.2 Output energy and efficiency for $C_s = C_p$

The optical output energy was firstly measured for the conventional approach as a function of the inductance, L_t , which determines the transfer time of the C-C circuit, as given by Equation 4.1. The capacitor size is $C_s = C_p = 11.04$ nF and the gas pressure is kept at $p = 1$ bar. Two different gas mixtures, a fast 1:1:3 and a standard 1:1:8 gas mixtures, have been investigated.

1:1:8 (N₂:CO₂:He) gas mixture

Two-dimensional and three-dimensional plots of the measured output energy as a function of the charging voltage V_0 and the inductance L_t are shown in Figures 4-12 and 4-13. As expected, the optical output energy increases with increasing charging voltage, because the electric pulse energy is increased (see Equation 4.2). Note that the output energy depends slightly on the inductance L_t , with a variation of approximately 20% in the output energy over the measured inductance range. This is also seen in the plots of the laser efficiency as a function of charging voltage and inductance, shown in Figure 4-14 and 4-15.

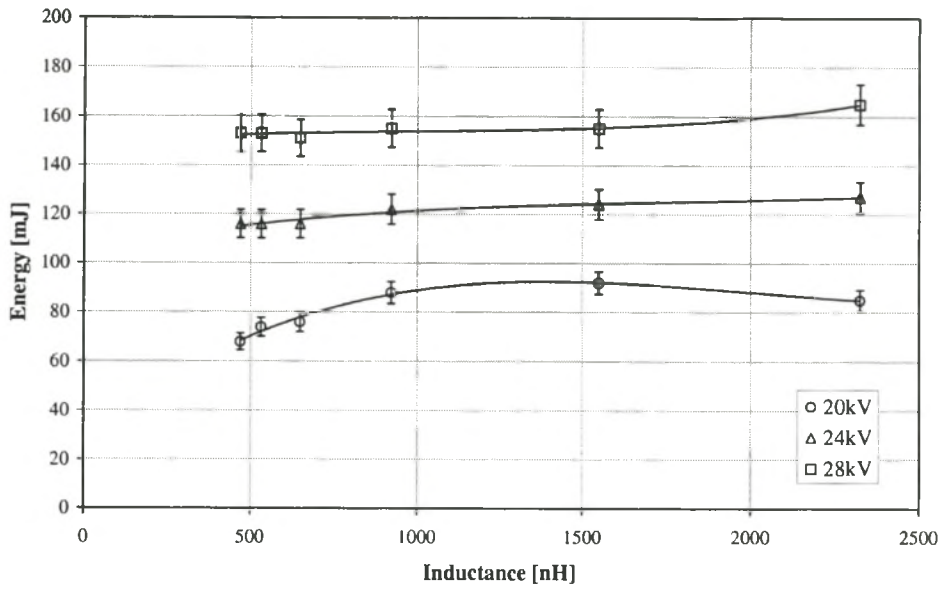


Figure 4-12: Optical output energy vs. inductance L_t for three charging voltages V_0 . (1:1:8 mixture)

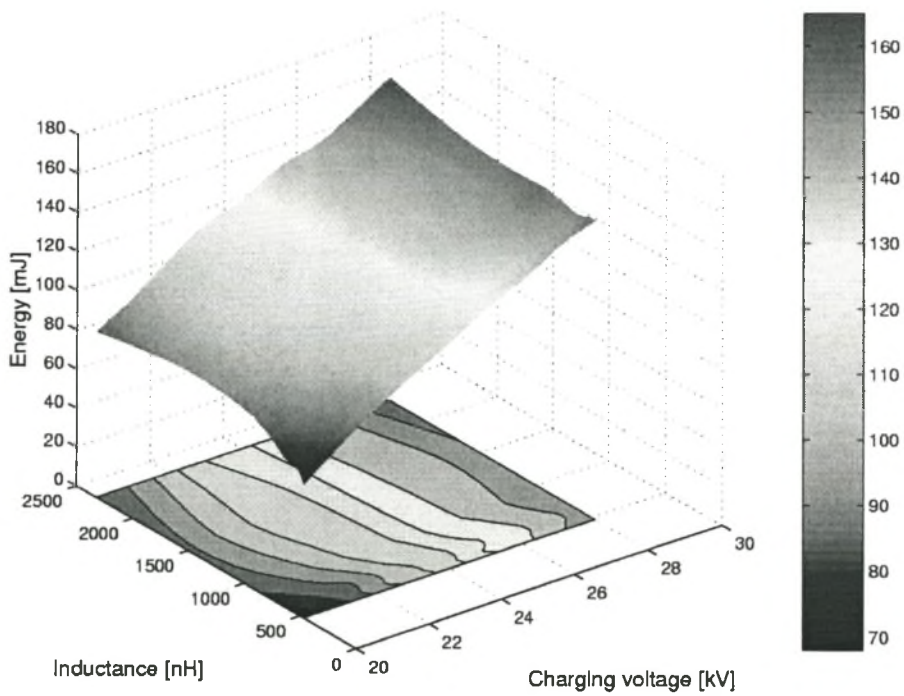


Figure 4-13: Optical output energy vs. charging voltage V_0 and inductance L_t . (1:1:8 mixture)

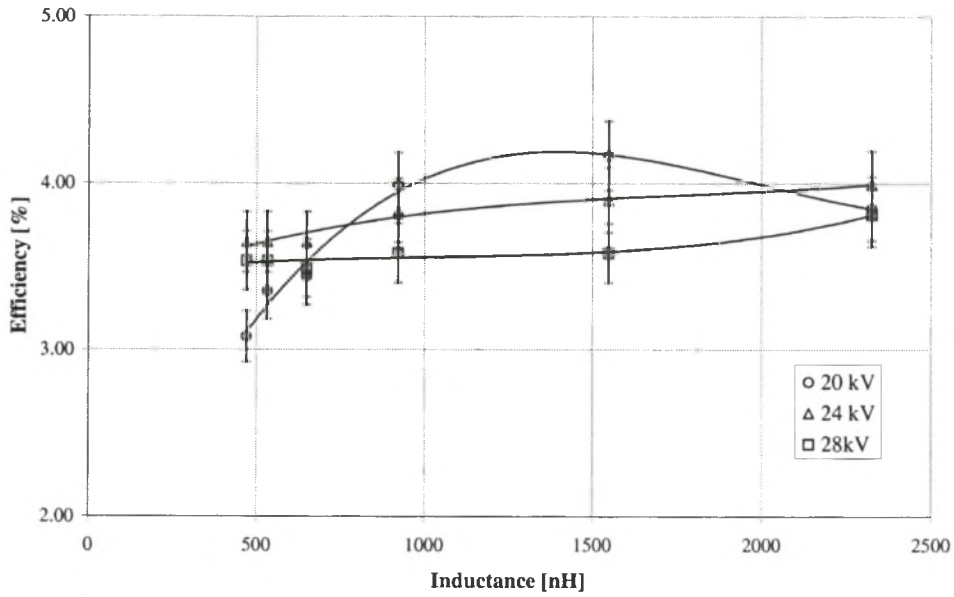


Figure 4-14: Efficiency vs. inductance L_t for three charging voltages V_0 . (1:1:8 mixture)

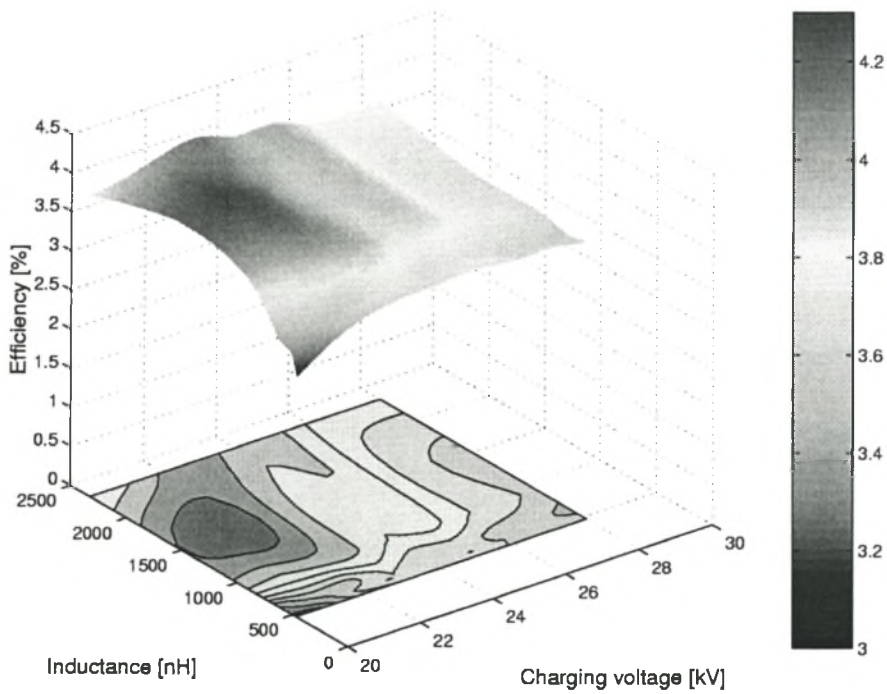


Figure 4-15: Efficiency vs. charging voltage V_0 and inductance L_t . (1:1:8 mixture)

There is also a slight dependence of the efficiency on the charging voltage, with a variation of approximately 10% in the output energy and efficiency over the measured voltage range. The best efficiency of approximately 4% is obtained with an transfer inductance of between 1.0 μH and

2.0 μH for charging voltages between 20 kV and 22 kV. The influence of the inductance on the output energy is more prominent for lower voltages (below 24 kV) with the best efficiency at a transfer inductance of approximately 1.5 μH . The maxima in the efficiency are most probably caused by a trade-off between the switching losses in the thyatron and matching between the electric excitation circuit and the laser discharge. For smaller inductances, faster transfer times are obtained, which implies a faster current rise during the switching period of the thyatron. This increases the switching losses in the thyatron during switching. For bigger transfer inductances the reverse overshoot voltages (see Section 4.2.4) increased. This indicates a deterioration of the matching of the laser for bigger transfer inductances, i.e. less energy is transferred from the electric excitation circuit into the laser discharge.

1:1:3 ($\text{N}_2:\text{CO}_2:\text{He}$) gas mixture

Three-dimensional plots of the output energy and efficiency for a 1:1:3 gas mixture are also shown in Figures 4-16 and 4-17. The output energy for the 1:1:3 gas mixture is approximately 20% higher than for the 1:1:8 gas mixture. The output energy and efficiency show a similar dependence on the transfer inductance L_t and charging voltage. The best efficiency is obtained with a transfer inductance of approximately 1.5 μH and a charging voltage between 24 kV and 26 kV.

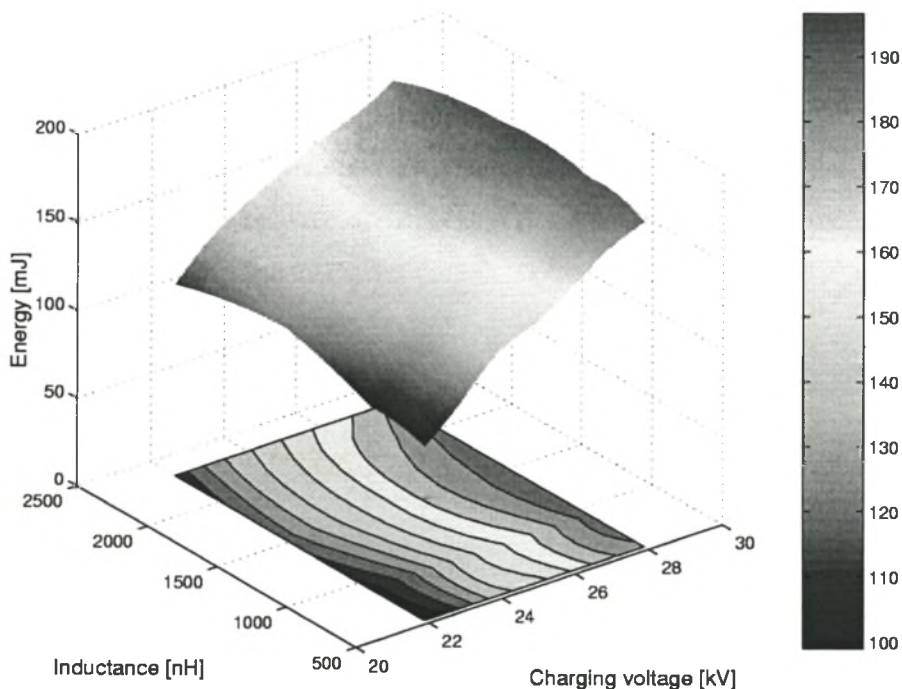


Figure 4-16: Optical output energy vs. charging voltage V_0 and inductance L_t . (1:1:3 mixture)

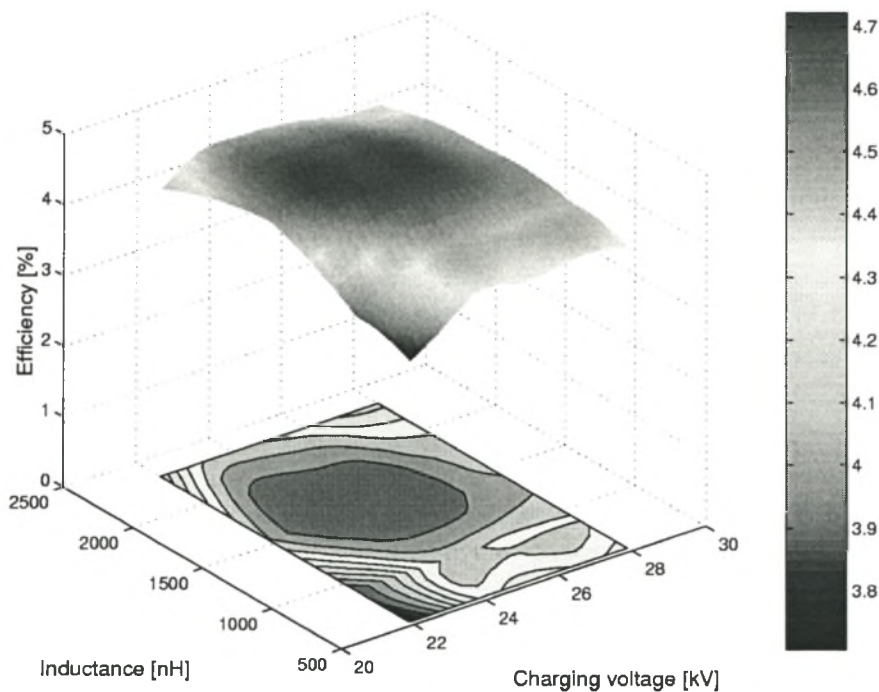


Figure 4-17: Efficiency vs. charging voltage V_0 and inductance L_t . (1:1:3 gas)

4.3.3 Output energy and efficiency for $C_s > C_p$

In order to determine the influence of the peaking capacitor size on the laser output, the inductance L_t and storage capacitor C_s are kept constant ($C_s = 11.04$ nF, $L_t = 920$ nH) and the peaking capacitor size is decreased. The gas pressure is kept at $p = 1$ bar. Although for $C_s = C_p$ the best efficiency is obtained at $L_t \cong 1500$ nH, it was found that $L_t \cong 920$ nH yields better discharge stability for both $C_s = C_p$ and $C_s > C_p$ (see Sections 4.2.3 and 4.2.4).

1:1:8 (N₂:CO₂:He) gas mixture

Three-dimensional graphs of the optical output energy and efficiency of the laser as a function of the charging voltage and peaking capacitor size are shown in Figures 4-18 and 4-19. There is a clear increase in optical output energy as the peaking capacitor size is reduced below 8 nF (approx. $0.7C_s$). The peaking capacitor size can only be decreased down to 3.68 nF, because for smaller values the discharge becomes unstable (see Section 4.2.2).

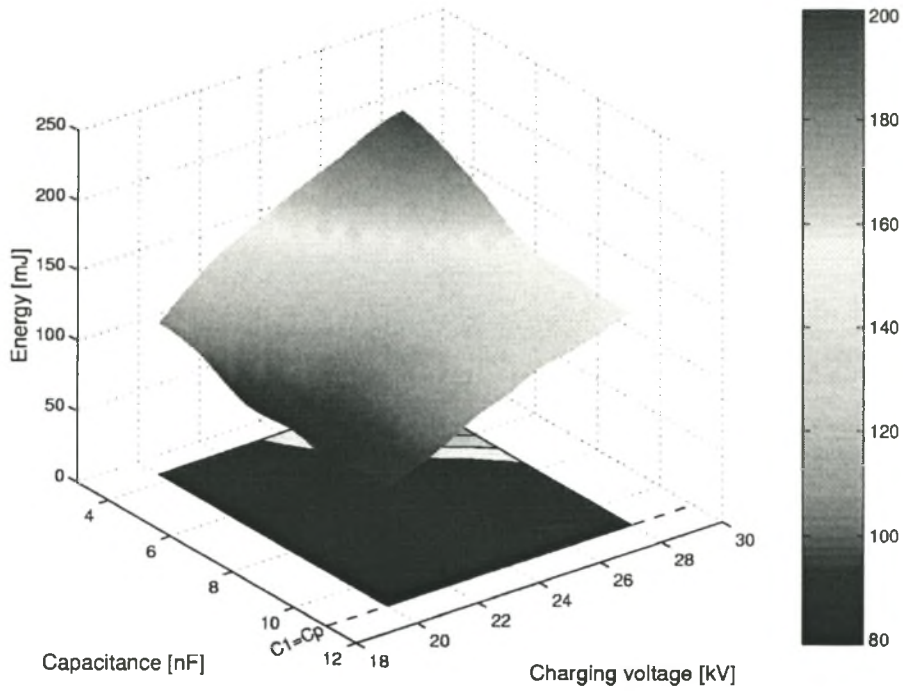


Figure 4-18: Optical output energy vs. charging voltage and peaking capacitor size. (1:1:8 mixture)

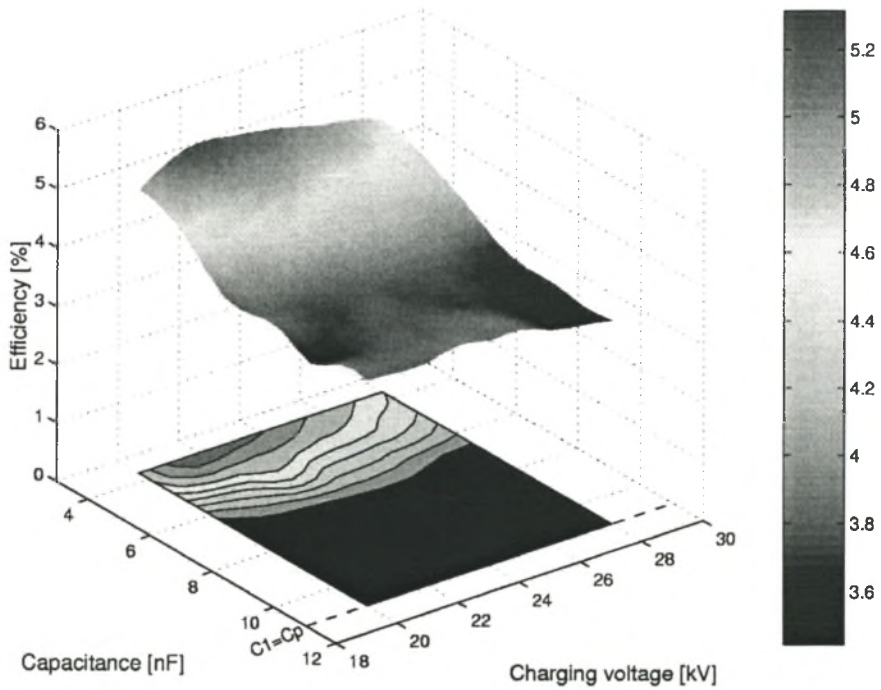


Figure 4-19: Efficiency vs. charging voltage and peaking capacitor size. (1:1:8 mixture)

There is an increase of approximately 35% in the laser output energy and efficiency as the peaking capacitor size is reduced from $C_p = C_s = 11.04$ nF to $C_p = \frac{1}{3}C_s = 3.68$ nF. The best efficiency that can be obtained is 5.3%, which is a very good result for a mini TEA CO₂ laser. The increase in efficiency is independent of the charging voltage. In order to better understand this effect, the voltage and current waveforms of the excitation circuit have to be analysed (see Section 4.4).

1:1:3 (N₂:CO₂:He) gas mixture

The same dependence of the output energy and efficiency on the peaking capacitor size was measured for the 1:1:3 gas mixture, shown in Figures 4-20 and 4-21. There is an increase of approximately 25% as the peaking capacitor size is reduced with the best efficiency of 5.8% and output energy of 240 mJ.

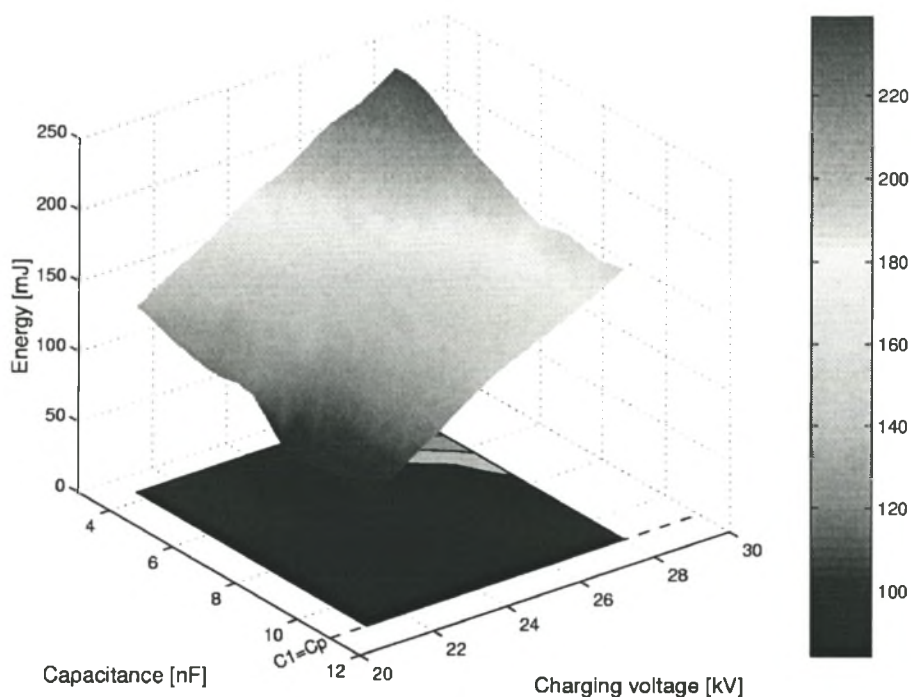


Figure 4-20: Optical output energy vs. charging voltage and peaking capacitor size. (1:1:3 mixture)

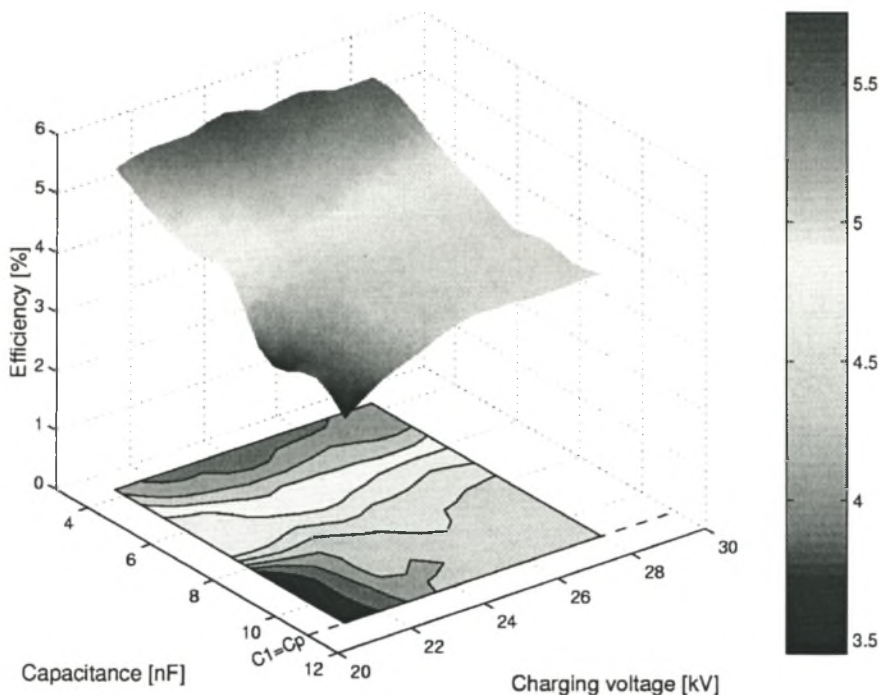


Figure 4-21: Efficiency vs. charging voltage and peaking capacitor size. (1:1:3 mixture).

4.3.4 Output energy and efficiency for commercial thyatron based pulsed power supply

The output energy and efficiency of the CO₂ laser obtained with a commercial thyatron driven pulsed power supply were also measured. The commercial pulser was supplied with the CO₂ TEA laser and was originally used to excite the laser. The pulser consists of a thyatron switched LC-inversion topology with a single MPC stage. The total initial storage capacitance of the commercial supply is $C_s = 11.04$ nF. This is equal to the storage capacitance of the experimental excitation circuit used in the previous sections (Sections 4.3.2 and 4.3.3). For equal initial charging voltages the commercial and experimental laser power supplies therefore have the same initial stored energy. Three-dimensional graphs of the output energy and efficiency as a function of the laser gas pressure and charging voltage are shown in Figures 4-22 to 4-25. Figures 4-22 and 4-23 are for a 1:1:8 (N₂:CO₂:He) gas mixture and Figures 4-24 and 4-25 are for a 1:1:3 (N₂:CO₂:He) gas mixture.

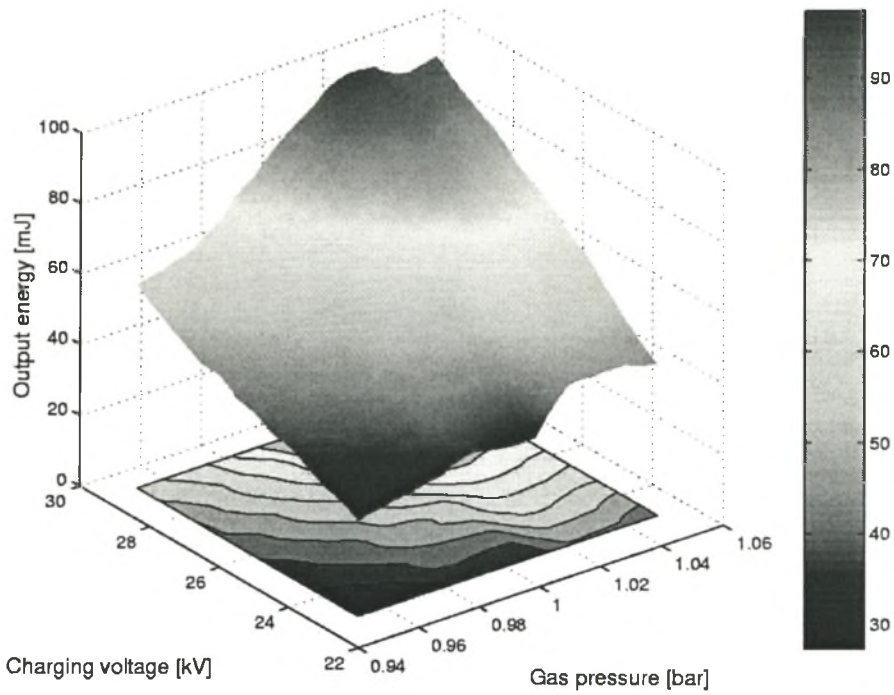


Figure 4-22: Optical output energy vs. charging voltage and gas pressure for commercial thyratron based pulsed power supply. (1:1:8 mixture)

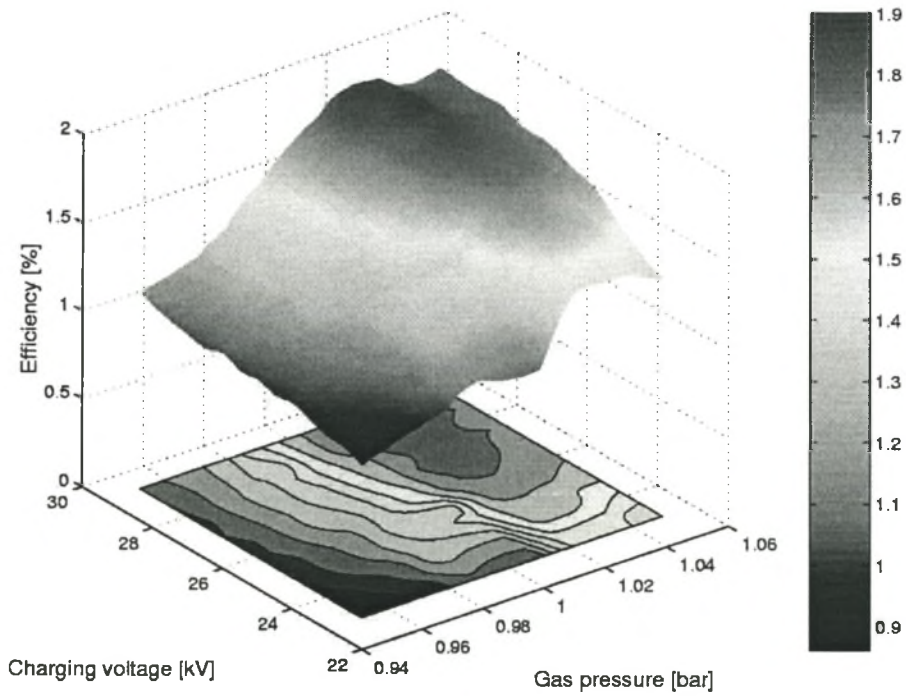


Figure 4-23: Efficiency vs. charging voltage and gas pressure for commercial thyratron based pulsed power supply. (1:1:8 mixture)

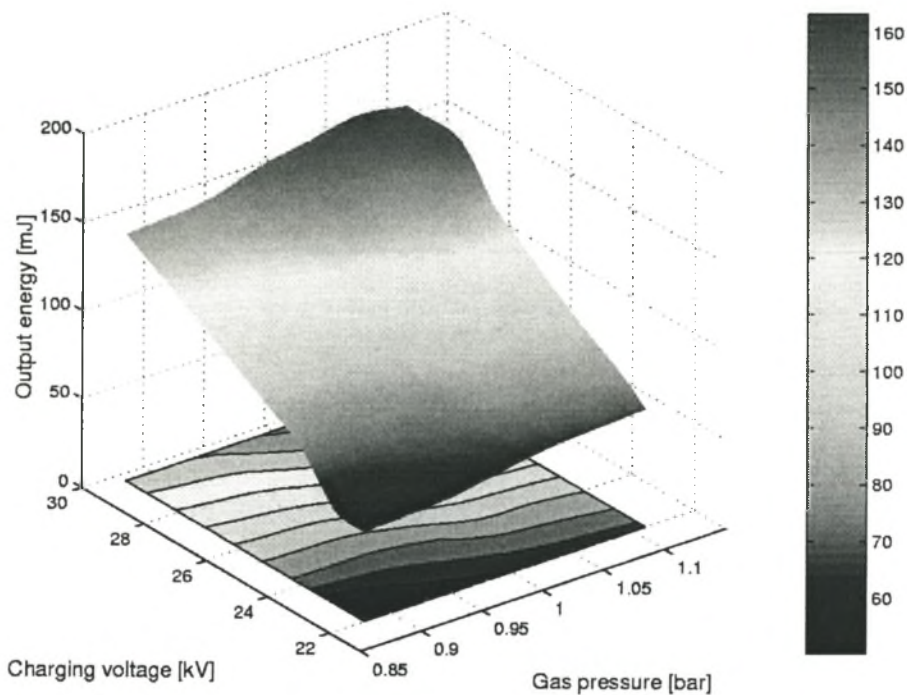


Figure 4-24: Optical output energy vs. charging voltage and gas pressure for commercial thyatron based pulsed power supply. (1:1:3 mixture)

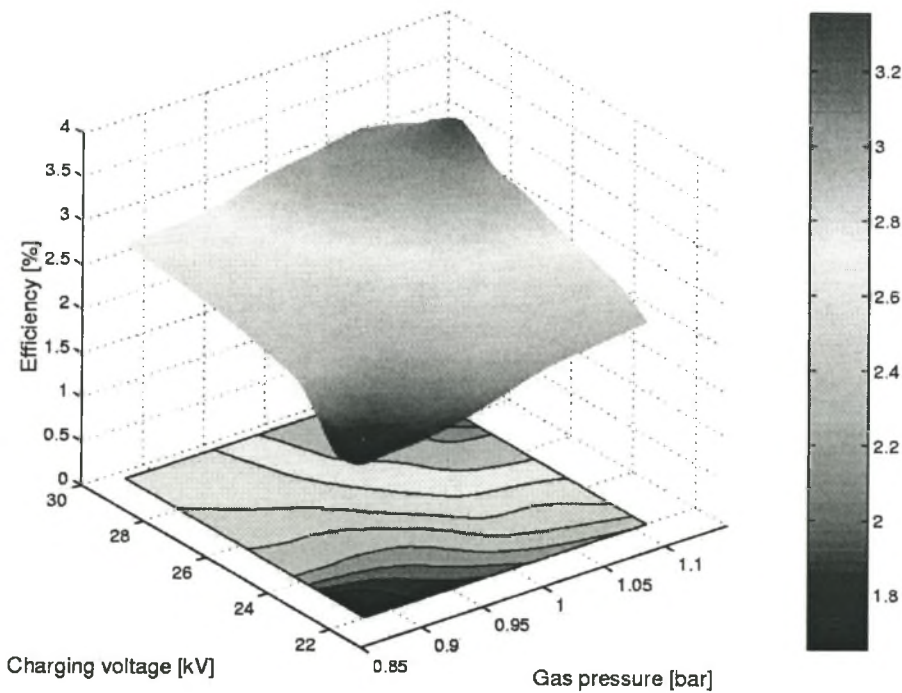


Figure 4-25: Efficiency vs. charging voltage and gas pressure for commercial thyatron based pulsed power supply. (1:1:3 mixture)

The peak optical output energy and efficiency of the commercial pulser for a 1:1:8 gas mixture is approximately 95 mJ and 1.9%, respectively (see Figure 4-22 and 4-23). For a 1:1:3 gas mixture a peak optical output energy and efficiency of approximately 160 mJ and 3.3% was obtained, respectively (see Figure 4-24 and 4-25). For both gas mixtures the peak output energy and efficiency is clearly less than results obtained with the optimised experimental excitation circuit with reduced peaking capacitor size (see Section 4.3.3).

For a direct comparison of the optimised experimental test circuit ($C_p = \frac{1}{3}C_s$ and $L_t = 920$ nH) and the commercial pulser the optical output energy and efficiency of the two pulsers are shown in Figures 4-26 and 4-27. The output energy and efficiency are plotted as a function of the charging voltage for a laser gas pressure of 1 bar. There is a significant improvement of the optical output energy and efficiency of the laser for the optimised pulser as used in Section 4.3.3. For both gas mixtures (1:1:8 and 1:1:3) the output energy and efficiency are more or less doubled over the whole charging voltage range.

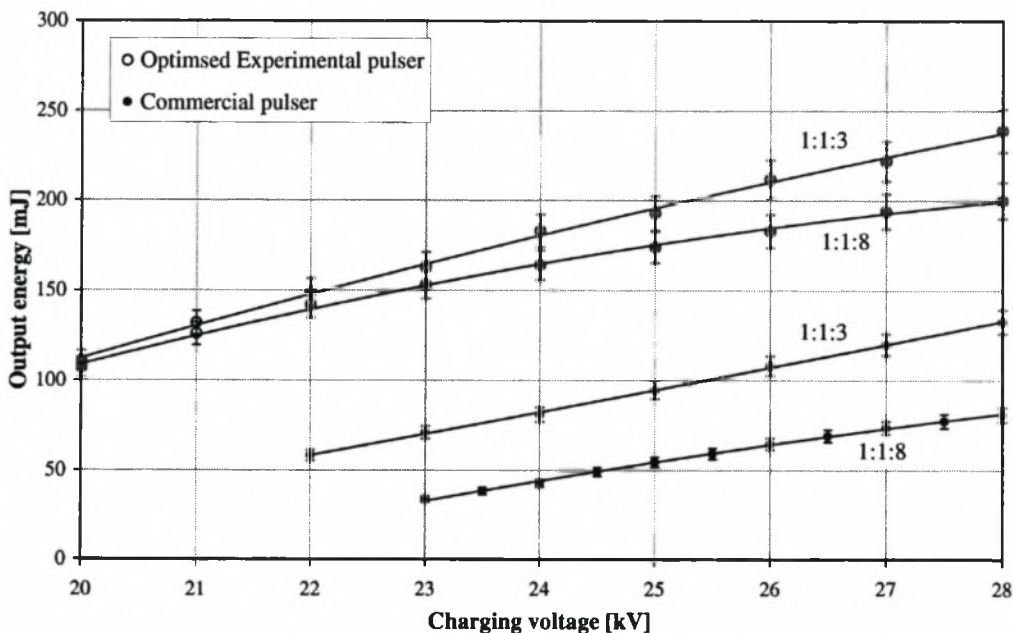


Figure 4-26: Comparison of optical output energy of commercial and optimised experimental pulsers.

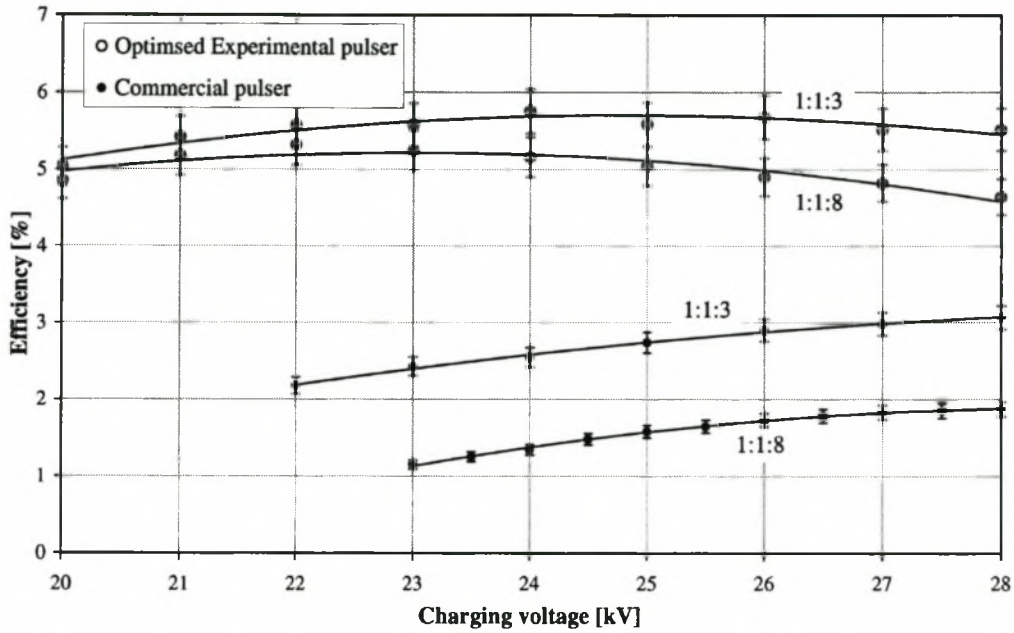


Figure 4-27: Comparison of efficiency of commercial and optimised experimental pulsers.

4.4 Voltage and current waveforms

The circuit voltages were measured with a Tektronix P6015A high-voltage probe (x1000, 70 MHz bandwidth). All voltages have to be measured with respect to a common ground point and the circuit voltages are indicated in Figure 4-28.

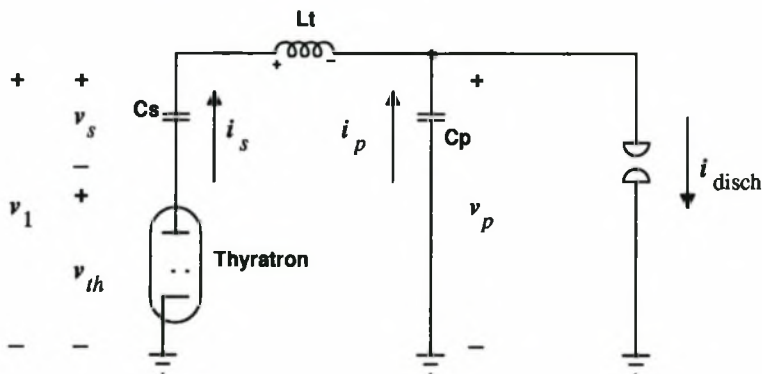


Figure 4-28: Diagram to indicate measured voltages and currents.

The voltage over the peaking capacitor v_p and the thyatron v_{th} can be measured directly. The voltage over the storage capacitor v_s can be calculated by measuring voltage v_1 and subtracting the thyatron voltage:

$$v_s = v_1 - v_{th}. \quad (4.3)$$

The currents could not be measured directly, because no appropriate current probe was available at the time of measurement. An indirect approach had to be used. The currents can be calculated from the measured voltages by differentiating the voltage over the capacitors C_s and C_p and/or integrating the voltage over the inductance L_t . It is not possible to determine the exact value of L_t , because of other series parasitic inductances. Thus, the voltages over the capacitors are used to determine the currents:

$$i_s = C_s \frac{dv_s}{dt}, \quad (4.4)$$

$$i_p = C_p \frac{dv_p}{dt}, \quad (4.5)$$

and
$$i_{\text{disch}} = i_s + i_p. \quad (4.6)$$

Note that these calculations are only valid if the capacitor values are constant with time and voltage, i.e. the capacitors do not change their properties during the discharge period. High-quality ceramic capacitors were used, which are relatively stable with a maximum change in capacitance of 20% over a voltage range of 40 kV. The change in capacitance is caused by the piezo-electric effect. The error introduced by this capacitance change can be approximated by the following expression:

$$\Delta I \approx V \frac{dC}{dt}, \quad (4.5)$$

with V the average voltage over the capacitor and dC/dt the average change in capacitance over the discharge or charging period. For an average voltage of 20 kV, an average capacitance change of 20% over a 150 ns discharge period and a capacitance of 10 nF, the error is approximately $\Delta I = 200$ A.

The energy transfer, E_{disch} , into the laser discharge can be calculated from the discharge voltage and current, by integrating over the instantaneous power deposited in the laser discharge:

$$E_{\text{disch}} = \int v_{\text{disch}} i_{\text{disch}} dt, \quad (4.6)$$

The discharge voltage v_{disch} was measured very close to the laser electrodes to reduce the effect of the inductance of the laser head between the peaking capacitor and laser electrodes. The voltage and current waveforms were measured for $C_p = C_s$ and $C_p = \frac{1}{3}C_s$. A transfer inductance of $L_t = 920$ nH, a storage capacitance of $C_s = 11.04$ nF and a charging voltage of 25 kV were used. The voltage over the discharge, the discharge current and the inductor current are discussed in the following section.

4.4.1 Comparison of discharge voltages

The discharge voltage is displayed in Figure 4-29 for the two cases $C_s = C_p$ and $C_s > C_p$.

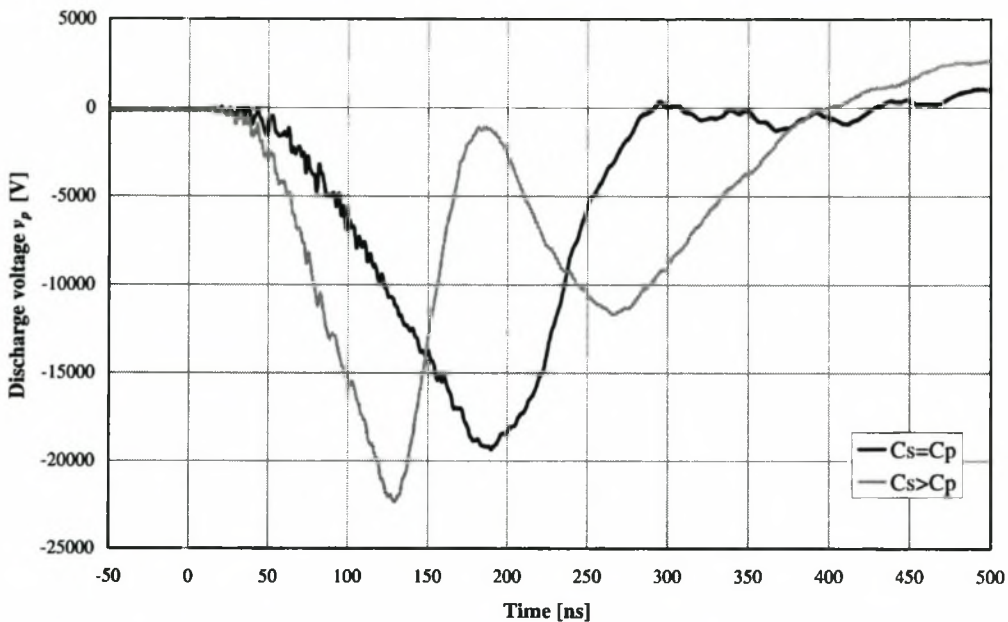


Figure 4-29: Comparison of discharge voltages for $C_s = C_p$ and $C_s > C_p$.

$C_s = C_p$: There is a single voltage pulse, which is caused by an almost total energy transfer from C_s to C_p . At $t = 180$ ns the discharge is initiated and energy is deposited from the peaking capacitor into the discharge between $t = 200$ ns and 280 ns. The voltage drops to almost zero, which indicates good matching.

$C_s > C_p$: There is an initial fast voltage pulse between $t = 0$ ns and 200 ns, which is caused by a partial energy transfer from C_s to C_p . The voltage pulse has a faster rise-time than for $C_s = C_p$, because of the smaller peaking capacitor size (see Equation 4.1). This results in an increase in the breakdown voltage and at $t = 120$ ns the discharge is initiated and energy is transferred from the peaking capacitor into the discharge. Between $t = 200$ ns and 400 ns there is a second smaller voltage pulse. This is caused by the remaining energy in the storage capacitor being deposited into

the discharge directly through inductor L_r . The electric excitation pulse is clearly stretched by approximately 200 ns in comparison to the case where $C_s = C_p$.

4.4.2 Comparison of current waveforms

The above discussion makes more sense when looking at the current waveforms shown in Figures 4-30 and 4-31.

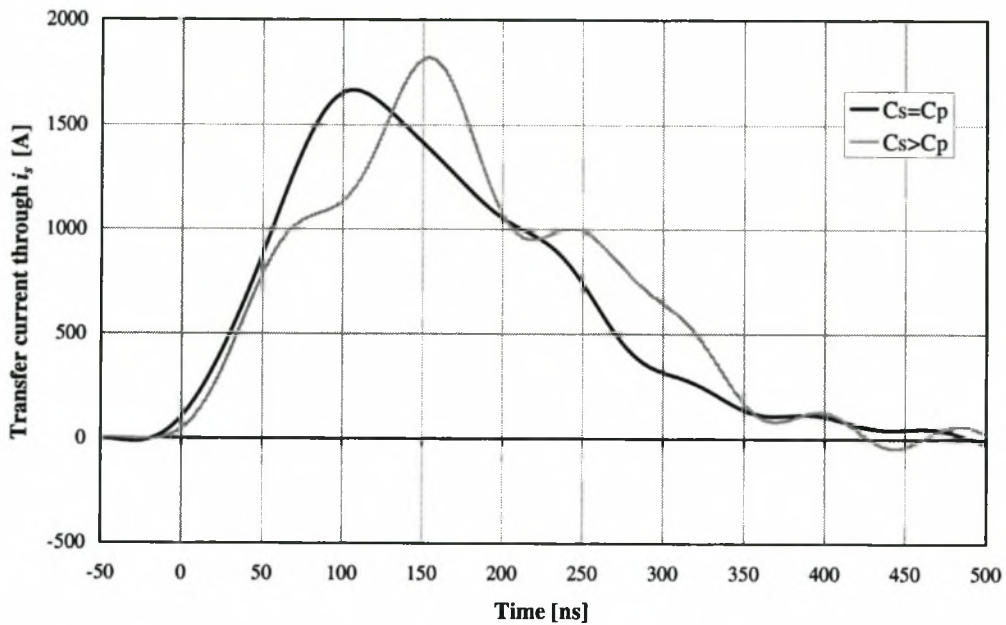


Figure 4-30: Comparison of inductor currents for $C_s = C_p$ and $C_s > C_p$.

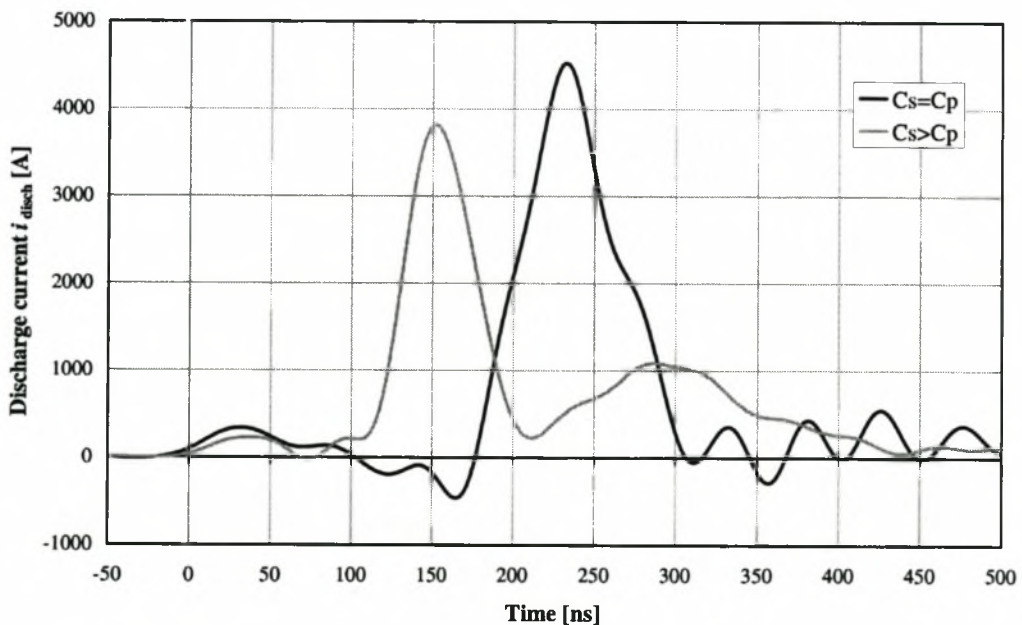


Figure 4-31: Comparison of discharge currents for $C_s = C_p$ and $C_s > C_p$.

$C_s = C_p$: There is only a single discharge current pulse (Figure 4-31), which is obtained between $t = 200$ ns and 300 ns, soon after the discharge is initiated. The discharge pulse is preceded by a C-C transfer pulse in the inductor current (Figure 4-30), which charges the peaking capacitor between $t = 0$ ns and 200 ns. The length of the discharge current pulse is determined by the internal inductance of the laser, between the peaking capacitor and the laser electrodes. Simulations, which are outside the scope of this discussion, show that the discharge current pulse is longer for bigger internal inductances. The length of the discharge pulse is approximately 100 ns.

$C_s > C_p$: Similar to the behaviour of the voltage pulse there is an initial discharge current pulse between $t = 100$ ns and 200 ns, followed by a smaller second pulse between $t = 200$ ns and 400 ns. The initial discharge current pulse is obtained during the C-C transfer pulse in the inductor current. A small second pulse can be observed in the inductor current between $t = 250$ ns and 350 ns, which overlaps with the second discharge pulse. This shows that the second discharge current pulse is obtained by a direct energy transfer from the storage capacitor into the laser discharge. The total length of the discharge pulse is approximately 300 ns.

4.4.3 Comparison of discharge energies

To complete the circuit analysis the energy transfer into the discharge was calculated and is shown in Figure 4-32.

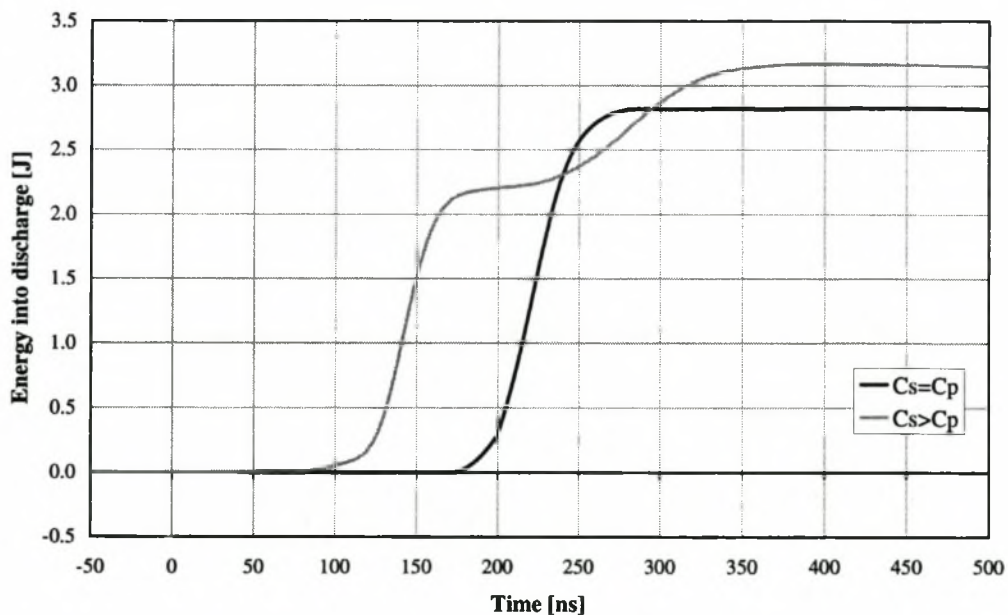


Figure 4-32: Comparison of energy transfers into discharge for $C_s = C_p$ and $C_s > C_p$.

$C_s = C_p$: As expected there is only energy transfer during the discharge current pulse between $t = 200$ ns and 250 ns. The energy is thus deposited within a time interval of 50 ns.

$C_s > C_p$: There is an initial energy transfer during the first voltage and discharge current pulse between $t = 100$ ns and 150 ns. An additional energy transfer occurs during the second smaller voltage and current discharge pulse between $t = 200$ ns and 350 ns. The energy is transferred within a time interval of 250 ns. This results in 10% to 20% more energy transfer than for $C_s = C_p$.

4.4.4 Comparison of optical pulse shapes

The optical pulse is obtained approximately 500 ns after the excitation pulse. The two capacitor configurations therefore only have a limited influence on the optical pulse shape. The optical pulse shapes were measured with a fast pyro-electric detector (Eltec 420, rise-time 2 ns into 50 Ω). The measured optical pulse shapes for $C_s = C_p$ and $C_p = \frac{1}{3}C_s$ are depicted in Figure 4-33. The initial intensity spike is the same for the two capacitor configurations. The second gain switched intensity spike and the tail region is stronger for the case where $C_s > C_p$. This is caused by more efficient energy transfer into the laser discharge as discussed in the preceding sections. Note that the optical pulses are up to 2.5 μ s long, which is much longer than the electrical excitation pulses. Thus, it becomes clear that the length of the electrical excitation pulses must also be in the order of a few microseconds in order to obtain stretching of the optical pulse through electrical excitation.

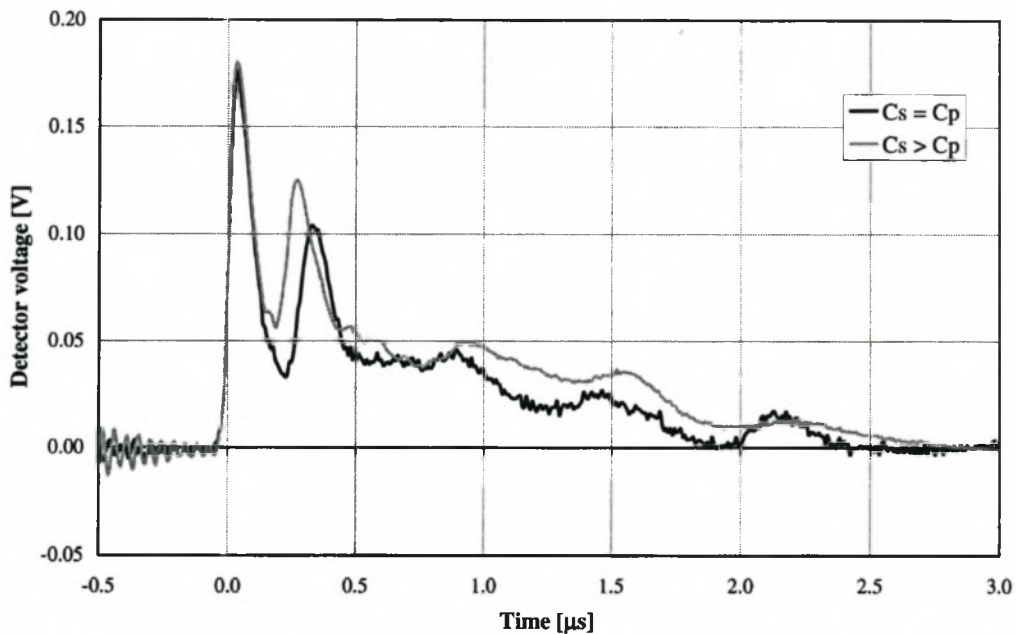


Figure 4-33: Optical pulse shape for $C_s = C_p$ and $C_s > C_p$.

4.5 Summary

Stability	<ul style="list-style-type: none"> • Best stability is obtained with series pre-ionisation, but probably with increased spark gap erosion. Thus, parallel pre-ionisation should rather be used if possible. • The peaking capacitor must be greater than $\frac{1}{3}C_s$ to obtain stable discharges. • Stable discharges can be obtained with voltage rise-times of approximately 180 ns (300 ns transfer time) • Discharges are less tolerant to O₂ formation due to dissociation of CO₂ for rise-times slower than 120 ns (200 ns transfer time). This leads to discharge instability and power loss. It is therefore advisable to use voltage rise-times between 100 and 120 ns (transfer times between 160 and 200 ns) • Matching (i.e. transfer efficiency into the laser discharge) is an important consideration with improved matching for faster voltage rise-times (< 150 ns). For $C_p < C_s$ even faster voltage rise-times (< 100 ns) are needed.
Inductance L_t	<ul style="list-style-type: none"> • There is a maximum in the output energy at approximately 1.5 μH for 1:1:8 and 1:1:3 gas mixtures and $C_s = C_p$. However, better discharge stability is obtained for transfer inductances smaller than 1 μH.
Capacitance C_p	<ul style="list-style-type: none"> • The output energy and efficiency increases by between 25% and 35% for both 1:1:8 and 1:1:3 gas mixtures by decreasing the peaking capacitor size to $C_p = \frac{1}{3}C_s$. Good discharge stability is obtained for a transfer inductance of approximately 1.0 μH.
Waveforms	<ul style="list-style-type: none"> • For $C_p = \frac{1}{3}C_s$: Measurements of current and voltage waveforms indicate an initial energy transfer from the peaking capacitor into the laser discharge followed by an additional energy transfer directly from the storage capacitor. • For $C_p = C_s$: Energy is mainly transferred from the peaking capacitor into the laser discharge. • Electric pulses are stretched for $C_p > C_s$.
Optical pulse	<ul style="list-style-type: none"> • Although the time interval of energy transfer into the discharge is stretched from approximately 50 ns ($C_p = C_s$) to 250 ns ($C_p = \frac{1}{3}C_s$), it does not affect the optical pulse shape dramatically, but only increases the output energy and efficiency of the laser.

Table 4-1: Summary of electrical measurement results.

Chapter 5

Laser pulsed power supply design and construction

In the previous chapters a mini CO₂ TEA laser was characterized and optimum excitation conditions were established. Different pulse power supply topologies were considered and the IGBT characteristics were analysed. The next step is to finally design the pulse power supply, which will generate the needed fast rising high voltage pulses for efficient and stable excitation of the CO₂ laser. The design parameters for the pulse power supply are summarized in Table 5-1. The parameters were mainly determined during the characterization of the CO₂ TEA laser (see Table 4-1) for which the power supply is being developed.

Output pulse energy	4 to 5 J
Maximum repetition rate	600 Hz
Maximum average power output	2.4 to 3.0 kW
Output voltage rise-time (10–90%), $C_s = C_p$	120 ns
Output Voltage at maximum energy	28 kV

Table 5-1: Design specifications of the pulsed power supply.

In the remainder of this chapter the design process is outlined, followed by a more detailed discussion on the design and construction of the pulse power supply.

5.1 Pulsed power supply design

5.1.1 Design outline

The design of a pulsed power supply is an iterative process [10]. The aim is to determine the circuit parameters of the pulse power supply (e.g. capacitor and inductor values of C-C transfer loops, core parameters of saturable inductors for the MPC unit, etc.) that will result in the specified output pulse characteristics. At the same time the switching currents and voltages may not exceed the peak ratings of the primary switching device. The design steps that were used for this project are outlined in the flow chart shown in Figure 5-1.

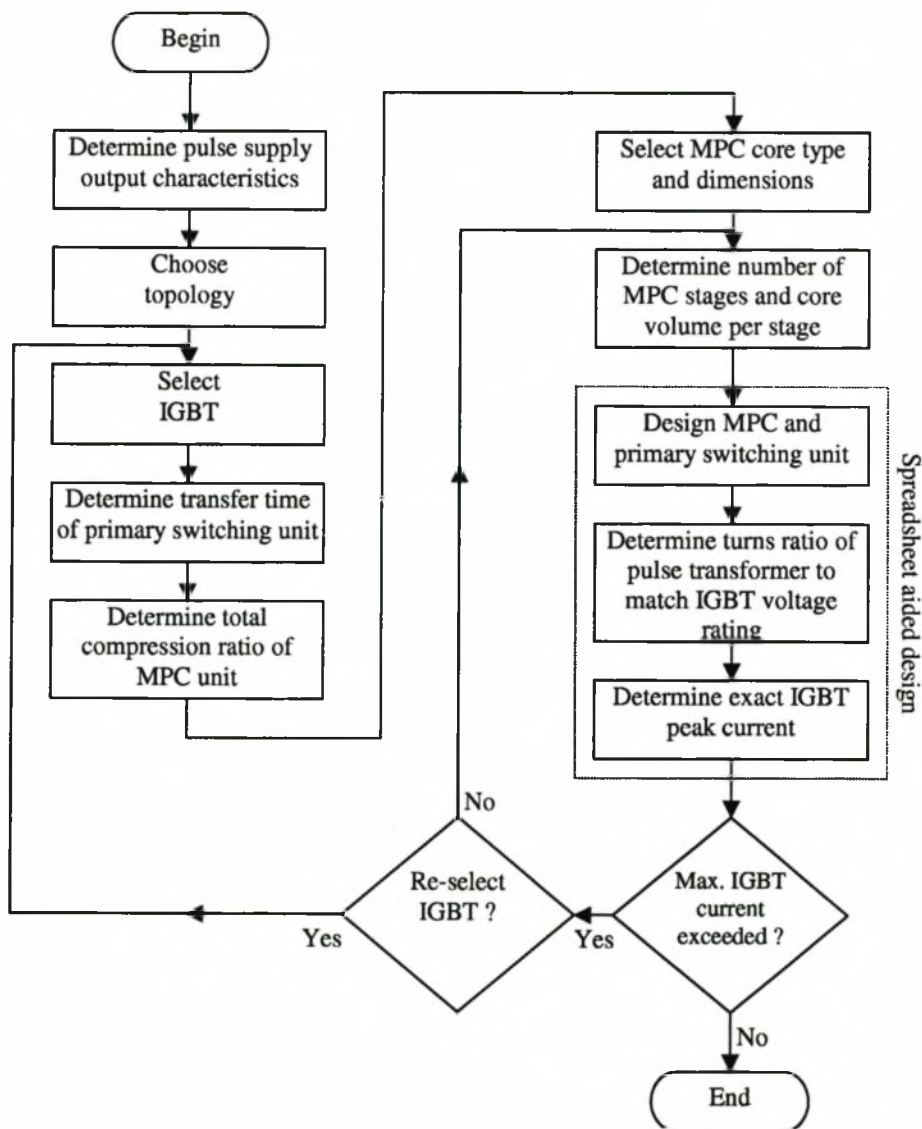


Figure 5-1: Flow chart of a laser pulsed power supply design procedure.

Step 1 Determine supply output characteristics

The supply output characteristics include the output pulse voltage rise-time and magnitude. Additional parameters that are important are the pulse energy and repetition rate. The optimum output parameters are determined by the laser characteristics as discussed in Chapter 4.

Step 2 Choose topology

The topology of the primary switching unit (e.g. switched C-C transfer loop, LC-inversion, etc.) and the MPC unit (e.g. series MPC circuit, parallel MPC circuit, etc.) have to be chosen. Details about different topologies are given in Chapter 2.

Step 3 Select IGBT

Using the analysis and guidelines given in Chapter 3 an IGBT can be selected.

Step 4 Determine transfer time of primary switching unit

From the IGBT ratings and output specifications the minimum transfer time of the switched C-C transfer loop in the primary switching unit can be estimated. The transfer time of the C-C loop must be such that the peak current of the IGBT is not exceeded (see sections on switching currents in Chapter 2) and the IGBT is sufficiently decoupled during the turn-on transient as discussed in Chapter 3. It is also important to estimate the junction temperature of the IGBT under the proposed conditions.

Step 5 Determine total compression ratio of MPC unit

From the estimated transfer time in step 4 and specified output pulse voltage rise-time the total compression ratio, G , of the MPC unit can be calculated.

Step 6 Select MPC core type and dimension

The core type and dimensions have to be chosen. Step 6 and 7 are often performed in parallel, because the core size is influenced by the number of chosen MPC stages and vice versa. Normally only a limited range of core types and dimensions are available making the choice less difficult. Important considerations are costs, availability and size.

Step 7 Determine number of MPC stages

It is not possible to give exact guidelines on choosing the optimum number of MPC stages. In Chapter 2 it was shown how the core volume of the MPC unit can be minimized, but this often results in a large number of MPC stages and is not feasible. It is advisable to take all possible

factors into account, including core volume, number of capacitor banks, number of needed MPC cores, costs and size. The needed core volume per MPC stage can be estimated by using Equation 2.32 or 2.33. The number of cores for each MPC stage can then be determined.

Step 8 Design primary switching and MPC units

A spreadsheet-aided design proposed by Swart et al. [40] can be used as a very efficient design tool. The results obtained from the discussion of the primary switching unit and MPC unit in Chapter 2 can be condensed into a spreadsheet containing the necessary formulas. The spreadsheet will accept a few input parameters (e.g. the output pulse voltage and rise-time, core dimensions of the saturable inductors, etc), which were determined in the previous design steps. The circuit values of the MPC and primary switching units, including circuit currents and voltages are automatically calculated.

Step 9 Determine turns ratio of pulse transformer

From the voltages calculated in step 8 and the IGBT voltage rating the transformer turns ratio of the pulse transformer can be determined.

Step 10 Determine exact IGBT current

Using the results obtained in steps 8 and 9 the exact IGBT peak switching current can be calculated. If the calculated peak IGBT current exceeds the peak allowable IGBT current, steps 7 to 9 have to be repeated or a different IGBT has to be chosen.

The spreadsheet aided design of the MPC and primary switching units can greatly simplify and accelerate the above design process. The design can therefore be easily changed until a design is obtained that satisfies both the pulse output specifications and peak IGBT ratings.

5.1.2 Design results

It is not possible to describe and retrace the iterative design process in detail and therefore mainly the design results are presented. Important design steps (e.g. IGBT selection, choice of topology, etc) are explained in more detail in order to clarify the design process.

Pulse power supply topology and layout

Following the discussion in Chapter 2 the basic topology for the primary switching and MPC units was chosen:

- The primary switching unit is a directly switched C-C transfer loop and makes use of two series-stacked IGBTs and a pulse transformer to step-up the voltage.
- The MPC unit consists of a two-stage series MPC circuit.
- Parallel pre-ionisation is applied.

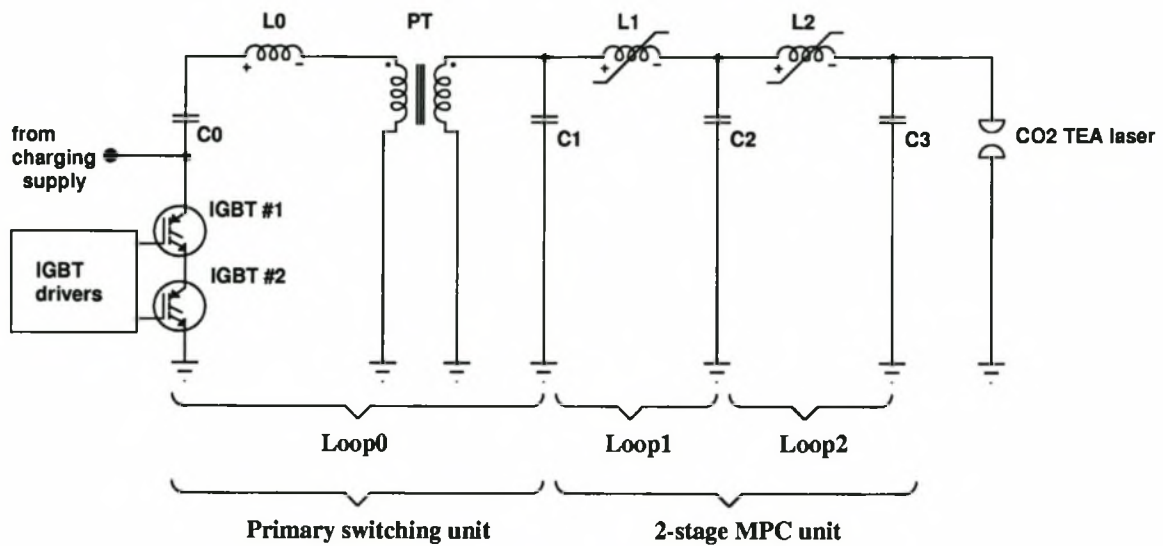


Figure 5-2: Proposed topology for the pulse power supply.

The basic power supply layout is shown in Figure 5-2. Two series-stacked IGBTs are used as the primary switching device in order to be able to switch higher voltages. This will result in lower switching currents. Additionally the response and viability of series-stacked IGBTs in a pulsed power supply can be investigated. The choice of a 2-stage pulse compressor is explained in Section 5.1.2. The reason for choosing parallel pre-ionisation, although the discharge stability is less compared to series pre-ionisation, is to reduce the erosion of the pre-ionisation spark gap.

IGBT selection

After taking all the factors (e.g. switching speed, current and voltage ratings, costs, availability, delivery times, etc.) into account the SKM300GB174D from Semikron was selected. The SKM300GB174D is an IGBT module, housing two series-connected IGBTs with a 300 A average current rating and a peak voltage rating of 1700 V per IGBT. The IGBT module can therefore

switch a maximum voltage of 3400 V. The data sheets of the device are given in Appendix C. Furthermore, it was found that the peak switching current should not exceed 5 times the rated current. For larger currents the IGBT saturates and effectively turns off. The IGBT should have a 40% voltage safety margin [17] to allow reliable turn-off of the IGBT as discussed in Chapter 6. The ratings of the IGBT module are summarized in Table 5-2.

IGBT Module	SKM300GB174D (Semikron)
Breakdown voltage, V_{ceo}	3400 V
Voltage safety margin	40 %
Max. switching (charging) voltage, V_0	2430 V
Peak switching current	1500 A (5x rated)
Gate-collector (Miller) capacitance, C_{gc}	2.6 nF
Gate-emitter capacitance, G_{ge}	14 nF

Table 5-2: Ratings of IGBT module used in primary switching unit.

Minimum transfer time of primary switching unit

Firstly, the minimum transfer time of the switched C-C loop is determined, which will result in a peak switching current not exceeding the peak rated current of the IGBT. Using the ratings specified in Table 5-2 and Equation 2.17 the minimum transfer time of the switched C-C transfer loop can be calculated. A minimum transfer time of $\tau \cong 4 \mu\text{s}$ for pulse energies between 4 and 5 J is obtained. Secondly, it is verified whether the calculated minimum transfer time will also result in sufficient decoupling of the IGBT during the turn-on transient. Using the decoupling criteria given by Equation 3.21 ($a \cong 25 \text{ A/V}$, $R_g \cong 2 \Omega$, $V_g = 18 \text{ V}$, $V_{Th} = 5.5 \text{ V}$) it is found that the transfer time should be larger than $0.42 \mu\text{s}$ for sufficient decoupling and a transfer time of $4 \mu\text{s}$ is therefore acceptable.

It is also important to consider the IGBT junction temperature under the pulse conditions estimated in the previous paragraph. Using the datasheets in Appendix C and applying Equations 3.22 and 3.23 the pulse and average power dissipation in the IGBT can be calculated:

$$P_{\text{IGBT,pulse}} \cong 7000 \text{ W} \quad (I_{s,\text{peak}} = 1500 \text{ A}, V_{\text{on}} = 1.5 \text{ V}, r_{CE} = 0.0065 \Omega)$$

and $P_{\text{IGBT}} \cong 16.8 \text{ W} \quad (f_{\text{rep}} = 600 \text{ Hz}, \tau = 4 \mu\text{s}, D = f_{\text{rep}} \tau = 0.0024).$

Therefore, the estimated average and peak junction-to-case temperature difference as calculated

using Equations 3.24 and 3.25 is:

$$\Delta T_{j_c, \text{peak}}^* \approx 10 \text{ }^\circ\text{C} \quad (Z_{ihjc} \approx 0.001 \text{ K/W})$$

and $\Delta T_{j_c, \text{peak}} \approx 1 \text{ }^\circ\text{C} \quad (R_{thjc} = 0.07 \text{ K/W}).$

Needless to say the peak and average temperature differences are very small. As long as the case of the IGBT is connected to a heatsink, which is able to cool away the average power dissipation of 16.8 W, there should be no problem.

Number of MPC stages

As determined in the previous section the transfer time of the primary switching unit is approximately 4 μs . The output voltage rise-time of the pulsed power supply is 120 ns, as specified in Table 5-1. This is equivalent to a transfer time of 200 ns in the final MPC stage. The total required compression ratio of the MPC is therefore approximately $G \cong 25$. Theoretically the number of stages that will minimize the volume of magnetic material in the MPC unit is given by Equation 2.35. For a minimum core volume 6 to 7 stages are needed. Although this relatively large number of stages will minimize the core volume (see Chapter 2) it is not practical. For a 7-stage MPC unit 8 high-voltage capacitor banks will be needed, which is excessively costly. Furthermore, the core sizes needed for the 7-stage MPC unit are not easily available. Taking costs of magnetic cores and high-voltage capacitors into account a 2-stage MPC is chosen.

MPC core selection and estimated core volume

The saturable cores available for the MPC unit are of the type Finemet FT-1H from Hitachi. The cores have a toroidal geometry and the core parameters are listed in Table 5-3.

Type	Finemet FT-1H
Saturated flux density, B_{sat}	1.265 T
Saturated permeability, μ_{sat}	$\mu_0 = 4\pi 10^{-7}$
Inner core diameter, r_i	0.085 m
Outer core diameter, r_o	0.140 m
Core height, h	0.010 m
Core volume, Vol	97.2 cm^2

Table 5-3: Core parameters and dimensions of MPC unit.

Using the core dimensions given in Table 5-3 and applying Equation 2.32 or 2.33, an estimate of the core volume per stage can be made. For a compression ratio of approximately $g_n = 5$ per MPC stage, the estimated core volume per stage is 135 cm^3 (core packing factor of $p = 0.8$, winding clearance of $\Delta r = 0.005 \text{ m}$ and a transfer energy of $E_0 = 5 \text{ J}$ are assumed). The total estimated core volume of the 2-stage MPC unit is 270 cm^3 . Thus, three of the above specified cores are needed for the construction of the MPC unit. A larger voltage hold-off is needed in the first compression stage. Consequently, two cores are used in the first MPC stage to reduce the number of inductor turns due to practical reasons (clearance between turns of the inductor winding, etc.). A single core is used in the last MPC stage.

Spreadsheet based design results

As mentioned earlier, a spreadsheet-aided design is used to calculate the circuit values, currents and voltages of the pulsed power supply. The design normally starts with the final output MPC stage of the pulse power supply for which the output voltage and rise-time are clearly specified. Subsequently starting from the output stage, each of the connected input stages are designed successively up to the initial C-C transfer stage of the primary switching unit [40]. The final results of the spreadsheet-aided design of the MPC and primary switching units are summarized in Table 5-4.

The input parameters in Table 5-4 are indicated by grey-shaded cells. The columns labelled 'Loop2', 'Loop1' and Loop0 correspond to the second (final) MPC stage, first MPC stage and primary switching loop, respectively, as indicated in Figure 5-2. In the spreadsheet-aided design the C-C transfer loops of both the MPC unit and the primary switching units are optimised using the optimisation method B (see Section 2.2.2).

Some of the input parameters – the parasitic stray inductance, core packing factor and transfer loss factor – can only be determined after the construction details of the pulse power supply have been finalised. The parasitic stray inductances L_{par} of the MPC stages and the core packing factor p of the saturable inductors are determined by the final construction details of the MPC unit and are discussed in more detail in Section 5.4. The transfer losses, including conduction and inductor core losses, are difficult to predict, but in general losses can be estimated to be more or less 5 % of the transferred energy per C-C transfer stage.

Circuit parameters			Loop2	Loop1	Loop0
Output energy	E_o	J	4.20	4.42	4.65
Transfer time	τ_n	s	180.0E-9	706.4E-9	4.3E-6
Output voltage	V_o	V	27000	28421	29917
Losses	n	%	5.00	5.00	5.00
Loss factor, $e^{-\gamma t}$	f_{loss}		950.00E-3	950.00E-3	950.00E-3
Damping factor	α	1/s	284.96E+3	72.61E+3	11.94E+3
Transformer ratio	a		1	1	13
Input energy	E_i	J	4.42	4.65	4.90
Input voltage	V_i	V	28421	29917	2422
Output capacitance	C_n	F	11.5E-9	10.9E-9	10.4E-9
Input capacitance	C_{n-1}	F	10.9E-9	10.4E-9	1.67E-6
Total loop inductance	L_n	H	584.80E-9	9.48E-6	2.18E-6
Parasitic stray inductance	L_{par}	H	20.00E-9	20.00E-9	
Saturated inductance	L_{sat}	H	564.80E-9	9.46E-6	
Hold-off time	$\tau_{n,hold}$	s	604.98E-9	3.68E-6	
Switching parameters					
Voltage switching ratio	k_{sw}		0.95	0.95	
Relative switching time	$\tau_{n,hold}/\tau_{n-1}$		0.856	0.856	
Timing factor	F_t		737.61E-3	737.61E-3	
Saturated flux content	Φ_{sat}	Vs	7.40E-3	47.39E-3	
Compression ratio	c		3.92	6.08	
Core parameters (toroidal)					
Core material			FINEMET	FINEMET	Air core
Number of cores			1	2	
Saturation flux density	B_{sat}	T	1.26	1.26	
Saturated permeability	μ_{sat}		1	1	
Max. flux density change	ΔB	T	2.53	2.53	
Core packing factor	p		0.92	0.92	
Inner core radius	r_i	m	0.0425	0.0425	
Outer core radius	r_o	m	0.0700	0.0700	
Core height	h	m	0.0100	0.0100	
Inter-core clearance	Δ_{core}	m	0.0030	0.0030	
Core x-section	A_{core}	m ²	212E-6	424E-6	
Magnetic x-section	A_{mag}	m ²	206E-6	413E-6	
Magnetic volume	V_{mag}	m ³	97E-6	194E-6	
Radial winding clearance	Δ_{radial}	m	0.0040	0.0040	
Vertical winding clearance	Δ_{vert}	m	0.0040	0.0040	
Turns	N		15	48	
Extra data					
Peak current	I_{peak}	A	2715	692	1405
Voltage rise-time (10%-90%)	$t_{rise,10-90}$	sec	108.0E-9	423.8E-9	2.6E-6
Maximum voltage rise time	V_{rise}	kV/ μ s	235.6	63.2	10.9

Table 5-4: Spreadsheet-aided design results for the MPC and primary switching units.

The design results are satisfactory, with an output voltage rise-time of 108 ns, which is even faster than specified, and an output pulse energy of 4.2 J. The switching voltage is within the specified rating (see Table 5-2). The peak switching current is marginally larger than the specified peak IGBT current and is also acceptable. Note, the calculated transfer inductance of the primary switching unit (Loop0) given in Table 5-4 is the primary equivalent transfer inductance. It is therefore the total transfer inductance of the primary switching loop referenced to the primary low-voltage side of the pulse transformer.

An important modification is made to the design results obtained. In Chapter 4 it was shown that the excitation of the CO₂ laser can be improved by reducing the size of the peaking capacitors, which in this case is the output capacitor C₃ of the final MPC stage (see Figure 5-2). The peaking capacitor size is reduced to a third of the calculated value in Table 5-4, i.e. C₃ = 3.8 nF. Furthermore, the transfer inductance in the final MPC stage is left unchanged to prevent reduced discharge stability (see Section 4.2.4). Thereby the transfer time of the final compression stage is reduced to 128 ns resulting in a voltage rise time of approximately 80 ns across the peaking capacitors.

5.1.3 Pulsed power circuit components

In a practical set-up it is possible to construct the saturable inductors of the MPC unit and the transfer inductance of the primary switching unit quite accurately. However, the C-C transfer capacitors have to be constructed as capacitor banks consisting of a number of parallel-connected capacitors, which are only available in discrete values. It is therefore not possible to exactly obtain the correct capacitor values calculated in Table 5-4. A summary of the values of the C-C transfer capacitors and more details about the composition of the capacitor banks are given in Table 5-5.

The capacitor values can be closely matched with a maximum difference of 3.9 % between the practical used and calculated capacitor values. This deviation is very small and can be neglected.

	Calculated value	Practical value	Difference	Detail
C_0	1.67 μF	1.65 μF	-1.2 %	2 series connected capacitor banks with 7 parallel 0.47 μF / 2000 V snubber capacitors each. Total voltage rating of 4000 V.
C_1	10.4 nF	10.76 nF	+3.5 %	6x 1.7 nF / 40 kV + 1x 560 pF / 40 kV parallel high-voltage ceramic capacitors
C_2	10.9 nF	11.32 nF	+3.9 %	6x 1.7 nF / 40 kV + 2x 560 pF / 40 kV parallel high-voltage ceramic capacitors
C_3	3.8 nF	3.68 nF	-3.2 %	4x 920 pF / 40 kV parallel ceramic capacitors

Table 5-5: Practical capacitor values.

5.1.4 Pulsed power circuit simulation

In order to verify the design carried out in the previous section the circuit has been simulated using PSpice. The complete circuit with MPC unit and laser discharge can be simulated by using the Jiles-Atherton model for the MPC cores and a physical discharge model for the laser discharge. The MPC core and laser discharge models are discussed in Appendix A. The advantage of using a physical discharge model is that the discharge process can also be simulated. This also makes it possible to simulate the circuit behaviour during and even after the laser discharge. The simulated circuit is depicted in Figure 5-3 and the simulated current and voltage waveforms are shown in Figures 5-4 and 5-5, respectively. The core reset windings are included to simulate the reset of the saturable cores. The transfer resistances were calculated from the damping factors given in Table 5-4. Each of the saturable inductors is simulated by two inductors. The inductors Lsat1 and Lsat2 simulate the voltage hold off and the other inductors L1 and L2 the saturated transfer inductance. A simple time-dependent switch was used to simulate the IGBT. Note that an inductance (Ldisch) has been added between the peaking capacitor and the laser electrodes. This inductance simulates the parasitic inductance of the laser head, which is approximately 20 nH.

The voltage and current waveforms of the different MPC stages are shown in Figures 5-4 and 5-5. The obtained voltage and current waveforms are satisfactory and the switching times of the MPC inductors, peak transfer currents and voltages correspond well to the values in Table 5-4, indicating that the design is satisfactory. Note that the output voltage waveform of the final MPC unit is

different than calculated in Table 5-4, due to the reduced peaking capacitor size [40]. Consequently, the output voltage rise-time is reduced.

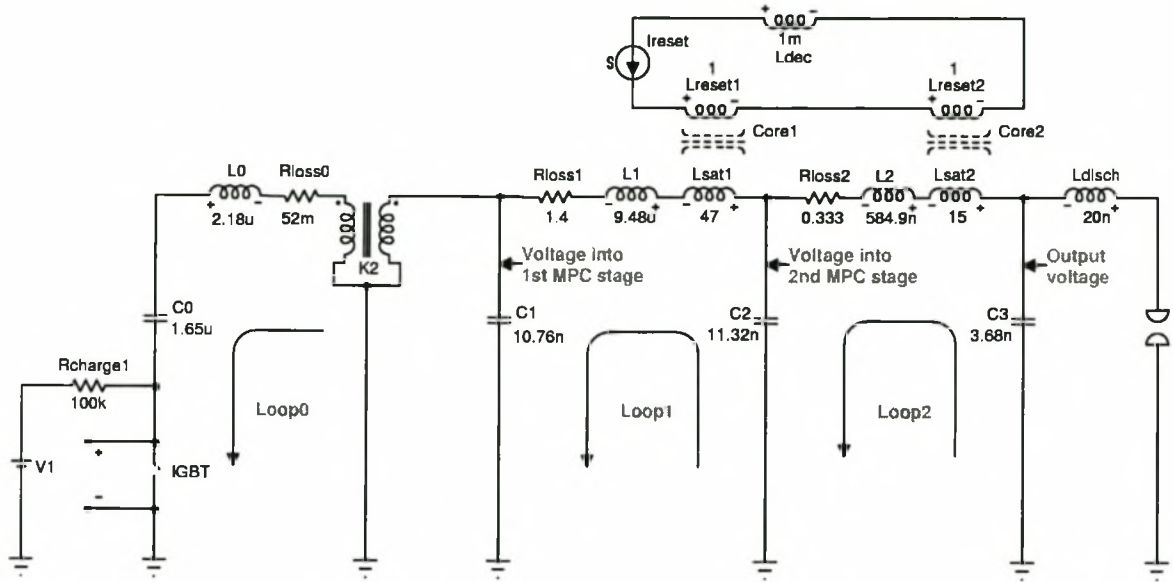


Figure 5-3: Simulated pulsed power supply circuit.

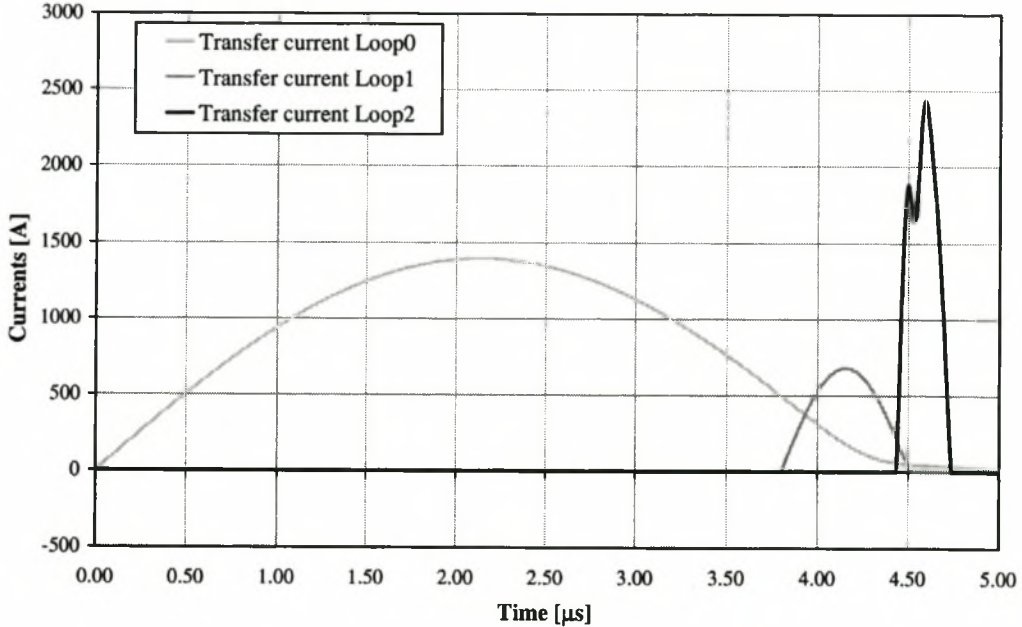


Figure 5-4: Simulated current waveforms.

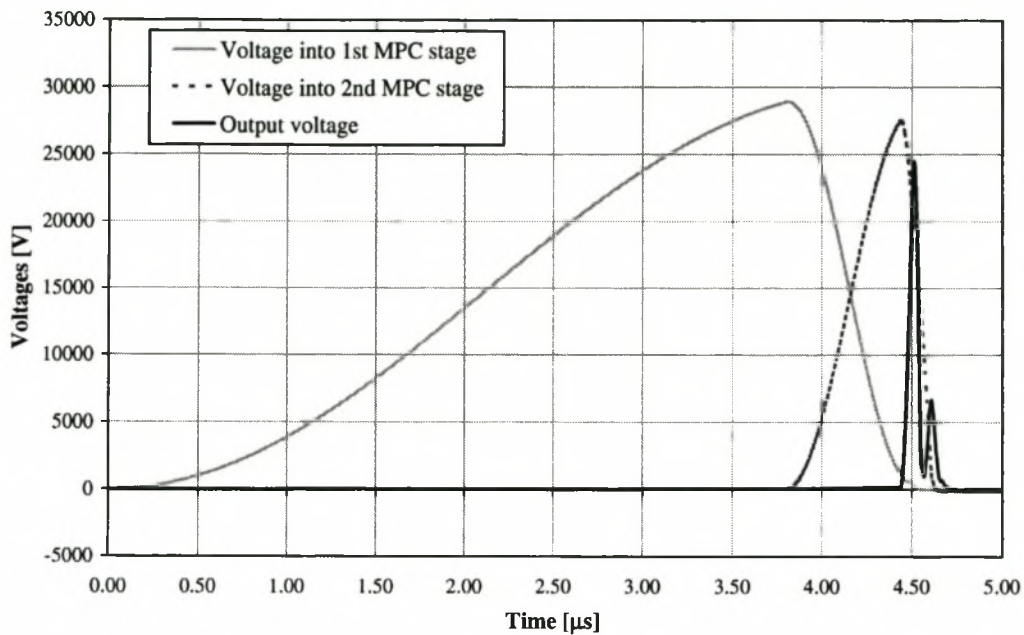


Figure 5-5: Simulated voltage waveforms.

In Figure 5-6 the output voltage waveform and transfer current in the final MPC stage are shown in more detail. The simulated discharge current is also shown. The simulated waveforms strongly resemble the measured waveforms in Chapter 4 (see Section 4.4) for the case where $C_p = \frac{1}{3}C_s$. As expected the initial electrode voltage rise-time is approximately 80 ns after which the laser discharge is initiated. As discussed in Chapter 4 an initial discharge current pulse, fed by the peaking capacitor, is obtained. This is followed by a secondary discharge, where the remaining energy is transferred from the previous capacitor bank (C2, see Figure 5-3) directly into the discharge. This is clearly shown by a second maximum in both the discharge current and the transfer current of Loop2. Furthermore, it can be seen that the reverse overshoot voltage is relatively small, indicating good matching conditions.

In Figure 5-7 the energy deposition into the discharge is shown as a function of time. The graph was calculated in the same way as discussed in Chapter 4 (see Section 4.4). Again, as measured in Chapter 4 (see Figure 4-32), the energy is deposited into the discharge in two successive steps. First, the initial discharge is obtained, followed by the secondary discharge. During the secondary discharge the remaining energy in capacitor C2 of the previous MPC stage is deposited into the discharge. According to the simulation approximately 3.5 J is transferred into the laser discharge. This is approximately 70 % of the initial stored energy in the primary storage capacitor.

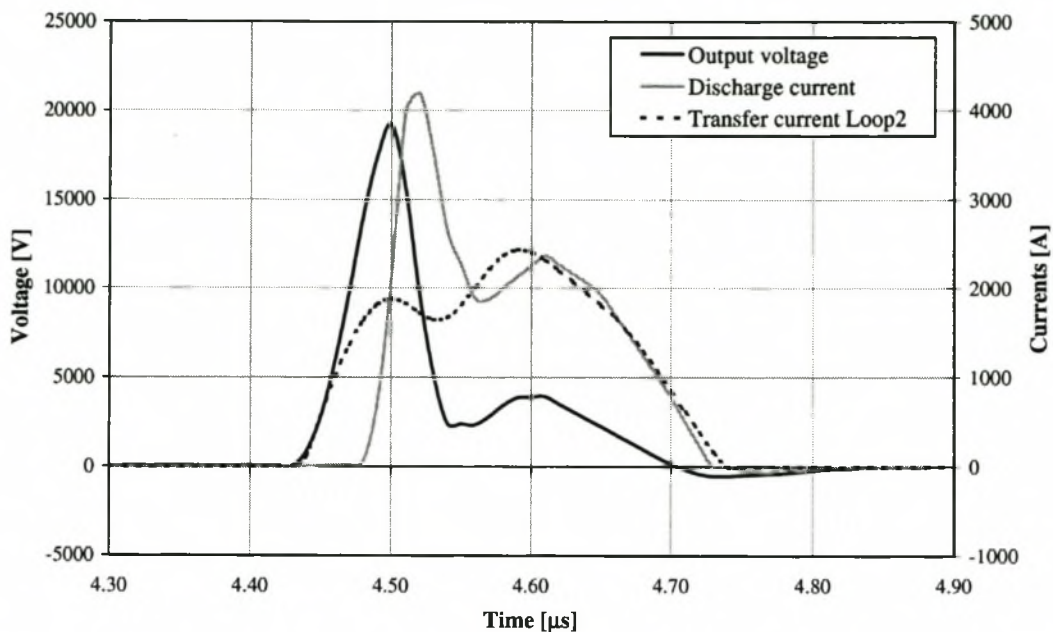


Figure 5-6: Close-up of simulated output voltage, discharge current and transfer current of Loop2.

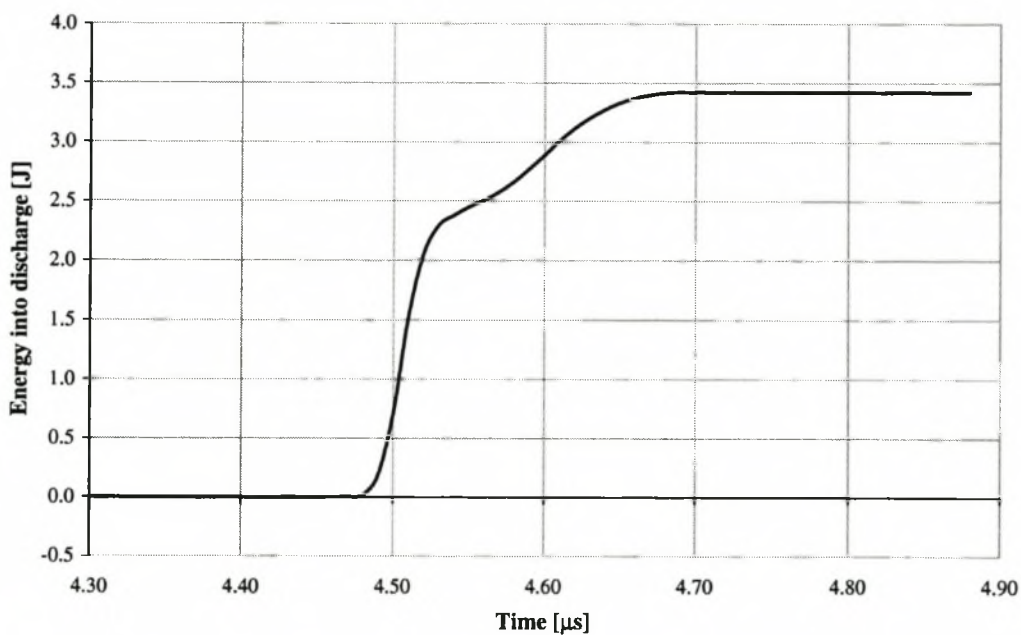


Figure 5-7: Energy deposited into discharge.

In general there is a close correlation between the waveforms measured in Chapter 4 and the simulated waveforms shown in Figures 5-6 and 5-7. This is an indication that the physical laser discharge model is a good approximation of the real discharge processes obtained in a CO₂ TEA laser. In Chapter 7 the simulated and measured output voltage waveforms are shown and compared (see Figure 7-4).

5.2 Primary switching unit construction

Aspects that have to be addressed during the construction of the primary switching unit include the construction of the IGBT drivers, charging of the initial storage capacitor and obtaining a transfer inductance that results in the correct transfer time of the primary C-C transfer loop.

5.2.1 Charging of the storage capacitor

The input storage capacitor C_0 (see Figure 5-8) is charged by a separate charging supply. During the charging cycle of the storage capacitor, the IGBT is off and the DC charging path is routed through the primary of the pulse transformer. The charging and pulse current magnetize the transformer core in opposite directions. Therefore, the charging current can simultaneously be used to reset the transformer core. Consequently, the total flux swing of the core is increased as discussed in Section 5.3.

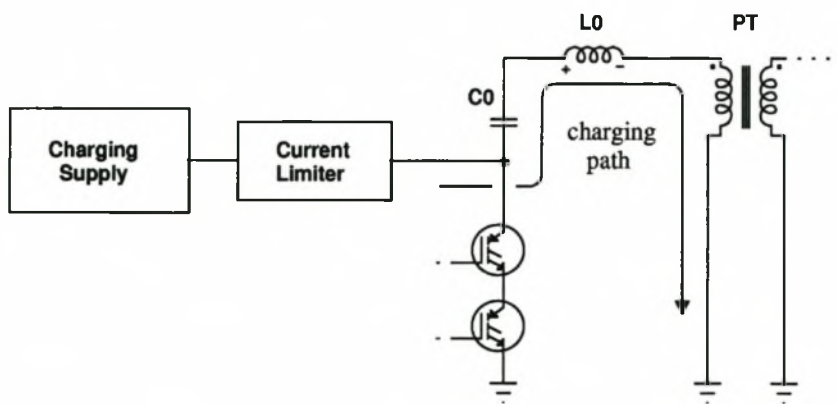


Figure 5-8: Charging supply protection.

It is important to notice that the charging supply is short circuited as soon as the IGBT is switched. This causes the output capacitance of the charging unit to discharge, resulting in large surge currents. In order to protect the charging supply a current limiting device has to be added as shown in Figure 5-8. The simplest way to limit the surge current is to make use of a decoupling inductor. However, a relatively large ferrite or iron powder core has to be used for the decoupling inductor, which can be very costly. A cheaper solid-state current limiter has been developed and is being used to protect the charging supply. The design is discussed in more detail in Appendix B.

5.2.2 IGBT drivers

The IGBTs are switched by special gate driver circuits. The drivers are electrically fully isolated by isolating DC-DC converters and opto-isolators. This reduces EMI (electromagnetic interference) and allows the floating IGBTs in a series-stacked configuration to be switched. The DC-DC converters supply power to the isolated gate driver stages. The IGBT driver unit is triggered via a fibre-optic cable further reducing the possibility of EMI. The basic layout of the IGBT drivers for two series-stacked IGBTs is shown in Figure 5-9 and a detailed circuit diagram is shown in Appendix B.

The driver unit circuit is constructed on a double-sided PCB where one side is used as a ground plane in order to reduce EMI and stray inductances in the gate driver circuit [27]. The IGBT driver unit has to be mounted as close as possible to the IGBT module to minimize the parasitic inductance of the connections between the gate drivers and the IGBT gate. The gate of each IGBT is protected by two back-to-back Zener diodes to prevent over-voltages and damage to the gate of the device. The parameters of the driver unit are summarized in Table 5-6.

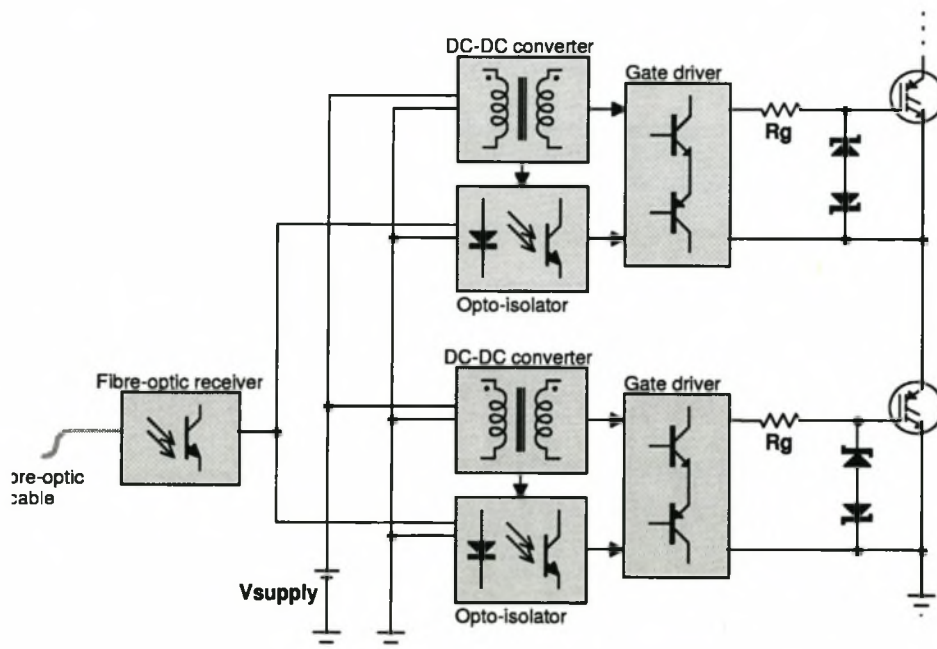


Figure 5-9: IGBT driver unit layout.

Gate resistor, R_g	2 Ω
On-state gate voltage, $V_{G(\text{on})}$	18 V
Off-state gate voltage, $V_{G(\text{off})}$	-6 V
Supply voltage, V_{supply}	12 to 18 V

Table 5-6: Design specifications of the IGBT driver unit.

The gate resistor was chosen as small as possible (see datasheets in Appendix C) to increase the switching speed of the IGBT, but without causing gate drive instabilities due to the gate inductor and internal gate capacitances as discussed in Chapter 3. Note that the applied off-state gate voltage is negative, resulting in a faster turn-off response and more immunity against EMI.

5.2.3 Transfer inductance

The C-C transfer loop of the primary switching unit includes the pulse transformer, which is used to step up the voltage to the needed excitation voltage. As discussed in Chapter 2 the total transfer inductance of the primary switching unit is comprised of the transformer leakage inductance and the external added inductance. The external inductance $L_{0,\text{ext}}$ that has to be added on the primary side of the pulse transformer to obtain the needed total transfer inductance is simply:

$$L_{0,\text{ext}} = L_0 - L_{0,\text{leak}},$$

where L_0 is the total needed transfer inductance given in Table 5-4 and $L_{0,\text{leak}}$ the total primary equivalent leakage inductance of the pulse transformer. As shown in Section 5.3 the constructed pulse transformer was measured to have a leakage inductance of $L_{0,\text{leak}} = 700 \text{ nH} \pm 5\%$. For a total transfer inductance of $L_0 = 2.18 \text{ }\mu\text{H}$ the externally added inductance must be $L_{0,\text{ext}} = 1.48 \text{ }\mu\text{H}$.

5.3 Pulse transformer design and construction

In this section the design and construction of the pulse transformer is discussed in more detail. In principle the design of pulse transformers for laser pulsed power supplies does not differ from switch mode power supplies, but in general the voltage ratings are higher and pulse durations are

shorter in laser pulsed power supplies. Consequently, the insulation of transformer windings and core saturation due to the high voltage ratings, as well as larger core losses due to the short transformed pulses pose additional problems, which have to be addressed.

5.3.1 Design outline

The design procedure for switch mode transformers is well documented [11][27] and can be adopted for pulse transformer design. A shortened version of a transformer design process proposed by N. Mohan, T.M. Underland and W.P. Robbins [27] is outlined in a flowchart shown in Figure 5-10. The proposed design procedure can be iterative as indicated in the flow chart. However, the transformer can most often be designed by a single pass through the design procedure by choosing the transformer core wisely. Another transformer design approach, which is not discussed in this thesis, is through frequency domain modelling [43] of the pulse transformer.

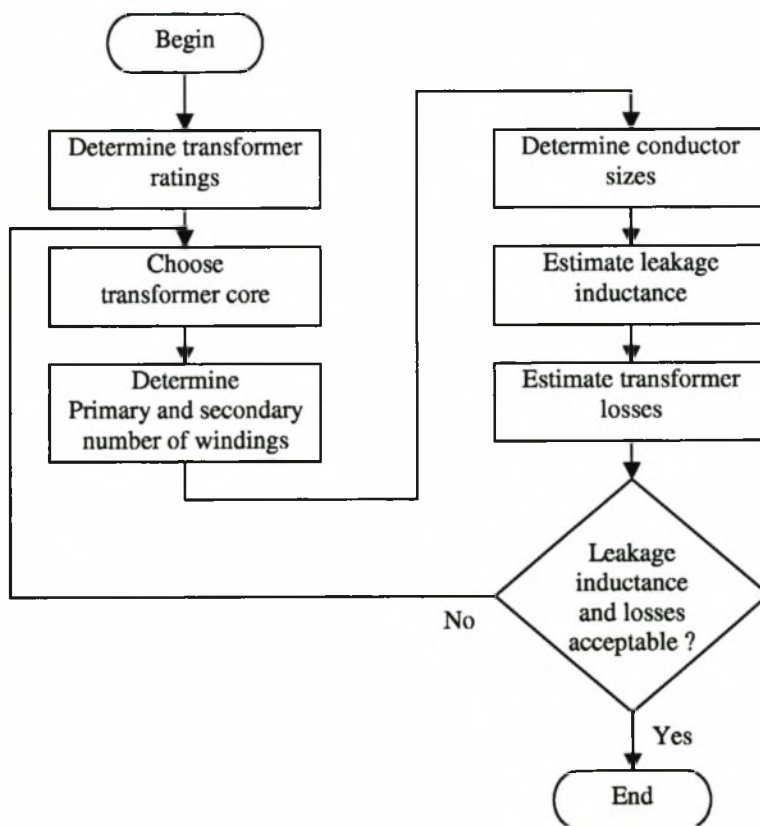


Figure 5-10: Flow chart of a pulse transformer design procedure.

Step 1 Determine transformer ratings

After completing the circuit design of the primary switching and MPC units (see Section 5.1) the resulting transfer current and pulse voltages at the transformer terminals are known. Other parameters that have to be determined are the maximum power throughput of the transformer and the pulse width of the applied current/voltage pulses.

Step 2 Choose transformer core

The core material can either be a ferrite material or a laminated iron core, but it is advisable to use laminated iron cores in high-voltage applications as discussed in Section 2.4.3. After choosing the core material the appropriate core size can be selected which will be able to handle the maximum power throughput as calculated in step 1.

Step 3 Determine primary and secondary number of turns, N_p and N_s

The minimum number N_p of primary turns, which will prevent core saturation can be calculated using Equation 2.42. Consequently, the secondary number of turns N_s can be calculated using the turns ratio determined in the primary switching unit design in Section 5.1.

Step 4 Determine conductor sizes

There are different approaches in choosing the transformer conductor size, but the simplest way is to choose a conductor size which will result in an acceptable current density. The large amount of electric insulation needed in high-voltage pulse transformers reduces the cooling of the transformer windings and a current density of between 2 and 4 A/mm is acceptable. The winding configuration (e.g. solid copper foil, Litz wire, etc.) is chosen to minimize the skin effect [27] for fast voltage pulses. Knowing the winding configuration, the copper fill factor p_{Cu} can be estimated and it can be determine whether the transformer windings will fit into the winding window of the transformer core.

Step 5 Estimate leakage inductance

The leakage inductance can be calculated using Equation 5.1 (see next section) and should not exceed the total transfer inductance of the C-C loop into which the transformer is inserted.

Step 6 Estimate transformer losses

Using equations given in Section 2.4.4 the transformer losses can be estimated. If the losses are too high the transformer has to be re-designed, using a different core and/or core material.

5.3.2 Design and construction

Transformer ratings

As shown in Figure 5-2 the pulse transformer is inserted into the C-C transfer loop of the primary switching unit. Using previous design results (see Table 5-4) the ratings of the pulse transformer can be specified and are shown in Table 5-7. The primary and secondary RMS currents were calculated using Equation 2.21.

Turns ratio, a	13
Peak primary pulse current, $I_{p,peak}$	1405 A
Primary switching unit charging voltage, V_0	2430 V
Pulse transfer time, τ	4.3 μ s
RMS primary current, $I_{p,RMS}$ @ $f_{rep} = 600$ Hz	50.4 A
RMS secondary current, $I_{s,RMS}$ @ $f_{rep} = 600$ Hz	3.88 A
Maximum allowable leakage inductance	1.25 μ H
Pulse energy	4.65 J
Maximum power throughput @ $f_{rep} = 600$ Hz	2790 W

Table 5-7: Design specifications of the pulse transformer.

Core selection

As already mentioned, in order to minimize the transformer size for high-voltage applications a core material with a large saturation magnetic flux density is needed (see Section 2.4.3). To prevent saturation of the transformer core a larger magnetic flux swing will result in smaller core cross-sections and/or less turns. Consequently, laminated iron cores are considered due to their relative large saturated flux density (between 1.2 and 1.7 T), but the lamination thickness of the core has to be small in order to reduce eddy current losses induced by fast transformer voltage pulses.

A laminated iron core with a lamination thickness of 50 μ m is used. A diagram of the core is shown in Figure 5-11 and a summary of the core dimensions and parameters is given in Table 5-8. The core consists of two U-type cores, which are placed face-to-face.

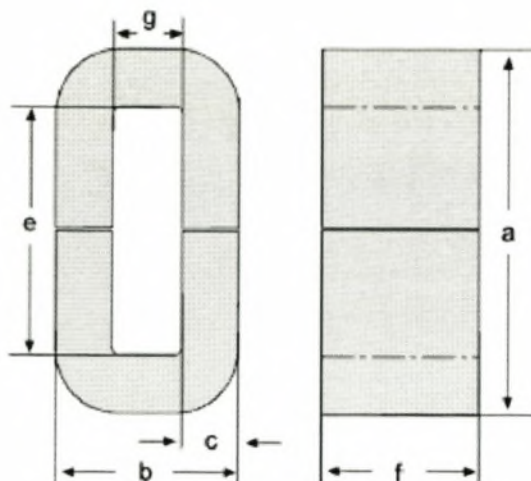


Figure 5-11: U-type core assembly.

Saturation flux density, B_{sat}	1.7 T
Dimensions:	
a	88.9 mm (3.4 in)
b	50.8 mm (2.0 in)
c	12.7 mm (0.5 in)
e	63.5 mm (2.5 in)
f	25.4 mm (1.0 in)
g	25.4 mm (1.0 in)
Winding window cross-section, A_w	16.1 cm ²
Core cross-section, A_{core}	3.2 cm ²

Table 5-8: Transformer core dimensions and parameters.

Number of primary and secondary turns

As discussed in Section 5.2.1 the charging current of the primary storage capacitor flows through the primary of the pulse transformer. Furthermore, charging current and pulse current flow in opposite directions. The charging current effectively resets the transformer core. Just before the IGBT switches to generate the primary voltage pulse the magnetic flux density in the core should be equal to the reverse remnant magnetic flux density, with $B_{\text{core}}(\text{reset}) \cong -0.5 \text{ T}$. The allowable change in the core flux density during the transfer of the pulse is therefore $\Delta B = B_{\text{sat}} - B_{\text{core}}(\text{reset}) \cong 2.3 \text{ T}$. Using Equation 2.40 the number of primary and secondary turns can be calculated.

N_p	8
$N_s @ a = 13$	104

Table 5-9: Number of turns for the primary and secondary transformer windings.

The calculated number of primary turns is 7, but an additional turn is added to allow a small amount of headroom in the magnetic flux swing. The resulting flux change due to 8 turns is $\Delta B = 2.0$ T. Additionally, the voltage difference per turn is $V_N = 303$ V @ $V_0 = 2422$ V.

Winding configuration

The most important consideration during the choice of the primary and secondary winding configurations is the maximum RMS transformer current and the skin effect of the conductor current:

Skin depth, δ : As shown in Table 5-7 the transfer time of the pulses applied to the transformer in the primary switching loop is $\tau = 4.3$ μ s, which results in a bandwidth of between 200 and 300 kHz. The resulting skin depth δ is approximately 0.15 mm [13][27].

Current density, J : The RMS current density J_{RMS} in the transformer windings should not exceed between 3 and 4 A/mm² [4]. In many switch mode transformers the current density can be higher, but due to the high secondary transformer voltages (up to 30 kV) it was decided to encapsulate the transformer windings. The encapsulation and insulation material used between winding layers has a poor thermal conductivity and increases the thermal resistance of the transformer windings to the surrounding environment.

It was found that the best winding configuration for the primary winding is a solid ribbon conductor due to the relatively high primary RMS current of $I_{p,\text{RMS}} = 50.4$ A (see Table 5-7). The ribbon conductor consists of a copper strip with a maximum thickness of twice the skin depth. Taking insulation into account the copper fill factor for the primary ribbon conductor is approximately $p_p = 0.5$. Details about the primary winding configuration are shown in Table 5-10.

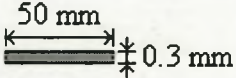
Conductor geometry	Solid ribbon 
Conductor cross-section, $A_{N,p}$	15.0 mm ²
Current density, $J_p @ I_{p,RMS} = 50.4$ A	3.4 A/mm ²
Copper fill factor, p_p	0.4
Primary winding window, $A_{w,p}$	3.0 cm ²
Average length of single winding, l_p	10.2 cm

Table 5-10: Primary winding configuration.

A ribbon cable, consisting of several individual enamelled copper wire strands placed side by side is used for the secondary winding. Litz wire was not considered due to a poor fill factor. The radius of a single strand of the ribbon cable should not exceed the skin depth of 0.15 mm. The fill factor for the chosen conductor geometry and taking insulation into account is approximately $p_s = 0.2$. Details about the secondary winding configuration are shown in Table 5-11.

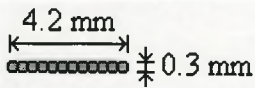
Conductor geometry	14-Wire ribbon 
Conductor cross-section, $A_{N,s}$	0.99 mm ²
Current density, $J_s @ I_{s,RMS} = 3.88$ A	3.9 A/mm ²
Copper fill factor, p_s	0.2
Primary winding window, $A_{w,s}$	5.1 cm ²
Average length of single winding, l_s	22.9 cm

Table 5-11: Secondary winding configuration.

For both the primary and secondary windings the current density is below 4 A/mm² and is therefore acceptable. The total area occupied by the primary and secondary windings is $A_{w,p} + A_{w,s} = 8.1$ cm², which is only 50 % of the total winding window cross-section A_w , leaving sufficient space for the transformer bobbin and winding encapsulation. A diagram of the transformer windings is shown in Figure 5-12.

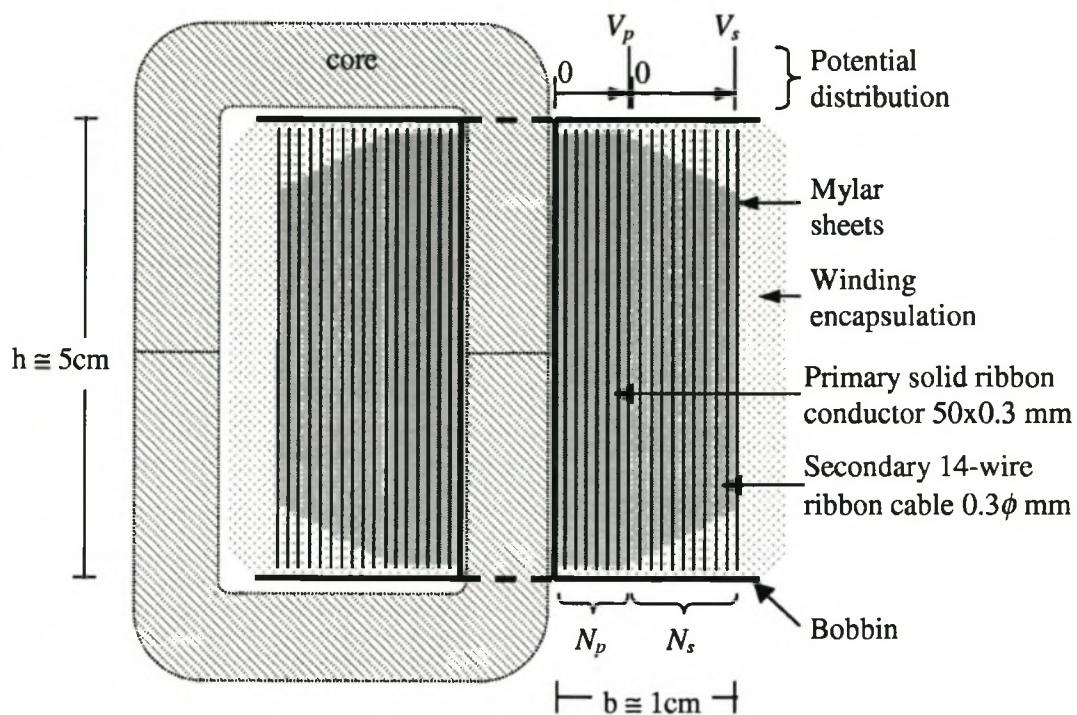


Figure 5-12: Cross-sectional diagram of the pulse transformer.

In high-voltage transformers insulation is an important issue. As mentioned earlier, the transformer is encapsulated in special insulating resins, with which inter-winding flashover and corona formation can be prevented. For the primary winding each winding layer consists of a single ribbon winding and the peak inter-layer potential difference is therefore equal to the potential difference per winding, $V_N = 303$ V. The inter-layer insulation of the primary winding is thus not too critical. For the construction thin Mylar sheeting or any other type of plastic sheeting that can handle temperatures up to 100 °C can be placed between the primary winding layers. The secondary winding is wound taper in order to increase the insulation clearance for the higher voltage windings. The maximum number of secondary turns per layer is 11 and the maximum secondary inter-layer potential difference is thus $22 \cdot V_N = 6700$ V. Special care must be taken to insulate the secondary layers. This can be achieved by placing a layer of Mylar sheeting (100 to 200 μm thickness) between the secondary layers.

Transformer leakage inductance

Mohan, et al. [27] gives an estimated solution for the integral Equation 2.39 for the winding

configuration shown in Figure 5-12:

$$L_{\text{leak}} \cong \frac{\mu_0 N_p^2 l b}{3h}, \quad 5.1$$

where l is the average length of a single winding, b the total radial width and h the total height of the primary and secondary windings (see Figure 5-12). Using the above formula the estimated leakage inductance of the designed transformer is $L_{\text{leak}} \cong 800 \text{ nH}$ ($l = 11 \text{ cm}$, $b = 1 \text{ cm}$, $h = 5 \text{ cm}$). This is acceptable, because it is less than the total transfer inductance of $2.18 \text{ }\mu\text{H}$ calculated for the primary switching loop (see Table 5-4).

Transformer losses and efficiency

The analysis of the transformer losses in Chapter 2 can now be used to calculate the transformer conduction and core losses.

Hysteresis losses: The hysteresis losses are difficult to calculate, because the exact BH-curve has first to be measured. Normally, the hysteresis losses for iron cores are specified in the core data sheets. For a complete magnetization cycle the specific energy loss due to hysteresis is approximately $E_{\text{hys,sp}} \cong 5 \text{ W/kg}$. The total core weight (of two U cores) is $m_{\text{core}} = 0.54 \text{ kg}$.

Eddy current losses: The resistivity of core iron is approximately $\rho_{\text{core}} = 4 \cdot 10^{-7} \text{ }\Omega\text{m}$ [27]. Using Equation 2.49 ($\Delta B = 2.0 \text{ T}$, $f_{\text{rep}} = 600 \text{ Hz}$, $d = 50 \text{ }\mu\text{m}$, $\tau = 4.3 \text{ }\mu\text{s}$) the specific eddy current loss can be calculated with $P_{\text{ec,sp}} = 1.82 \cdot 10^6 \text{ W/m}^3$ (total core volume is $\text{Vol}_{\text{core}} = 70.2 \text{ cm}^3$).

Conduction (copper) losses: From the conductor cross-sections, average wire length and current densities specified in Tables 5-10 and 5-11 the conduction losses can be calculated using Equation 2.55 ($\rho_{\text{Cu}} = 2.2 \cdot 10^{-8} \text{ }\Omega\text{m}$).

A summary of the transformer losses and efficiency at the maximum repetition rate, $f_{\text{rep}} = 600 \text{ Hz}$, and power throughput, $P = 2790 \text{ W}$, is given in Table 5-12.

Hysteresis losses, P_{hys}	1.6 W
Eddy current losses, P_{ec}	128 W
Primary conduction losses, $P_{c,p}$	3.1 W
Secondary conduction losses, $P_{c,s}$	3.5 W

Table 5-12: Summary of transformer losses.

The total estimated transformer losses are approximately 136 W resulting in an efficiency of 95.1 %.

Thermal considerations and cooling

The chosen transformer core has typically a thermal resistance in air (core to ambient) of $R_{\theta,\text{core}} = 2.74 \text{ }^{\circ}\text{C}/\text{W}$. For the core losses calculated in the previous section this will result in a temperature difference of $\Delta T \cong P_{\text{losses}} R_{\theta,\text{core}} = 350 \text{ }^{\circ}\text{C}$. This is much too high since a temperature difference of not more than $\Delta T = 100 \text{ }^{\circ}\text{C}$ is desirable. It is not possible to lower the transformer losses dramatically, because the eddy current losses contribute more than 80% of the total transformer losses. The eddy current losses can only be reduced by using a smaller core, thinner laminations and/or a longer current pulse. None of the above solutions are feasible, because cores with thinner laminations are not easily available and a longer current pulse will necessitate more MPC material, which is costly. The only solution is to use oil cooling which will also improve insulation between the external transformer terminals. Generally it is not desirable to use oil cooling in conjunction with lasers and laser optics, because of possible leaks and spills that can destroy sensitive optics. Oil cooling will however allow a much more compact design of both the pulse transformer and the magnetic pulse compression circuit, which will be discussed in the next section.

5.3.3 Transformer measurement

Open and short-circuit tests [28] were performed on the pulse transformer to experimentally determine the leakage inductance and magnetization impedance. The results obtained are summarized in Table 5-13. Note that all measured values are referenced to the primary side of the transformer.

Total leakage inductance, L_{leak}	700 ± 20 nH
Magnetization inductance, L_{mag}	80 ± 5 μ H
Inter-winding capacitance, C_N	5 nF ± 2 nF
Transformer ratio, a	13.05 ± 0.05

Table 5-13: Summary of transformer measurements.

The measured leakage inductance is close to the estimated value. Furthermore, the magnetization inductance is much larger than the leakage inductance and the inter-winding capacitance is much smaller compared to the capacitors (approx. $1.67 \mu\text{F}$) in the C-C transfer loop. Thus, the pulse transformer satisfies the condition that the magnetization impedance must be much larger than the transfer impedance of the C-C transfer loop, i.e. $i_{\text{mag}} \ll i_t$, as discussed in Section 2.4.1.

5.4 MPC unit construction

During the construction of the MPC unit special emphasis was placed on minimizing the size and simplifying the assembly of the MPC unit. A modular construction approach was used. The different components of the MPC unit, saturable inductors and capacitor banks, were pre-assembled separately as modules. The complete MPC unit can then be constructed quickly and easily. The construction of the saturable inductor modules and the final geometry of the MPC unit are discussed in the following sub-sections.

5.4.1 Saturable inductor module assembly

As already mentioned, the saturable inductors were pre-assembled, and the pre-assembled modules can simply be bolted to the final MPC assembly. The assembly details of a saturable inductor with one core is shown in Figure 5-13.

The saturable core is placed between two PCBs. The PCBs are used to construct the inductor windings (not shown in Figure 5-13) by etching part of the windings onto the PCBs and soldering connection wires between the top and bottom PCBs to complete the winding configuration. The core is supported by flat core support plates that slide into grooves in the support pillars. The core

support plates also provide a 3 mm spacing between the PCB plates and the core, to provide insulation between the etched windings on the PCBs and the inductor core. The top and bottom PCBs are simply bolted to the support pillars. Special mounting plates are bolted onto the top and bottom of the inductor assembly and are used to mount the inductor modules to the final MPC unit. The assembly of a MPC module with two saturable cores is similar to the assembly shown in Figure 5-13, except the support pillars are elongated and additional core support plates are added to hold an additional core. An additional advantage of the proposed inductor module assembly is that support pillars, core support plates, spacers, mounting plates and PCBs can be manufactured in large quantities and assembled easily and quickly. Note that holes in the middle of the mounting plates and PCBs are provided for the reset winding, which consists of a single turn fed through the centre of the inductor module.

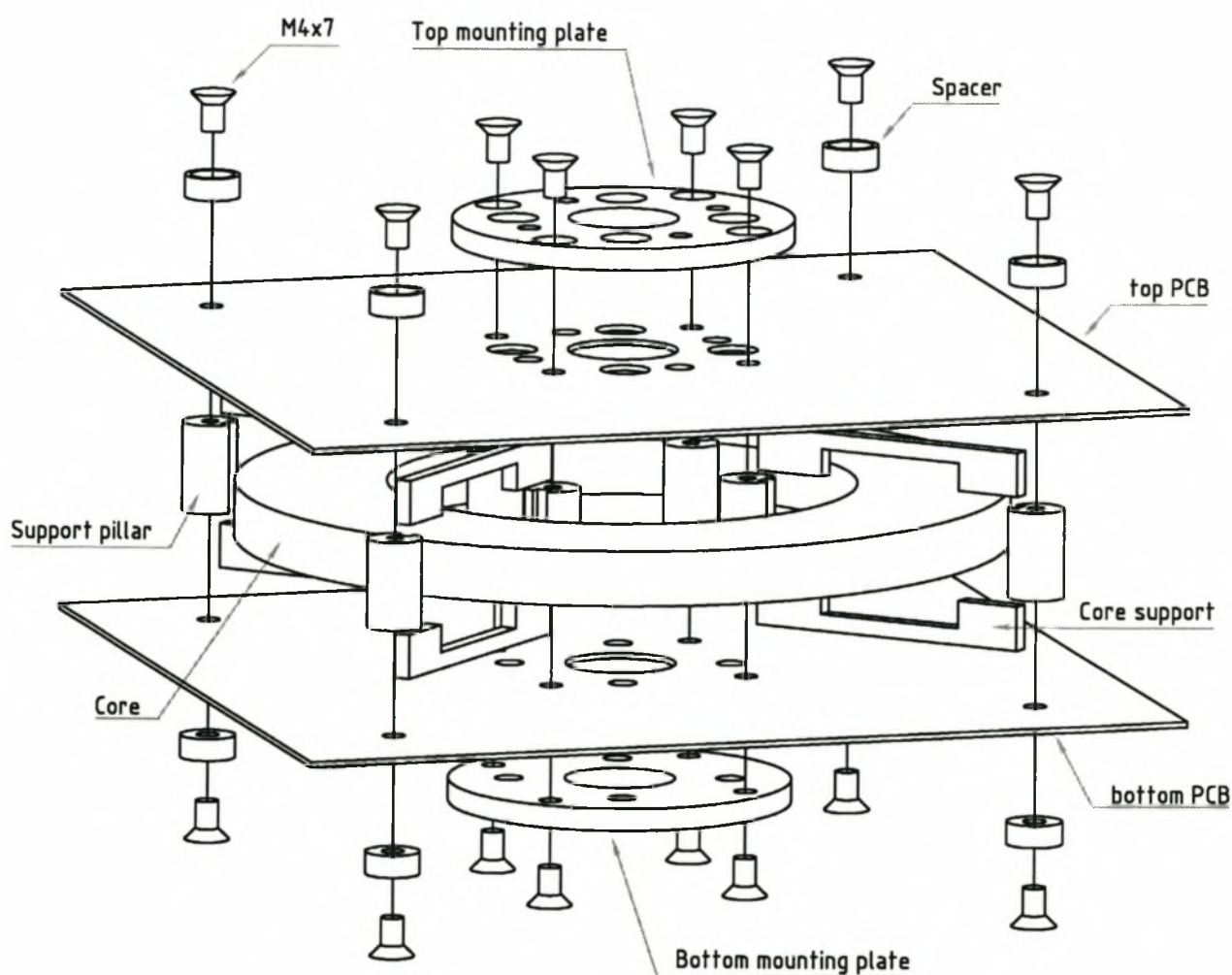


Figure 5-13: Assembly of a MPC inductor module.

After the inductor module has been assembled connection wires are soldered between the top and bottom PCBs to complete the inductor winding. To illustrate the method of using PCBs to construct inductor windings the PCB artwork of the 15-turn MPC inductor of the second MPC stage is shown in Figure 5-14. The artwork of the top and bottom PCB's are identical, but are rotated 90° with respect to each other. The winding assembly consists out of four paralleled 15-turn windings each wound around one quarter of the inductor core. The windings terminate 90° apart and are therefore well separated with good electrical insulation between the inductor terminals.

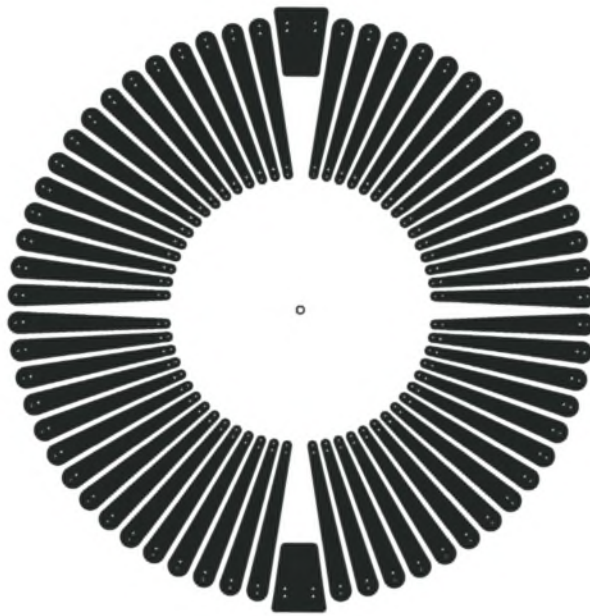


Figure 5-14: PCB artwork used for the winding configuration of MPC inductors.

5.4.2 MPC unit assembly

The complete MPC unit assembly is enclosed in an oil tank and placed on top of the laser head. Due to the high voltages the MPC unit has to be submerged in transformer oil to improve the electric insulation. Furthermore, the transformer oil improves the cooling of the MPC inductor cores.

Usually the MPC unit layout is based on a coaxial design in order to minimize the parasitic (external) inductance in the MPC C-C transfer loops. This could otherwise result in poor compression ratios. The coaxial layout is often used in the excitation of Excimer lasers where very

fast voltage rise times (< 80 ns) are needed and the parasitic inductances must be very small. However, in CO₂ TEA lasers the voltage rise-times are less critical (see Chapter 4) and different approaches in the MPC unit layout can be used.

It was decided to use a rectangular geometry to construct the MPC unit. The basic electrical and mechanical layout of the MPC assembly is shown in Figure 5-15. The two MPC stages are stacked vertically and the capacitors of the MPC stages are connected on either side of the MPC inductors. The last stage is located at the bottom of the MPC stack and rests on top of the feed-throughs that connect the peaking capacitor bank to the laser electrodes. The mounting brackets and mounting plates also act as electrical connections between the capacitors and inductors of the MPC assembly. A three-dimensional model of the complete MPC assembly is shown in Figures 5-16 and 5-17.

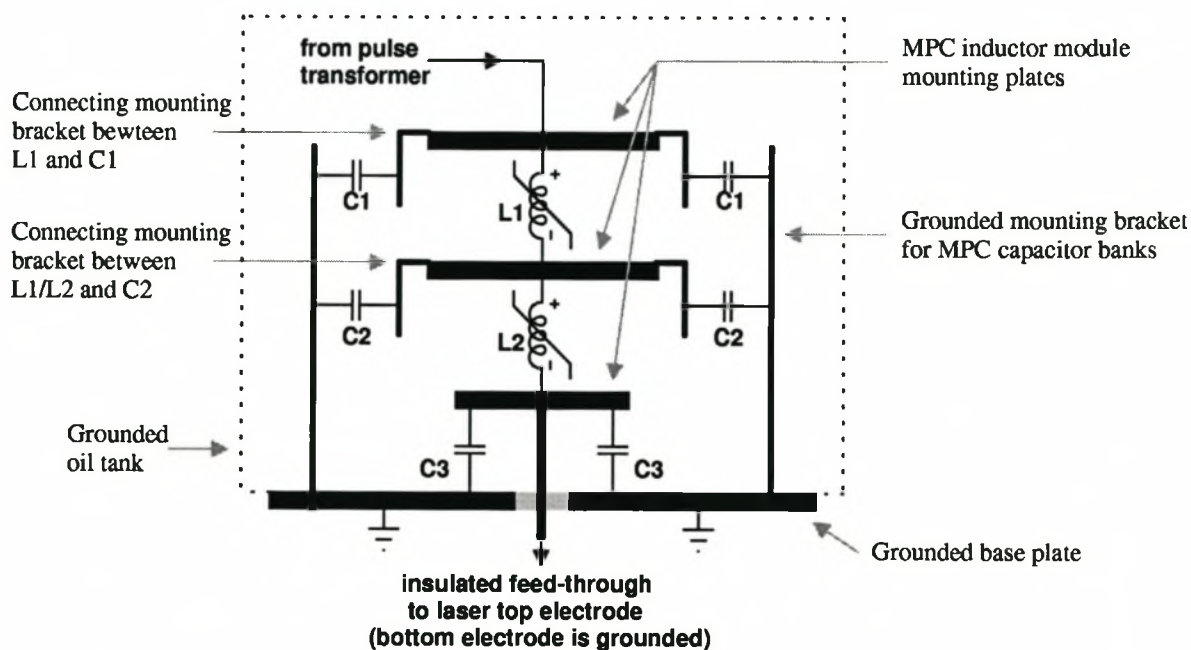


Figure 5-15: Basic electrical and mechanical layout of the MPC unit assembly.

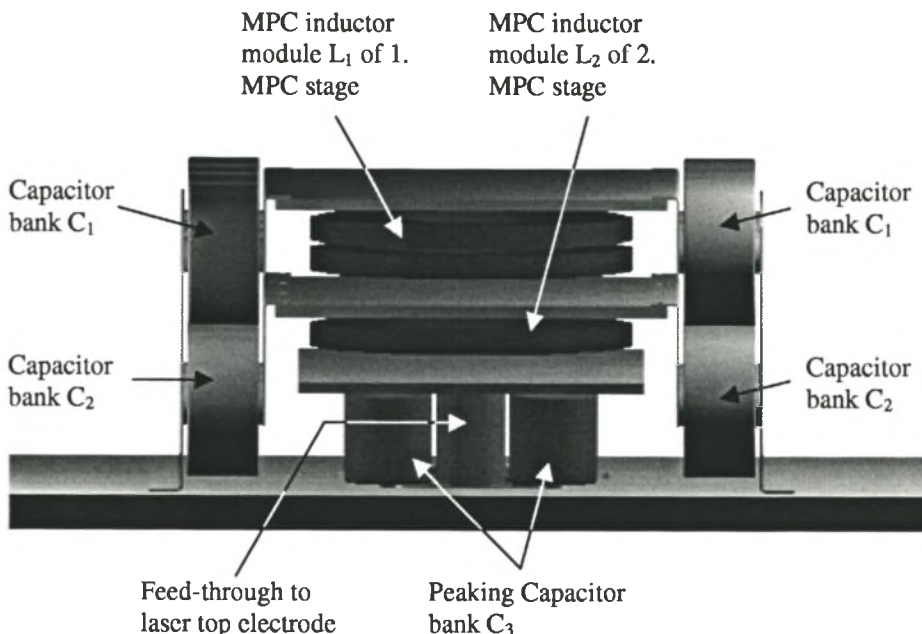


Figure 5-16: Three-dimensional model of complete MPC unit assembly (front view).

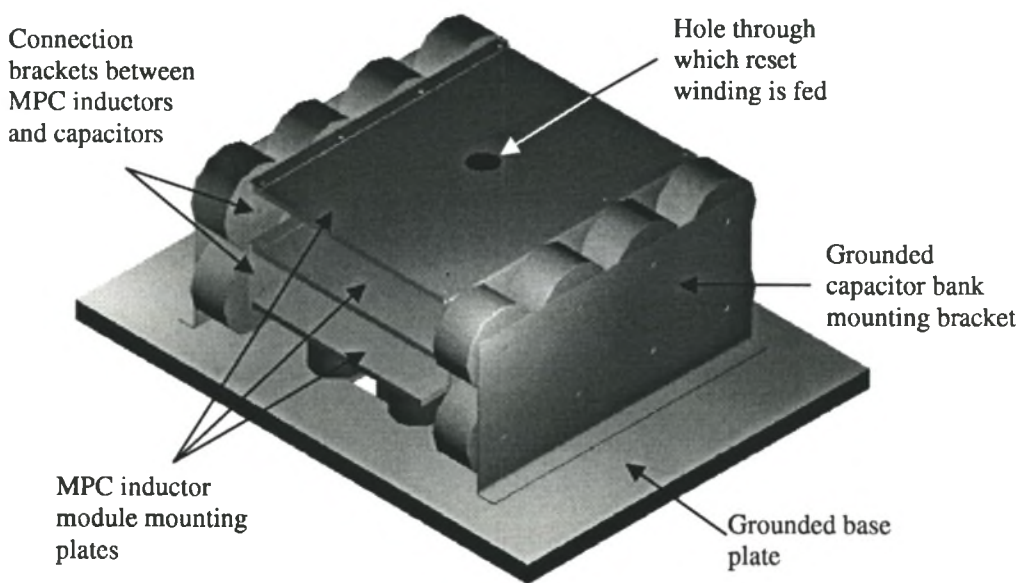


Figure 5-17: Three-dimensional model of complete MPC unit assembly (elevated view).

The transfer capacitors of the MPC unit, C_1 , C_2 and C_3 are constructed as capacitor banks by paralleling high-voltage high-performance ceramic capacitors (TDK high-voltage capacitors) to obtain the correct capacitance values as specified in Table 5-5. The two capacitor-bank-assemblies on either side of the MPC inductors, consisting of the ceramic capacitors banks and capacitor

mounting brackets can also be pre-assembled. To complete the MPC unit assembly the capacitor banks are bolted to the grounded base plate and the mounting plates of the inductor modules .

To determine the exact parasitic inductances of the proposed MPC layout the exact current distribution in the MPC unit during pulse compression must be known, which is practically impossible. As a first-order estimate, the parasitic inductance of the MPC stages can be approximated by rectangular tubes as shown in Figure 5-18. The two loops created by C_1 , C_2 and L_1 can be approximated as two identical rectangular tubes each with an inductance L_{tube1} . Similarly, the two loops created by C_2 , C_3 and L_2 can also be approximated as two rectangular tubes with inductance L_{tube2} . The inductance of a tube with length l and cross section A is given by [13]:

$$L_{\text{tube}} = \mu_o \frac{A}{l} \quad (5.2)$$

The two tube inductances for each MPC stage are effectively in parallel and $L_{\text{par1}} = \frac{1}{2}L_{\text{tube1}}$ and $L_{\text{par2}} = \frac{1}{2}L_{\text{tube2}}$, where L_{par1} and L_{par2} are the parasitic inductances of the first and second MPC stages, respectively. For the two constructed MPC assemblies the cross-sections of tube 1 and tube 2 are approximately $A_1 = 65 \text{ cm}^2$ and $A_2 = 70 \text{ cm}^2$, respectively. The length of the MPC unit is approximately $l = 20 \text{ cm}$. Using Equation 5.2 the parasitic inductances of the first and second MPC stages can be estimated, with $L_{\text{par1}} \cong 20 \text{ nH}$ and $L_{\text{par2}} \cong 22 \text{ nH}$. These results are close to 20 nH estimated for the MPC design (see Table 5-4).

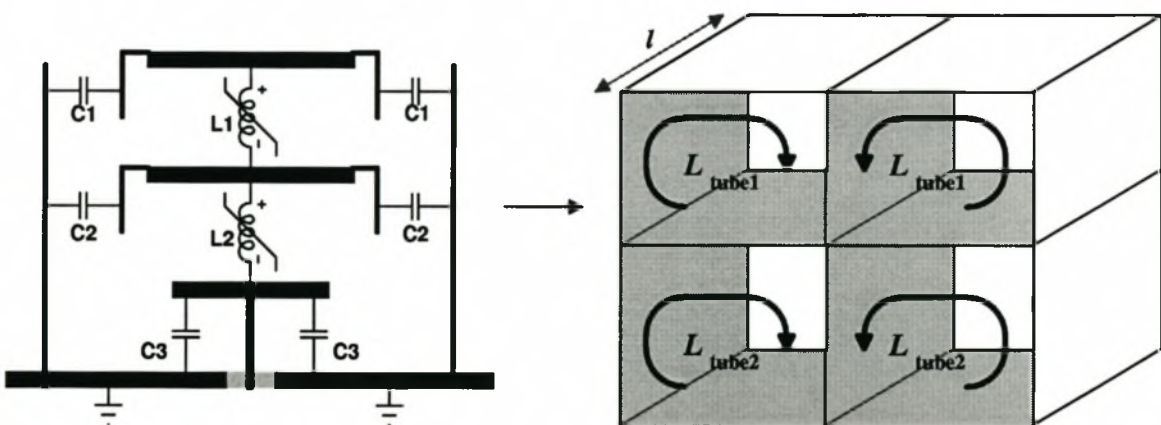


Figure 5-18: Approximation of MPC stage parasitic inductance for rectangular MPC unit layout.

Chapter 6

Reliability

Before the pulsed power supply designed in the previous chapter can be finally implemented it is important to determine the reliability of the proposed IGBT (SKM300GB174D from Semikron). The reliability of the IGBT includes the following:

- The IGBT should have a long lifetime, which is comparable or even better than the lifetime of Thyratrons ($>10^9$ shots)
- The IGBT should withstand fault conditions (e.g. laser arcing, etc.)

In this chapter the experimental test set-up for determining the lifetime of an IGBT in a pulsed power supply is discussed as well as the results obtained from the lifetime tests are presented. The second part of this chapter also deals with the fault handling capability of an IGBT including protection circuits that can be used to improve the overall reliability of the IGBT switch. Finally, the effect of EMI is discussed and design considerations are identified with which EMI can be reduced.

6.1 Lifetime testing

As discussed previously the IGBT switches short pulses with a large peak current, but with a relatively small average current. It is therefore economical advantageous if the average current rating of the IGBT can be less than peak pulse switching current. In the design proposed in the

previous chapter the peak switching current of the IGBT is between 4 and 5 times the rated current of the device. Little information is available on the reliability and lifetime of IGBTs under these conditions. In this section a test set-up for lifetime testing is discussed.

During lifetime testing the device under test (DUT), in this case the IGBT, has to be subjected to similar conditions as would be obtained during normal operation in a laser pulsed power supply. Normal operation refers to operational conditions without circuit errors and fault conditions, i.e. no flash-over on the high voltage side of the circuit and no unstable discharges. The aim is to switch the IGBT for up to 10^9 times. For each switching cycle the IGBT is subjected to current and voltage waveforms, which are similar to waveforms obtained under normal operating conditions.

Additional useful information can be obtained if the IGBT is also monitored during the lifetime testing in order to determine changes in the characteristics of the device. Changes in the IGBT's electrical and thermal characteristics can be used to determine degradation of the IGBT's performance before the device fails [34].

6.1.1 Test set-up

As mentioned earlier the experimental test set-up for lifetime testing should provide switching voltage and current waveforms similar to waveforms obtained in the proposed pulsed power supply. The simplest circuit that can be used to obtain the needed switching conditions is a damped RLC (resistor R , inductor L and capacitor C) circuit and a diagram of the test set-up for lifetime testing is shown in Figure 6-1.

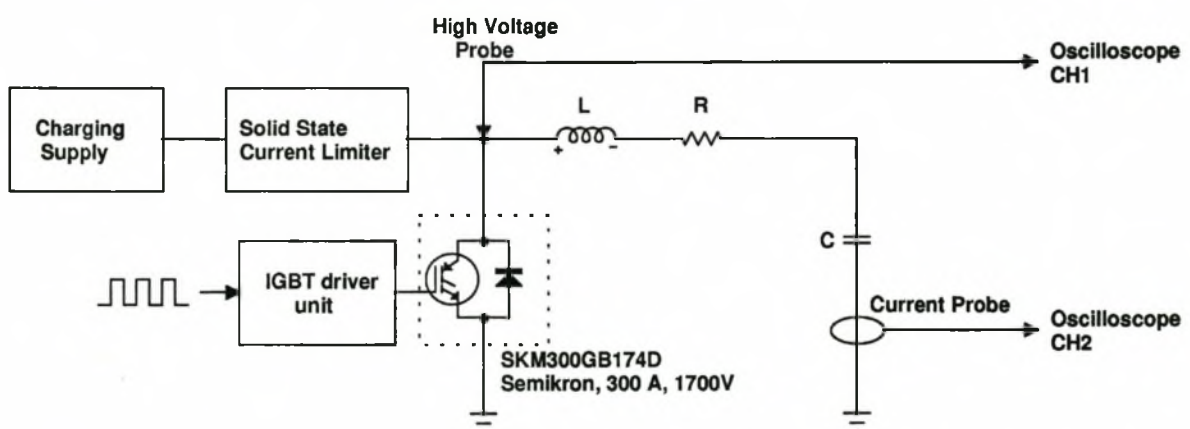


Figure 6-1: Experimental set-up for IGBT lifetime testing.

The RLC circuit is very similar to the C-C transfer circuit discussed in Chapter 2. The capacitor C of the RLC circuit is charged by a high-voltage charging supply to an initial voltage V_0 . A current limiter is used to protect the charging unit against a short circuit during the turn-on cycle of the IGBT as discussed in Chapter 5. As soon as the IGBT is turned on by the IGBT driver unit, the RLC circuit can freely oscillate through the IGBT. It is important to note that the IGBT module has a built-in reverse diode and the current through the IGBT module can therefore reverse. Consequently, while the IGBT is turned on the IGBT module acts as a bi-directional switch. The switching voltage and current waveforms are monitored by a high voltage probe (Tektronix P6015A high voltage probe, X1000 and 70 MHz bandwidth) and a current probe (Pearson 1025 current probe, rise-time 100 ns), respectively. The component values of the RLC loop are now chosen to obtain a switching current waveform that best matches the simulated sinusoidal current pulse shown in Figure 5.4.

To determine the needed RLC component values the current response of the RLC loop has to be determined. The response is identical to the response of a damped C-C transfer loop (see Equation 2.1) except that only a single capacitor is used instead of two:

$$i_{\text{IGBT}}(t) = \frac{V_0}{\omega L} e^{-\alpha t} \sin(\omega t), \quad (6.1)$$

$$\text{with} \quad \alpha = \frac{R}{2L} \quad \text{and} \quad \omega = \sqrt{\frac{1}{LC} - \left(\frac{R}{2L}\right)^2}.$$

Note that the switching voltage in Chapter 5 is specified for two series-stacked IGBTs where the voltage is shared equally between the two IGBTs. For the lifetime tests only one IGBT at a time is tested and the switching voltage per IGBT is half the total switching voltage specified in Chapter 5. To match the response of the RLC circuit, the RLC components must be chosen to obtain a peak switching current of $I_{\text{IGBT,peak}} \cong 1405$ A at a charging voltage of $V_0 \cong 1215$ V with an effective transfer time of $\tau \cong 4.3$ μs . Furthermore, to obtain a current pulse the RLC oscillation must be sufficiently damped so that only the first half oscillation cycle is prominent and any further oscillations are suppressed. The chosen RLC component values are specified in Table 6-1.

R	0.4Ω
L	780 nH
C	$3.8 \mu\text{F}$

Table 6-1: Circuit values for lifetime test set-up.

The measured IGBT current waveforms of the RLC circuit as compared to a current waveform obtained in the proposed pulsed power supply is shown in Figure 6-2. The RLC current waveform is approximately 30% longer than typical pulses obtained in the pulsed power supply due to the relatively strong damping. The peak current and current rise-time are well matched. The oscillation of the RLC current cannot be completely eliminated and after the positive current pulse the current overshoots and a relatively small negative current pulse is obtained. The overshoot of the negative current pulse is approximately -300 A . This is within the current rating of the IGBT's internal reverse diode and should therefore not pose a problem.

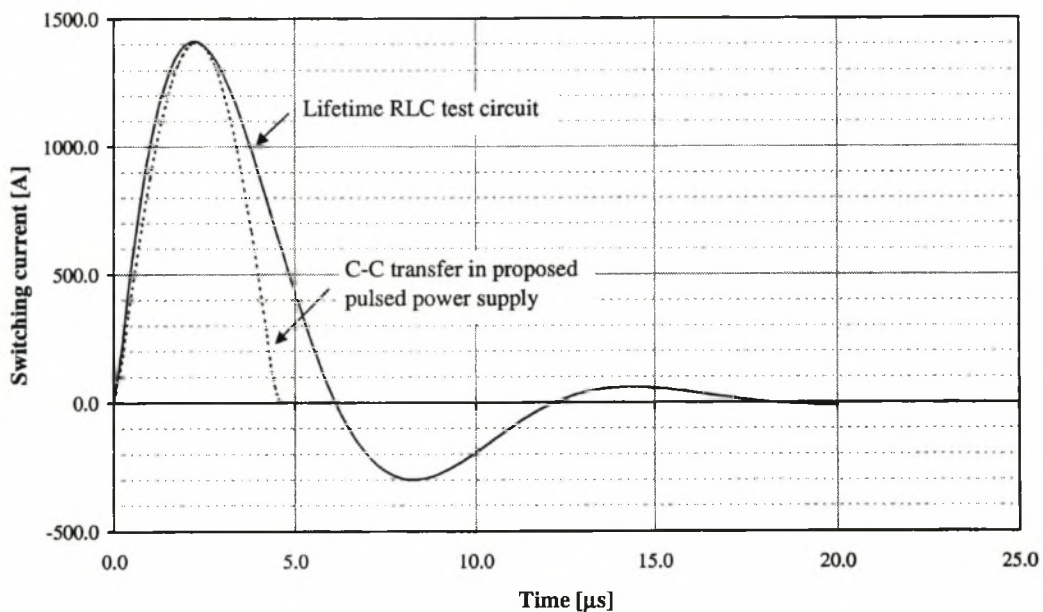


Figure 6-2: Current waveform obtained for IGBT lifetime testing.

6.1.2 Measurement of IGBT characteristics

As discussed in Chapter 3 the switching of pulses with large peak currents can lead to the formation of cracks inside the IGBT due to thermal stresses. The formation of cracks mainly occurs at

material interfaces, i.e. between layers inside the IGBT's silicone wafer and between the silicone wafer and solder contacts [16]. Degradation of the IGBT due to crack formation changes the IGBT characteristics over time, resulting in an increase in thermal resistance and on-state voltage drop [34]. As already mentioned, measurement of the IGBT characteristics during the lifetime tests can give an indication whether the switching conditions induce degradation in the device before the IGBT completely fails. Measurement procedures for measuring the thermal resistance and electrical characteristics of the IGBT are discussed in the remainder of this sub-section.

Thermal resistance

In principle to determine the steady state junction-to-case thermal resistance R_{thjc} power has to be dissipated inside the device and the difference ΔT_{jc} between the internal junction temperature T_j and the external case temperature T_c of the IGBT has to be measured. The thermal resistance as used in Equation 3.24 is defined as

$$R_{thjc} = \frac{\Delta T_{jc}}{P_{IGBT}}, \quad (6.2)$$

where P_{IGBT} is the power dissipated in the IGBT. It is practically impossible to directly measure the junction temperature of the IGBT with a temperature probe. Fortunately the internal reverse diode of the IGBT module is located closely to the IGBT and the temperature dependence of the diode forward voltage drop can be used to measure the internal wafer temperature. The wafer temperature can be assumed to be equal to the junction temperature of the IGBT [33]. In the following paragraphs a procedure for measuring the thermal resistance of an IGBT is discussed and the measurement set-up is shown in Figure 6-3.

The IGBT is mounted on a large heatsink with a relatively large thermal capacity in order to keep the case temperature as close as possible to the ambient temperature and to reduce variations in the heatsink temperature. Thus, with a large heatsink it can be assumed that the heatsink temperature is constant compared to the internal junction temperature of the IGBT [2][33]. With good thermal coupling between the heatsink and the IGBT case it can be assumed that the heatsink and IGBT case temperatures are equal, $T_c \cong T_{heatsink}$. The case temperature of the IGBT can be determined by measuring the heatsink temperature close to the IGBT with a temperature probe.

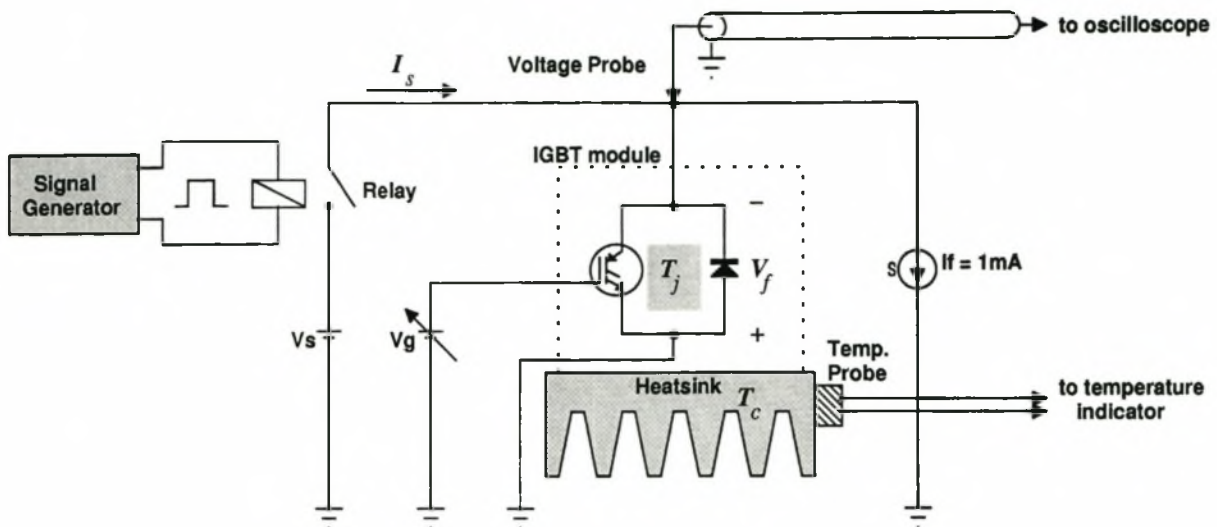


Figure 6-3: Measurement set-up to determine the thermal resistance of an IGBT.

It is not possible to simultaneously heat the IGBT and measure the internal temperature of the IGBT. Therefore, the thermal resistance measurement consists of two steps [2][33]:

1. *Heating cycle:* First the IGBT is heated internally by conduction losses. The relay in Figure 6-3 is turned on and a voltage source V_s is connected across the collector and emitter of the IGBT. A gate voltage is applied with which the IGBT is turned on to conduct in a saturated state (see Chapter 3). The gate voltage is adjusted to obtain an acceptable collector current not exceeding the current rating of the voltage source. The internal conduction loss of the IGBT during the heating cycle is simply

$$P_{\text{IGBT}} = V_s I_c.$$

For this experiment a voltage source with $V_s = 20$ V was used and the gate voltage was set to obtain a collector current $I_c = I_s = 5$ A (the probe current I_f can be ignored). The resulting conduction loss is thus $P_{\text{IGBT}} = 100$ W. The duration of the heating cycle has to be long enough to obtain thermal equilibrium, i.e. until the internal temperature of the IGBT has stabilized. This eliminates the effect of the internal heat capacity of the IGBT. The duration of the heat cycle can be estimated from the transient thermal impedance graph of the IGBT shown in Figure 3-17. The transient thermal impedance of a single pulse increases with the pulse duration until for relatively long pulse durations the transient thermal impedance stays more or less constant. The minimum pulse duration for which an increase in pulse duration does not dramatically change the transient thermal impedance is more or less equal to the

thermal time constant τ_{th} of the IGBT. In a practical set-up to be certain to obtain thermal equilibrium the heating cycle must be much longer ($> 10 \cdot \tau_{th}$) than the thermal time constant. For large IGBT modules, like the SKM300GB174D used for this project, the estimated thermal time constant is approximately $\tau_{th} = 0.5$ s and the heating cycle was chosen to be 10 seconds long. Excessively long heating cycles ($> 100 \cdot \tau_{th}$) are also not desirable and will only lead to an increase in the heatsink temperature.

2. *Temperature measuring cycle:* After the heating cycle the relay is turned off and a reverse probe current I_f is passed through the IGBT module, thereby forward biasing the internal diode of the module. As mentioned earlier the forward voltage drop V_f over the diode can now be used to measure the junction temperature T_j of the IGBT. The junction temperature must be measured immediately after the relay has switched before the IGBT starts cooling down. The voltage of the diode was calibrated by placing the IGBT module on a hot plate and measuring the diode forward voltage drop at a fixed diode current as a function of temperature. Results for the SKM300GB174D module are shown in Figure 6-4. Note that over a temperature range from 20 to 85 °C the relationship between the diode forward voltage drop and temperature is linear and can be approximated by the equation shown in Figure 6-4.

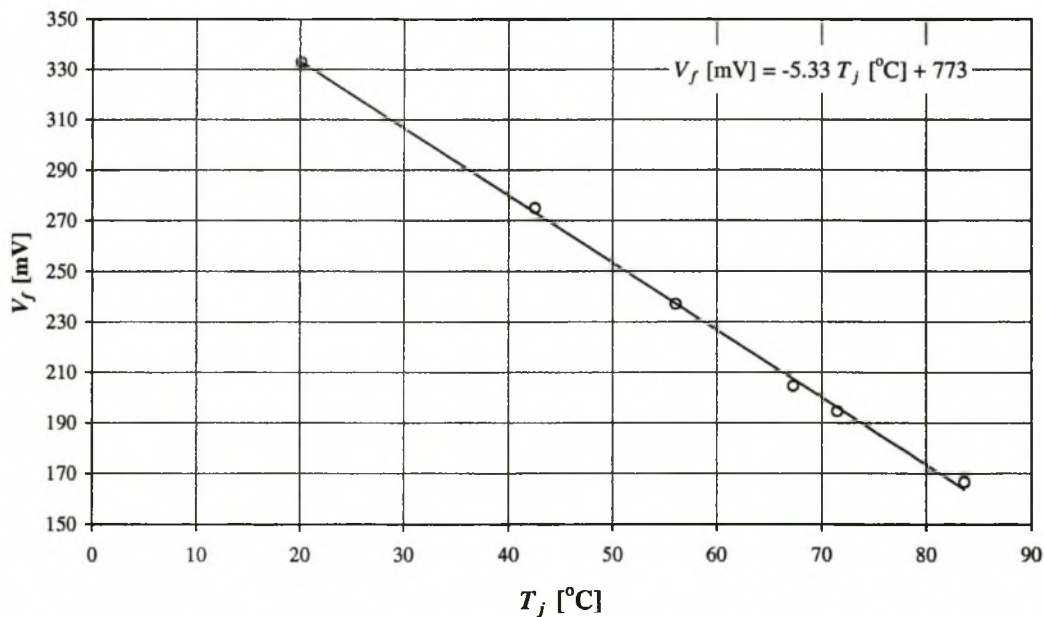


Figure 6-4: Forward voltage drop vs. junction temperature ($I_f = 1$ mA) of the internal reverse diode of the SKM300GB174D IGBT module from Semikron.

Knowing the internal junction temperature for the power dissipated during the heating cycle and measuring the heatsink temperature the thermal resistance can be calculated using Equation 6.2.

Electrical characteristics

The electrical characteristics of an IGBT can be determined by conducting three different measurements as proposed by IGBT manufacturers [16]. The basic measurement set-up consists of a sine wave signal generator, which is connected to the IGBT terminals in three different combinations. The voltage across the connected IGBT terminals and the current into the terminals are measured and displayed as an XY-trace on an oscilloscope. The set-up and typical XY-traces for the three different measurements are shown in Figure 6-5 [16].

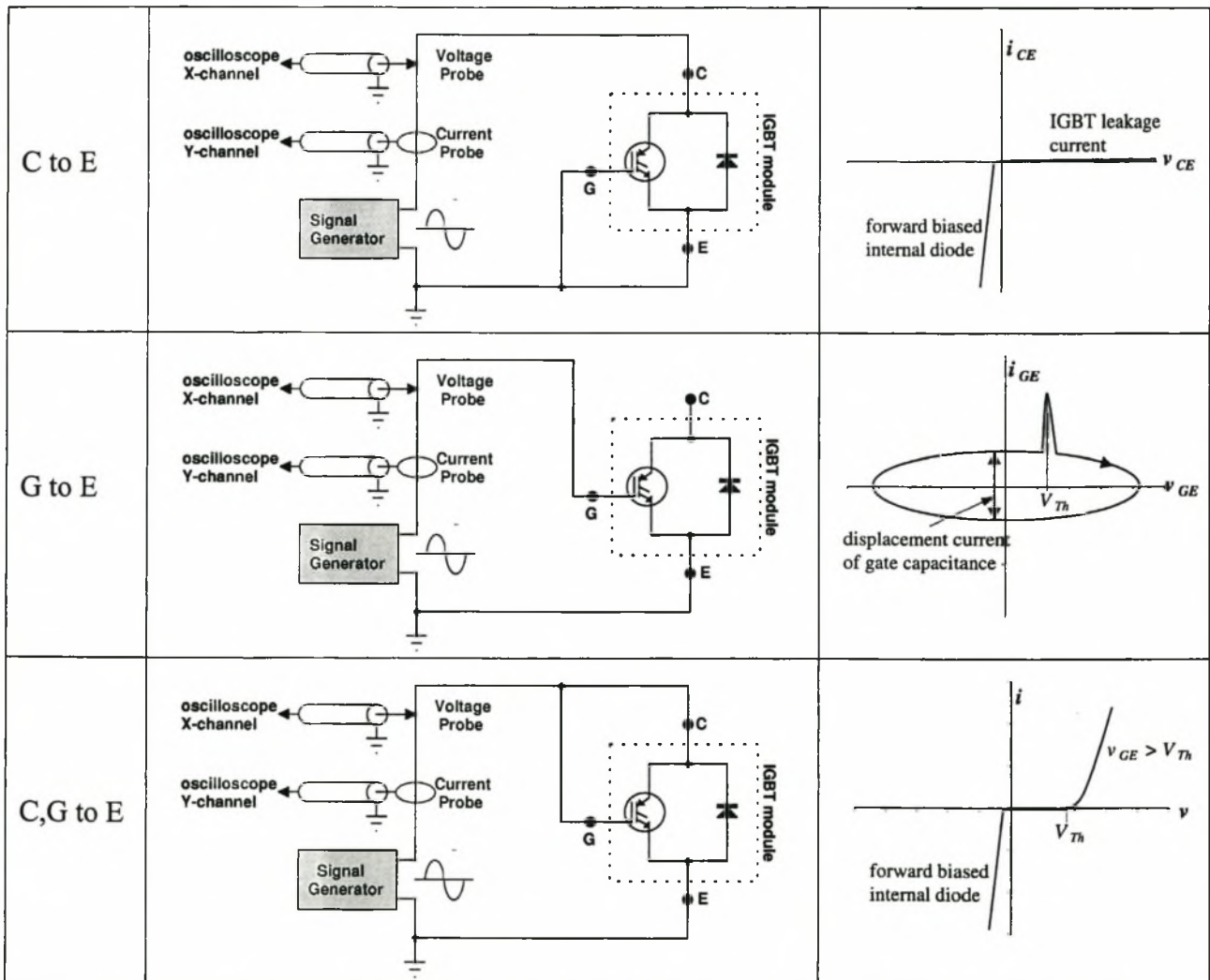


Figure 6-5: Measurement set-ups to determine the electrical characteristics of an IGBT.

C to E: The gate of the IGBT is shorted to the emitter, $v_{GE} = 0$, and the gate-emitter voltage is below the threshold voltage of the IGBT. For a positive collector-emitter voltage the IGBT may therefore not conduct and only the IGBT leakage current is observed. For negative collector-emitter voltages the internal diode starts conducting for $v_{CE} < -V_f$, where V_f is the forward bias voltage of the internal diode. The following IGBT parameters can be tested:

- Leakage current of IGBT, $I_{CE,leak} < \text{specified value}$
- Observed voltage drop of diode, $V_f \cong \text{specified value}$

G to E: In this configuration the gate of the IGBT is tested. The gate of the IGBT is insulated and due to a large gate resistance only a small gate current should be observed. The gate current is equal to the displacement current of the gate capacitance. Consequently, the amplitude of the gate current depends on the frequency of the applied signal and the gate capacitance value. A small current spike should be observed at the point where the gate-emitter voltage reaches the threshold voltage of the IGBT. The observed waveform must have the following characteristics:

- $i_{GE} = 0$ at maximum v_{GE} , i.e. the gate must be capacitive with voltage and current 90 degrees out of phase.
- A current spike at $v_{GE} = V_{Th}$ must be observed, indicating that the IGBT turns on at the threshold voltage.

C,G to E: The gate and collector are connected. This configuration is identical to the C-to-E configuration for negative applied voltages. For positive applied voltages the IGBT starts conducting as soon as the applied voltage is increased beyond the threshold voltage V_{Th} . Therefore:

- Observed $V_{Th} \cong \text{specified } V_{Th}$.

6.1.3 Results

A single IGBT of a SKM300GB174D module was tested for $0.5 \cdot 10^9$ shots at an average repetition rate of $f_{rep} = 500$ Hz for a total test period of 278 hours. The amplitude of the switched current pulses was increased stepwise from 1300 A up to 1500 A and a summary of the test conditions is given in Table 6-2.

Range [10 ⁶ shots]	Current pulse amplitude [A]	Switching voltage [V]	Pulse width [μ s]	Ambient temperature [°C]
0 to 100	1300	1110	4.3	21
100 to 400	1400	1200		
400 to 500	1500	1290		

Table 6-2: Test conditions for lifetime testing.

During the test period the thermal and electrical characteristics of the IGBT were monitored in regular intervals. The measured thermal resistance R_{thjc} for the test period is shown in Figure 6-6. The thermal resistance was initially measured to be 0.068 K/W, which is very close to the thermal resistance of 0.07 K/W specified by the manufacturer. After the first 100·10⁶ shots the thermal resistance drops by approximately 15% to between 0.057 and 0.058 K/W. Thereafter the thermal resistance stays constant within the measurement accuracy. This is an indication that no measurable degradation in the thermal characteristics of the IGBT can be detected. The thermal resistance also stays constant for the test period, from 400·10⁶ to 500·10⁶ shots, where the peak pulse current is 1500 A, which is 100 A above the peak current that will be obtained in the final pulsed power supply. The initial drop in thermal resistance is most probably caused by settling of the heat conducting paste inside the IGBT module. This in turn is caused by internal heating of the IGBT due to switching and conduction losses, which lowers the viscosity of the heat conducting paste [34].

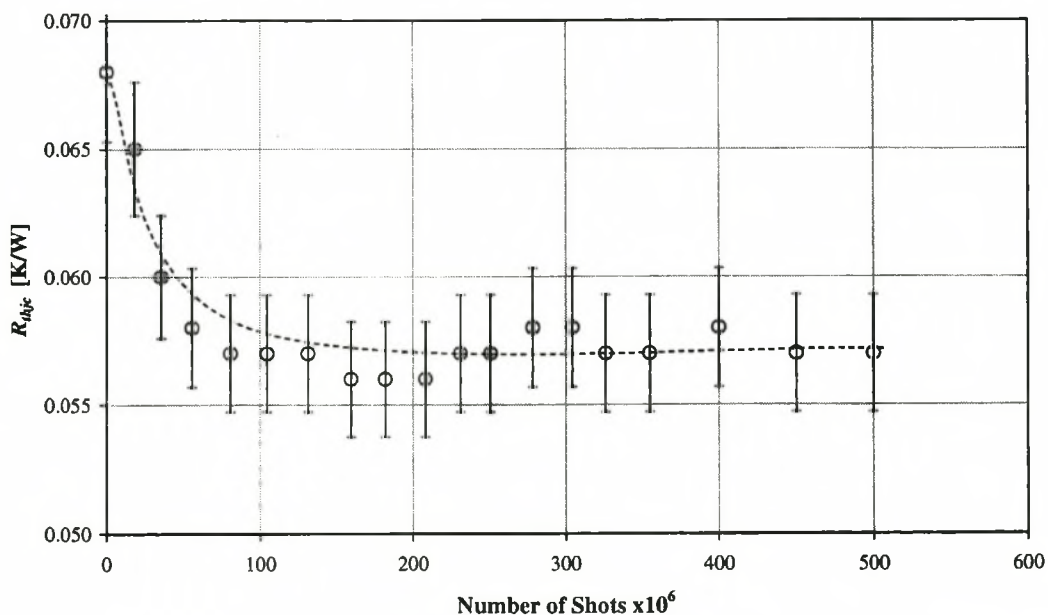


Figure 6-6: Measured thermal junction-to-case resistance of IGBT during lifetime test.

The measured electrical characteristics, namely the C-to-E, G-to-E and CG-to- E (see Section 6.1.2) traces are shown in Figures 6-7 to 6-9 for 0, 100, 200, 300, 400 and 500 million shots. All traces were obtained with a 20 V / 500 Hz sine wave signal and a signal generator output resistance of 50 Ω .

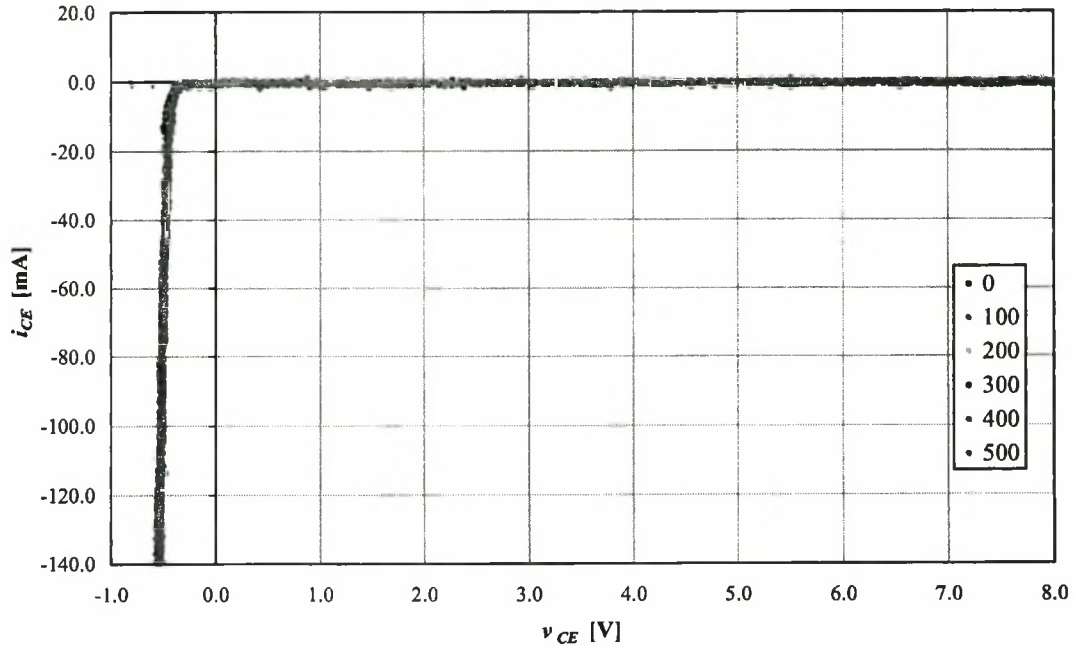


Figure 6-7: Measured IGBT C-to-E electrical characteristics during lifetime test.

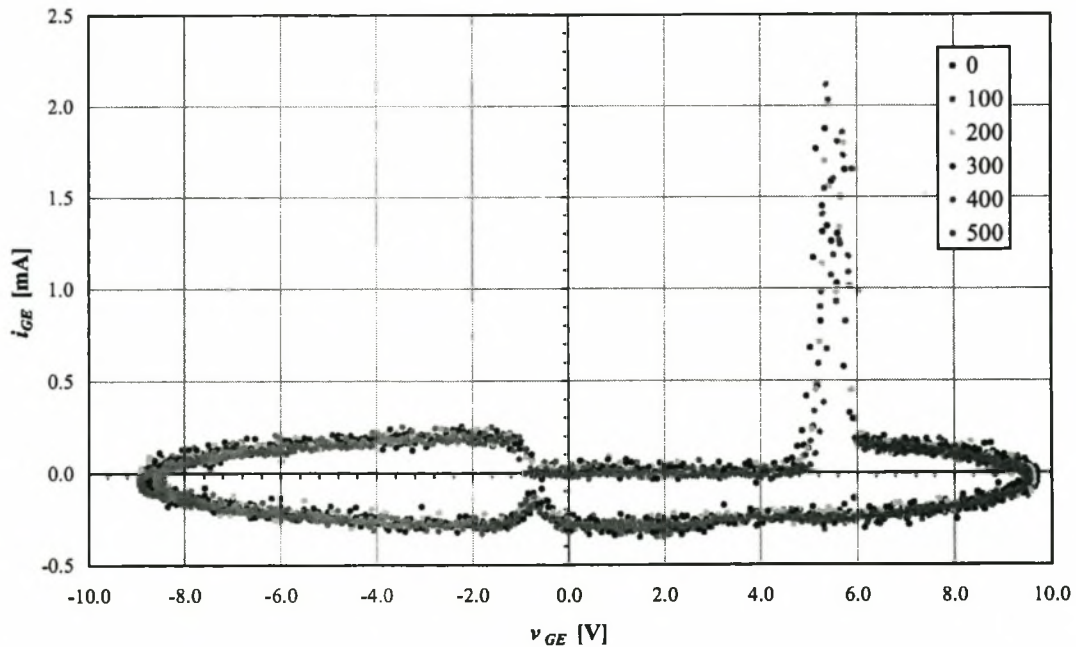


Figure 6-8: Measured IGBT G-to-E electrical characteristics during lifetime test.

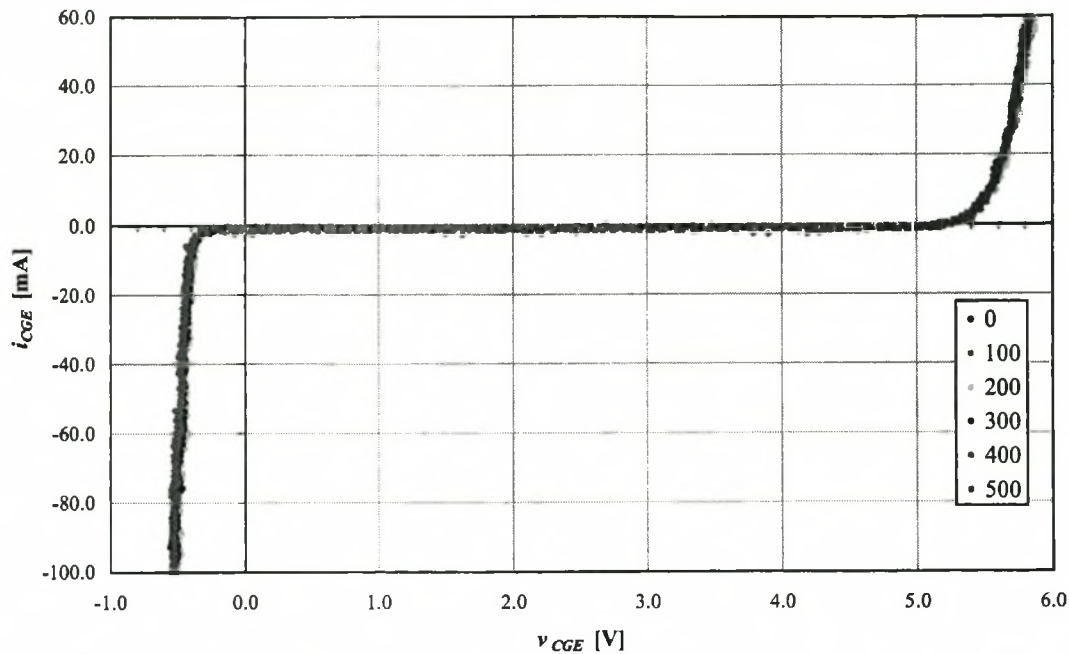


Figure 6-9: Measured IGBT CG-to-E electrical characteristics during lifetime test.

From the traces no measurable degradation or change in the electrical characteristics of the IGBT can be detected. Furthermore, the IGBT characteristics that can be determined from the traces are summarized in Table 6-3 and correspond well to the manufacturer's specifications (see Appendix C). Additionally, in the G-to-E trace the current spike at $v_{CE} = V_{Th}$ can be observed and the gate-emitter current is zero where the gate-emitter voltage is a maximum indicating that the gate is capacitive.

V_{Th}	5.4 ± 0.1 V
$V_f @ 100$ mA	0.5 ± 0.05 V
$I_{CE,leak}$	< 1 mA

Table 6-3: Measured IGBT parameters.

6.1.4 Conclusion

From both the thermal and electrical measurements it can be concluded that the IGBT under test survived $0.5 \cdot 10^9$ switching cycles without showing signs of degradation. This is satisfactory for a preliminary test. However, it is not possible to build statistics on the lifetime of IGBTs in pulsed power supplies based on a lifetime test conducted on a single IGBT. It is therefore advisable to conduct more extensive lifetime tests, where at least 6 devices (according to Hitachi quality

standards [16]) are tested for at least 10^9 switching cycles. Nonetheless, it is shown that IGBTs can be used in pulsed power supplies. In case of an IGBT failure it will also be much cheaper to replace an IGBT module compared to a thyatron, which can be between 5 and 10 times more expensive than an IGBT used in an equivalent pulsed power supply.

6.2 Fault handling capability

The possibility of fault conditions may not be excluded and some fault conditions occur relatively frequently (e.g. arcing between the laser electrodes). It is important to protect the IGBT against fault conditions to improve overall reliability.

6.2.1 Fault conditions and behaviour

The first step is to identify different fault conditions that may occur:

- *Flashover*: Flashovers are true circuit failures, which should not occur and are caused by insufficient electric insulation on the high-voltage side of the pulsed power supply, i.e. the pulse transformer secondary and MPC unit. A flashovers can be approximated as a low-impedance connection between the two points of the flashover. Critical points in the pulsed power supply are the MPC saturable inductors and the pulse transformer secondary. Although the MPC unit is submerged in transformer oil, impurities in the oil may lead to non-destructive flashovers between the winding and core of the MPC inductors. Breakdown of the secondary insulation in the pulse transformer will lead to destructive flashovers inside the transformer winding and hence the transformer will have to be replaced.
- *Laser arcing*: Unstable discharges between the laser electrodes result in arcing. There are many causes for unstable discharges [20] and this type of fault condition is the most frequent. Arcing discharges have a much lower impedance than typical stable discharges and arcing discharges can therefore be approximated as a short-circuit between the laser electrodes. However, a large portion of the pulse energy is dissipated in the arc discharge thereby significantly reducing the remaining energy in the pulsed power supply.
- *No laser discharge*: No laser discharge is obtained when the excitation voltage is below the breakdown voltage of the laser gas medium or the laser is operated with an unsuitable gas

mixture. With the absence of a laser discharge no energy can be deposited into the laser medium. Most of the pulse energy remains in the pulsed power supply and is reflected back to the primary switching unit.

Flashovers have highly non-linear characteristics, which can cause very unpredictable circuit behaviour and are also very difficult to simulate. In general it can be argued that flashovers disturb the propagation of the generated pulses through the MPC unit and will cause unwanted oscillations in the resonant transfer circuits of the MPC unit and primary switching unit. These unwanted oscillations can reduce the life-time of the IGBT. Due to the unpredictable nature of flashovers it is highly advisable to prevent flashovers by careful construction of the MPC unit.

Laser fault conditions, i.e. laser arcing and absence of laser discharges, on the other hand are not easily preventable and can occur frequently. Under laser fault conditions the initial C-C transfers in the pulsed power supply are unchanged and the voltage pulse propagates through the MPC unit as described in Chapter 2. As soon as the excitation pulse reaches the laser head, the fault occurs. Due to the fault condition not all the pulse energy can be deposited into the laser medium and a portion of the energy is reflected back to the primary switching unit. To illustrate this behaviour the circuit in Chapter 5 (see Figure 5-3) is simulated for the case where the laser fails to discharge. The simulated switching current waveform is shown in Figure 6-10. The reflection of the pulse energy causes the C-C transfer circuits in the pulsed power supply to oscillate unpredictably. The initial normal C-C transfer can be clearly seen in Figure 6-10, which is then followed by oscillations caused by the absence of a laser discharge. Note that the oscillations are weakly damped due to the low dissipative losses in the pulsed power supply and can last in the order of hundreds of microseconds. Similar waveforms were also measured and are shown in Chapter 7.

It is important to note that the absence of a laser discharge is a more severe fault condition than laser arcing. With the absence of a laser discharge no energy can be deposited into the laser medium and all the pulse energy is reflected back to the primary switching unit, whereas with laser arcing a large portion of the pulse energy is dissipated in the arc discharge.

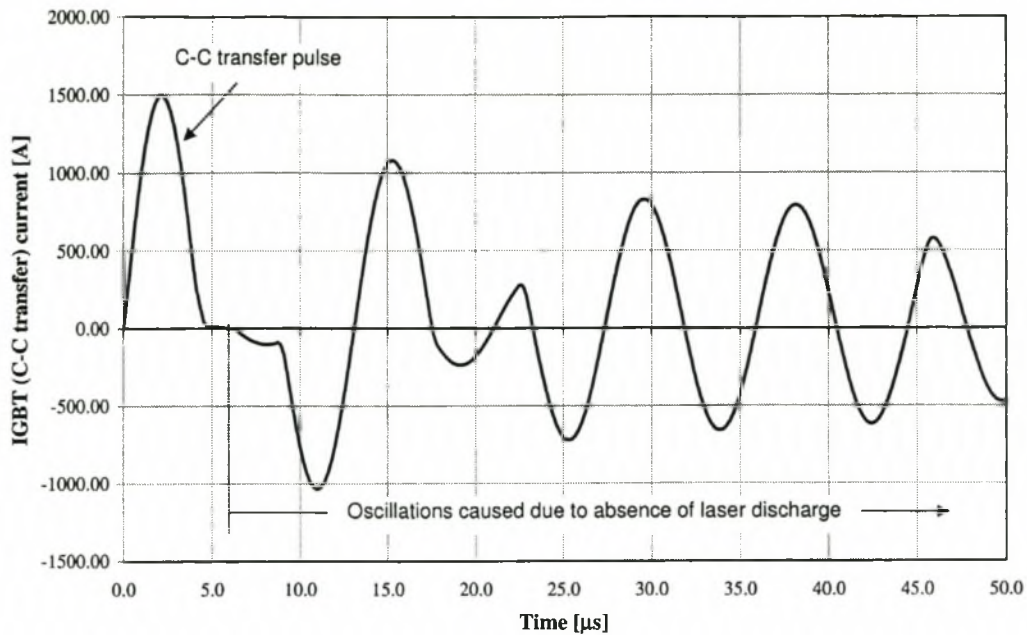


Figure 6-10: Simulated IGBT switching current under laser fault condition (laser fails to discharge).

6.2.2 IGBT protection

Oscillation in the switching current due to fault conditions can pose two problems:

- The weakly damped oscillations with current amplitudes much larger than the rated current of the IGBT place larger strains on the IGBT and internal diode of the IGBT module and therefore reduces the lifetime of the device.
- The IGBT must be switched off at some stage to allow the input storage capacitor of the primary switching unit to be recharge for the next pulse. Keeping in mind that the IGBT is connected in series with the transfer inductance of the C-C transfer loop, an attempt to switch the IGBT off while current is still flowing through the transfer inductor will cause a large di/dt . This induces large voltages in the transfer inductor resulting in dangerously high over-voltages over the IGBT.

The aim is therefore to suppress oscillations caused by fault conditions and to protect the IGBT during turn-off. This can be achieved by timing the turn-off of the IGBT and using over-voltage snubbers.

IGBT timing

The fact that the initial C-C transfer after the IGBT switches is unchanged by a laser fault condition can be used to time the turn-off of the IGBT. After the initial C-C transfer pulse the IGBT current drops to zero or close to zero and at this point the IGBT can be turned off. This prevents any further oscillations through the IGBT. Under fault conditions it can also happen that the IGBT current reverses after the initial C-C transfer, thereby forward biasing the internal diode of the IGBT module. Under such conditions it is also perfectly safe to turn the IGBT off, because at that stage the diode and not the IGBT is conducting.

Another advantage of switching the IGBT on only for the duration of the C-C transfer is that automatic energy recovery can be obtained. Note that the diode conducts reverse currents and in case of a fault condition the diode will only conduct the reverse portions of the fault current oscillations. This effectively recharges the input storage capacitor and is illustrated by measured waveforms in Section 6.2.3.

Over-voltage snubber

As mentioned earlier, an over-voltage spike is obtained when the IGBT switches off while current is still flowing through the IGBT. Over-voltage spikes can also be obtained when the diode switches off, due to the reverse recovery currents during the turn-off transient of the diode [27]. It is important to provide an over-voltage snubber [27], which clamps the IGBT voltage during turn-off of both the diode and IGBT. The circuit diagram of an over-voltage snubber is shown in Figure 6-11.

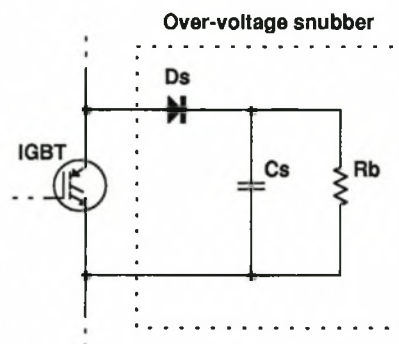


Figure 6-11: Circuit diagram of an over-voltage snubber.

Initially, the IGBT is off and the snubber capacitor C_s is charged by the high-voltage charging supply to a voltage equal to the initial voltage drop V_i over the IGBT. When the IGBT is turned on, the snubber diode D_s prevents the snubber capacitor from discharging through the IGBT, which could otherwise result in very large currents. At turn-off the IGBT voltage increases until the snubber diode is forward biased and the IGBT voltage v_{CE} is equal to the voltage over the snubber capacitor (ignoring the voltage drop of the snubber diode; see Figure 6-12a). At this point the inductor current is transferred from the IGBT to the snubber capacitor. The energy stored in the transfer inductor L_t is deposited into the snubber capacitor. The voltage over the snubber capacitor is thereby increased.

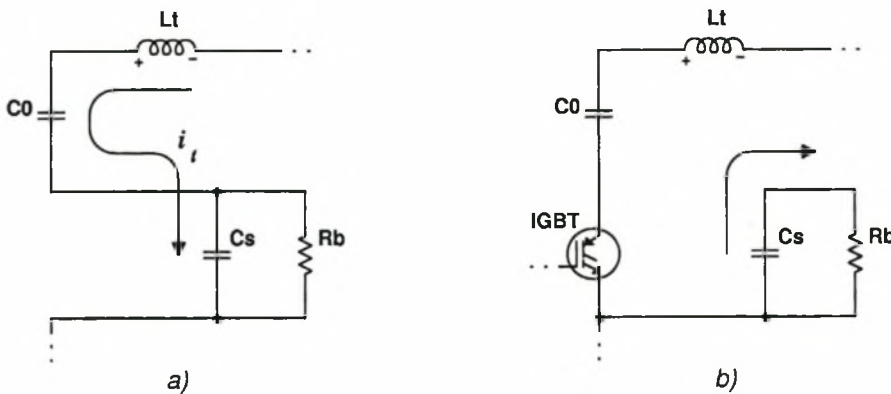


Figure 6-12: Over-voltage snubber behaviour.

Once the inductor current has been transferred to the snubber capacitor, the snubber diode becomes reverse biased. The over-voltage on the snubber capacitor discharges through the bleeding resistor R_b as shown in Figure 6-12b until the initial charging voltage V_i is reached again. Using energy considerations and assuming that the snubber capacitor is not significantly discharged during the turn-on period of the IGBT, the following expression is obtained:

$$\Delta V_{CE} = \sqrt{\frac{L_t}{C_s} I_0^2 + V_i^2} - V_i, \quad (6.3)$$

where ΔV_{CE} is the increase in voltage over the IGBT beyond the initial voltage drop V_i and I_0 is the current through the IGBT and transfer inductor at turn-off. Ideally, the voltage across the IGBT should not exceed 80% of the rated voltage [17]. The bleeding resistor has to discharge the capacitor to V_i before the next pulse is generated. Assuming that $\Delta V_{CE} \ll V_i$ the following must

hold true:

$$R_b C_s < \frac{1}{f_{\text{rep}} \Delta V_{CE}}, \quad (6.4)$$

with f_{rep} the repetition frequency of the generated pulses. It is interesting to note, that for series-stacked IGBTs the bleeding resistors also act as a voltage divider network. This ensures equal voltage sharing between the stacked IGBTs during the off-state (see Chapter 3). Furthermore, the over-voltage snubber acts as an additional failsafe to ensure equal voltage sharing between stacked IGBTs during the turn-on and turn-off transients. An additional safety feature is to add a transient suppressor diode, avalanche diode or varistor parallel to the snubber capacitor to clamp the maximum capacitor voltage below the breakdown voltage of the IGBT. The final circuit diagram of the snubber is shown in Appendix B.

6.2.3 IGBT lifetime under fault conditions

The protection scheme, i.e. IGBT timing and the over-voltage snubber, discussed in the previous sub-section was tested by using the same test circuit shown in Figure 6-1. A fault condition is simulated by removing the damping resistor and allowing the weakly damped LC-circuit to oscillate through the IGBT after turn-on. A similar current waveform as shown in Figure 6-10 is obtained. An additional IGBT timing unit was implemented. The timing unit switches the IGBT on only for the duration of the initial C-C transfer as discussed previously. A circuit diagram of the timing unit is given in Appendix B. The experimental set-up for testing the IGBT lifetime under simulated fault conditions is shown in Figure 6-13 and the circuit values are summarized in Table 6-4.

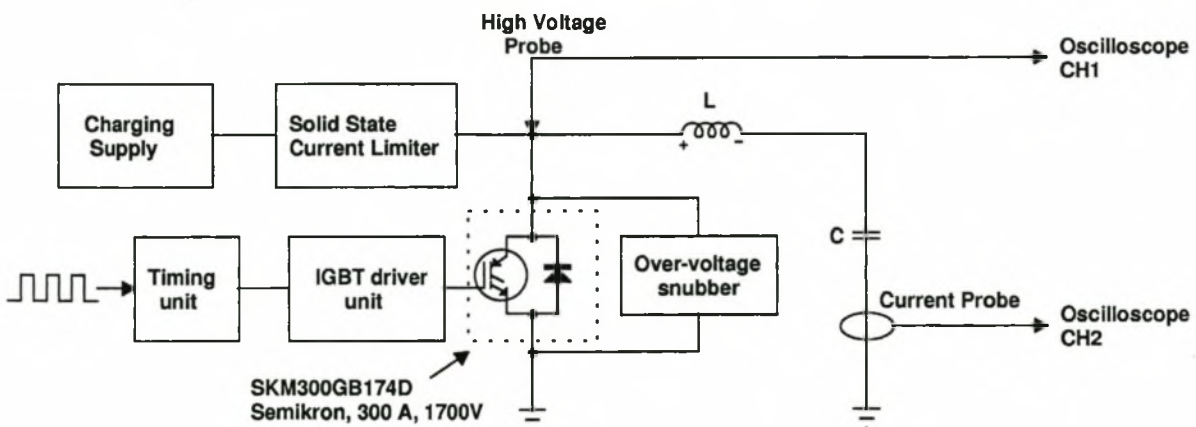


Figure 6-13: Experimental set-up for IGBT lifetime testing under fault conditions.

R	$< 0.1 \Omega$
L	$1.13 \mu\text{H}$
C	$1.65 \mu\text{F}$

Table 6-4: Circuit values for test set-up to simulate fault conditions.

The circuit diagram of the over-voltage snubber is also shown in Appendix B. A $0.47 \mu\text{F} / 2000 \text{ V}$ snubber capacitor is used, which for the circuit values in Table 6-4 and for a charging voltage of 1200 V will be able to absorb a maximum current of 400 A during turn-off without causing an over-voltage ($< 80\%$ of the rated IGBT voltage) across the IGBT.

The waveforms obtained with the test set-up for the case when no snubber is used and for the case when an over-voltage snubber is used are shown in Figures 6-14 and 6-15, respectively. Normally, the weakly damped LC circuit would continue oscillating freely after the IGBT is turned on. As can be seen in both Figures 6-14 and 6-15 the IGBT is timed and is only turned on by the gate voltage for the duration of the positive current pulse. The positive current pulse is equivalent to the initial current pulse obtained in a C-C transfer of the pulsed power supply. The negative half of the LC current oscillation is conducted through the internal diode of the IGBT module. This negative half cycle also mimics the reflected current pulses obtained under a laser fault conditions, i.e. when no laser discharge is obtained (see Figure 6-10). At the end of the negative current pulse the current through the diode reverses and the diode becomes reverse biased. However, the diode does not immediately turn off and for a short period a reverse recovery current is obtained before the diode finally turns-off resulting in a relatively large di/dt [27]. As can be seen in Figures 6-14 and 6-15 the reverse recovery current at the point when the diode turns off can be significantly high (in this case approximately 300 A) and causes large voltages across the IGBT during the diode turn-off. For the snubberless operation (see Figure 6-14) the over-voltages induced by the diode turn-off can be clearly seen. On the other hand, when using an over-voltage snubber the voltage across the IGBT is clamped and no over-voltages are obtained.

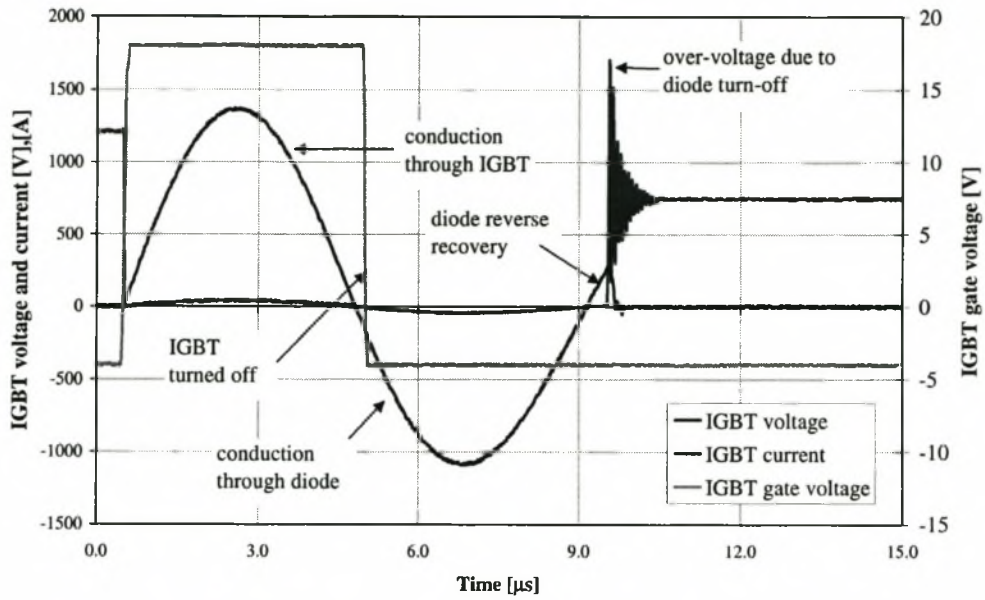


Figure 6-14: Waveforms obtained under mimicked fault conditions with IGBT timing, but without snubber.

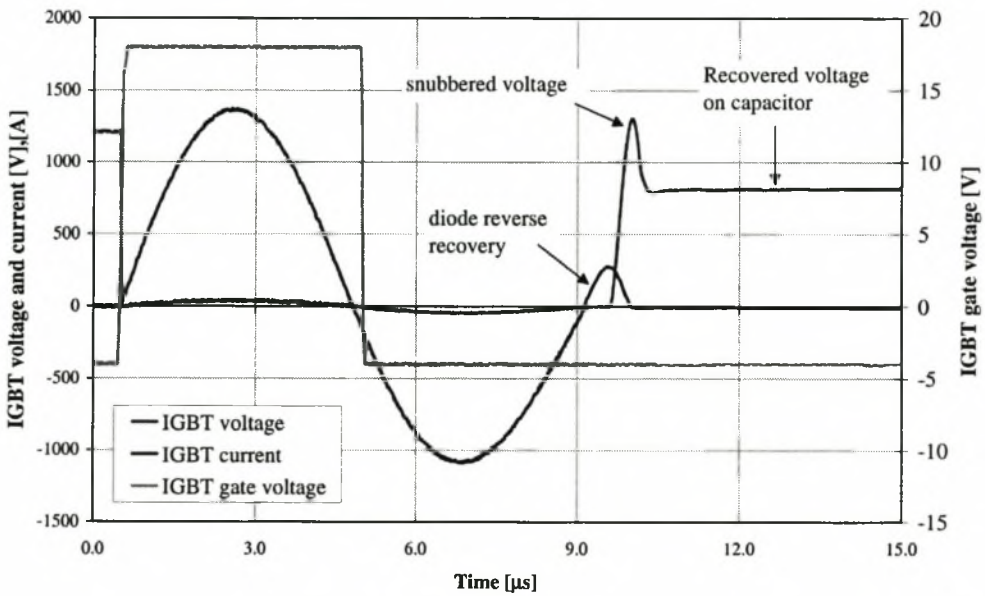


Figure 6-15: Waveforms obtained under mimicked fault conditions with IGBT timing and over-voltage snubber.

The lifetime of the IGBT was tested for both cases, i.e. with and without snubber and the results are summarized in Table 6-5.

	Snubber	Number of shots	Failure
IGBT #1	No	100,000	Short-circuit
IGBT #2	Over-voltage	25,000,000	Short-circuit
IGBT #3	Over-voltage	36,000,000	Short-circuit

Table 6-5: Results of lifetime tests under fault conditions.

In all cases a short-circuit failure of the IGBT module was obtained, but a clear improvement in the lifetime can be seen for the cases where an over-voltage snubber was used. Although all the tested IGBTs failed, it is important to realize that the test conditions were very stringent. The negative current pulses conducted through the internal diode of the IGBT module are larger than would normally be obtained in a pulsed power supply (see measurements in Chapter 7). Furthermore, the test conditions mimicked current waveforms that would normally be obtained when the laser fails to discharge, which is the worst laser fault condition. However, it is possible to prevent this type of laser fault. Normally, the laser fails to discharge when the laser gas pressure is too high or the charging voltage of the primary switching unit is too low. It is possible to measure the gas pressure and charging voltage thereby disabling the pulsed power supply if either the gas pressure is too high or the charging voltage too low. The light emitted from the laser discharge can also be monitored and absence of discharges as well as arcing can be detected.

It is interesting to note that G-to-E tests (see Section 6.1.2) were performed on the failed devices and the test yielded satisfactory results, indicating that the IGBTs were still functional. The short-circuit failure of the IGBT modules can therefore most probably be blamed on the internal diode of the IGBT modules.

6.2.4 Conclusion

A clear improvement in the IGBT lifetime under fault conditions can be obtained when using over-voltage snubbers and timing the IGBT turn-on. Although all the IGBTs failed during the fault lifetime testing, it is important to realize that the test conditions were very stringent. In a pulsed power supply the most common fault condition is laser arcing, which is much less severe than the applied test conditions.

It seems as if the internal reverse diode of the IGBT module caused the IGBT module failure. The probable reason for this is that IGBT manufacturers use soft recovery diodes. Soft recovery diodes turn off more slowly than fast recovery diodes, thereby reducing the di/dt of the diode current during turn-off. The aim of this behaviour is to reduce over-voltages and to allow snubberless operation in switch mode power supplies, but due to the soft diode recovery the diode losses are increased [17]. Furthermore, the internal diodes of IGBT modules normally have a smaller current rating and transient thermal impedance than the IGBTs (see data sheets in Appendix C). Consequently, in pulsed power supplies the soft recovery of the internal diode together with large reverse recovery currents obtained under fault conditions can cause excessively large diode losses resulting in diode failure. To improve the reliability of the IGBT module in pulsed power applications it is advisable to use an IGBT module without internal diode and adding an external reverse diode. The ratings of the external diode can be chosen to suit the conditions encountered in laser pulsed power supplies.

6.3 Electromagnetic interference (EMI)

Electromagnetic interference (EMI) can also result in unpredictable behaviour. As discussed in Chapter 5, for this project two series-stacked IGBTs are used, each with a separate driver unit. It was found that EMI from the laser head sometimes latched the driver unit of one of the two stacked IGBTs. This caused only one of the two IGBTs to switch resulting in an over-voltage across the non-switched IGBT, resulting in the over-voltage failure of the IGBT module. It is therefore important to reduce EMI and also make the system less vulnerable to EMI. The following precautions can be taken to reduce the effect of EMI:

- Shielding of the IGBT driver units.
- Driving stacked IGBTs with a single driver unit through small isolating pulse transformers. If the driver unit latches all the IGBTs will be disabled thereby preventing only one of the stacked IGBTs to switch.
- A gap between the oil tank containing the MPC unit and the metal housing of the laser head will result in electromagnetic radiation being radiated from the laser discharge (Figure 6-16a). It was found that EMI can be significantly reduced by electrically connecting the oil

tank and the laser head housing, thereby shielding the radiation emitted from the laser discharge (Figure 6-16b).

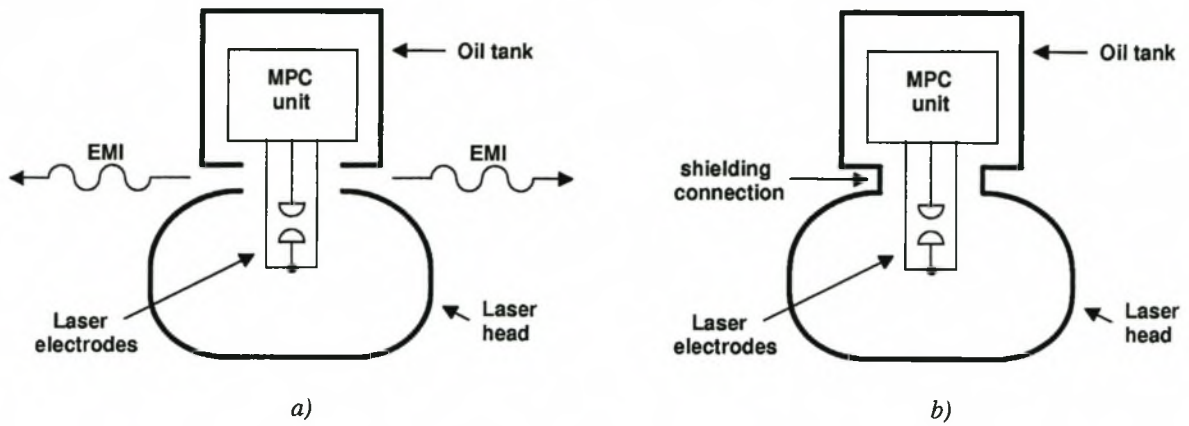


Figure 6-16: Shielding of laser head and MPC unit.

Chapter 7

Pulsed power supply measurements

Finally, after completing the construction of the pulsed power supply, the complete assembled pulsed power supply was mounted on the laser head. In this chapter the measurements of the performance and behaviour of the pulsed power supply are presented. Measurements include the pulse current and voltage waveforms, stable operating region, transfer efficiency, optical output energy and total efficiency. The CO₂ TEA laser was also originally supplied together with a thyatron-based pulsed power supply. Hence, it is possible to also compare the efficiency and optical output energy of the laser for the original thyatron-based and the new solid-state-based pulsed power supplies.

7.1 Voltage and current waveforms

The general circuit behaviour of the primary switching and MPC units were measured for both normal operating conditions (stable laser discharges and no circuit errors) and for laser fault conditions (arcing and absence of laser discharges). Furthermore, the IGBT turn-on and turn-off transients were measured with special focus on the voltage sharing between the two series-stacked IGBTs that were used for this design. The transfer efficiencies of the MPC stages were also measured.

7.1.1 Normal operating conditions

The voltage and switching current waveforms of the pulsed power supply under normal operating conditions and at the rated charging voltage of $V_0 = 2420$ V (see Chapter 5) are shown in Figure 7-1.

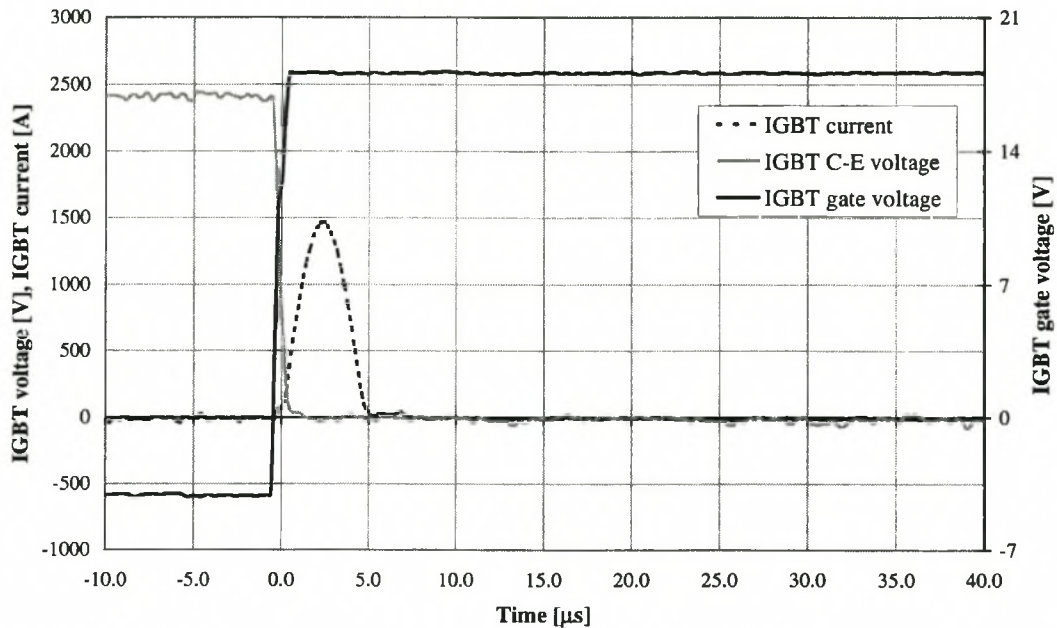


Figure 7-1: Voltage and current waveforms of the primary switching unit under normal operating conditions.

As expected, as soon as a positive gate voltage above the IGBT threshold voltage is applied, the IGBT turns on and the collector-emitter voltage of the IGBT drops to approximately zero. A single positive current pulse is obtained due to the C-C transfer in the primary switching unit. The absence of any further IGBT currents after the transfer pulse is an indication that no energy is reflected back to the primary switching unit and that the system is well matched to the laser discharge with efficient energy transfer into the laser discharge.

The voltage waveforms of the MPC unit under normal rated conditions are shown in Figure 7-2. The voltages at the input of the two MPC stages, as well as the output of the last MPC stage are shown. The MPC unit is well timed and the voltage waveforms obtained closely resemble the simulated waveforms in Chapter 5. Compared to voltage waveforms measured in Chapter 4 (see Figure 4-10) there are less oscillations in the excitation (output) voltage after the discharge is

obtained. The reverse overshoot voltage is also smaller, indicating good energy transfer into the laser discharge, thereby minimizing the remaining energy on the peaking capacitors. Note that due to a smaller peaking capacitor size, the leakage current of the saturable inductor in the last MPC causes a notable increase in the output (discharge) voltage before the main excitation pulse is obtained.

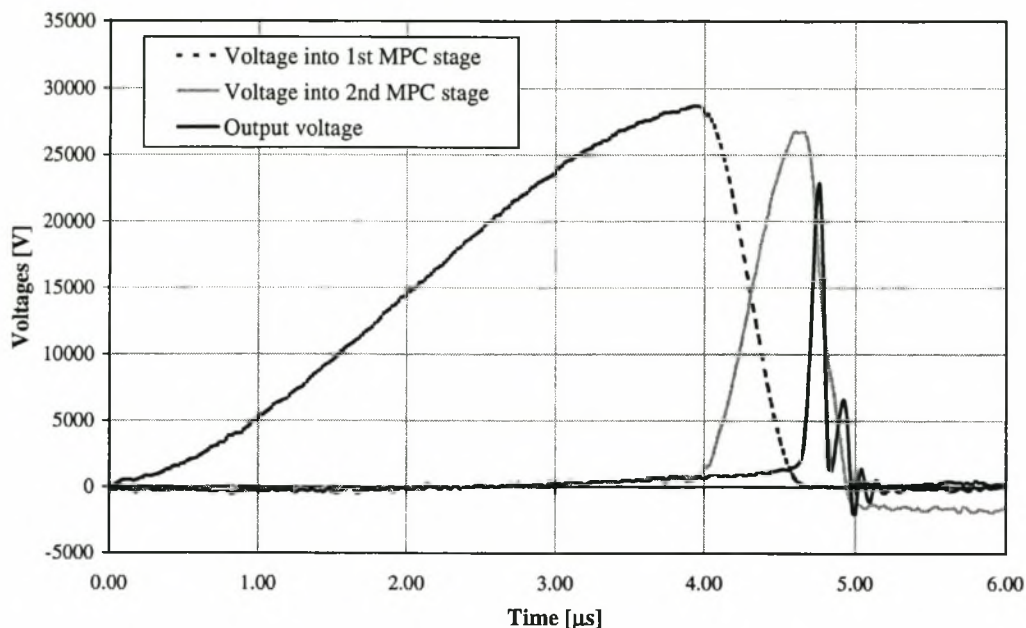


Figure 7-2: Voltage waveforms of the MPC unit under normal operating conditions.

From the waveforms shown in Figure 7-2 the transfer efficiency of the primary switching unit and the first MPC stage can be determined. Since the MPC inductors saturate before the voltages across the input capacitors of the MPC stages reach a maximum, a fit of Equation 2.6 has to be made onto the rising edge of the measured voltage waveforms. By extrapolating the fitted curve the maximum voltage that would be obtained across the input capacitors of the corresponding MPC stage can be determined. The curve fitting of Equation 2.6 to the measured waveforms was performed with MATLAB and the results are summarized in Table 7-1. Due to the reduction of the peaking capacitor size (output capacitor of second MPC stage) it is not possible to determine the transfer efficiency of the second MPC stage. The obtained transfer efficiencies are satisfactory with a transfer efficiency of 95.9 % for the primary switching unit including the pulse transformer and 95.5 % for the 1st MPC stage.

Description	capacitor	Max. voltage	Peak energy
Input storage capacitor	$C_0 = 1.65 \mu\text{F}$	2420 V	4.84 J
Transfer efficiency of primary switching loop (C_0 to C_1) = $95.9 \pm 0.2 \%$			
Input capacitor of 1. MPC stage	$C_1 = 10.8 \text{ nF}$	$29300 \pm 100 \text{ V}$	$4.64 \pm 0.03 \text{ J}$
Transfer efficiency of 1. MPC stage (C_1 to C_2) = $95.5 \pm 0.2 \%$			
Input capacitor of 2. MPC stage	$C_2 = 11.3 \text{ nF}$	$28000 \pm 100 \text{ V}$	$4.43 \pm 0.03 \text{ J}$

Table 7-1: Transfer efficiencies of primary switching unit and 1st MPC stage.

A close-up of the excitation voltage pulse is shown in Figure 7-3. The discharge pulse consists of the initial voltage rise after which the laser discharge is initiated followed by a second smaller voltage pulse. This is the typical behaviour that was also observed in Chapter 4 for reduced peaking capacitor sizes. Improved energy transfer into the laser discharge, coupled with an increase in optical output energy and efficiency is achieved. The observed waveform in Figure 7-3 is a very satisfactory result, indicating that the principle of reducing the peaking capacitor size can also be successfully implemented in the final MPC stage of a pulsed power supply. As expected, the initial rise-time of the excitation pulse is $t_{\text{rise}} = 80 \pm 5 \text{ ns}$. The main discharge is preceded by the parallel pre-ionisation discharge by approximately 10 ns.

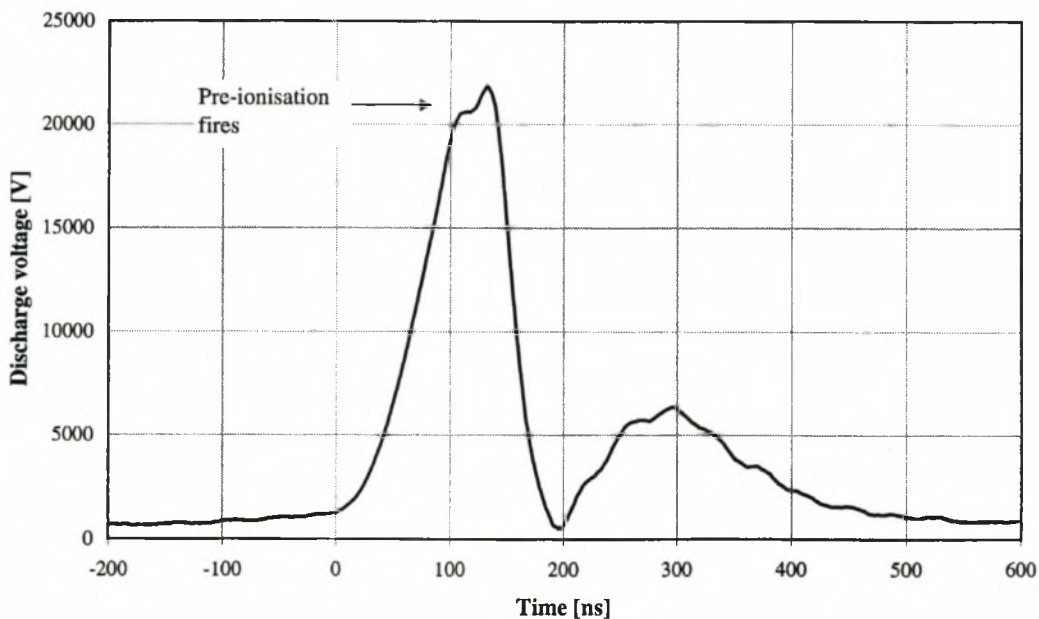


Figure 7-3: Output (laser excitation) voltage waveform.

In order to compare the simulated excitation waveform in Chapter 5 (see Section 5.1.4) the measured and simulated output voltage waveforms of the excitation circuit are shown in Figure 7-4. The simulation was performed for a 1:1:8 gas mixture at a laser gas pressure of 1 bar. The measurements were performed for the same gas mixture and pressure. A relatively good agreement between the simulated and measured results is found. The breakdown voltage is very similar for both the measured and simulated traces. However, during the secondary discharge (between 200 and 500 ns) the simulated waveform deviates from the measured trace. This is most probably caused by more complex processes in the laser discharge, which are not accurately modelled by the physical discharge model. Furthermore, the discharge model used for this simulation also approximates some of the discharge processes (see Appendix A). Nonetheless, the simulated waveform can be used as a comparatively good prediction of the general discharge behaviour of the laser.

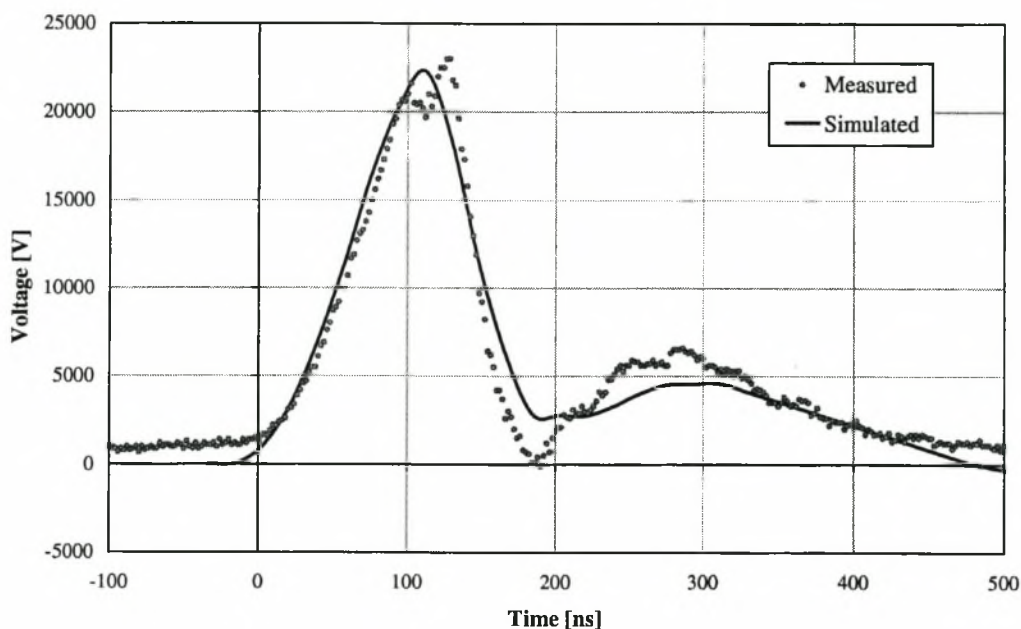


Figure 7-4: Comparison of the simulated and measured output voltage waveforms.

7.1.2 Fault conditions

The behaviour of the pulsed power supply for the two laser fault conditions, i.e. laser arcing and absence of laser discharge, was measured and is discussed in the following sub-sections.

No laser discharge

In order to measure the behaviour of the excitation circuit in the absence of a laser discharge, the laser gas pressure was increased and the charging voltage was reduced below the voltage needed to initiate a laser discharge. The IGBT was switched on longer than 1 ms in order to observe the circuit behaviour without IGBT timing as discussed in Chapter 6. The IGBT voltage and current waveforms obtained are shown in Figure 7-5. As simulated in Chapter 6, the initial C-C transfer current pulse is obtained followed by oscillations caused by the pulse energy being reflected from the power supply output. The duration of the circuit oscillations is remarkably long, lasting for more than 80 μs .

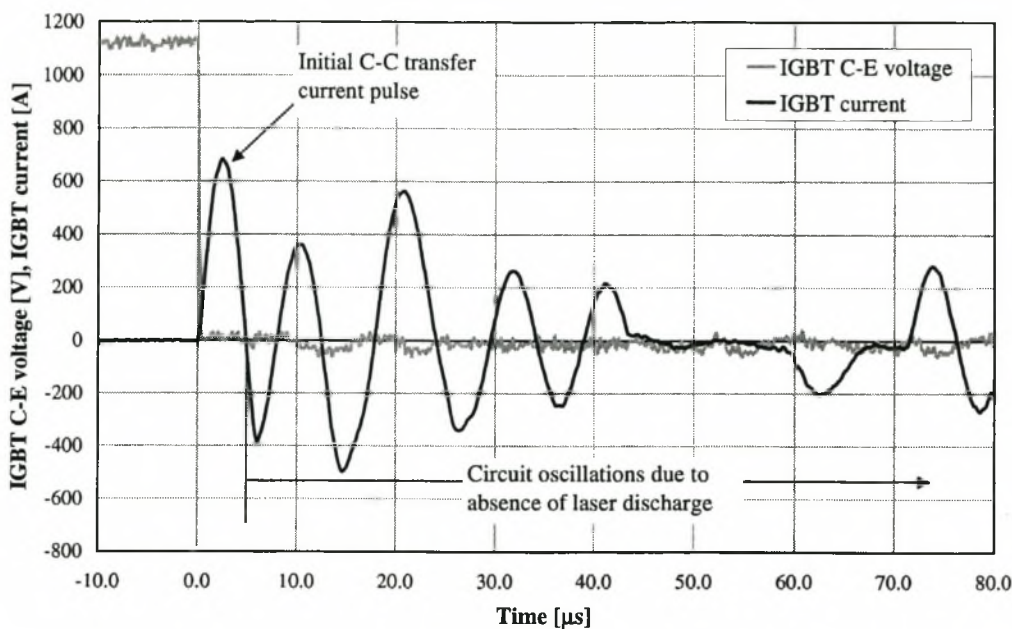


Figure 7-5: IGBT current and voltage waveforms in the absence of a laser discharge.

The IGBT voltage and current waveforms with IGBT timing and over-voltage snubber (see Section 6.2.2) is shown in Figure 7-6. The IGBT is only switched on for the duration of the initial C-C transfer pulse and is switched off just after the C-C transfer is completed. As discussed in Chapter 6 it is safe to turn the IGBT off, because at that stage the current is flowing through the internal diode of the IGBT module. In comparison to Figure 7-5 the amount of circuit oscillations is significantly reduced and the oscillations are totally suppressed after less than 20 μs . The voltage spike caused by the reverse recovery current and turn-off of the diode is absorbed by the over-voltage snubber. Reverse (reflected) currents pass through the internal diode of the IGBT module, thereby recharging the input storage capacitor of the primary switching unit and partially recovering the reflected pulse energy.

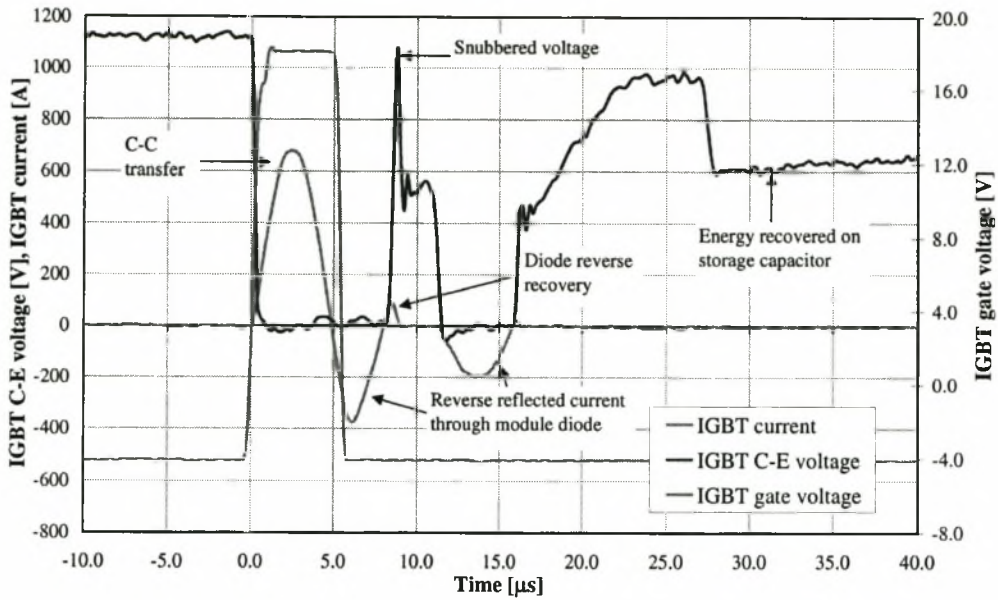


Figure 7-6: IGBT current and voltage waveforms in the absence of a laser discharge with IGBT timing and over-voltage snubber.

Laser arcing

Laser arcing was easily obtained by adding a small amount (approx. 20 mbar) of normal air to the laser gas. The IGBT voltage and current waveforms with IGBT timing and over-voltage snubber are shown in Figure 7-7.

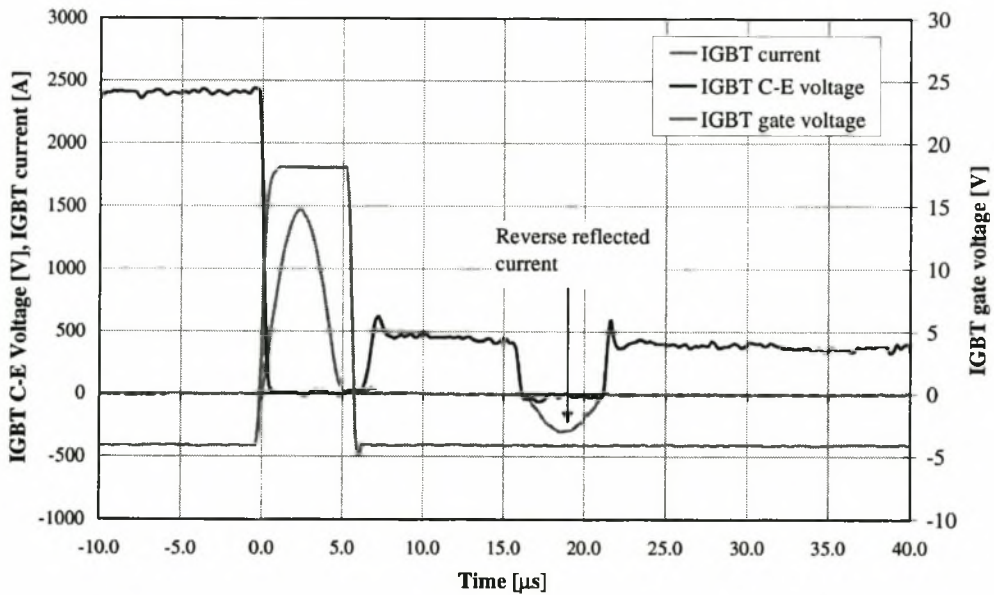


Figure 7-7: IGBT current and voltage waveforms in case of laser arcing with IGBT timing and over-voltage snubber.

The waveforms are similar to those obtained in Figure 7-6, but the amplitude of the reflected current is much smaller, because a large portion of the pulse energy is dissipated in the arc discharge. The obtained waveforms therefore illustrate that arcing fault conditions are less severe than absent discharges.

7.1.3 IGBT voltage sharing

Good voltage sharing between the two series-stacked IGBTs was obtained during both the turn-on and turn-off transients. This can be verified by the two IGBT voltage waveforms shown in Figure 7-8, which are almost identical even under fault conditions (absence of laser discharge).

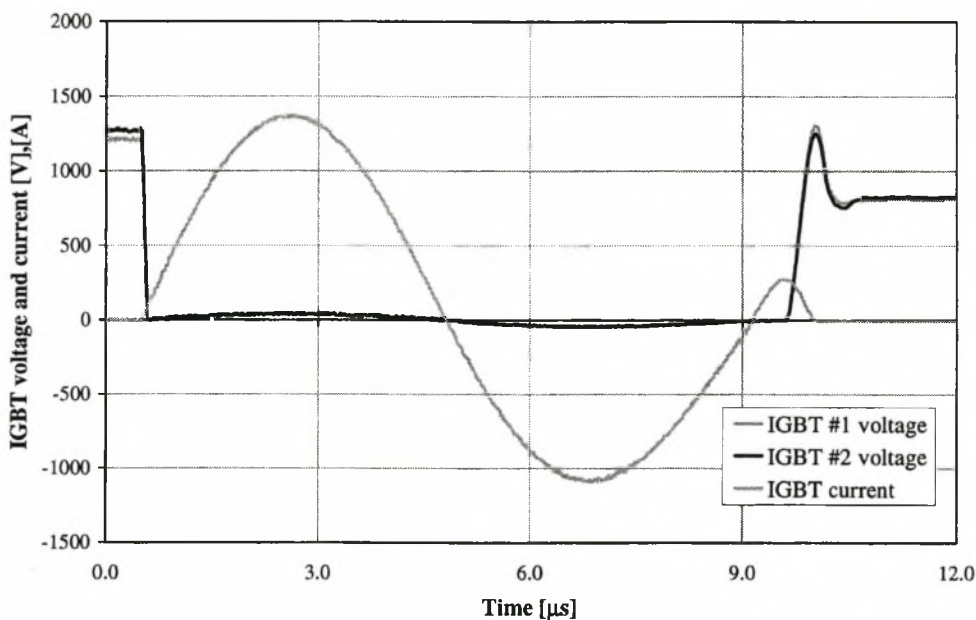


Figure 7-8: IGBT voltage sharing during turn-on and turn-off under fault conditions.

The theoretical results obtained in Chapter 3 on voltage sharing during turn-on of IGBTs therefore seem to be valid and give a good prediction of the behaviour of IGBTs in C-C transfer circuits. The turn-off transient is also satisfactory.

7.1.4 Conclusion

The designed MPC unit works satisfactorily with good transfer efficiency and timing. The improved energy transfer into the laser discharge due to the reduction of the peaking capacitor size also proves to be possible in the final MPC stage.

The measured circuit behaviour during laser fault conditions shows that excessive circuit oscillations can be obtained. These oscillations can be suppressed by using IGBT timing and an over-voltage snubber as described in Chapter 6. Measurements also show that the circuit oscillations obtained in the absence of a laser discharge are more severe than in case of laser arcing.

Lastly, satisfactory voltage sharing between the two series stacked IGBTs is obtained during both the turn-on and turn-off transient of the IGBT.

7.2 Stability

The stability of the laser was determined with a 1:1:3 (CO₂:N₂:He) gas mixture. Stable discharges were obtained for primary switching unit charging voltages larger than 1500 V and for the pressure range of 0.8 to 1.1 bar. The laser tended to be less stable at higher pressures, which can be expected with a 1:1:3 gas mixture. Notably, it was found that with parallel pre-ionisation the pre-ionisation discharge tended to fire too late. This caused the laser to operate on the brink of stability. For better discharge stability it is therefore advisable to convert the laser to series pre-ionisation.

7.3 Output energy and efficiency

The optical output energy was measured as a function of the input energy, regulated by the charging voltage of the initial storage capacitor of the primary switching unit, and the laser gas pressure. The optical output energies and efficiencies are shown in Figures 7-9 and 7-10. The efficiency was calculated with respect to the initial stored energy in the primary switching unit. Therefore, the same equation as used for the measurements in Chapter 4 can be applied:

$$\eta = \frac{E_{\text{output}}}{E_{\text{stored}}} = \frac{2E_{\text{output}}}{C_0 V_0^2},$$

with E_{output} the optical output energy, V_0 the charging voltage and C_0 the input storage capacitor of the primary switching unit. A 1:1:3 (N₂:CO₂:He) laser gas mixture was used for the measurements. A peak output energy of approximately 125 mJ is obtained at the rated input energy of 4.9 J. Unexpectedly, the peak energy output is obtained at the minimum laser gas pressure and the output

energy decreases with an increase in laser gas pressure. The efficiency of the laser varies between 1.7 % and 2.7 %, with the peak efficiency of 2.7 % at the rated input energy (4.9 J) and at the lowest pressure (0.8 bar).

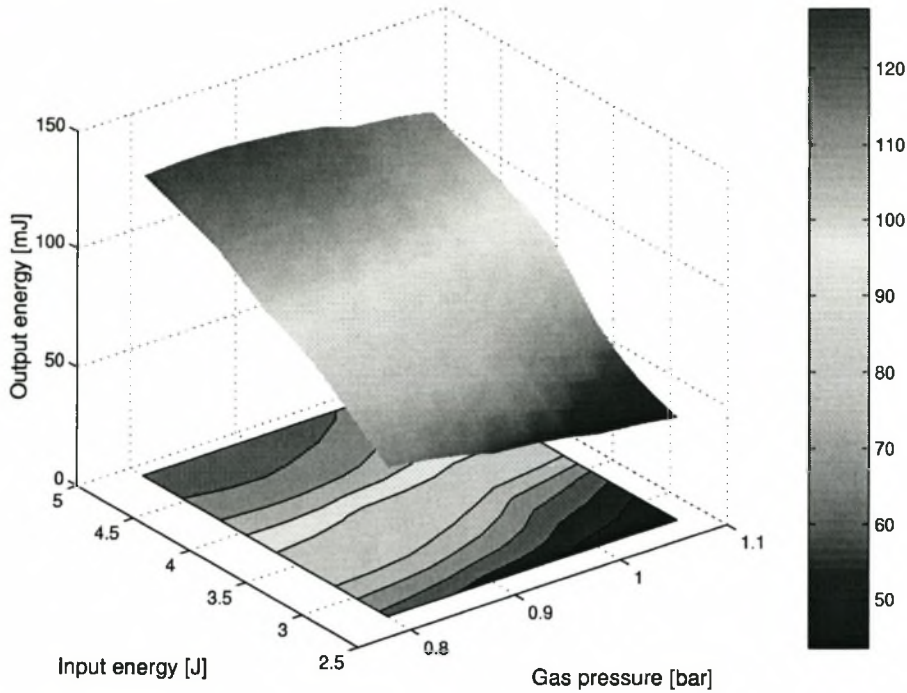


Figure 7-9: Optical output energy vs. input energy and laser gas pressure with new solid-state pulsed power supply. (1:1:3 mixture)

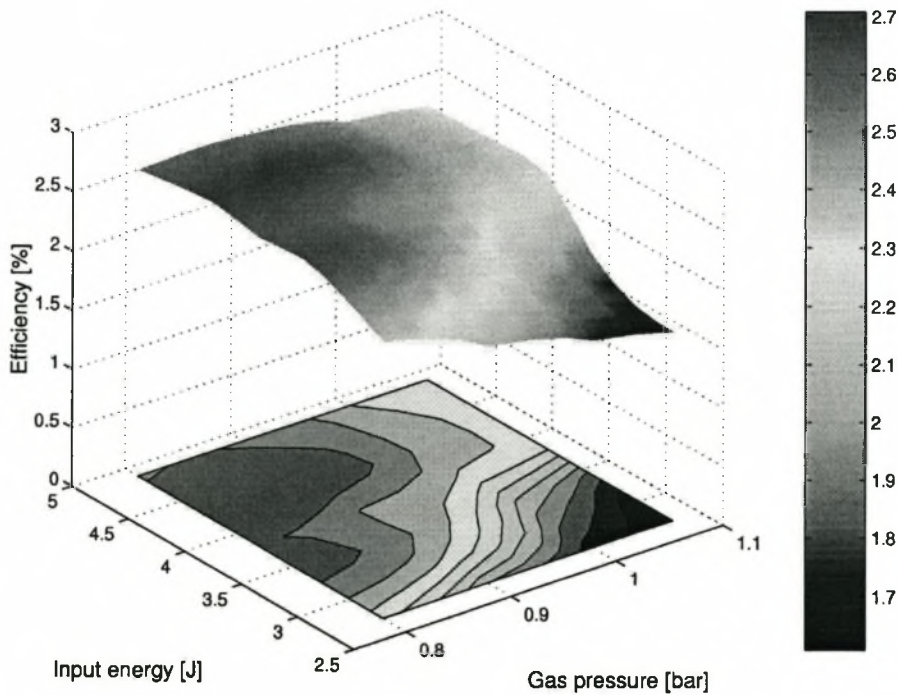


Figure 7-10: Optical output energy vs. input energy and laser gas pressure with new solid-state pulsed power supply. (1:1:3 mixture)

After the measurements conducted in Chapter 4 and during the construction phase of the new solid-state pulsed power supply, irreversible changes have been made to the CO₂ laser. This includes changes in the laser optics and the insertion of a ceramic catalyst into the laser cavity. The changes in the laser resulted in a general decrease of the laser performance. Furthermore, the original commercial thyatron-based pulser was disassembled in order to build the experimental excitation circuit discussed in Chapter 4. This makes a direct comparison of the performance of the new solid-state pulser and the original commercial thyatron based pulser impossible.

However, the performance of the altered laser was again measured with the optimised experimental excitation circuit (see Chapter 4, $C_p = \frac{1}{3}C_s$, $C_s = 11.04$ nF and $L_t = 920$ nH) before employing the new solid-state pulser. In Figures 7-11 and 7-12 the output energy and efficiency of the laser for the experimental pulser and the new solid-state pulser are shown. Measurements were performed for a 1:1:3 (N₂:CO₂:He) gas mixture at a pressure of 0.9 and 1.0 bar. Note, that the output energy and efficiency obtained with the experimental pulser also dropped with an increase in laser gas pressure. This behaviour can therefore not be blamed on the use of the new solid-state pulser. In comparison to the measurements in Chapter 4 the performance of the laser has clearly decreased.

Nonetheless, in general the output energy and efficiency obtained with the experimental and new solid-state pulser compare well. The output energy and efficiency of the solid-state power supply are between 10% and 20% lower than for the optimised experimental excitation circuit. Compared to the experimental excitation circuit the performance of the solid-state pulser is worse for lower input energies than for higher input energies. This is caused by mismatches in the MPC unit at lower input energies, since the MPC unit is specifically designed for a given input energy and pulse voltage. At the rated input energy of 4.8 J a decrease of approximately 10% is obtained in the output performance of the solid-state pulser compared to the experimental pulser. This can be caused by increased losses obtained in the MPC unit of the solid-state power supply. The total losses in the MPC unit at the rated input energy were measured to be approximately 10% (see Table 7-1). This correlates well with the comparative decrease in output energy and efficiency of the solid-state pulser.

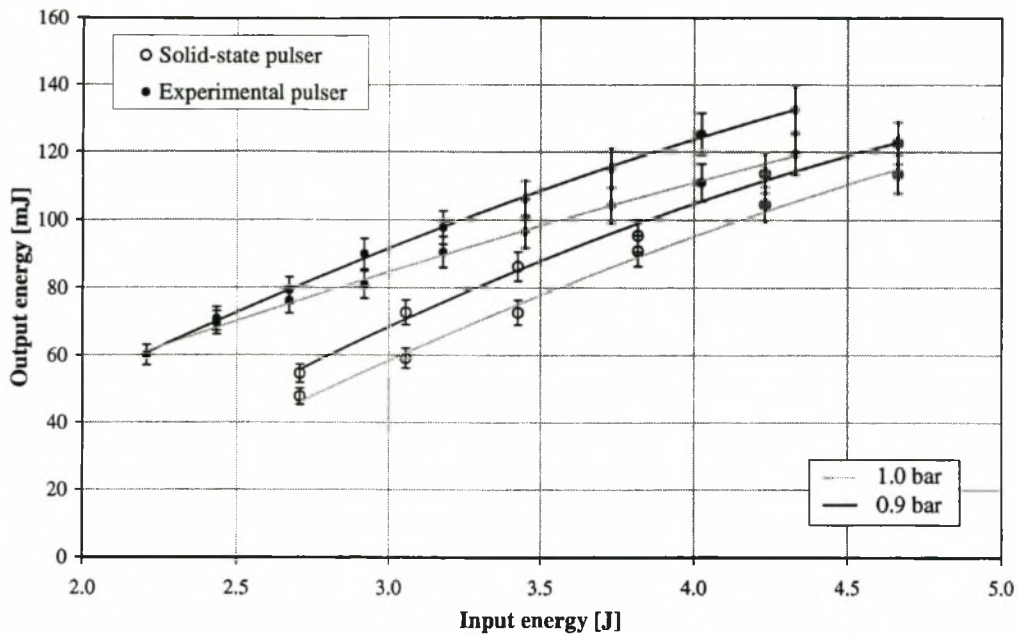


Figure 7-11: Optical output energy vs. input energy for the optimised experimental and new solid-state pulser. (1:1:3 mixture)

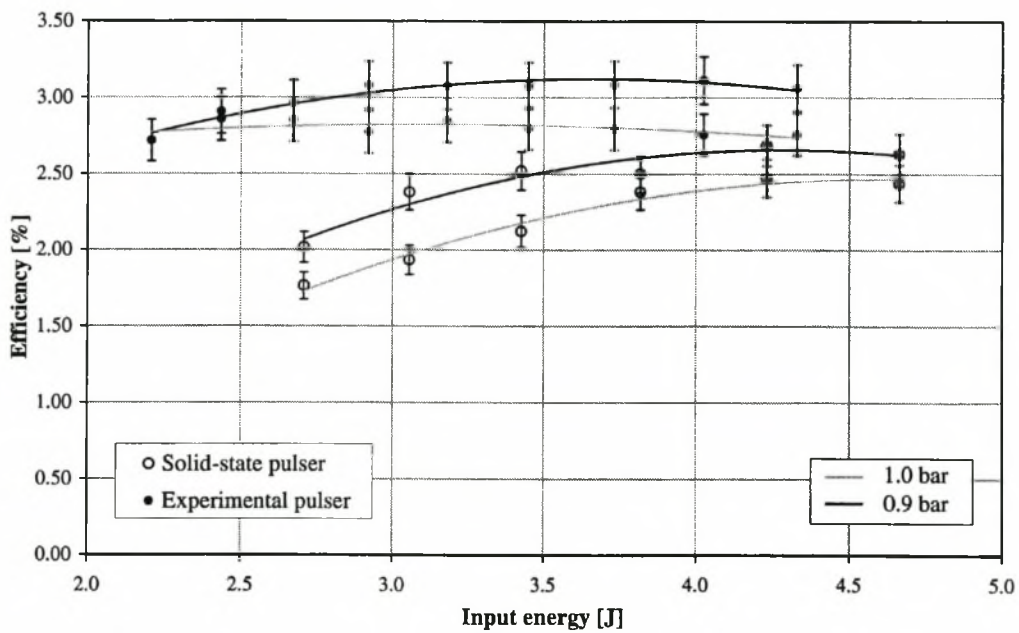


Figure 7-12: Efficiency vs. input energy for the optimised experimental and new solid-state pulser. (1:1:3 mixture)

7.3.1 Conclusion

Unfortunately, irreversible changes have been made to the laser, which resulted in a general decrease of the laser performance. Although this makes a direct comparison between the original thyatron-based pulsed power supply with the new solid-state pulser impossible, good results have been obtained with the solid-state pulser. Up to 125 mJ optical output energy with an efficiency of 2.7% were obtained. This is only 10% below the results obtained with the optimised experimental excitation circuit, as used in Chapter 4.

It is however still advisable to conduct comparative output energy measurements with both the original thyatron and new solid-state pulser on the same laser under closely matched conditions. Furthermore, it will be interesting to investigate the changes that were made to the laser (e.g. insertion of catalyst), which ultimately led to the degradation in laser performance.

Chapter 8

Conclusion

8.1 IGBTs in laser pulsed power supplies

The increased switching speeds and easy gate control of IGBTs can be used very effectively in pulsed power supplies based on a C-C transfer topology. It is therefore possible to switch pulses with pulse energies of a few Joules and with pulse durations of a few microseconds without magnetic assist. The problem of latch-up [27] during turn-on caused by large di/dt in the switching current is also eliminated in the new generation of IGBTs.

The limitations in the minimum switchable pulse width is caused by the following factors:

- For a given pulse energy and switching voltage the peak pulse current is inversely proportional to the pulse width of the switched pulse (see Equation 2.17). Too large peak pulse currents can saturate the IGBT, thereby causing the IGBT to effectively turn off. This results in an increase in the IGBT voltage coupled with large dissipative losses.
- The initial increase, di/dt , in the switch current has to be below a certain threshold determined by the switching speed of the IGBT. Too large di/dt in the switch current during the turn-on of the IGBT will prevent the IGBT from completely switching on. For C-C transfers a criteria for the minimum transfer time was derived for which satisfactory IGBT turn-on can be achieved (see Equations 3.20 and 3.21).

- The thermal stresses introduced by switching short high-current pulses can cause long-term degradation of the device thereby limiting the lifetime of the IGBT.

It is possible to reduce the above-mentioned limitations by either stacking or paralleling of IGBTs. With series-stacked IGBTs larger voltages can be switched, which leads to a reduction of the switching current. With parallel IGBTs the pulse current can be shared between IGBTs. Although the latter is more robust, the reduced switching current obtained with series-stacked IGBTs is beneficial and will also reduce the step-up pulse transformer current rating. It is found that excellent voltage sharing between series stacked IGBTs is obtained when using the criteria (Equations 3.20 and 3.21) mentioned earlier. IGBT switching speeds much faster than the transfer time of the switched C-C transfer loop will result in decoupling of the IGBTs, allowing each device to individually turn-off without effecting other series connected IGBTs.

The increased gate control, i.e. the ability to turn the IGBT on and off by the gate voltage, can be used very effectively to handle laser fault conditions. The laser fault conditions include laser arcing and the absence of laser discharges. A switching scheme is proposed with which oscillations in the pulsed power supply, caused by laser fault conditions, can be suppressed:

- The IGBT is timed to only turn on for the duration of the switched pulse. By turning off the IGBT after the transfer of the pulse any further oscillations in the pulsed power supply can be suppressed.
- Together with the above IGBT timing an over-voltage snubbers have to be used to protect the IGBT during turn-off against over voltages induced by the C-C transfer inductance.

8.2 IGBT peak current rating, lifetime and reliability

Costs can be reduced if the average current rating of the IGBT can be less than the peak switched pulse current. The same limitations that apply to the minimum pulse width, discussed earlier, also apply to peak switchable pulse current. It is found that the peak current of the IGBT in general should not exceed 4 to 5 times the rated average current of the device. Larger peak pulse current will result in saturation of the device, thereby inducing large losses. Lifetime tests show that it is possible to switch short pulses with peak currents between 4 to 5 times the rated average current of the IGBT reliably and for extended periods of time.

The reliability of IGBTs under fault conditions can be significantly improved by using the proposed switching scheme and over-voltage snubbers. The reliability of IGBT modules under fault conditions, however, can pose a problem. It seems that the internal soft-recovery diodes supplied in IGBT modules are a weak point. Lifetime tests under fault conditions revealed that the diodes eventually fail, resulting in a short-circuit across the IGBT module. Reliability can most probably be increased by using IGBTs without internal diodes and adding a separate external diode that is better suited for the conditions encountered in laser pulsed power supplies. Furthermore, it was found that the absence of a laser discharge is a much more severe laser fault condition compared to laser arcing, resulting in excessive oscillations in the pulsed power supply. It is therefore advisable to prevent situations that cause the laser not to discharge (e.g. excitation voltage too low, gas pressure too high, etc.). Additional circuitry has to be implemented that will shut down the laser under the prevalence of laser fault conditions. The additional circuitry should at least include an arc detector that can detect normal discharges, arc discharges and also the absence of discharges.

The problem of EMI must be addressed especially for series stacked IGBTs. It is found that the commercially available gate driver circuits for IGBTs can be latched by the EMI emitted from the MPC unit and laser discharge. Therefore, in series-stacked IGBTs where each IGBT is driven by a separate gate driver, EMI can result in over-voltage failure of the IGBT for which the gate drive circuit is latched. Reliability can be increased by using a single gate driver circuit. The single gate drive circuit then drives the series stacked IGBTs through small pulse transformers. Additionally, the laser cavity and MPC unit must be enclosed and well shielded, preventing the emission of EMI reaching the IGBTs and IGBT driver circuits.

8.3 MPC unit construction

A new approach in the MPC unit layout was used, which results in a more compact design. Instead of using a coaxial layout for the MPC inductors and capacitors a compact rectangular layout has been used. The capacitor banks and saturable inductors are modular and pre-assembled, thereby simplifying the final assembly of the MPC unit.

8.4 Optimisation of a mini CO₂ TEA laser

A simple thyatron-switched C-C transfer circuit was used to characterize a mini CO₂ TEA laser. For the C-C transfer based laser pulsed power supply the transfer capacitors of the MPC unit are chosen more or less equal in order to maximize the transfer efficiency of the MPC unit (see Equation 2.15). However, it is found that the output energy and efficiency of the laser can be increased significantly by reducing the peaking capacitor (output capacitor of last MPC stage) size. An increase of up-to 35 % (1:1:8 gas mixture) in the laser output energy and efficiency was observed by decreasing the peaking capacitor to a third of its original size. The improved efficiency is obtained due to a better transfer efficiency of the electric pulse energy into the laser discharge. The transfer inductance should not be increased when reducing the peaking capacitor size. Increased transfer inductance leads to decreased discharge stability. Therefore, associated with the smaller peaking capacitor size a faster voltage rise-time over the laser electrodes is obtained resulting in improved discharge stability.

Series pre-ionisation showed better discharge stability margins than parallel pre-ionisation, due to better timing and less jitter of the pre-ionisation discharge with respect to the main laser discharge. However, parallel pre-ionisation is preferable, because of the possible excessive erosion of the pre-ionisation spark gap encountered with series pre-ionisation. Furthermore, stable discharges can be obtained with maximum electrode voltage rise-times of up to 180 ns (approx. 300 ns C-C transfer time), but the discharge is less tolerant to the formation of O₂, resulting in a drop in laser output energy. Better discharge stabilities are obtained with voltage rise-times of less than 120 ns (200 ns C-C transfer time).

Since the measurements conducted in Chapter 4, changes have been made to the laser (e.g. insertion of a catalyst, changes to the laser optics, etc). These changes caused a general decrease in the laser performance. The decrease in laser performance was already measured with the experimental excitation circuit discussed in Chapter 4. Unfortunately, the changes are irreversible. A direct comparison of the performance of the new solid-state and original commercial thyatron-based pulsers is not possible. However, measurements conducted with the experimental excitation circuit on the altered laser compared favourably with results obtained with the solid-state power supply.

8.5 Future work

To improve laser efficiency and energy output it is advisable to investigate different excitation topologies, including the pre-pulse-main-pulse (magnetic spiker) topologies [3][9][19][22][46], in conjunction with solid-state switches. The advantage of magnetic spiker excitation is the reduction of the solid-state switch ratings compared to other topologies.

The reliability of the internal reverse diode in IGBT modules has to be investigated in more detail in order to improve the reliability of the IGBT under fault conditions. Safeguards must also be developed to detect the occurrence of laser fault conditions, especially the absence of laser discharges. Under potentially harmful fault conditions the pulsed power supply can be disabled.

Paralleling of IGBTs can be investigated in order to determine the advantages and disadvantages compared to series stacking of IGBTs.

Appendix A

PSpice simulation models

The simulation of circuits is an important design step with which possible design errors can be identified and basic circuit behaviour can be analysed. Saturable inductors and high pressure laser discharges are not standard circuit components available in PSpice. In order to simulate pulsed power supplies, models for a saturable inductor and laser discharge have to be implemented and are discussed in more detail in the following two sections.

A.1 Saturable inductor model

In order to model saturable inductors, PSpice must be able to model the BH-curve of an inductor or transformer core. A model often used in this respect is the Jiles-Atherton model [38] for non-linear cores. A summary of the model parameters is given in Table A-1.

Parameter	Units	Description
AREA, (AC)	cm ²	Mean of magnetic core cross section. AC is an alias of AREA
PATH, (LC)	cm	Mean of magnetic core path length. LC is an alias of PATH
MS	amp/meter	Magnetization saturation
A	amp/meter	Characterizes the shape of the anhysteretic magnetization
ALPHA		Represents the coupling between the magnetic domains
C		Domain flexing parameter
K	amp/meter	Domain anisotropy parameter

Table A-1: Parameters of the Jiles-Atherton core model.

A.2 Discharge model of a high-pressure CO₂ laser

Circuit simulations with PSpice can be used very effectively to optimise laser pulse power supplies. It is therefore advantageous to include the laser discharge in circuit simulations in order to determine the circuit response with a laser as electric load. The laser discharge can be either modelled by an equivalent circuit model [30] or by modelling the physical discharge process [25]. The physical model tends to give better results with less of a trial-and-error-approach in comparison to the equivalent circuit model. Therefore in this section only the physical discharge model is discussed.

For simplicity the gas discharge is modelled as a homogenous positive column [25] and the electron balance equation becomes:

$$\frac{dn_e}{dt} = W_e n_e (\alpha - \eta) - n_e^2 \gamma, \quad (\text{A.1})$$

where n_e is the electron density, α the ionisation coefficient, η the attachment coefficient, γ the recombination coefficient and W_e the electron drift velocity. Further, it is assumed that recombination is negligible. Equation A.1 then reduces to a first order linear differential equation with the following solution:

$$n_e(t) = n_{e0} e^{\exp\left(\int_0^t (\alpha - \eta) W_e dt'\right)}, \quad (\text{A.2})$$

where n_{e0} is the pre-ionisation charge density at $t = 0$. It is assumed that the discharge is homogeneous without electrode effects. The discharge current can be obtained by differentiating Equation A.2:

$$i_d(t) = en_e W_e A = en_{e0} W_e A \exp\left(\int_0^t (\alpha - \eta) W_e dt'\right), \quad (\text{A.3})$$

where i_d is the discharge current, A the discharge cross-section and e the electron discharge.

Equation A.3 seems relatively simple, but the ionisation and attachment coefficients and the electron drift velocity are functions of the applied discharge voltage v_d , i.e. the voltage between the anode and cathode of the laser. The discharge current therefore depends on the applied voltage and in return the applied voltage is regulated by the external circuit elements and the discharge current. This results in a complex feedback system that can cause convergence problems during PSpice simulations.

The ionisation and attachment coefficients and electron drift velocity are normally expressed as functions of E/N , where

$$\frac{E(t)}{N} = \frac{v_d(t)}{Nd}, \quad (\text{A.4})$$

and E is the electric field between the laser electrodes, which is assumed to be homogeneous, N is the neutral particle density and d the distance between the electrodes of the laser. The E/N dependencies of the ionisation and attachment coefficients and the electron drift velocity for a 1:1:8 ($\text{CO}_2:\text{N}_2:\text{He}$) gas mixture were taken from Lowke, et al. [23] and are shown in Figures A-1 and A-2.

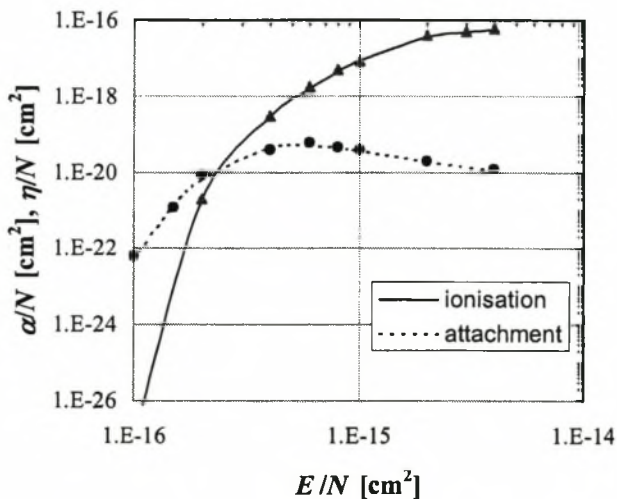


Figure A-1: Ionisation and attachment coefficients as a function of E/N in CO_2 TEA lasers with a 1:1:8 gas mixture.

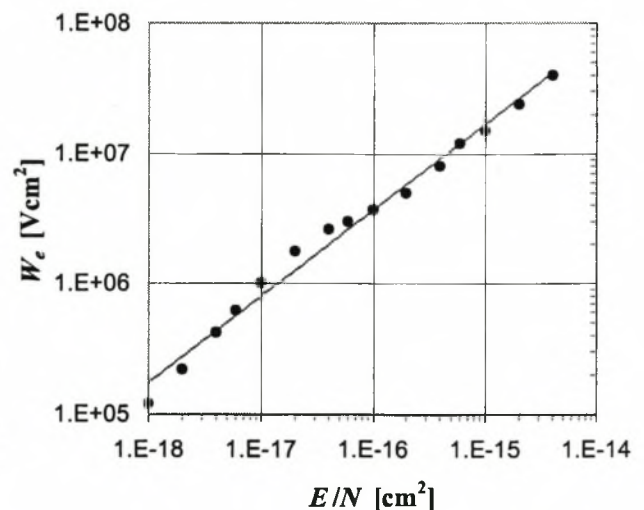


Figure A-2: Drift velocity as a function of E/N in CO_2 TEA lasers with a 1:1:8 gas mixture.

The dependence of the ionisation and attachment coefficients and drift velocity on the applied voltage v_d (i.e. the E/N value) is highly non-linear as apparent from Figures A-1 and A-2. In order to

obtain an acceptable curve fit, polynomial fits are done on the log-log values, which are shown in Figures A-3 and A-4. The curve fits as well as the fitting functions are shown in Figures A-1 and A-2.

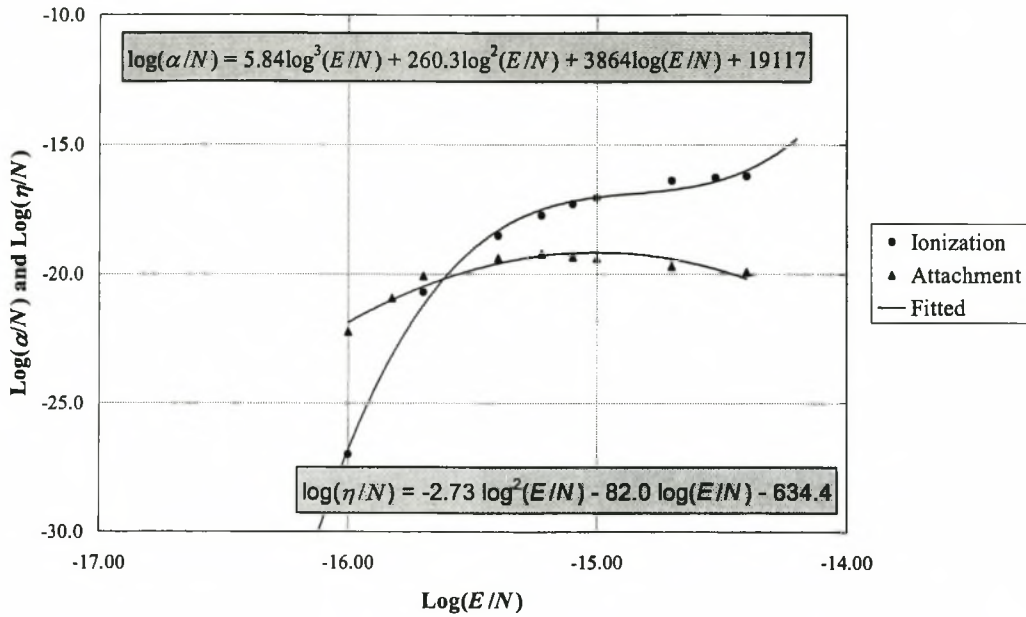


Figure A-3: Polynomial fits of the attachment and ionisation coefficients vs. E/N .

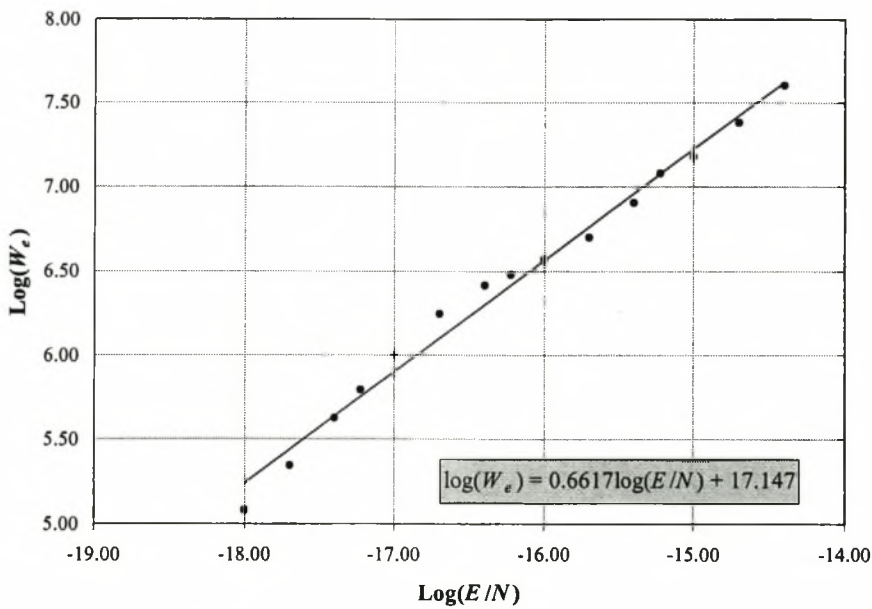


Figure A-4: Polynomial fit of the drift velocity vs. E/N .

Equations A.3 and A.4 can be implemented in PSPICE by several voltage sources and a voltage-dependent current source as depicted in Figure A-5. Firstly, the value of E/N is calculated from the

input voltage between the anode and cathode and is represented by the voltage source $V(E/N)$. The three voltage sources, $V(\log_{ion})$, $V(\log_{att})$ and $V(\text{drift})$ represent the ionisation coefficient, attachment coefficient and drift velocity respectively, which are calculated from the voltage value of $V(E/N)$ using the fitting functions shown in Figures A-3 and A-4. The voltage source $V(\text{dint})$, which calculates $(\alpha - \eta)W_e$, is integrated and $V(\text{int})$ represents the integral in Equation A-3. From the voltages $V(\text{int})$ and $V(\text{drift})$ the discharge current is calculated and implemented by the voltage controlled current source G1. The laser parameters n_{eo} , N , d and A are given as input parameters.

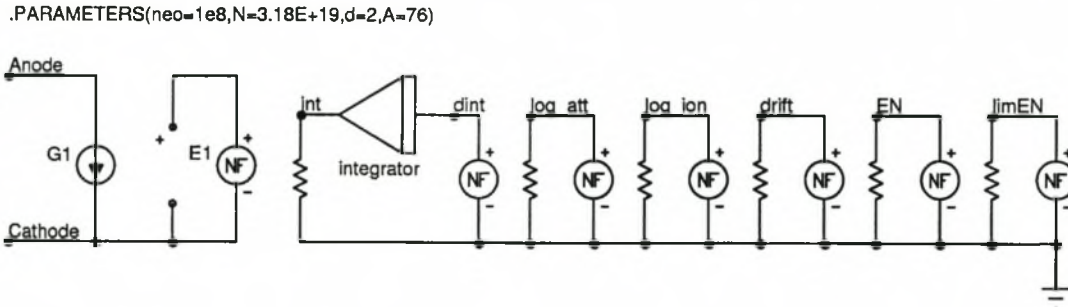


Figure A-5: Implementation of the physical discharge model in PSpice.

Appendix B

Circuit diagrams

B.1 IGBT timing unit

The IGBT timing unit is based on the 555 timer chip which is operated in mono-stable mode. A trigger pulse fed in at the SGN terminal resets the timer. After this the output of the timer is driven high for a preset period of time, T_{on} . The period T_{on} can be adjusted by the potentiometer R6. The output of the 555 timer drives a fibre optic transmitter diode which is connected via a fibre optic cable to the fibre optic receiver on the IGBT driver unit. Therefore, by adjusting R6 the turn-on period of the IGBT can be adjusted.

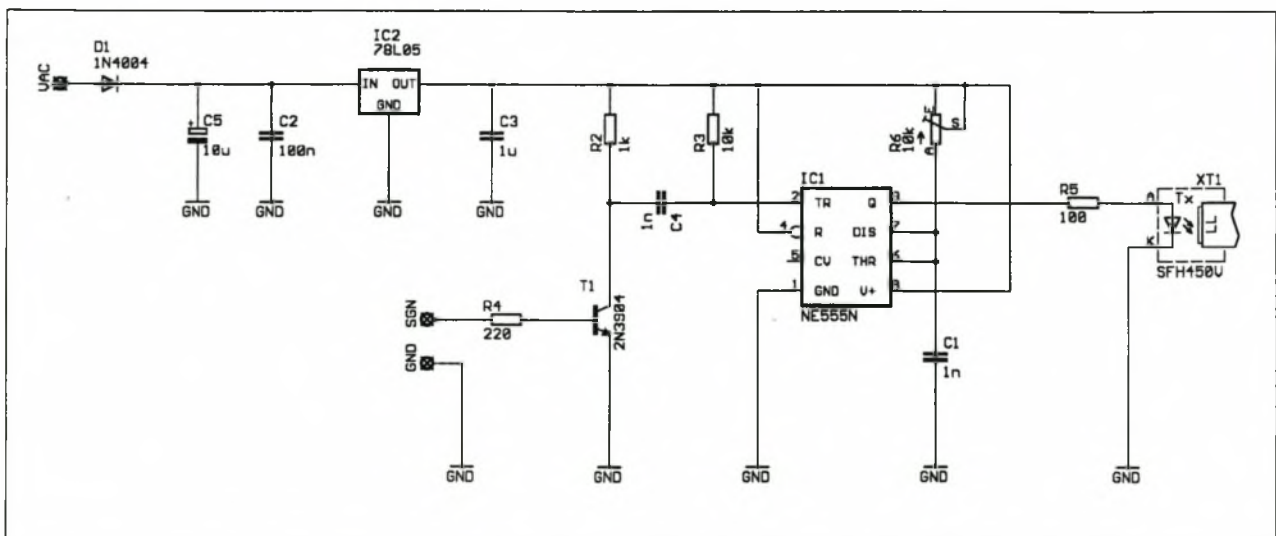


Figure B-1: Circuit diagram of IGBT timing unit.

B.2 IGBT driver unit

The IGBT driver unit is based on the DC-DC converter M57145L-01 and gate driver M57962, both from Powerex. Two gate drivers are used, each driving one of the IGBTs in the SKM300GB174D IGBT module. The turn-on (control) signal is obtained via fibre optical cable. The unit is powered by an external DC voltage source (12 to 18 V).

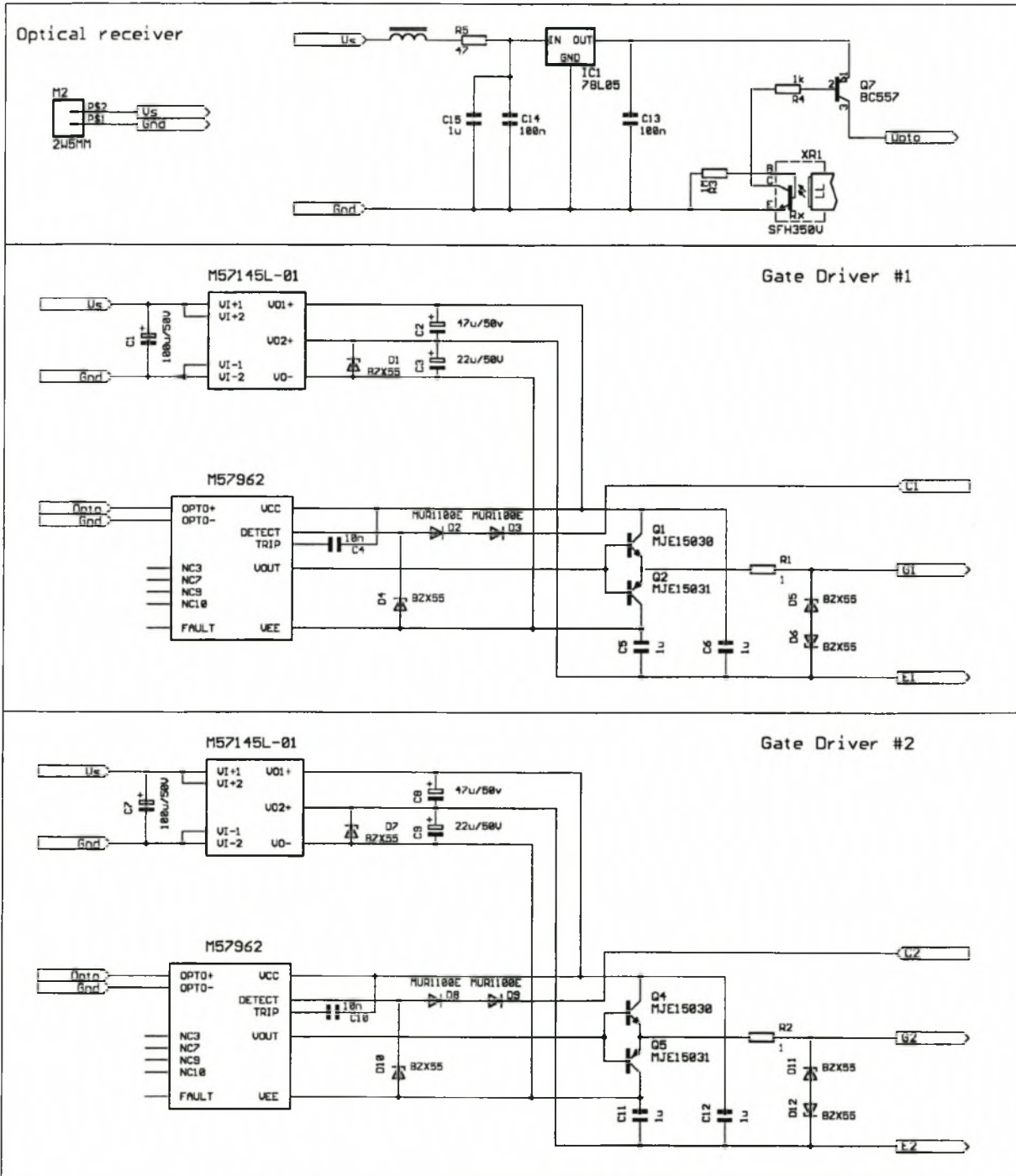


Figure B-2: Circuit diagram of IGBT driver unit.

B.3 Current limiter

The current limiter is used to prevent short-circuiting of the charging supply. The circuit consists of four identical solid-state constant current sources with over-voltage protection. The current sources are connected in series. The current limiter can directly be connected between the charging supply and the input of the pulsed power supply. Each current source is constructed from a high-voltage 1000V / 12A MOSFET and the current limiter can handle a maximum voltage of 4000 V. Each of the four MOSFETs, source resistors (R12, R22, R33 and R44) and zener diodes (D1, D2, D3 and D4) are connected in a typical constant current configuration [14]. The maximum current that can pass through the current limiter is set by the values of the emitter resistors and zener diodes. Even small differences in component values of the four current source stages can lead to an uneven voltage distribution across the four stages. Therefore, the bipolar transistors (T2, T3, T5 and T7) and JFET's (T1, T4, T6 and T8) are used to protect the MOSFETs against over-voltages. If the voltage across a MOSFET reaches a certain maximum threshold the corresponding bipolar transistor will turn on, thereby turning off the corresponding JFET. This results in an increased gate voltage, turning on the MOSFET more strongly and decreasing the voltage across that MOSFET.

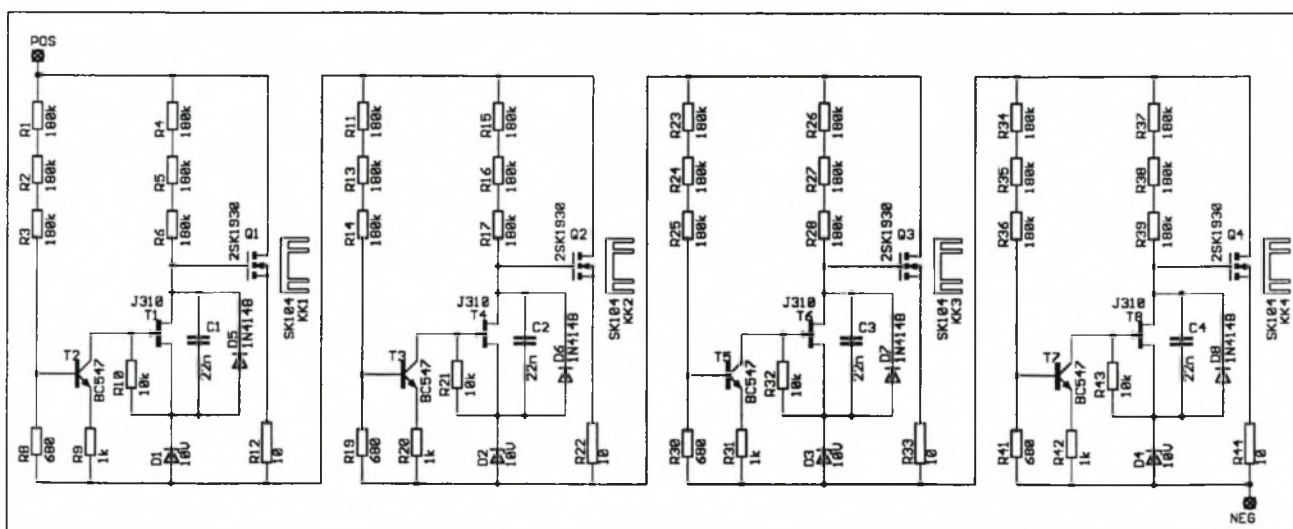


Figure B-3: Circuit diagram of solid-state current limiter.

B.4 Over-voltage snubber

The complete over-voltage snubber circuit for two IGBTs, as discussed in Chapter 6, is shown in Figure B-4. As additional safety feature, transient suppressor diodes (P1.5KE400A or P600KE400A) are used.

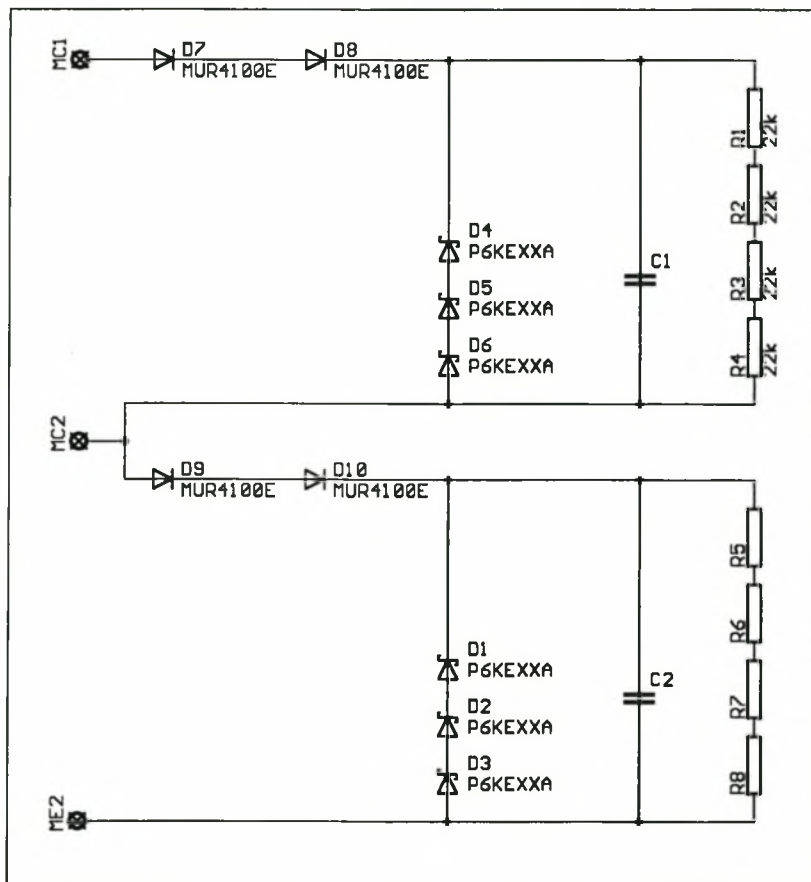


Figure B-4: Circuit diagram of over-voltage snubber.

Appendix C

IGBT data sheets

On the following pages the data sheets of the SKM300GB174D from Semikron, which is a 300A/1700V IGBT are given.

SKM 300 GB 174 D

Absolute Maximum Ratings		Values	Units
Symbol	Conditions ¹⁾		
V _{CES}		1700	V
V _{CGR}	R _{GE} = 20 kΩ	1700	V
I _C ; I _{CM}	T _{case} = 25/80 °C	320 / 230	A
I _{CM}	T _{case} = 25/80 °C; t _p = 1 ms	640 / 460	A
V _{GES}		± 20	V
P _{tot}	per IGBT, T _{case} = 25 °C	1800	W
T _J (T _{stg})		-40 ... +150 (125)	°C
V _{isol}	AC, 1 min. ⁴⁾	3400	V
humidity	IEC 60721-3-3	class 3K7/IE32	
climate	IEC 68 T.1	40/125/56	
Inverse Diode ⁸⁾			
I _F = -I _C	T _{case} = 25/80 °C	390 / 260	A
I _{FM} = -I _{CM}	T _{case} = 25/80 °C; t _p = 1 ms	640 / 460	A
I _{FSM}	t _p = 10 ms; sin.; T _J = 150 °C	2200	A
² t	t _p = 10 ms; T _J = 150 °C	24200	A ² s

SEMİTRANS® M
Low Loss IGBT Modules

SKM 300 GB 174 D



SEMİTRANS 3



GB

Features

- N channel, homogeneous Silicon structure (NPT- Non punch-through IGBT)
- Low inductance case
- High short circuit capability, self limiting
- Fast & soft inverse CAL diodes ⁸⁾
- Without hard mould
- Isolated copper baseplate using DCB Direct Copper Bonding
- Large clearance (13 mm) and creepage distances (20 mm)

Typical Applications

- AC inverter drives on mains 575 - 750 V_{AC}
- DC bus voltage 750 - 1200 V_{DC}
- Public transport (auxiliary syst.)
- Switching (not for linear use)

Characteristics		min.	typ.	max.	Units
Symbol	Conditions ¹⁾				
V _{(BR)CES}	V _{GE} = 0, I _C = 6 mA	≥ V _{CES}	-	-	V
V _{GE(th)}	V _{GE} = V _{CE} , I _C = 9 mA	4,5	5,5	6,5	V
I _{CES}	V _{GE} = 0 } T _J = 25 °C	-	0,1	1	mA
	V _{CE} = V _{CES} } T _J = 125 °C	-	8	-	
I _{GES}	V _{GE} = 20 V, V _{CE} = 0	-	-	0,2	µA
V _{CEsat}	I _C = 200 A } V _{GE} = 15 V;	-	2,8(3,25)	3,3(3,8)	V
	I _C = 300 A } T _J = 25 (125) °C }	-	3,3(3,8)	-	
g _{fs}	V _{CE} = 20 V, I _C = 200 A	80	110	-	S
C _{CHC}	per IGBT	-	-	0,7	nF
C _{ies}	V _{GE} = 0	-	14	-	nF
C _{oes}	V _{CE} = 25 V	-	2,0	-	nF
C _{res}	f = 1 MHz	-	0,6	-	nF
L _{CE}		-	-	20	nH
t _{d(on)}	V _{CC} = 1200 V	-	100	-	ns
t _r	V _{GE} = -15 V / +15 V ³⁾	-	100	-	
t _{d(off)}	I _C = 200 A, ind. load	-	900	-	ns
t _f	R _{Gon} = R _{Goff} = 6,8 Ω	-	150	-	
E _{on}	T _J = 125 °C (V _{CC} = 900 V/1200 V)	-	90/125	-	mWs
E _{off}	L _S = 60 nH (V _{CC} = 900 V/1200 V)	-	65/95	-	mWs
Inverse Diode ⁸⁾					
V _F = V _{EC}	I _F = 200 A } V _{GE} = 0 V;	-	2,15(1,9)	2,4(2,25)	V
V _F = V _{EC}	I _F = 300 A } T _J = 25 (125) °C }	-	2,4(2,2)	2,75(2,5)	
V _{TO}	T _J = 125 °C	-	1,3	1,5	V
r _t	T _J = 125 °C	-	3	4	mΩ
I _{RRM}	I _F = 200 A; T _J = 25 (125) °C ²⁾	-	100(200)	-	A
Q _{rr}	I _F = 200 A; T _J = 25 (125) °C ²⁾	-	24(50)	-	µC
E _{rr}	I _F = 200 A; T _J = 25 (125) °C ²⁾	-	10(18)	-	mWs
Thermal characteristics					
R _{thjc}	per IGBT	-	-	0,07	°C/W
R _{thjc}	per diode D	-	-	0,125	°C/W
R _{thch}	per module (50 µm grease)	-	-	0,038	°C/W

¹⁾ T_{case} = 25 °C, unless otherwise specified
²⁾ I_F = - I_C, V_R = 1200 V, -di_F/dt = 2000 A/µs, V_{GE} = 0 V
³⁾ Use V_{GEoff} = -5 ... -15 V
⁴⁾ Option V_{isol} = 4000V/1 min add suffix „H4“ - on request
⁸⁾ CAL = Controlled Axial Lifetime Technology

SKM 300 GB 174 D

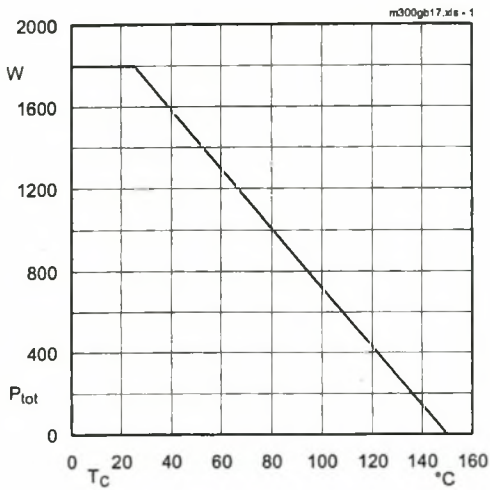


Fig. 1 Rated power dissipation $P_{tot} = f(T_C)$

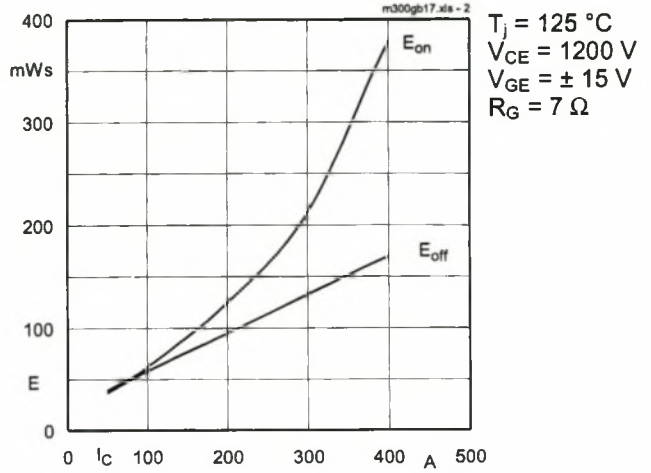


Fig. 2 Turn-on /off energy $= f(I_C)$

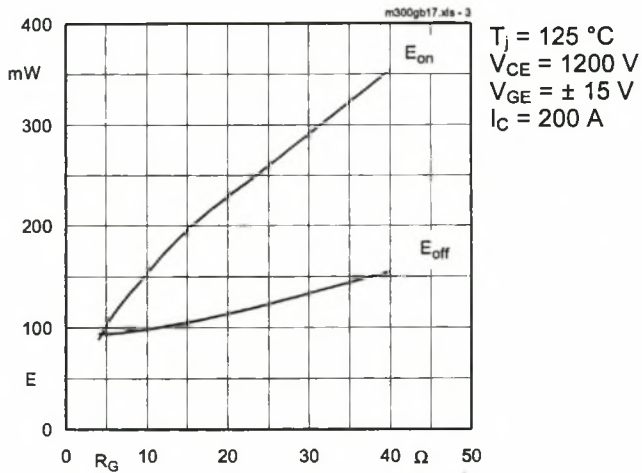


Fig. 3 Turn-on /off energy $= f(R_G)$

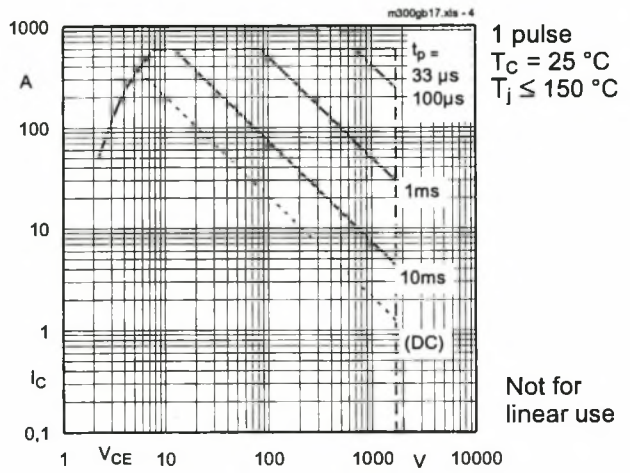


Fig. 4 Maximum safe operating area (SOA) $I_C = f(V_{CE})$

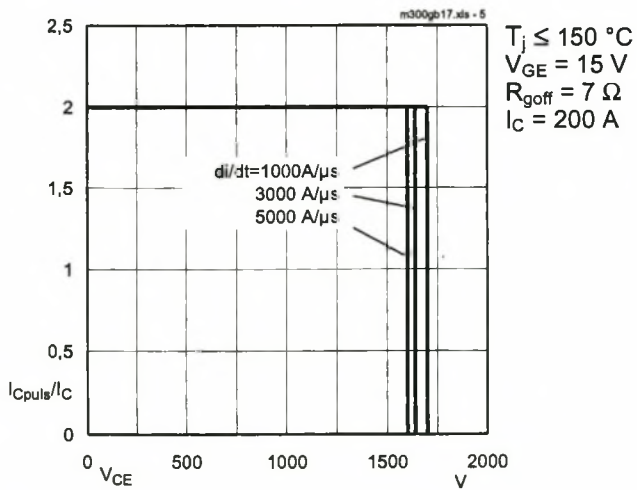


Fig. 5 Turn-off safe operating area (RBSOA)

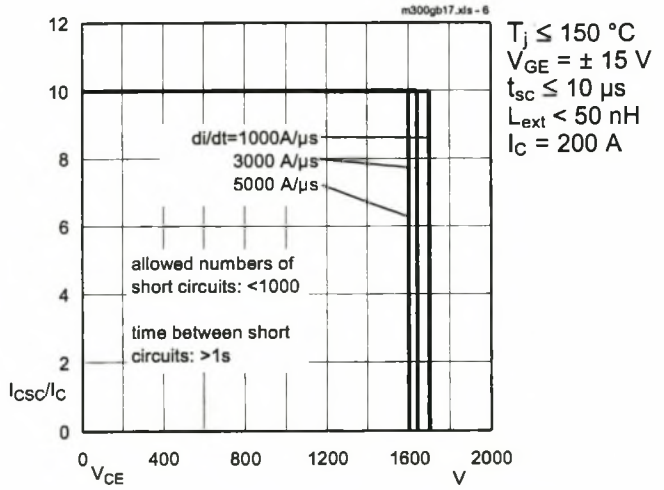


Fig. 6 Safe operating area at short circuit $I_C = f(V_{CE})$

SKM 300 GB 174 D

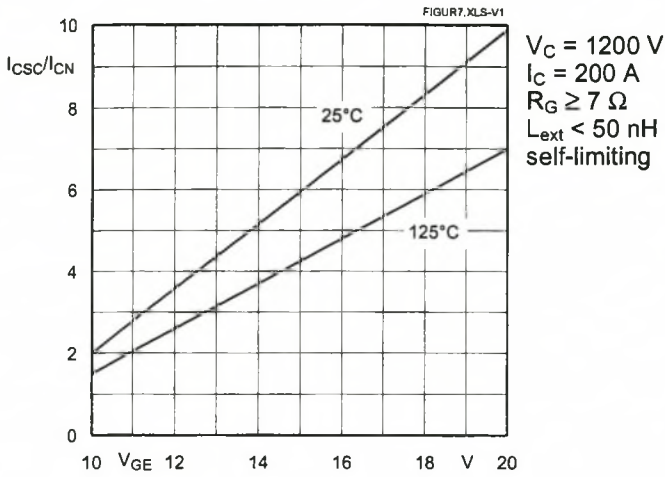


Fig. 7 Short circuit current vs. turn-on gate voltage

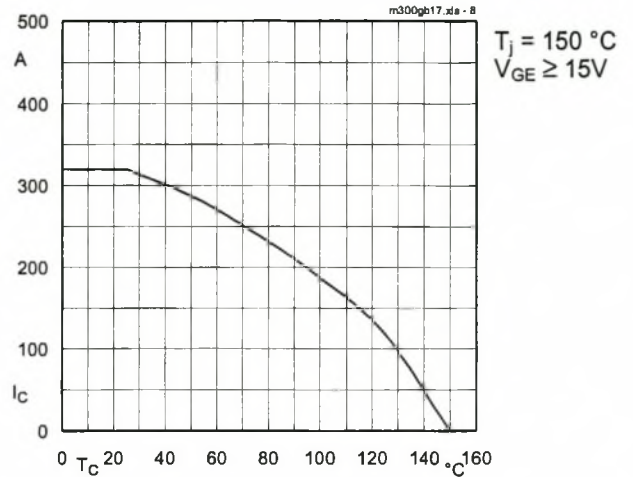


Fig. 8 Rated current vs. temperature $I_C = f(T_C)$

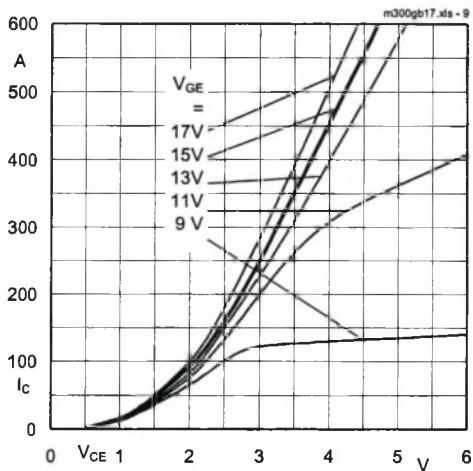


Fig. 9 Typ. output characteristic, $t_p = 250 \mu s$; $T_j = 25 \text{ }^\circ\text{C}$

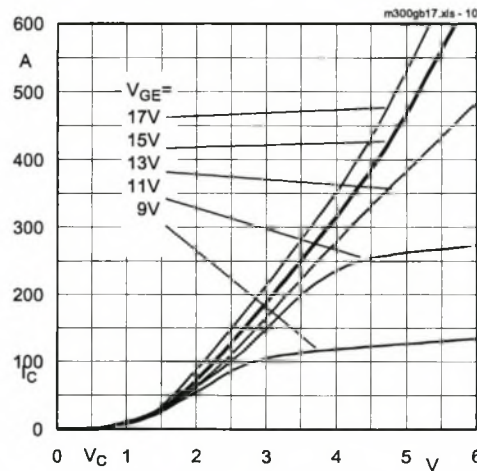


Fig. 10 Typ. output characteristic, $t_p = 250 \mu s$; $T_j = 125 \text{ }^\circ\text{C}$

$$P_{cond(t)} = V_{CEsat(t)} \cdot I_{C(t)}$$

$$V_{CEsat(t)} = V_{CE(TO)(T_j)} + r_{CE(T_j)} \cdot I_{C(t)}$$

$$V_{CE(TO)(T_j)} \leq 1,5 + 0,001 (T_j - 25) \text{ [V]}$$

$$\text{typ: } r_{CE(T_j)} = 0,0065 + 0,000018 (T_j - 25) \text{ [\Omega]}$$

$$\text{max: } r_{CE(T_j)} \leq 0,0088 + 0,000023 (T_j - 25) \text{ [\Omega]}$$

$$\text{valid for } V_{GE} \leq +15 \begin{matrix} +2 \\ -1 \end{matrix} \text{ [V]; } I_C \geq 0,3 I_{Cnom}$$

Fig. 11 Typ. saturation characteristic (IGBT)
Calculation elements and equations

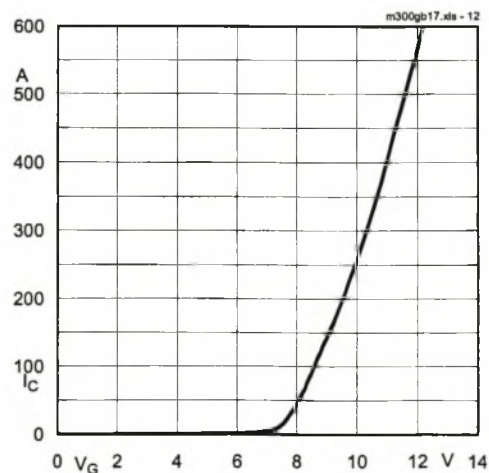


Fig. 12 Typ. transfer characteristic, $t_p = 250 \mu s$; $V_{CE} = 20 \text{ V}$

SKM 300 GB 174 D

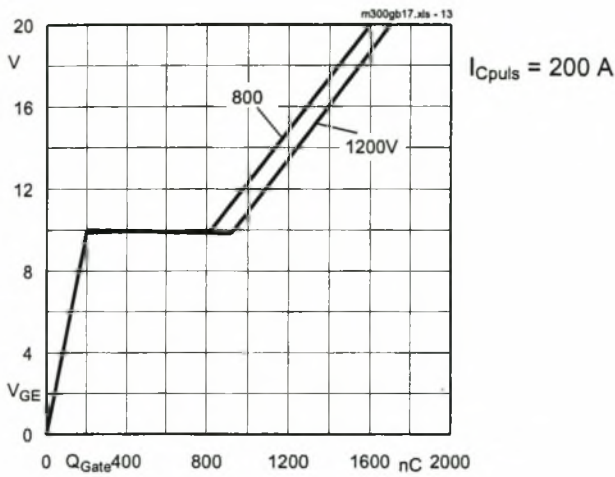


Fig. 13 Typ. gate charge characteristic

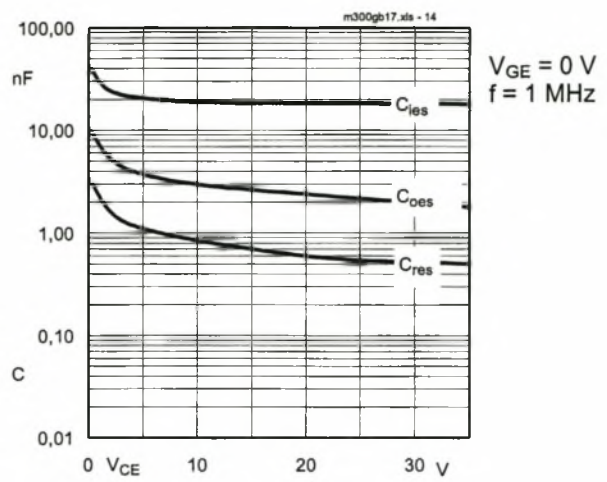


Fig. 14 Typ. capacitances vs. V_{CE}

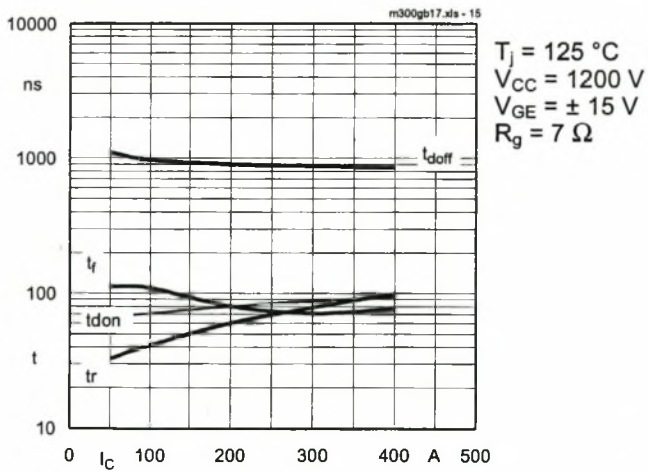


Fig. 15 Typ. switching times vs. I_C

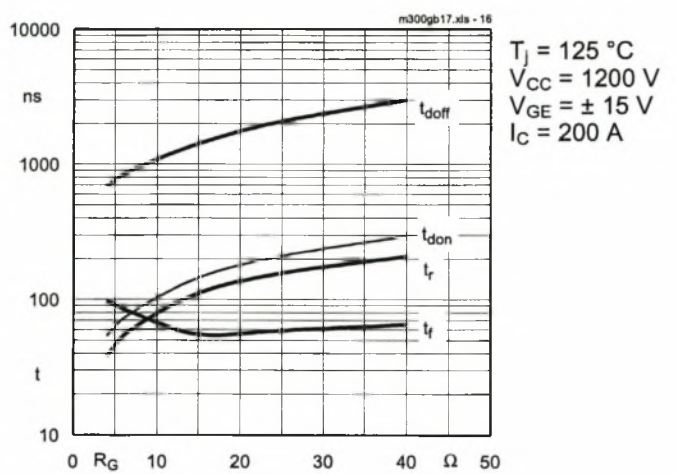


Fig. 16 Typ. switching times vs. gate resistor R_G

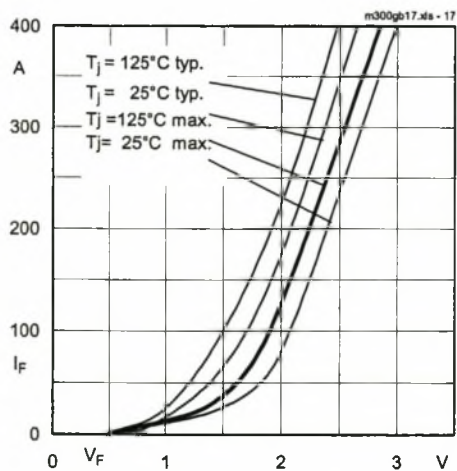


Fig. 17 Typ. CAL diode forward characteristic

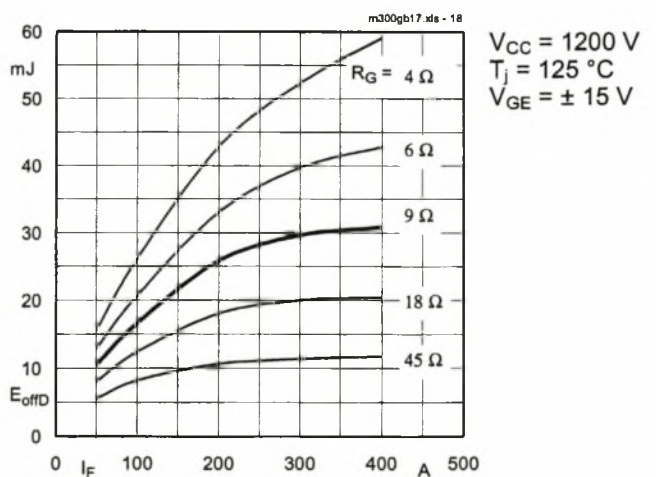


Fig. 18 Diode turn-off energy dissipation per pulse

SKM 300 GB 174 D

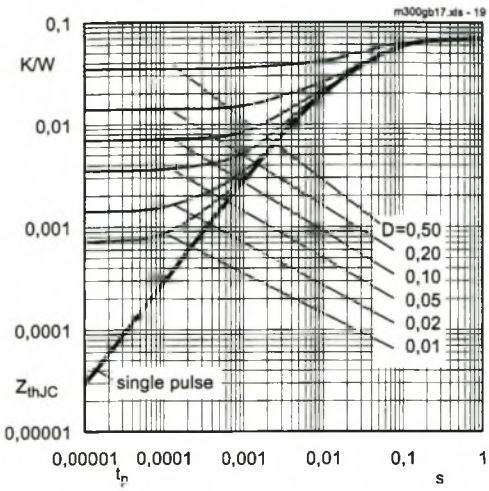


Fig. 19 Transient thermal impedance of IGBT
 $Z_{thJC} = f(t_p)$; $D = t_p / t_c = t_p \cdot f$

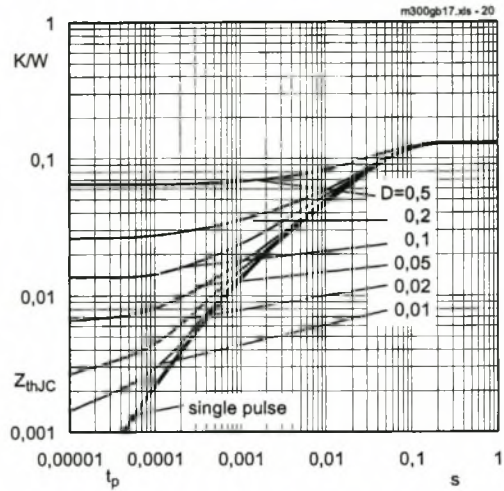


Fig. 20 Transient thermal impedance of inverse CAL diodes
 $Z_{thJC} = f(t_p)$; $D = t_p / t_c = t_p \cdot f$

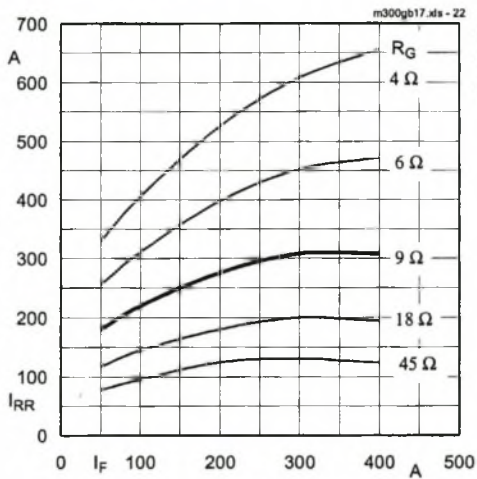


Fig. 22 Typ. CAL diode peak reverse recovery current $I_{RR} = f(I_F; R_G)$

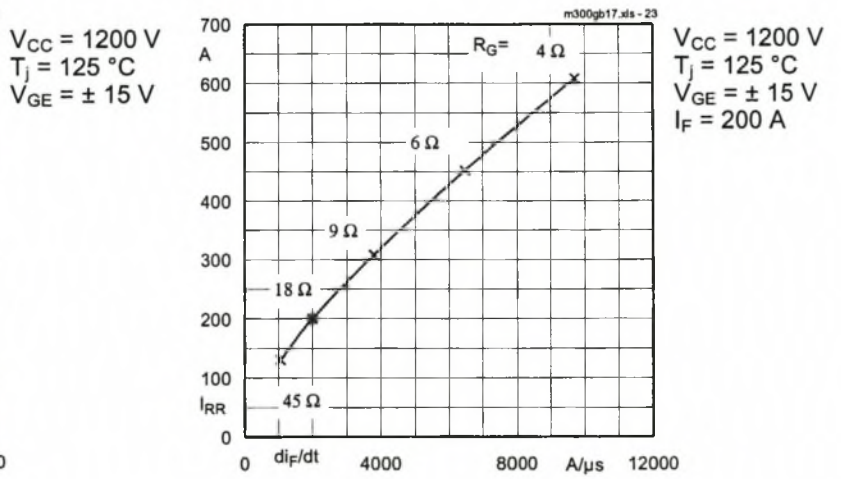


Fig. 23 Typ. CAL diode peak reverse recovery current $I_{RR} = f(di/dt)$

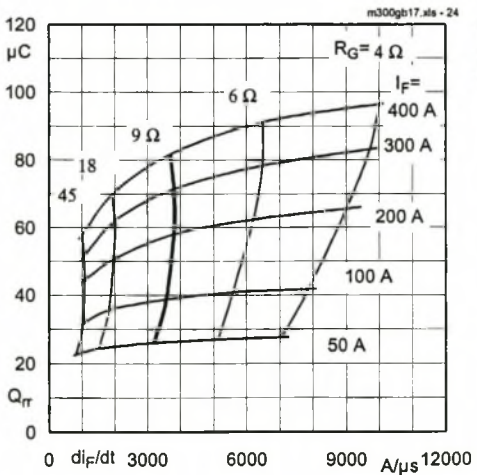
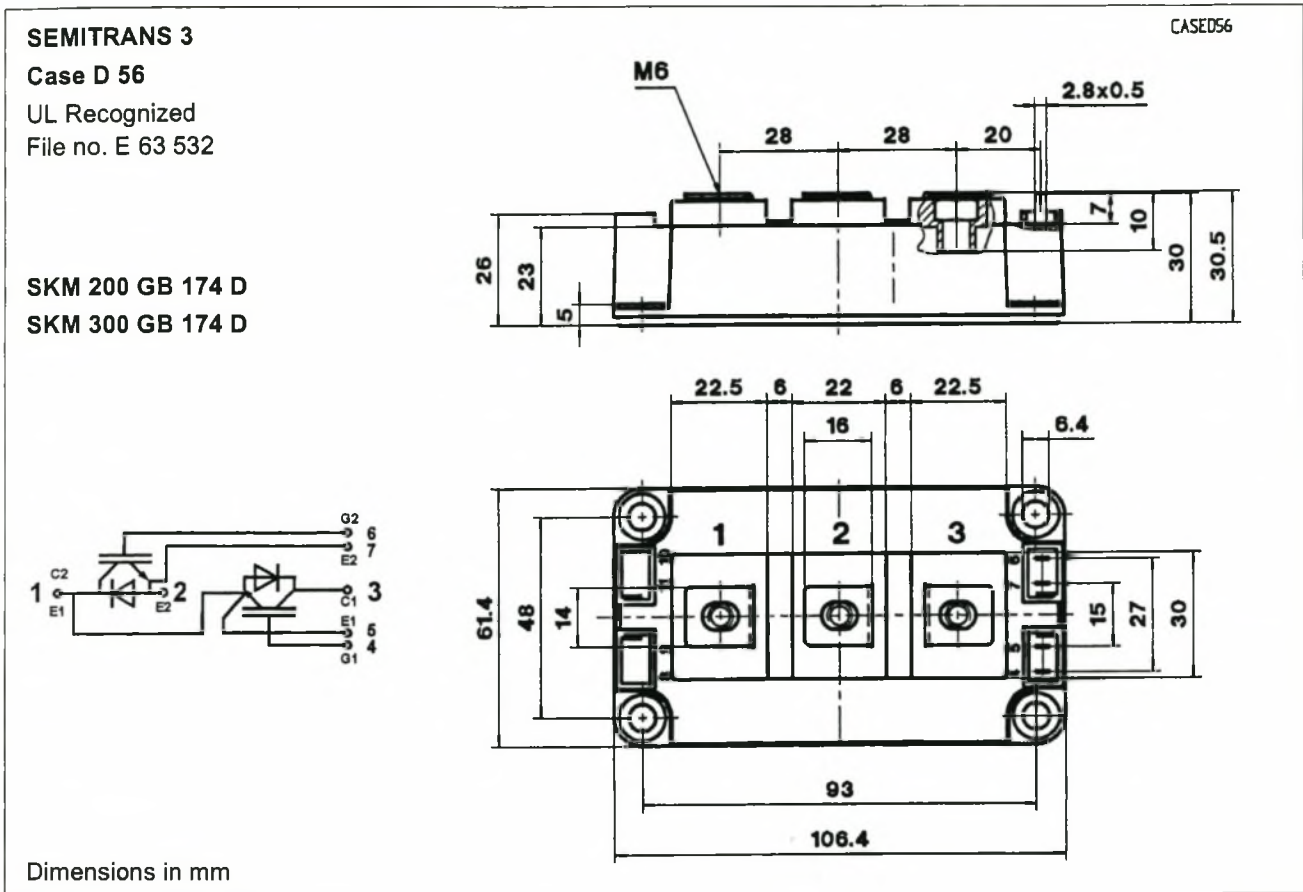


Fig. 24 Typ. CAL diode recovered charge

SKM 300 GB 174 D



Case outline and circuit diagram

Symbol	Conditions	Values			Units
		min.	typ.	max.	
M ₁	to heatsink, SI Units (M6)	3	—	5	Nm
	to heatsink, US Units	27	—	44	lb.in.
M ₂	for terminals, SI Units (M6)	2,5	—	5	Nm
	for terminals, US Units	22	—	44	lb.in.
a		—	—	5x9,81	m/s ²
w		—	—	325	g

This is an electrostatic discharge sensitive device (ESDS). Please observe the international standard IEC 747-1, Chapter IX.

Twelve devices are supplied in one SEMIBOX D without mounting hardware, which can be ordered separately under Ident No. 33321100 (for 10 SEMITRANS 3)

This technical information specifies semiconductor devices but promises no characteristics. No warranty or guarantee expressed or implied is made regarding delivery, performance or suitability.

Bibliography

- [1] Ball, S.E., "Optimum Switching Time for Magnetic Switches," Physics International Company, San Leandro.
- [2] *Basic Semiconductor Thermal Measurement*, ref.no. AN1570, Motorola, <http://www.onsemi.com/pub/Collateral/AN1570-D.pdf> (July 2002)
- [3] Bhadani, P.K. and Harrison, R.G., "Novel discharge circuit for a multijoule TEA CO₂ laser," *Rev. Sci. Instrum.*, vol. 65, no. 3, March 1994, pp. 563-566.
- [4] Biddulph, D., *Radio Communication Handbook*, Sixth Edition, Radio Society of Great Britain, 1994, Chapter 22, p. 22.3.
- [5] Cridland, J.V., and Howells, S., "The dependence of transversely excited atmospheric CO₂ laser performance on circuit configuration," *J. Appl. Phys.*, vol. 53, no. 6, June 1982, pp. 4016-4019.
- [6] Dittmer, K.J., et al., "Failure analysis of aluminium wire bonds in high power IGBT modules", *Materials Research Society Symposium Proceedings*, San Fransisco, 1995, pp. 251-256.
- [7] Druckmann, I., Gabay, S., and Smilanski, I., "A new Algorithm for the Design of Magnetic Pulse Compressors," report, Beer Sheva, Israel.
- [8] Georgescu, N., "A new look at the energy efficiency of a series pulse compressor with resistive losses," *Proc.10th IEEE Pulsed Power Conference*, Arlington, Virginia, 1995.

- [9] Gerritsen, J.W., Keet, A.L., Ernst, G.J., and Wittemann, W.J., "High-efficiency operation of a gas discharge XeCl laser using a magnetically induced resonant voltage overshoot circuit," *J. Appl. Phys.*, vol. 67, no. 7, Apr. 1990, pp. 3517-3519.
- [10] Greenwood, M., Gowar, J., and Grant, D.A., "Integrated High Repetition Rate Pulse Compressor Design," *8th IEEE International Pulsed Power Conference*, San Diego, California, 1991, pp. 750-753.
- [11] Gumhalter, H., *Power Supply systems in Communication Engineering*, Siemens, John Wiley & Sons, Chichester, 1985.
- [12] Hatanaka, H., et al., "All Solid State Magnetic Pulse Compressor Switched with Insulated Gate Bipolar Transistors for a 5-kW TEA CO₂ laser," *9th IEEE International Pulsed Power Conference*, Albuquerque, New Mexico, 1993, pp. 312-315.
- [13] Haus, H.A., and Melcher, J.R., *Electromagnetic Fields and Energy*, Prentice-Hall, 1989, Chapter 9.
- [14] Horowitz, P. and Hill, W., *The art of electronics*, Second Edition, Cambridge University Press, Cambridge, Massachusetts, 1995, Chapter 2, pp.72-76.
- [15] Hudgins, J.L., et al., "High di/dt Switching with Thyristors", *IEEE Transactions on Power Electronics*, vol. 2, no. 2, 1987, pp. 143-147.
- [16] *IGBT Module Application Manual*, ref.no. IGBT-01 (Rev.2), Hitachi Ltd., 1990.
- [17] *IGBT Ratings And Characteristics*, ref.no. AN4503, Dynex semiconductor, http://www.dynexsemi.com/assets/DNX_AN4504_Jul02.pdf (current December 2002).
- [18] Keet, A.L., and Groenenboom, M., "High voltage solid-state pulser for high repetition-rate gas lasers," *Seventh International Symposium on Gas Flow and Chemical Laser*, 1988, pp. 440-442.
- [19] Kobhio, M.N., et al., "Kinetics and Electrical Modeling of a Long Pulse High Efficiency XeCl Laser with Double Discharge and Fast Magnetic Switch," *Eighth International Symposium on Gas Flow and Chemical Laser*, 1990, pp. 555-558.

- [20] Lademann, J., *Untersuchungen zur Entladungsstabilität von TEA CO₂-Lasern*, Dissertation, Friedrich-Schiller-Universität Jena, Berlin, 1990 (in German).
- [21] Large, S., and Walker, P., "Rapid Cycle Testing of High Current IGBT Powerswitch Modules", *8th International Conference on Power Electronics and Variable Speed Drives as Flow and Chemical Lasers, IEE Conference Publications*, London, 2000, pp. 235-240.
- [22] Letardi, T., et al., "Theoretical Study of Prepulse-main Discharge XeCl Lasers," *Lasers*, 1991, pp. 676-683.
- [23] Lowke, J.J., Phelps, A.V., and Irwin, B.W., *Journal of Applied Physics*, vol. 44, no. 10, 1973, p. 4664.
- [24] Mallwitz, R., *GTO-Thyristoren in Hochspannungs-Impulsanwendung*, Diplomarbeit, Institut Allgemeine Elektrotechnik und Leistungselektronik, Technische Universität "Otto von Guericke" Magdeburg, 1994 (in German).
- [25] McDonald, D.W. and Watson, I.A., "Modelling Gas Laser Discharges as Pulsed Power Components," *Proceedings of the Tenth International Conference on Gas Discharges and their Applications*, Swansea, UK, 1992, pp. 156-160.
- [26] Merrit, B.T., and Dreifuerst, G.R., "Development and operation of a solid-state switch for thyatron replacement", *Eighth IEEE International Pulsed Power Conference*, San Diego, California, June, 1991.
- [27] Mohan, N., Undeland, T.M., and Robbins, W.P., *Power Electronics*, Second Edition, John Wiley & Sons, New York, 1995, Chapters 25, 27 and 30.
- [28] Nasar, S.A., *Electric Energy Systems*, Prentice Hall, New Jersey, 1996, Chapter 4.
- [29] Neaman, D.A., *Electronic Circuit Analysis and Design*, McGraw-Hill, Bodston, Massachusetts, 1996, chapter 5.
- [30] Nehmadi, N., Ifrah, Y., and Druckmann, I., "Experimental result study and design enhancement of magnetic pulse compression circuit by using PSPICE simulation Program," *Rev. Sci. Instrum*, vol. 61, no. 12, Dec. 1990, pp. 3807-381.

- [31] Nilsson, J.W. and Riedel, S.A., *Electric Circuits*, Fifth Edition, Addison-Wesley Publishing Company, Massachusetts, 1996, Chapter 14.
- [32] Nunnally, W.C., *Magnetic Switches and Circuits*, tech. report LA-8862-MS, Los Alamos National Laboratory, Los Alamos, New Mexico, 1981.
- [33] *Package Thermal Characterization Methodologies*, ref.no. SZZA003, Texas Instruments Incorporation, 1999, <http://www-2.ti.com/sc/techlit/szza003.pdf> (July 2002)
- [34] Scheuermann, U., and Hecht, U., "Power Cycling Lifetime of Advanced Power Modules for Different Temperature Swings", tech. report, Semikron, 1992, http://www.semikron.com/pdf/pcim2002_usuh.pdf (August 2002).
- [35] Smith, C.H., "Magnetic losses in metallic glass under pulsed excitation," *IEEE Transactions on Nuclear Science*, vol. NS-30, no. 4, August 1983, pp. 2918-2920.
- [36] Smith, C.H., "Magnetic Pulse Compression by Metallic Glasses," *J. Appl. Phys.*, vol. 64, no. 10, November 1988, pp. 6032-6034.
- [37] Smith, C.H., and Nathasingh, D.M., "Magnetic Characteristics of Amorphous Metal Saturable Reactors in Pulsed Power Systems," *3rd European Particle Accelerator Conference*, Berlin, Germany, March 1992.
- [38] *Star-HSpice Manual*, Avant, 1998, <http://www.eecs.umich.edu/~lding/research/hspice/hspice.html> (November 2002).
- [39] Swart, P., and von Bergmann, H.M., "Comparative evaluation of pulsing circuits for kHz Excimer laser systems," *7th IEEE International Pulsed Power Conference*, Monterey, California, 1989, pp. 293-296.
- [40] Swart, P., Bredenkamp, G., and von Bergmann, H., "Computer spreadsheet design, numerical simulation and practical evaluation of a lossy series pulse compressor," *6th IEEE International Pulsed Power Conference*, Arlington, Virginia, 1987, pp. 680-683.
- [41] Swart, P., Bredenkamp, G., and von Bergmann, H., "Computer Spreadsheet Designs, Numerical Simulation and Practical Evaluation of a Lossy Series Pulse Compressor," *Proc. 6th IEEE Pulsed Power Conf.*, Arlington, Virginia, 1987, pp. 680-683.

- [42] Swart, P.H., "Resonant Inversion Pulser Topology with Reduced Semiconductor Ratings," tech. report, University of Potchefstroom.
- [43] Swart, P.H., and Bredenkamp, G.L. "The Design of High Frequency, High Repetition Rate, Pulse Power Transformers through Frequency Domain Modelling," tech. report, Rand Afrikaans University.
- [44] Swart, P.H., van Wyk, J.D., Pretorius, J.H., and von Bergmann, H.M., "Strategies for Multistage Pulse Compressor Design and Optimization," *Proc. 20th Intern. Power Modulator Symp.*, Myrtle Beach, South Carolina, 1992, pp. 209-212.
- [45] Swart, P.H., von Bergmann, H.M., and Pretorius, J.H.C., "All Solid State Switched Pulser for Multi-kilowatt, Multi-kilohertz Excimer and CO₂ TEA lasers," *Proc. 8th IEEE Pulsed Power Conf.*, San Diego, California, 1991, pp. 743-749.
- [46] Taylor, R.S. and Leopold, K.E., "Magnetic-spiker excitation of gas-discharge lasers," *Appl. Phys. B*, vol. 59, 1994, pp. 479-508.
- [47] von Bergmann, H.M., and Stehmann, T., "Energy efficiency of the lossy series magnetic pulse compressor," *SAIP conference*, Potchefstroom, South Africa, 2002.
- [48] Yamaguchi, M., et al., "DC-type voltage reset characteristics for soft magnetic cores at high frequencies," *J. Appl. Phys.*, vol. 64, no. 10, November 1988, pp. 6038-6040.
- [49] Yatsui, K., et al., "All-Solid-State Excitation Circuit using Saturable Transformer for Excimer Laser Excitation", *Gas Flow and Chemical Lasers*, vol. 1810, 1992, pp. 396-399.